

CRITICAL EVALUATION OF STRENGTH-CONTROLLING VARIABLES IN CERAMICS

BY

BRIAN MICHAEL PINTO

A THESIS
SUBMITTED TO THE FACULTY OF

ALFRED UNIVERSITY

IN PARTIAL FULFILLMENT OF THE REQUIREMENTS
FOR THE DEGREE OF

DOCTOR OF PHILOSOPHY

IN

CERAMICS

ALFRED, NEW YORK
FEBRUARY, 2006

Alfred University theses are copyright protected and may be used for education or personal research only. Reproduction or distribution in part or whole is prohibited without written permission from the author.

CRITICAL EVALUATION OF STRENGTH-CONTROLLING
VARIABLES IN CERAMICS

BY

BRIAN MICHAEL PINTO

B.S. ALFRED UNIVERSITY (1999)

M.S. ALFRED UNIVERSITY (2001)

SIGNATURE OF AUTHOR _____ (Signature on file)

APPROVED BY _____ (Signature on file)

WILLIAM M. CARTY, ADVISOR

(Signature on file)

JAMES R. VARNER, ADVISORY COMMITTEE

(Signature on file)

PAUL F. JOHNSON, ADVISORY COMMITTEE

(Signature on file)

SCOTT MISTURE, ADVISORY COMMITTEE

(Signature on file)

DAVID EARL, CHAIR, ORAL THESIS DEFENSE

ACCEPTED BY _____ (Signature on file)

ALASTAIR CORMACK, DEAN,
KAZUO INAMORI SCHOOL OF ENGINEERING

ACCEPTED BY _____ (Signature on file)

ALASTAIR CORMACK,
DIRECTOR OF GRADUATE STUDIES,
ALFRED UNIVERSITY

ACKNOWLEDGEMENTS

First and foremost, I would like to thank Dr. William Carty. Not only has he been my advisor, but my mentor as well. Throughout the years his faith in my abilities has given me the confidence to achieve something that I initially did not think I was capable of. I can't thank him enough for all the guidance and support he has provided me in times of both academic and personal need. Without his counsel and expertise, this project never would have been the success it turned out to be.

I would also like to acknowledge my thesis advisory committee, Dr. James Varner, Dr. Scott Misture, and Dr. Paul Johnson. Not only did they assist me at various stages of this investigation, they also challenged me and continually provided different perspectives on the subject matter that allowed me to critically evaluate my own viewpoints and more effectively focus my efforts.

Thanks to NYSERDA for funding this investigation. My thanks also to Lapp Insulators and Victor Insulators for use of their materials and facilities. Thanks to Andrew Wereszczak, Mithilesh Kumar, Terry Guild, Hyojin Lee, Ungsoo Kim, Brett Schulz and the rest of Dr. Carty's graduate group, past and present, for their advice and assistance.

Thanks to my fiancée, Amanda, for her love, patience, and emotional support through good times and bad. This achievement is a stepping-stone to our new life together, and I am grateful that she will be there to share my success and life with me.

Special thanks to my family for all their unconditional love and support throughout my entire college career and life. Mom, Bob, Phil- thanks for always being there for me. Dad, I accredit to you my strength and perseverance – the will to fight on when times were tough and I didn't know if I could make it through this. I know that you always were and are proud of me. Until we meet again. I love you.

TABLE OF CONTENTS

Title Page	i
Signature page	ii
Acknowledgements	iii
Table of Contents	iv
List of Tables	viii
List of Figures	x
Abstract	xv
1. Introduction	1
1.1 Fracture Mechanics	4
1.2 The Griffith Criterion	8
1.2.1 <i>Failure Stress</i>	12
1.2.2 <i>Elastic Modulus</i>	13
1.2.3 <i>Fracture Surface Energy</i>	16
1.2.4 <i>Flaw Size</i>	19
1.3 Microstructural Strength Parameters	23
1.3.1 <i>Porosity</i>	23
1.3.2 <i>Volume Fraction of Dispersed Phase</i>	25
1.3.3 <i>Grain Size Effects</i>	27
1.4 Raw Material Effects	30
1.4.1 <i>Thermal Stresses</i>	30
1.4.2 <i>CTE Mismatch</i>	31
1.4.3 <i>Filler Particles in Whitewares and Porcelains</i>	35
1.5 Overview of Porcelain (Subject of Study)	40
1.6 Prevailing Porcelain Theory	42
1.6.1 <i>Mullite Theory</i>	43
1.6.2 <i>Dispersion Theory</i>	46
1.6.3 <i>Prestress Theory</i>	49
2. Experimental Overview	50
2.1 Compositions	50
2.1.1 <i>Porcelain A</i>	50
2.1.2 <i>Porcelain B</i>	50
2.1.3 <i>Porcelain C</i>	51
2.1.4 <i>Stoneware Porcelain</i>	52

2.2	Fillers/ Particle Size	52
2.2.1	Quartz (SiO_2)	52
2.2.2	Alumina (Al_2O_3)	53
2.2.3	Mullite ($3\text{Al}_2\text{O}_3 \cdot 2\text{SiO}_2$)	53
2.2.4	Mg-Al Spinel (MgAl_2O_4)	53
2.2.5	Filler Particle Size	54
2.3	Nomenclature	55
3.	General Procedures	56
3.1	Sample Forming	56
3.1.1	Slip Casting	56
3.1.2	Filter Pressing	57
3.1.3	Baroid Filtration	58
3.1.4	Extrusion	59
3.2	Property Analysis	60
3.2.1	Bulk Density/ Apparent Porosity	60
3.2.2	Flexure Strength (Failure Stress)	60
3.2.3	Elastic Modulus/ Poisson's Ratio	61
3.3	General Results	63
3.3.1	Bulk Density/ Apparent Porosity	63
3.3.2	Mechanical Properties	64
4.	Determining Flaw Size Via Griffith Equation	66
4.1	Overview	66
4.2	New Fracture Surface Energy Measurement Technique	67
4.2.1	Qualification of New Technique	67
4.2.2	Crazing	69
4.2.3	Use of Griffith Equation	72
4.3	Procedure	73
4.3.1	Sample Preparation	73
4.3.2	Dip Glazing	73
4.3.3	Failure Testing	74
4.3.4	Mechanical Properties	74
4.3.5	Microscopic Analysis	76
4.4	Experimental Results	77
4.4.1	Observed Flaw Size	77
4.4.2	Measured Fracture Surface Energy	78

4.5	Derived Property Relationships	80
4.5.1	<i>Fracture Surface Energy vs. Elastic Modulus</i>	80
4.5.2	<i>Flexure Strength vs. Elastic Modulus</i>	84
4.6	Predictions	87
4.6.1	<i>Fracture Surface Energy</i>	87
4.6.2	<i>Critical Flaw Size</i>	88
4.7	Summary	91
5.	Evaluation of Fired Microstructure and Strength	93
5.1	Overview	93
5.2	Preliminary Investigation (Gradient Furnace)	93
5.2.1	<i>Experimental Procedures</i>	93
5.2.2	<i>Over-/Under-Firing</i>	94
5.2.3	<i>Firing Range</i>	96
5.3	<i>Main Investigation</i>	97
5.3.1	<i>Experimental Procedures</i>	97
5.4	Experimental Results	98
5.4.1	<i>Bulk Density vs. Temperature</i>	98
5.4.2	<i>Microstructures</i>	98
5.4.3	<i>Mechanical Properties</i>	108
5.5	Property Analysis	110
5.5.1	<i>Fracture Surface Energy vs. Temperature</i>	110
5.5.2	<i>Critical Flaw Size vs. Temperature</i>	111
5.5.3	<i>Bulk Density Effects</i>	113
5.6	Summary	114
6.	Evaluation of Filler Particle Contribution to Strength	116
6.1	Overview	116
6.2	Porcelain Fillers	116
6.2.1	<i>Filler Particles / Size Effects</i>	116
6.2.2	<i>Residual Stresses and Strains (CTE Mismatch)</i>	118
6.3	Experimental Procedure	118
6.3.1	<i>X-ray Residual Filler Strain Measurement</i>	119
6.3.2	<i>Mechanical Testing</i>	122
6.4	Experimental Results	122
6.4.1	<i>Residual Filler Strain</i>	122
6.4.2	<i>Mechanical Properties</i>	126

6.5	Derived Results	128
6.5.1	<i>Critical Flaw Size</i>	128
6.5.2	<i>Favorable Glass Prestresses</i>	129
6.6	Summary	132
7.	Critical Flaws and Strength	134
7.1	Overview	134
7.2	Independence of Filler Size to Measurable Properties	134
7.3	Constant Flaw Size Hypothesis	136
7.4	Flexure Test Simulation	137
7.4.1	<i>Analysis of Testing Methods</i>	137
7.4.2	<i>Theoretical Model Parameters</i>	140
7.4.3	<i>Experimental Procedure</i>	142
7.5	Experimental Results	144
7.5.1	<i>Flexure Test Simulation</i>	144
7.5.2	<i>Estimation of Flaw Concentration</i>	145
7.6	Origin of Critical Flaws	146
7.6.1	<i>Processing Defects</i>	146
7.6.2	<i>Inhomogeneous Microstructure (Agglomerates)</i>	148
7.6.3	<i>Degree of Mixedness</i>	152
7.7	Elimination of Intrinsic Flaws (Reduction of $2c$)	154
7.8	Summary	158
8.	Conclusions	160
9.	Suggestions for Future Work	168
9.1	Technique to Reduce Flaw Size	168
9.2	Effect of Number of Surface Flaws on Strength	171
9.3	Triangulation of Fracture Origins	172
	References	175
	APPENDIX A. List of Experimental Variables.	183
	APPENDIX B. Raw Data from Material Property Testing.	184
	APPENDIX C. Raw Data from Mechanical Property Testing.	187
	APPENDIX D. Flaw Size Evaluation Data.	191

LIST OF TABLES

I.	Bond Stiffness and Elastic Moduli for Various Types of Materials.	14
II.	Summary of Results Regarding Various Investigations on Optimum Filler Particle Size and Strength.	28
III.	Approximate Thermal Expansion of Some Body Ingredients.	35
IV.	Primary Raw Materials Used in the Manufacture of Porcelains.	41
V.	Porcelain A Base Batch Composition.	50
VI.	Raw Materials Used to Make Various Porcelain A Compositions.	51
VII.	Porcelain B Chemical Compositions.	51
VIII.	Silica Porcelain C Chemical Composition.	52
IX.	Stoneware Porcelain Chemical Composition.	52
X.	Chemical Analysis of Quartz Filler Material.	53
XI.	Chemical Analysis of Alumina Filler Material.	53
XII.	Chemical Analysis of Mullite Filler Material.	53
XIII.	Chemical Analysis of Spinel Filler Material.	54
XIV.	Mean Initial Filler Particle Sizes Used in All Aspects of this Investigation.	54
XV.	Bulk Density of Porcelain Compositions Used in this Investigation.	64
XVI.	Four-point MOR and Elastic Modulus Values for All Compositions Tested, Including a Ratio of the Two Properties.	64
XVII.	Glaze Composition and Raw Materials.	74
XVIII.	MOR Values for Glazed and Unglazed Porcelain Samples.	79
XIX.	Surface Energies and Elastic Moduli of Various Materials (Experimental and Literature Values).	83
XX.	Measured and Calculated Material Properties for Silica B and Alumina B Porcelain Compositions.	90
XXI.	Firing Temperatures Selected for Study.	98
XXII.	Grain Composition and CTE for all Filler Materials Investigated.	117
XXIII.	Number of Quartz Particles Contained Within the X-ray Diffraction Interaction Volume as a Function of Particle Size.	121
XXIV.	Critical Flaw Size for All Experimental Porcelain Compositions.	135

XXV.	Example of Sieve Analysis for Industrial-Grade Quartz Raw Material.	151
XXVI.	Pyroplastic Deformation and Four-Point Flexure Strength Versus Mixing Mode Where Assumed Degree of Mixedness Decreases From Top to Bottom.	155
XXVII.	Bulk Density Raw Data for Porcelain A Compositions.	184
XXVIII.	Bulk Density Raw Data for Porcelain B Compositions and Stoneware.	185
XXIX.	Linear Shrinkage Raw Data from Gradient Furnace Experiment.	186
XXX.	Four-Point Flexure Strength Raw Data for Mullite A and Spinel A Porcelain Bodies.	187
XXXI.	Four-Point Flexure Strength Raw Data for Alumina A Porcelain Body.	187
XXXII.	Four-Point Flexure Strength Raw Data for Silica B Porcelain Body.	188
XXXIII.	Four-Point Flexure Strength Raw Data for Alumina B Porcelain Body.	188
XXXIV.	Four-Point Flexure Strength Raw Data for Stoneware Porcelain Body.	188
XXXV.	Elastic Modulus Raw Data for Porcelain A Bodies.	189
XXXVI.	Elastic Modulus Raw Data for Porcelain B and Stoneware Bodies.	190
XXXVII.	Three-Point Flexure Data and Measurements of Flaw Depth (Glaze Thickness).	191

LIST OF FIGURES

1.	Schematic of a typical crack growth curve.	4
2.	The three pure modes of loading.	5
3.	Schematic depicting the energy balance for a crack in an infinite plate.	9
4.	Breakaway position of crack front from two pairs of pinning positions, separated by distance x .	18
5.	Schematic of glass-particle system showing a) residual stress distribution, b) crack orientation, and c) crack propagation through a microstructure in which $CTE_{\text{glass}} < CTE_{\text{particle}}$.	32
6.	Schematic of glass-particle system showing a) residual stress distribution, b) crack orientation, and c) spontaneous crack behavior in a microstructure in which $CTE_{\text{particle}} > CTE_{\text{glass}}$.	33
7.	Schematic of glass-particle system showing the path of a surface crack when a) $CTE_{\text{particle}} < CTE_{\text{glass}}$ b) $CTE_{\text{particle}} > CTE_{\text{glass}}$ and c) $CTE_{\text{particle}} = CTE_{\text{glass}}$.	34
8.	Plot of phase concentration and four-point flexure strength of a silica porcelain composition as a function of filler particle size.	46
9.	Plot of residual strain versus filler particle size of two porcelain bodies, showing a difference in maximum residual strain.	48
10.	Schematics of gypsum casting mold, containing sample.	57
11.	Schematic of a baroid filtration cell.	58
12.	Schematic of pulse-echo apparatus used for elastic modulus measurement.	62
13.	Schematic of SENB apparatus and setup with magnification of notch showing radius of flaw tip and microcrack.	68
14.	Schematic of a micro-indented marking on a sample surface, including radial cracks.	69
15.	Photograph of pottery surface containing crazing effect.	70
16.	SEM secondary electron image showing the glaze/body interface with a crack caused by crazing.	71
17.	Photograph of glazed porcelain rod with crazing, with magnification of glaze surface.	75
18.	Schematic of three-point flexure setup for fracture surface energy testing, along with a cut-way view of a typical sample, denoting the flaw length (c) and rod length (L) and diameter (d).	76
19.	SEM secondary electron image showing the glaze/body interface with cracks caused by crazing.	77

20.	SEM micrograph showing the glaze/body interface with crack running through a bubble.	78
21.	Plots of σ_R versus $1/c$ for all samples.	80
22.	Flexure strength versus CTE mismatch of a series of glazes on Silica B and Alumina B body compositions.	81
23.	Plot of experimental results; fracture surface energy versus elastic modulus.	82
24.	Plot of elastic modulus versus fracture surface energy for various ceramics and glasses (listed in Table XVIII).	84
25.	Plot of MOR versus elastic modulus of all porcelain compositions studied in this investigation.	85
26.	Plots of lines $y = x$ and $y = (x^2-x)^{1/2}$ illustrating that both are linear in the (x, y) region of interest, along with $y = (x)^{1/2}$ for comparison.	87
27.	Plot of MOR versus elastic modulus for all porcelain bodies investigated, including a linear regression.	88
28.	Plot of fracture surface energy versus elastic modulus of all porcelain compositions, assuming a linear relationship: $y = 0.0683x - 0.1691$.	89
29.	Schematic showing a) the dimension of surface flaw versus b) the dimension of an internal flaw.	90
30.	Characteristic secondary electron SEM images of a) under-fired porcelain, ideally fired porcelain, and c) over-fired porcelain.	94
31.	Linear firing shrinkage versus soak temperature for porcelain compositions within a gradient furnace.	95
32.	Bulk density versus soak temperature for porcelain compositions fired in a gradient furnace.	96
33.	Plot of shrinkage versus firing temperature of Silica B composition with parabolic fit to data.	97
34.	Bulk density versus firing temperature for porcelain compositions including preliminary and main investigation results.	99
35.	SEM secondary electron image of Silica B porcelain fired at 1160°C (3-hour dwell).	100
36.	SEM secondary electron image of Silica B porcelain fired at 1210°C (3-hour dwell).	100
37.	SEM secondary electron image of Silica B porcelain fired at 1225°C (3-hour dwell).	101
38.	SEM secondary electron image of Silica B porcelain fired at 1245°C (3-hour dwell).	101

39.	SEM secondary electron image of Silica B porcelain fired at 1290°C (3-hour dwell).	102
40.	SEM secondary electron image of Alumina B porcelain fired at 1225°C (3-hour dwell).	102
41.	SEM secondary electron image of Alumina B porcelain fired at 1245°C (3-hour dwell).	103
42.	SEM secondary electron image of Alumina B porcelain fired at 1270°C (3-hour dwell).	103
43.	SEM secondary electron image of Alumina B porcelain fired at 1290°C (3-hour dwell).	104
44.	SEM secondary electron image of Alumina B porcelain fired at 1310°C (3-hour dwell).	104
45.	SEM secondary electron image of Stoneware porcelain fired at 1160°C (3-hour dwell).	105
46.	SEM secondary electron image of Stoneware porcelain fired at 1225°C (3-hour dwell).	105
47.	SEM secondary electron image of Stoneware porcelain fired at 1245°C (3-hour dwell).	106
48.	SEM secondary electron image of Stoneware porcelain fired at 1270°C (3-hour dwell).	106
49.	SEM secondary electron image of Stoneware porcelain fired at 1310°C (3-hour dwell).	107
50.	MOR versus firing temperature for Porcelain B compositions and Stoneware.	108
51.	Normalized strength versus firing temperature for Porcelain B and Stoneware body compositions.	109
52.	Effect of firing temperature variations on elastic modulus for porcelain B and Stoneware body compositions.	110
53.	Fracture surface energy versus firing temperature for Porcelain B and Stoneware body compositions.	111
54.	Critical flaw size versus firing temperature for Porcelain B and Stoneware body compositions.	112
55.	Critical flaw size versus normalized bulk density for Porcelain B and Stoneware body compositions.	113
56.	Equilibrium X-ray diffraction pattern of spinel powder.	120
57.	Plot of residual strain versus filler particle size for all Porcelain A compositions.	123
58.	Residual stress versus filler particle size for alumina and silica porcelain bodies.	124

59.	XRD pattern showing the (121) mullite peak in Mullite A porcelain composition for specimens containing 45- μm and 105- μm mullite particles.	126
60.	Comprehensive plot of MOR and residual strain versus filler particle size for all Porcelain A body compositions.	127
61.	Plot of critical flaw size versus filler particle size for all Porcelain B body compositions.	128
62.	Plot of MOR versus filler particle size for Silica A composition showing increase in strength for bodies with grain sizes between 10 – 25 μm .	130
63.	Schematic of in-situ filler grains with residual compressive stress field overlap in the glass phase.	131
64.	Comprehensive plot of critical flaw size versus filler particle size (Porcelain A) and firing temperature (Porcelain B).	135
65.	Secondary electrons SEM image of Silica B microstructure, with residual quartz grains highlighted for ease of viewing.	136
66.	Schematic showing a) pure tensile forces acting on a tensile specimen versus b) bending forces acting on a flexure specimen.	138
67.	Schematic of four-point flexure apparatus with exploded view of stress- strength profile as a function of the inner span volume below the neutral axis.	140
68.	Schematic of 10 x 10 x 10 cube subdivided into 1000 unique domains, each 'layer' in the z direction corresponding to an different stress state.	141
69.	Schematic of side-view of four-point flexure specimen showing specific flaw placement and stress levels.	143
70.	Plot of expected MOR versus number of flaws within a fixed volume during a simulation of a four-point flexure test.	145
71.	Plot of strength standard deviation versus flaw concentration fitted with logarithmic equation.	146
72.	Graphical representation of the different processing routes taken to create Porcelain A, B, and C bodies.	147
73.	Schematic of particle agglomerates including a) two-particle agglomerate, b) three-particle agglomerate with interstitial defect, and c) multi-particle agglomerate resulting in large defect.	149
74.	SEM Secondary electron image of Silica A porcelain surface showing a cluster of agglomerated particles.	150
75.	Plot of frequency versus grain distance for two near-identical porcelain bodies processed with different mixing routes.	152
76.	Schematic of glass-particle matrices illustrating nearest neighbor distances relative to a reference particle for a) a well-mixed system and b) a poorly-mixed system containing particle clusters.	153

77.	Schematic showing simplified four- and three-particle clusters and their dimensions ($R =$ particle radius).	156
78.	Schematic showing possible discontinuous strength regimes with changes in agglomerate size.	156
79.	Flexure strength versus filler particle size plot showing possible discontinuous strength behavior with particle size.	157
80.	Schematic of particle-suspension systems showing a) agglomerate of non-plastic particles in suspension, and b) application of new technique in which clay particles coat primary grains preventing re-agglomeration.	168
81.	Predicted relationship between mechanical strength and mixing efficiency.	169
82.	Plot of flexural strength versus raw material milling time for a porcelain body composition.	170
83.	Schematic of experimental setup for using transducers to triangulate the exact location of a fracture origin.	174

Abstract

Porcelain bodies were created to test the hypothesis that critical flaws govern the strength of ceramics. By systematically evaluating controlled changes to the porcelain body on mechanical properties and critical flaw size, further insight was gained regarding their relationship to strength, as well as increased understanding of the complexities inherent to porcelain itself.

Results of this study indicated the independence of critical flaw size to bulk density, firing temperature, and filler particle size; three parameters that, in literature, are continually cited as major factors that affect porcelain strength. Analysis also revealed the thermal expansion mismatch between filler particles and the porcelain glass phase does not favor glass matrix cracking in a quartz or alumina system shown to have a stronger, lower CTE glass phase. This idea challenges many central arguments that primary filler particles are critical flaws themselves or induce matrix cracks that become critical flaws.

Statistical and microstructural evidence supports the hypothesis of a relatively large population of particle agglomerates residing within porcelain bodies, on the order of several times primary filler particle or pore size that control mechanical strength. Based on experimental data, it is proposed that critical flaws found in these bodies are particle agglomerates introduced to the microstructure, the result of inefficient mixing during the processing step. Efforts to increase mechanical strength must incorporate techniques to eliminate these particle clusters; several experimental suggestions are noted.

1. Introduction

Traditional and advanced ceramics fulfill the needs of two unique niches in today's society. Traditional ceramists use clays and plastic-body materials to continually develop structural materials with higher mechanical properties and optimum aesthetic characteristics. Advanced ceramics focus more on maximizing thermal, optical, and electrical properties to serve their purpose. On an empirical level, however, traditional and advanced ceramics are quite similar. They both are brittle materials created using high temperature, they all have defects, and, with some notable exceptions (Si_3N_4 , PSZ, etc.), are all bound by the rules of brittle fracture mechanics, which determine their overall performance.

It is believed that the key to understanding the nature of mechanical properties of ceramics is to characterize their defects, as well as the role of these defects to act as critical flaws under certain conditions, whether temperature, compositional, or stress-state related. In the case of many ceramics, it has been found that although all three of these factors play a decisive role in affecting strength, it is flaws that will ultimately control strength. Having recognized this fact, a critical evaluation of flaws was undertaken, because it is believed to be the foundation for developing high-strength bodies.

For this thesis porcelain was selected as the subject of study. It is a prime candidate material as the porcelain composition combines the relative ease of specimen fabrication with a uniquely complex multiphase structure that allows for a broad range of systematic changes, and exhibits purely brittle fracture behavior. In addition, the use of this material provides the opportunity to simultaneously study overall porcelain behavior. The literature is replete with seemingly contradictory theories and data about fundamental porcelain behavior that propagate historically. This study employs novel techniques, as well as some previously used for the characterization of advanced ceramics, in an attempt to evaluate existing theories and hypotheses. This investigation aims to better learn how to control and minimize flaws, as well as maximize the benefits of using less-expensive fillers, such as quartz, which remains a necessity within the industrial arena.

Using a systematic approach, different fundamental aspects of the porcelain composition were altered in controlled and measurable ways in an attempt to understand what affects the development and size of flaws. Microstructural characterization and fractographic analysis proves to be troublesome for complex microstructures such as porcelains, and as a result the identity of strength-controlling defects is often difficult to ascertain through visual methods. Therefore, in this series of experiments flaw size was measured, not observed, with the aid of well-established analytical testing techniques and fracture mechanics. Historically, quartz particles have been argued to be the source of strength-controlling defects in porcelains. Data suggest that this assertion is suspect. As results of this study will show, attention paid to quartz grains as critical flaws may be misplaced, due to the measurement of flaw sizes in excess of two to three times the diameter of a filler grain. Based on these findings, a primary filler particle cannot be the critical flaw. This is not to imply that under extenuating circumstances errant particles cannot function as a critical flaw, but what was observed was a consistent trend applied to multiple commercial porcelain compositions that routinely use filler grains of maximum initial size 44 μm (325-mesh). Even by changing the filler material itself, results were inconsistent with the existing theory, as supporting data using Al_2O_3 and other fillers demonstrate. Instead, it is proposed that something more universal and intrinsic to the fabrication process is responsible for generating large flaws in the microstructure. Based on the literature, several trends and relationships observed experimentally were unexpected, yet with alternative analyses, they could be explained in terms of logical porcelain behavior. These results paint a more holistic view of the nature of both porcelains specifically and ceramics in general.

The overall goal of this thesis is not to produce or develop a 'recipe' for a high-strength ceramic material, but rather to investigate the complex interactions between different material properties of existing ceramic bodies to provide a more comprehensive understanding of the underlying nature of flaws and ceramic materials. It also aims to explore how and why changes in different variables affect material properties that control overall mechanical performance. It is hypothesized that the literature to date does not provide sufficient agreement amongst authors on

matters regarding the behavior of porcelain materials to adequately lead the reader to draw a comprehensive conclusion. It is proposed that these results present important implications regarding the fabrication of all ceramics.

1.1 Fracture Mechanics

Structural failure of a material under loading conditions well below the typical yield stress is attributed to cracks or flaws within its microstructure. These failures indicate that conventional strength analysis alone is insufficient to guarantee the structural integrity of the material under operating conditions. Structural study that considers crack extension behavior as a function of applied loads is called fracture mechanics.¹ Considering a structure in which a crack develops; due to the application of loads the crack will grow with time as a result of chemical interactions with the atmosphere and the new crack surface (e.g., stress corrosion). The longer the crack, the higher the stress concentration induced by it. This implies that the rate of crack propagation will increase with time. The crack propagation as a function of time can be represented by a rising curve, shown in Figure 1.²

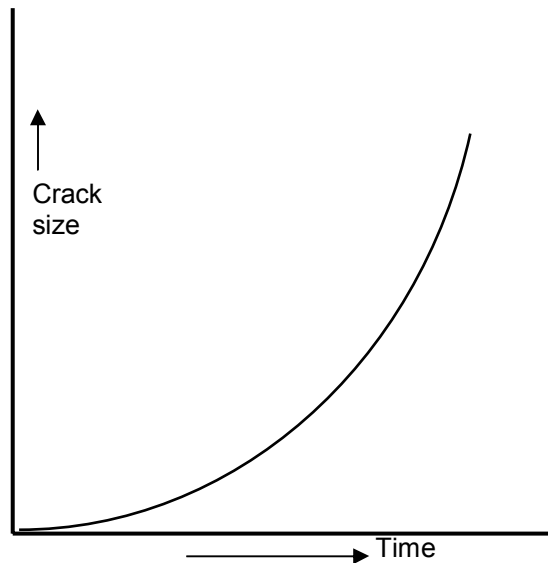


Figure 1. Schematic of a typical crack growth curve. (Redrawn from Broek, 1986).²

After a certain time the strength will have been reduced to the point where the structure cannot withstand sporadic high loads (e.g., impact) that may occur in service. From this moment on, the structure is susceptible to failure. Over time, the crack may grow to the point of failure under

normal service loading. Through the use of fracture mechanics, several questions can be answered, including:

- a. What is the residual strength as a function of crack size?
- b. What is the critical crack size?
- c. What size of pre-existing flaw can be permitted at the moment a material begins its service life?

Several disciplines are involved with the development of fracture-mechanics design procedures. Mechanical engineers are typically concerned with load-and-stress analysis. Applied mechanics provides the crack-tip stress fields as well as the elastic deformations of the material in the vicinity of the crack. Predictions about fracture strength can be verified through experimentation. Materials science concerns itself with the fracture processes on size scales ranging from atoms and dislocations to impurities and grains. With a thorough understanding of these processes the criteria that govern growth and fracture should be obtainable. These criteria can be used to predict the behavior of a crack in a given stress-strain field.²

A crack in a solid can be stressed in several different modes. In general, there are three pure modes of loading, as shown in Figure 2. Under practical conditions, solids are commonly exposed to complex combinations of these modes (e.g., opening with tearing), but for analytical testing, the aim is typically to load a material in one of the pure modes.

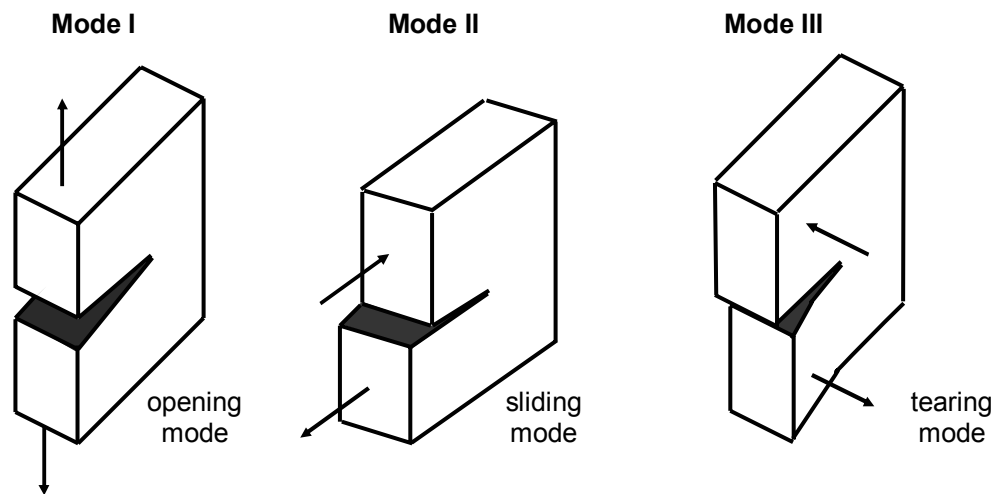


Figure 2. The three pure modes of loading.

Normal stresses give rise to the “opening mode” or Mode I loading. The displacement of the crack surfaces is perpendicular to the plane of the crack. In-plane shear results in Mode II loading or “sliding mode.” In this orientation the displacement of the crack surfaces is in the plane of the crack and perpendicular to its leading edge. The “tearing mode” or Mode III loading is caused by out-of-plane shear. Crack surface displacements are in the plane of the crack and parallel to the leading edge of the crack. Mode I is technically the most important, and for purposes of this investigation all mechanical testing takes place in flexure (generating tensile stresses), therefore discussions will be limited to Mode I.

The theoretical strength, σ_{th} , of a perfect material is estimated by some to be on the order of $E/10$, where E is the elastic modulus.³ This may occur for some specially handled specimens (glass fibers, filaments, etc.) but in practice the strengths of ceramic materials are orders of magnitude lower. Crystalline alumina has been observed having $\sigma_{th} \approx E/80$.⁴ The strength of alumina whiskers and freshly drawn glass fibers is on the order of $\sim E/100$; most bulk ceramics typically measure in the vicinity of $\sim E/1000$.³ The reason for this difference has to do with the presence of flaws that inherently reside within normally fabricated ceramics.⁵ In many ceramic materials, failure occurs due to a pre-existing flaw within the microstructure. For a perfectly brittle extension of a crack by cleavage, the criterion for crack propagation is relatively straightforward. Cleavage failure occurs due to the breaking of atomic bonds; therefore crack propagation occurs when the stresses at the crack tip exceed the interatomic cohesive forces. For two atoms separated a distance b , the force required to separate them to a distance of $b+x$ increases for increasing x until the maximum cohesive force is reached (x_m), at which total separation occurs. The force displacement curve can be approximated by a half sine wave of wavelength (λ); hence the stress or force per unit area to separate two planes of atoms (σ) is given by:

$$\sigma = \sigma_c \sin 2\pi x/\lambda \quad (1)$$

where σ_c is the cohesive stress. For small displacements, $\sin x/\lambda \approx x/\lambda$, and Equation (1) can be simplified to:

$$\sigma = 2\pi x \cdot \sigma_c / \lambda \quad (2)$$

The relationship between elastic strain, $E = x/r$, and stress is shown in Equation (3) as:

$$\sigma = \varepsilon E = \frac{x E}{b} \quad (3)$$

where ε is the strain between the two atoms. Combination of Equations (2) and (3) yields:

$$\sigma_c = \frac{\lambda \cdot E}{2\pi \cdot b} \quad (4)$$

The area under the curve represents the work required to separate the planes of atoms. Because two surfaces are created, the area represents twice the true surface energy (γ):

$$2\gamma = \int_0^{\lambda/2} \sigma_c \sin \frac{2\pi x}{\lambda} dx = \frac{\lambda \sigma_c}{\pi} \quad \text{or} \quad \lambda = \frac{2\pi \gamma}{\sigma_c} \quad (5)$$

Combination of Equations (4) and (5) gives the cohesive stress:

$$\sigma_c = \sqrt{\frac{E \gamma}{b}} \quad (6)$$

When the stress at one atomic distance from the crack tip exceeds the cohesive stress, cleavage occurs.

According to linear-elastic fracture mechanics, the stress at the tip of a crack is:

$$\sigma_{ij} = \frac{K_I}{\sqrt{2\pi r}} f_{ij}(\theta) \quad (7)$$

where σ_{ij} are the stresses acting on a material element ($dx dy$) at a distance r from the crack tip at an angle θ from the crack plane and f_{ij} are known functions of θ . The factor K_I is the stress intensity factor in Mode I loading. By taking $r = b$, then:

$$\sigma_{tip} = \sigma_n \sqrt{\frac{c}{2b}} \quad (8)$$

where σ_n is the nominal stress and c represents one-half the total crack length. By setting Equations (6) and (8) equal to one another, cleavage crack propagation is predicted to occur when:

$$\sigma_c = \sqrt{\frac{2E\gamma}{c}} \quad (9)$$

Equation (9) is a familiar one as it parallels one of the most well known equations associated with strength of ceramics; the Griffith equation.

1.2 The Griffith Criterion

Griffith (1920) stated that crack propagation occurs if the energy released upon crack growth is sufficient to provide all the energy that is required for crack growth, with no energy dissipative mechanisms.⁶ Crack growth under plane-stress conditions occurs if:

$$\frac{d}{dc} \left(-\frac{\sigma^2 \pi c^2}{E} + 4cT \right) = 0 \quad (10)$$

The first term in the parenthesis represents the elastic energy loss of a plate of unit thickness under a stress σ measured far away from a crack with length $2c$. The second term represents the energy gain of the plate due to the creation of new surface having a surface tension, T (more commonly represented as γ). This is illustrated in Figure 3, which is a schematic representation of the two energy terms and their sum as a function of crack dimension. When the elastic energy release due to an increment of crack growth, dc , outweighs the demand for surface energy for the same crack growth, the crack becomes unstable.

The Griffith condition for crack growth is:

$$\frac{dU}{dc} = \frac{dW}{dc} \quad (11)$$

where U is the elastic energy and W is the energy required for crack growth. Based on stress-field calculations for an elliptical flaw carried out previously by Inglis (1913), Griffith calculated dU/dc as:⁶

$$\frac{dU}{dc} = \frac{2\pi\sigma^2c}{E} \quad (12)$$

where E is Young's modulus. dU/dc can be replaced by:

$$G_I = \frac{\pi\sigma^2c}{E} \quad (13)$$

which is called the elastic strain energy release rate. G_I is also called the crack driving force.* Its dimensions are force per unit crack extension.

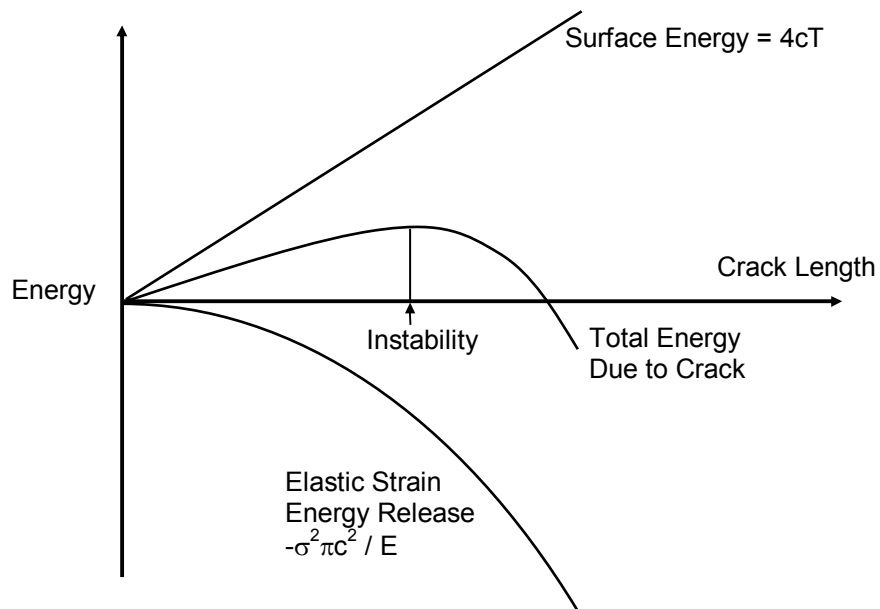


Figure 3. Schematic depicting the energy balance for a crack in an infinite plate.

* The variable 'G' is commonly used to represent shear modulus, not to be confused with elastic strain energy release rate, G_I

The energy consumed during propagation of a crack is denoted by:

$$R = \frac{dW}{dc} \quad (14)$$

where the variable R is called the crack resistance. It can be assumed that the energy required to produce a crack (de-cohesion of atomic bonds) is the same for each increment dc . This means that R is a constant. This being the case, Equation (13) now indicates that G_I must be at least equal to R before crack propagation can occur. If R is a constant, then G_I must exceed a critical value G_{Ic} . Hence, crack growth occurs when:

$$G_{Ic} = \frac{\pi\sigma^2c}{E} \quad \text{or} \quad \sigma_c = \sqrt{\frac{EG_{Ic}}{\pi c}} \quad (15)$$

The critical strain energy release rate (G_{Ic}) can be determined by measuring the stress σ_c required to fracture a plate with a crack size of $2c$ and applying Equation (15). In ductile materials such as metals, plastic deformation occurs at the crack tip, therefore for metals R (resistance to crack growth) is mainly plastic energy; surface energy is so small comparatively that it is neglected. However, for brittle materials, such as ceramics and glasses, it is assumed that R consists of surface energy only.² Therefore, for a brittle material the energy for crack growth (W) is equal to the surface energy required to form new free surfaces. This is represented by:

$$W = 2\gamma c \quad (16)$$

where γ is the surface energy (more precisely the *fracture* surface energy). The factor of 2 in the equation accounts for the fact that a crack consists of two newly formed surfaces. This relationship combined with those in Equations (14) yields:

$$R = \frac{dW}{dc} = 2\gamma = G_{Ic} \quad (17)$$

For crack growth to occur dU/dc must equal dW/dc . Substituting this result back into Equation (15) yields the familiar relationship known as the Griffith equation:

$$\sigma_c = \sqrt{\frac{2E\gamma}{\pi c}} \quad (18)$$

The Griffith equation is one of the more fundamental equations that can be used to relate mechanical properties of a material to its flaws.² The significance of this equation is that it contains three of the main factors upon which the strength of a material can be analyzed; elastic modulus (E), fracture surface energy (γ), and flaw size (c). The Griffith equation is a necessary and sufficient criterion for the fracture of truly brittle materials. The theoretical strength of the material is reached at the crack tip, and there is sufficient energy for the crack to grow.³ An equivalent fracture criterion developed by Weertman⁷ is based on the intensity of the stress singularity at the crack tip. If this singularity is sufficiently intense, the stresses at the crack tip can rupture atomic bonds and create new surfaces of energy γ . His equation, mathematically equivalent to the energy balance criterion put forth by Griffith is:

$$\sigma_r = \left[\frac{4G\gamma}{c(\pi\alpha - 2\beta)} \right]^{\frac{1}{2}} \quad (19)$$

where G is the shear modulus, γ is the surface energy, and $\alpha = 1-\nu$ where ν is Poisson's ratio for a crack under Mode I loading. The constant β depends upon the exact form of the stress-strain curve but cannot be larger than $\pi\alpha/2$; otherwise the plastic work term would be larger than the elastic energy release rate. The significance of this equation is that it unifies both the energy approach and the stress intensity approach to fracture for a Griffith crack.

Although the Griffith criterion is one of the most commonly accepted theories, there have been some alternative hypotheses, such as the idea that strength-controlling flaws are actually generated by the application of stress through natural fluctuations biased by the stress field. In mathematical form the resulting equations for many factors (size effect, crack propagation rate, strength variability, and static fatigue) all seem reasonable. However, they are so similar to the relationships derived using the Griffith theory that they are virtually indiscernible. A radically different approach put forth by Phillips,⁸ however, proposes the maximum breaking fracture

strength of glass is limited to 3.5 GPa (5×10^5 psi) and that higher breaking stresses result from plastic flow (with a large increase in specific fracture energy) around the crack tip. This theory appears invalid since documented failure stresses of glasses can approach, if not exceed, 10 GPa.^{6,9} Based on these measured failure stresses, in order to be accurate, this theory requires an overwhelming contribution of stress due to plastic flow, which seems unlikely. In fact, weak glass strengths are attributed to stress corrosion, or accelerated crack growth due to the presence of water. Under high-vacuum conditions, flaw-free glass has been shown to withstand tensile loads greater than 13 GPa (2×10^6 psi). In the presence of water, however, the amount of energy required to rupture silicon-oxygen bonds is only 78 calories per gram (cpg), versus 1,300 cpg required in a vacuum.¹⁰

1.2.1 Failure Stress

The intensity of a stress, σ , is measured by the force, F , divided by the area, A , yielding the equation:

$$\sigma = \frac{F}{A} \quad (20)$$

Equation (20) is somewhat of an oversimplification for failure stress, since in practice the total force does not always act upon the total area, especially in a flexure test. Instead, components of an applied force act on an effective area that depends on the bending moment of the system. Therefore, a proper failure-stress-testing experiment will use an appropriate modulus of rupture (MOR) equation, which accounts for specimen and testing geometry as well as the bending moments involved. These equations are discussed in more detail in Section 3.2.2.

Under the action of external loads an elastic body undergoes deformation during which forces do a specific amount of work. The work is transformed into strain energy. As stress increases, so does the strain. The quantity of strain energy stored per unit volume of a material is sometimes used as a basis for determining the limiting stress at which failure occurs. There is a limit to the amount of strain a material can undergo before failure occurs. This is referred to as the elastic

strain limit. A critical value of stress is associated with this limit; below this critical value the system can sustain the stress. If the stress is higher than the critical value, the corresponding strain exceeds the elastic strain limit, and the material fails. The stress value at which a material fails catastrophically is called the failure stress. This value is used in the Griffith equation (Equation 18) to relate to other properties of a material. For a material that is experiencing Mode I loading (e.g., the tensile surface of a four-point flexure specimen containing a crack oriented perpendicular to the stress direction), there is no acting stress in the direction parallel to the applied load. This condition is known as plane stress. For practical purposes, the failure stress of a ceramic rod in flexure is equivalent to its mechanical strength, since the material experiences plane stress on the tensile side of the specimen, and the strength corresponds to the load at failure (via the MOR equation), which is a function of the force applied to a specific area of the specimen. Both parameters have units of N/m^2 or Pa. For most engineering applications this is inconveniently small; therefore the typical unit is the MPa (or GPa).¹¹

1.2.2 Elastic Modulus

Elastic modulus (Young's modulus, modulus of elasticity) is a parameter that describes the relative stiffness of bonds within a solid. It is related to the structure of the material as well as the types of bonds contained within it. The stiffness of a bond, S_0 , is defined as:

$$S_0 = \left(\frac{d^2U}{dr^2} \right)_{r=r_0} \quad (21)$$

where U is the potential energy of the bond and r is the distance between bonded atoms. For small strains, S_0 is constant (it is the spring constant of the bond). This means the force between a pair of atoms, stretched apart to a distance r (when $r \approx r_0$) is:

$$F = S_0(r - r_0) \quad (22)$$

The total force exerted across a unit area, if two crystal planes are pulled apart a distance $(r - r_0)$, is defined as the stress (σ) with:

$$\sigma = NS_0(r - r_0) \quad (23)$$

N is the number of bonds per unit area; equal to $1/r_0^2$ since r_0^2 is the average area per atom. Displacement ($r - r_0$) is converted to strain by dividing by the equilibrium atomic spacing, r_0 , so that:

$$\sigma = \left(\frac{S_0}{r_0} \right) \varepsilon \quad (24)$$

where ε is the strain. According to Equation (25), the elastic modulus is therefore:

$$E = \frac{S_0}{r_0} \quad (25)$$

The greater the energy of the bond is, the higher the stiffness and, hence, the higher the elastic modulus. The energy of the bond itself is related to the bond type (e.g., ionic vs. covalent) and the strength that accompanies it. Table I lists the hierarchy of bond stiffness in general terms. Ceramics and glasses typically contain mixed bonding character; therefore, their elastic moduli (E (SiO_2) \approx 90 GPa; E (Al_2O_3) \approx 400 GPa) are higher than a purely ionic material but lower than a purely covalent material.

Table I. Bond Stiffness and Elastic Moduli for Various Types of Materials.

Bond Type	S_0 (N/m)	Approximate E (from S_0/r_0) (GPa)
Covalent, C – C bond	180	1000
Pure Ionic, e.g. Na – Cl bond	9 – 21	30 – 70
Pure metallic, e.g. Cu – Cu bond	15 - 40	30 - 150
H – bond, e.g. $\text{H}_2\text{O} - \text{H}_2\text{O}$	2	8
Van der Waals (waxes, many polymers)	1	2

The main factors that influence the elastic modulus of a material are porosity, volume fraction of phases (if multiphase material), internal stresses, and homogeneity of microstructure. In general, increasing elastic modulus results in an increase in strength for polycrystalline ceramics, two-phase composites,^{12,13} and porcelain,¹⁴ which empirically supports the Griffith equation. Frey and

Mackenzie¹³ observed that for glasses with dispersions of particles of either Al₂O₃ or ZrO₂, the load to fracture increased in proportion to the increase in the modulus of the systems. Therefore, for a given flaw size, a higher-modulus material will have a higher strength. Likewise, Borom studied the effects of elastic modulus on strength of two-phase glass-crystal composites.¹² For a material containing a specific flaw size, a crack will propagate through the matrix when the applied load produces strain at a flaw, generating a stress in excess of the theoretical strength of the material at the flaw tip. When the elastic modulus is increased by addition of a second phase with a higher modulus, larger loads are required to produce the strain at the flaw tip necessary for crack propagation due to the sharing of the load, related to the modulus of each component.¹² This is easily illustrated by examining the relationship between stress and strain as reported by Steere.¹⁵ Consider the following equation:

$$\sigma = \epsilon E \quad (26)$$

If all components within the material share the applied load in proportion to their elastic modulus, the tensile strain in all components will be the same. Therefore, both the glass and crystalline phase deform equally. At constant strain, higher-modulus particles experience more of the stress than the glass; therefore, it would require a higher applied load to propagate the crack in the glass.¹⁵

The negative effects of porosity on the elastic modulus of polycrystalline ceramics, composites and porcelain have been extensively investigated. Spriggs proposed the following logarithmic equation to explain the effect in polycrystalline alumina:¹⁶

$$E = E_0 e^{-bP} \quad (27)$$

where E_0 is the elastic modulus at zero porosity, P is the volume fraction porosity and b is an empirical constant on the order of 4.0. Hasselman and Fulrath studied the effect of controlled amounts of spherical porosity on the elastic modulus of glass at low porosity (0 – 3%) and observed the following linear relationship between elastic modulus and porosity:

$$E = E_0(1 - \alpha_e P) \quad (28)$$

where α_e is a constant.^{17,18} For a porcelain composition, Kalnin et al. demonstrated a linear relationship between elastic modulus measured from stress-strain curves and porosity values between 5 – 33%.¹⁹

$$E = E_0[1 - (2.70 \pm 0.05)P] \quad (29)$$

The equation calculated from the data is essentially the same as that proposed by Hasselman but with a different constant.^{17,18} Kalnin's analysis included both open and closed porosity, while Hasselman incorporated open porosity only, which likely accounts for the different constant values. He also studied the effect of mullite content on strength and showed a somewhat linear relationship between mullite content and elastic modulus. From the existing literature, it would seem that there are many theoretical approximations that can be derived from various experimental data sets but no universal relationship that applies to all materials. This may be due to variations in pore morphology (shape, size distribution) or whether both open and closed porosity are included in the analysis. In some cases values of percent closed porosity are not easily measured; therefore, percent porosity often reflects only the concentration of open pores.

1.2.3 Fracture Surface Energy

From a thermodynamic standpoint, the surface energy of a material (for liquids called *surface tension*) is related to the amount of work (energy) required to create a unit area of new surface under conditions of constant temperature and volume. In the case of a brittle material containing a crack, the propagation of that crack creates two new surfaces. The surface energy is referred to as fracture surface energy, and correlates to the amount of energy required to break atomic bonds in the material (per unit area). Its units are J/m². In other terms, fracture surface energy is the work required to create a unit of new crack surface, or the energy absorbed per unit area of newly formed fracture surface.²⁰ Originally, Griffith defined γ_0 as the surface energy of the material without stating the other energy-absorbing processes that may also be included in this

factor.⁶ Lange^{21,22} has done an extensive evaluation of fracture energy and proposed that both the volume fraction of the dispersed phase in a composite and grain size are the main parameters that influence the fracture energy of ceramic composites. To date, no fracture energy determinations have been performed on porcelain compositions, but it is believed they should behave similarly to the glass-crystal composite systems.²¹

The incorporation of a second-phase dispersion into a brittle matrix phase has been shown to increase the fracture energy, mechanical strength, and toughness of composite systems. This increase is mainly due to the fact that a second-phase dispersion affects the plastic deformation associated with the high stresses at a crack tip that absorb energy as the crack propagates.²⁰ As noted by Davidge and Evans, the fracture energies of most brittle materials are about an order of magnitude larger than their thermodynamic surface energies; thus, some amount of plastic deformation is thought to accompany crack propagation in all materials.⁵ It was also found that a dispersed phase increases the surface area of the fracture surface due to the irregular path the crack travels, thereby increasing a material's toughness, since the dispersed phase interacts directly or indirectly with the crack front. Lange presented a model describing the effect of second-phase dispersions that relates fracture energy to the average spacing between particles. As a crack begins to propagate, the crack front moves between each pair of pinning positions interacting with the second-phase dispersions within the brittle matrix forming newly fractured surfaces and increasing the length of the crack. Assuming the crack front has a line energy, which, in turn, is related to the length of the crack front and elastic modulus of the material, energy must be supplied to increase its length (break bonds). Energy must also be supplied to create new surfaces as the crack front moves between the pinning positions. Just before catastrophic failure (which is assumed to occur when the crack front breaks away from its pinning positions), the fracture energy should depend not only on the energy required to form new surfaces, but also on the spacing between dispersed particles. The breakaway position is theoretically defined by an arc of a circle with a diameter that is two times the distance between particles.²² Figure 4 illustrates this model.

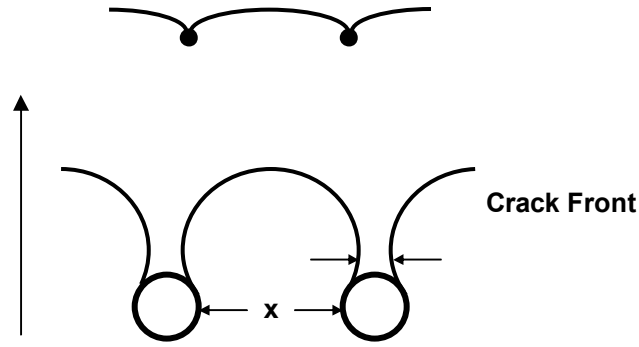


Figure 4. Breakaway position of crack front from 2 pairs of pinning positions, separated by distance x . Distance between two arms of crack front anterior to each pinning position (indicated by 2 arrows) is hypothesized to control breakaway position because of overlapping stress field. Large arrow is direction of propagation. (Redrawn from Lange, 1971).²¹

At this position, the crack front should meet on both sides of the particle or void and break away, causing failure. The amount of bowing of the crack front between pinning positions depends on how well they hold the crack front as it bows between them. As shown in Figure 4, the distance between the two sets of pinning positions is the same, but the amount of bowing is much larger in the lower set. Formalization of Lange's model for crack propagation resulted in the following expression for fracture surface energy:

$$\gamma_i = \gamma_0 + \frac{L}{d} \quad (30)$$

where γ_0 is the energy per unit area required to form new fracture surface, L is the critical line energy per unit length of the crack front, and d is the distance between pinning positions.

Equation (30) suggests that the contribution to fracture energy by the introduction of a dispersed phase is proportional to the line energy per unit length of the crack front and inversely proportional to the distance between dispersed particles. Therefore, increasing the volume fraction of dispersed phase should decrease the distance between particles, increasing the length of the crack front with a corresponding increase in line energy; thus, the fracture energy of the material should increase. This is true provided the dispersed phase has increased properties (strength, modulus, etc.) compared to the matrix.

Lange fabricated a glass-alumina composite system to study the effect of both volume fraction and grain size on the fracture energy and the strength of composites.²¹ The results not only indicated a linear relationship between fracture energy and inverse interparticle spacing, but also demonstrated an effect of particle size. At low volume fractions (<20%) increasing particle size resulted in higher measured fracture energy. This effect was thought to be due to the relative effectiveness of the particles pinning the crack front as the crack moved between particles. In Lange's fracture energy model, catastrophic failure is governed by the overlapping stress field of both segments of the crack front behind the pinning positions. For small particle sizes, the stress fields should overlap with only a small amount of bowing because the pinning positions are small. As particle size increases, a greater amount of bowing occurs before the stress fields can overlap and cause breakaway from the pinning positions. Consequently, by increasing the particle size, the pinning position should increase, becoming more effective at pinning the crack front and increasing its length prior to catastrophic failure.

In summary, Lange showed that an increase in volume fraction of a dispersed phase in a glass-crystal composite will result in an increase in the fracture energy of a system.^{21,22} It was also determined that large particle sizes are more effective in increasing the fracture energy relative to smaller particle sizes. Therefore, an increase in fracture energy with increasing volume fraction should also result in increased strength according to the Griffith equation. In reality, however, this does not occur, as shown by Lange²¹ and other investigators.^{5,23-25} At low volume fractions, incorporation of a second phase usually resulted in a decrease in strength due to an increase in flaw size.

1.2.4 Flaw Size

As stated previously, the bulk strength of a brittle material is much lower than its theoretical strength due to the presence of flaws generated during fabrication or in service. From Griffith's equation, increasing flaw size results in a lower strength due to the increasing stress concentrations at the flaw tip at a particular applied load. Since the flaw size in the Griffith

equation corresponds to the overall size of surface flaws but only half the length of internal flaws, Davidge suggested that fracture usually initiates at surface flaws in bending, assuming a homogeneous microstructure, thus the condition of a brittle material's surface is vitally important when determining the strength of the material.⁵ In polycrystalline ceramics and composite systems (including porcelain) the overall flaw size can be related to various microstructural parameters including grains and pores. Large flaws can also be introduced into the surface via handling or machining. In this case, the largest surface flaw usually determines strength, provided it is atomically sharp.⁵

It is generally accepted that the strength of polycrystalline ceramics varies as some inverse power function of grain size. The first author to empirically show the dependence of strength based on grain size was Knudsen,²⁶ who observed that strength could be expressed by:

$$\sigma_f = kD^{-a} \quad (31)$$

where σ_f is strength, D is grain size and k and a are constants. Equation (31) assumes constant fracture energy and elastic modulus with varying grain size; therefore, it is equivalent to the Griffith equation relating flaw size with strength if $a = 1/2$. In practice, however, the constant a is frequently much less than $1/2$, ranging from $1/6$ to $1/3$. In a review article, Rice observed that all data were consistent with the following equation:

$$\sigma_f = M + HD^{-1/2} \quad (32)$$

where M and H are constants that depend on the surface finish and/or internal stresses.²⁷ When $M=0$, the equation reduces to the Griffith relationship. When $M>0$, plastic deformation may be included. Other factors that affect M are thermal expansion and elastic anisotropy. Locally they should add to the applied stress in aiding fracture, so the applied stress need not be as high as in a single crystal; thus thermal expansion mismatch can result in a situation where $M<0$. Elastic anisotropy can affect the value of M , as shown by Hasselman, in that local increases of 5 – 15%

in applied stress can occur in materials with equiaxial grains.²⁸ In materials with grain length-to-diameter ratios of at least 2:5, stress increases of 10-80% can occur.

Much work has been done on evaluating the effects of grain size and consequently flaw size for glasses, glass-crystal composites and porcelains. For glasses, Levengood found a linear relationship between the depth of large visible flaws and the reciprocal of strength when fracture origins were of the large, visible type.²⁹ When the flaws were minute, strength was found to be a linear function of the square root of fracture depth. Investigators have shown that the introduction of a second-phase dispersion into a glass matrix initially decreases the strength of the composite at low volume fractions because the particles produced a flaw greater than the intrinsic flaw size of the glass.^{13,24} At a particular volume fraction, increasing grain size usually resulted in a strength decrease because of the larger flaw size produced by particles.

The introduction of a particle into a glass matrix is often considered a site from which cracks develop due to internal stresses produced within and around the particle. During cooling of a glass composite or porcelain, thermal stresses develop around the particles due to differences in thermal expansion between the glass and the imbedded particles. Each phase is restrained to the same overall contraction. In some cases, these stresses can cause deformation or cracks which decrease strength and elasticity in ware and lead to thermal expansion hysteresis.³⁰ Selsing³¹ calculated the magnitude and distribution of these stresses around a particle and determined that for a given particle shape, the magnitude of the stress was dependent only on elastic properties, thermal expansion of each phase, and the change in temperature. The equation determined that the magnitude of the stress was independent of particle size. Conversely, recent experiments by Pinto^{4,32} have resulted in the observation of residual cooling stresses that generate spontaneous cracks in porcelains containing quartz grains exceeding a threshold size (87 μm), indicating that stress is a function of particle size. Davidge and Green also observed that cracking due to thermal expansion mismatch occurred only for particles of a certain critical size.³³ They introduced a concept showing that both the development of residual stress and the presence of stored strain energy were required to produce cracking around

certain-sized grains. They concluded that although the magnitude of the stress is independent of particle size, the total stored strain energy depends on the volume of material under the influence of these stresses, which is dependent on particle size. Also, at a particular particle size, increasing the volume fraction may produce overlapping stress fields and reduce the critical size necessary for cracking. This concept can only be valid in the event that the thermal expansion coefficient of the glass is higher than that of the included particle, the mismatch generating tensile stresses in the glass phase compounded by increased particle concentration. In porcelain bodies containing quartz, the presence of quartz places the glass phase in compression; therefore this cannot occur (see Section 1.4.2).

The concepts of Davidge and Green should also apply in the presence of nucleation and/or growth of Griffith flaws during stressing of an un-cracked body. When thermal stresses govern flaw nucleation, the applied stresses during loading should enhance the already present residual strain energy fields, and the critical size at which cracks appear will be reduced.²⁰ When the thermal expansion of the glass and particle phase is similar, flaws still nucleate with the application of load due to elastic anisotropy between the two phases. In this case, new stress concentrations can arise which are caused by the different responses of both the particle and the matrix to the applied stresses.^{25,33} Lange calculated the flaw size in sodium borosilicate glass-alumina composites and determined that the addition of a second-phase dispersion increased the crack size in the glass by an amount one to three times the average particle size of the dispersion, though his analysis was limited to only three different specimens.²¹ Borom¹² calculated flaw sizes from Hasselman's data for glass-alumina composites²⁴ and determined that the introduction of particles generates flaws three times larger than the average particle diameter. He observed that hoop tensile stresses caused by thermal expansion mismatch ($CTE_{\text{glass}} > CTE_{\text{alumina}}$) between glass and alumina exist at a distance of three radii from the particle center, accounting for the three-fold relation between flaw size and particle diameter.¹² In quartz and alumina porcelain bodies, as will be addressed later (Section 1.4.2), $CTE_{\text{glass}} < CTE_{\text{particle}}$, therefore hoop tensile stresses are not generated in the glass phase. The glass phase is instead

placed under compression in the presence of the included particles. Therefore, this theory cannot be directly applied to analysis of porcelain bodies.

Pores can also act as flaws if the pore size is much larger than the grain size. This happens frequently in polycrystalline ceramics because pores contain sharp angles where a grain boundary emerges at a pore surface. In glassy materials such as porcelain, however, pores are generally more spherical and, with the absence of defects at the pore surface, will have little weakening effect, as their stress intensity factor is quite small ($\sim 3.0 \text{ MPa}\cdot\text{m}$).⁵

1.3 Microstructural Strength Parameters

1.3.1 Porosity

The deleterious effect of porosity on the strength of polycrystalline ceramics, glass-crystal composites and electrical porcelain is well known. Initially, Knudsen^{16,26} and Spriggs^{16,26} observed that the strength of polycrystalline ceramics was related to porosity by the following equation:

$$\sigma_f = \sigma_0 e^{-bP} \quad (33)$$

where σ_f is fracture stress, σ_0 is fracture stress at zero porosity, P is volume fraction porosity and b is an empirical constant on the order of 4.0. The above equation also follows Equation (27), relating elastic modulus with porosity given by Spriggs.^{16,26} Studt and Fulrath³⁴ investigated the mechanical properties in mullite-glass systems and found an exponential dependence on porosity similar to Knudsen's equation (Equation 33). Also, in a study of strength-porosity relationships for various porcelain compositions, Dinsdale and Wilkenson³⁵ found strong agreement with Knudsen's equation. In Dinsdale's analysis varying porosity was produced by firing the porcelains at different soak temperatures; thus by under-firing or over-firing, his results also included open and closed porosity.

Hasselmann¹⁷ studied the effect of controlled amounts of spherical porosity on the strength of glass at low porosities (0-3%) and reported a linear relationship between mechanical strength (σ_f) and volume fraction porosity, expressed as:

$$\sigma_f = \sigma_0(1 - bP) \quad (34)$$

where b is the same numerical constant as in Equation (33). He also developed a relationship between porosity and elastic modulus, as shown in Equation (35).³⁶

$$E = E_0 \left[1 - \frac{bP}{1 + (b-1)P} \right] \quad (35)$$

Further refinement of this equation by Piatasik and Hasselman³⁷ chose to incorporate the effects of both open and closed porosity, which they deemed to be distinctly different, resulting in Equation (36):

$$E = E_0 \left[1 - \frac{b_0 P_0}{1 + (b_0 - 1)P_t} - \frac{b_c P_c}{1 + (b_c - 1)P_t} \right] \quad (36)$$

where b_0 and b_c are numerical constants, P_0 is volume fraction open porosity, P_c is volume fraction closed porosity and $P_t = P_0 + P_c$. Porcelain bodies typically have a low volume fraction of porosity, and as such its effect on elastic modulus is negligible. For example, Kalnin et al.^{14,19} reported a linear relationship between strength and dynamic elastic modulus at low strengths and similarly observed a linear dependence of elastic modulus on porosity (5 – 35%) in a mullite-glass system agreeing with the results of Hasselman¹⁷ at low porosities for polycrystalline alumina.

Porosity decreases the strength of all brittle materials by reducing the load-bearing area of the material resisting an applied stress. In effect, the elastic modulus is reduced. The size and shape of the pores can also influence the strength of a material. Hasselman and Fulrath calculated stress concentrations around pores with an applied stress and observed a sharp decrease in strength with the addition of a low volume fraction pores followed by a linear decrease in strength with further increases in volume fraction.²⁵ They attributed the large

decrease in strength at low volume fractions to an increase in stress concentration at the flaw produced by the pore. Davidge and Evans stated that in polycrystalline materials where large pores contain grain boundaries in their surface, the pores can act as flaws, but in glassy materials, if pores are spherical they have little weakening effect.⁵ Consequently, the introduction of porosity into any brittle material will result in a strength decrease due to a decrease in elastic modulus and/or increase in flaw size depending on the size and shape of the pores.

1.3.2 Volume Fraction of Dispersed Phase

It has been shown that a significant strength improvement can be obtained when introducing a sufficient volume fraction of higher modulus particles into a glass matrix. It has been observed that increasing volume fraction resulted in an increase in composite fracture energy,^{21,22,38} elastic modulus,^{13,18,19} and consequently strength as predicted by the Griffith equation. Hasselman found that elastic modulus increased from 92 GPa to 168 GPa upon the inclusion of 10-50% (by volume) 50- μm Al_2O_3 particles in a sodium borosilicate glass matrix.¹⁸ However, other investigations have indicated that at low volume fractions (up to 10%) the strength of many large-particle-size composite systems was actually less than the glass itself.^{21,24,25,34,39} With further increases in volume fraction (above 10%) the strength then increased above that of the glass. Lange theorized that the initial decrease in strength at low volume fractions was due to an increased flaw size produced by the particle relative to the inherent flaw size of the glass; thus the increase in γ_i and E due to the introduction of the second phase was not great enough to counteract the deleterious effect of increasing flaw size.²¹ This idea contradicts the theory proposed by Hasselman, Nivas and Fulrath,^{24,39} which suggests that the introduction of Al_2O_3 particles in a thermally matched glass increased the load to fracture at certain combinations of volume fraction because the dispersed phase limits the size of the surface flaws to less than that present in the glass containing no particles. Hasselman plotted strength as a function of reciprocal square root of mean free path and observed two distinct regions. At low volume fractions, no strength improvement occurred because the mean free path between particles was greater than the flaw size of the glass. For higher volume fractions, strength was shown to

increase with decreasing mean free path because, according to Hasselman, increasing volume fraction lowered the mean free path below the flaw size of the glass; thus, the size of the surface flaws were reduced. Lange,²¹ Borom,¹² and Miyata and Jinno⁴⁰ have all rejected this theory. Lange measured the strength and fracture energy of glass-alumina composites with known elastic modulus and calculated crack size as a function of volume fraction. He found that the addition of a very small amount of particulate phase decreased strength by increasing flaw size, but increasing the volume fraction of that particular grain size did not further increase flaw size. Borom reviewed Hasselman's data and suggested that the initial decrease in strength at low volume fractions was due to an increase in flaw size. Increasing strength at higher volume fractions was not due to the limitation of flaw size but rather an increase in elastic modulus, as it required a higher stress to produce the necessary critical strain to failure.

This constant-strain-to-failure system parallels work performed by Frey and Mackenzie, who observed that for alumina-glass composites, the load to fracture increased in direct proportion to the increase in the modulus of the system.¹³ The discrepancy between the above authors and Hasselman is that Hasselman assumed that, since the fracture propagates through the glass phase even in the presence of a dispersed phase, the elastic modulus and the fracture energy in the Griffith equation should be those for the glass itself. However, since an applied stress is distributed unevenly between the glass matrix and the dispersed phase, the stress to failure becomes a measure of the ability of the system, not the matrix alone, to support the load.

In summary, an evaluation of the literature indicates that the introduction of a second phase with a high modulus raises the fracture energy of the composite, increases the overall elastic modulus of the system by increasing the load-bearing ability in proportion to the rise in system modulus. The competing effect of flaw size with elastic modulus and fracture energy usually results in a decrease in strength below that of the glass at low volume fractions (<10%). Then as the load-bearing ability of the composite increases with increasing elastic modulus along with increasing fracture energy, a significant strength improvement occurs at high volume fractions.

1.3.3 Grain Size Effects

The effect of grain size on strength has been thoroughly studied with respect to polycrystalline alumina systems, glass-alumina composites and porcelains. As shown previously in this section, the strength of polycrystalline ceramics varies as an inverse power function of grain size according to the equation proposed by Knudsen²⁶ and later refined by Rice.²⁷

Particulate size influences the strength of glass-crystal composites by affecting both the fracture energy and the flaw size of the composite. It has no effect on the composite elastic modulus. Initial investigations by Davidge et al. suggest that at a particular volume fraction and no thermal expansion mismatch, significant strength improvement could be realized by reducing particle size.³³ Lange observed that at a particular volume fraction increasing particle size resulted in an increase in fracture energy but a reduction in strength.²¹ He calculated crack sizes with increasing particle size knowing the fracture energy and elastic modulus at a particular volume fraction and determined that the average flaw size in the glass increased by an amount one to three times the average particle size of the dispersion as the particle size increased. The increase was much larger for the larger 44- μm particle size series than for the 3.5- μm series. Consequently, although larger particle size dispersions result in higher fracture energy, the flaw size produced by the larger particles generally degraded the strength of the glass-crystal composites.

With regard to filler particles dispersed in a porcelain glass matrix, Table II lists many of the reported results from various investigations regarding the determination of the optimum filler particle size for maximizing strength. As shown, there is a fairly broad range of particle sizes viewed to be optimum for quartz. Banda and Messer determined that the maximum values for strength and toughness increased as the quartz size decreased down to 4 μm .⁴¹ They concluded that previous published filler size estimates for optimum strength found to be in the region of 20 μm to 30 μm were the result of over-firing bodies containing very fine quartz. Parmelee and Morgan reported an 84% increase in bend strength, from 30 MPa (4350 psi) to 55 MPa (8000 psi) when quartz particle size was decreased from 40 μm to 10 μm .⁴² This was attributed to the finer

quartz particles' effectiveness in reducing porosity. Warshaw and Seider²³ measured the strength of quartz and alumina porcelains and observed an exponential strength dependence on filler particle size but did not attempt to explain the relationship. The sizes that yielded maximum strength for quartz and alumina porcelains were 25 μm and 7 μm , respectively.

Table II. Summary of Results Regarding Various Investigations on Optimum Filler Particle Size and Strength.

Author(s)	Optimum Filler Size	Notes	Ref.
Banda & Messer	4 μm (Q)	Estimates of 20–30- μm quartz yielding optimum strength are the effect of over-firing	41
Parmelee & Morgan	10 μm (Q)	Decreasing particle size decreases porosity	42
Hamano et al.	variable (Q)	Temperature dependence on optimum quartz size: 10–20 μm (1400°C); 5–10 μm (1250°C); <5 μm (1200°C)	50
Ece & Nakagawa	10 – 20 μm (Q)	Firing temperature range (1300 - 1350°C)	43
Mattyasovszky-Zsolnay	10 – 30 μm (Q)	Cracking around large quartz grains reduces strength	47
Lee & Kim	25 – 30 μm (Q)	Increasing particle size results in increased stress, strength	49
Storch et al.	45 μm (Q)	>50 μm quartz grains seriously degrade strength	45
Fassbender	20 μm (Q); 5 μm (A)	Agglomerated alumina grains can reduce strength; primary grains improve strength	44
Warshaw & Seider	25 μm (Q); 5 μm (A)	Exponential strength dependence on filler size	23
Harada et al.	1 – 2 μm (A)	Alumina does not experience quartz transformation.	48
Dinsdale & Wilkenson	5 μm (A)	Quartz particles cause matrix cracking; substitute alumina	35

Ece and Nakagawa⁴³ stated that maximum bending strength is found in 10–20- μm quartz grain sizes at the 1300–1350°C interval, as they can better tolerate the negative effects of flaws. Fassbinder also recommended quartz grains are to be no larger than 20 μm without negative consequences.⁴⁴ Storch et al. found that for large filler particle sizes (>50 μm), bending strength decreased as particle size increased, but for smaller sizes, they discovered a strength peak at 20 μm .⁴⁵ Dinsdale concluded that larger grains would generate larger stresses; therefore, if the

grain size could be reduced, then mechanical strength would increase.⁴⁶ Mattyasovszky-Zsolnay reported that quartz grains more than 10–30 μm in diameter may be weakened by the crystalline transformations and may crack as they are stressed, thereby reducing the strength of the porcelain.⁴⁷ In a similar study using quartz particles, Lee and Kim⁴⁸ determined that increasing particle size resulted in greater residual quartz content, as well as increased strength due to the increased stress in the system. Furthermore, they recommended cooling rates dependent on quartz particle size. In order to increase the strength, fast cooling was deemed suitable for small quartz particle sizes and slow cooling for larger particles. By varying firing temperatures, Hamano et al. obtained various strength maxima for different starting quartz particle sizes, namely 10–20 μm at 1400°C, 5–10 μm at 1250°C, and <5 μm at 1200°C.⁴⁹ Both smaller and larger quartz grains resulted in lower strength, reportedly because of extensive dissolution and crack generation, respectively. Harada et al. studied the effects of alumina particle size and found that smaller particle sizes resulted in increased strength, reporting maximum strength in a body containing 1–2 μm .⁵⁰ Dinsdale and Wilkenson³⁵ measured the effect of alumina grain size on the strength of alumina porcelain and obtained a relationship similar to Knudsen. In this case the constant $a = 0.75$ (Equation 31). However, as the size of the filler was reduced to 5 μm , a maximum strength was reached, and further decreases in grain size resulted in a decrease in strength. This was thought to be due to poor particle packing and poor wetting of the alumina grains by the flux. Overall, Rice replotted Dinsdale's data according to his strength-grain size Equation (32) and determined the constant M to be less than zero, which he reasoned to be due to the thermal expansion mismatch between the alumina and the glass matrix.²⁷ Steere reported that the introduction of a small amount of quartz grains larger than the maximum grain size of alumina will seriously degrade strength of a high-strength alumina porcelain by increasing the overall flaw size.¹⁵ Although the reduction in grain size has been linked to strength increases, the fracture toughness may decrease as fineness increases, as coarse particles are proposed to either prevent or stunt an incident fracture, or cause it to branch, dissipating its energy.⁵¹

1.4 Raw Material Effects

1.4.1 Thermal Stresses

It has been proposed that one of the major mechanisms controlling the mechanical strength of porcelain is thermally induced stress between the particulate constituents and glass matrix due to a thermal expansion mismatch between them. Initial investigations of glass-crystal composites indicated that with large particle size dispersions, maximum strength could be achieved when the thermal expansion mismatch between particles and glass was minimal.^{12,40,52,53} Davidge and Green developed a concept that showed the development of residual stress and the presence of stored strain energy were both requirements for cracking around certain sized grains.³³ Borom suggested that particles in a glass matrix generate flaws ~3 times larger than the diameter of the particle, because significant hoop tensile stress can exist at a distance of three radii from the particle center due to a thermal expansion mismatch between phases.¹² This situation is only possible if the CTE of the glass is higher than that of the included particles.⁴

Borom¹² and Studt et al.^{12,34} found a significant strength improvement with small-particle-size glass-ceramic and mullite-glass systems. Both demonstrated a high degree of thermal expansion anisotropy. Borom observed that the glass-ceramic system exhibited an increase in strength three to four times greater than could be attributed to a one-to-one increase in elastic modulus.¹² Studt determined that the development of a high-expansion second phase (cristobalite) significantly increased the strength of 11- μm mullite-glass composites.³⁴ Borom attributed his strength improvement to the development of a state of variable compressive stress in the glass as a result of the higher-expansion dispersed phase; thus, particles near the surface would create biaxial compression at the surface which would hinder both crack initiation and growth.

High tensile stresses produced by thermal expansion mismatch may also influence the direction of fracture propagation and increase or decrease the energy absorbed during fracture, thereby affecting the material fracture toughness, or K_{Ic} value.^{33,52,54} If the expansion coefficient of the particle is sufficiently higher than the glass, there will be both radial tensile and tangential compressive forces between the particle and matrix and the fracture may be deflected around the

particles by the stress fields. The increased tortuosity of the crack path results in an increase in fracture toughness. In addition, these tensile stresses may create spontaneous microcracks within the two components upon cooling that are subject to these forces.⁵⁵ If the expansion coefficient of the particle is sufficiently smaller than the glass, there will be tangential tensile stresses between the particle and the matrix. This may lead to the formation of radial cracks emanating from the particles and a fracture should be directed toward a particle, thereby lowering the toughness. When expansion coefficients are similar (or equal), very small thermal stresses are present and fracture should be trans-granular in nature. These effects are directly related to the relative CTE coefficients of the glass and matrix phases, and will be examined with more detail in Section 1.4.2.

When a glass-crystal composite is stressed, either by residual thermal stresses or by applied loading, microcracks will first originate at the weaker sites in the system through a heterogeneous nucleation process. In a system where crystals are imbedded in a glass, these sites are assumed to lie in the glass region near the interface, where structural imperfections may lie, as well as macroscopic stress concentrations due to differences in elastic properties of the two materials.⁴⁰ Consequently, large differences in thermal expansion coefficient have been shown to significantly affect the fracture behavior of large-particle-size glass-crystal composites due to the presence of various types of cracking which increase the flaw size relative to the glass and also decrease the composite elastic modulus. Strengthening can be obtained by reducing the particle size of the dispersed phase below the critical size necessary for cracking. This is only a valid argument in the event the glass is weaker than the particle and $CTE_{\text{glass}} > CTE_{\text{particle}}$. What has been observed in porcelains, however, is that neither of these criteria is met.

1.4.2 CTE Mismatch

When two materials with different CTE values are interfacially bonded, heating and cooling introduces thermal strains into the materials due to the mismatch between the expansion coefficients. In the case of porcelains, filler grains and the glass phase experience this mismatch upon cooling, which results in the evolution of residual stresses within the fired microstructure.

The orientation of these stresses depends entirely on the relative values of CTE. That is, depending on which phase (glass or filler) has the higher expansion coefficient, the resultant stress distributions will vary. As well, depending on the relative strength and toughness of the phases, crack morphology will also vary.

For a situation where the CTE of the glass phase is higher than that of the filler particle (Figure 5), upon cooling the glass wants to contract more than the filler particle. The residual stresses are radially compressive and tangentially tensile (Figure 5a). This is the effect observed in the glass-alumina composites created by Borom,¹² as well as the stress distribution that causes crazing on a glazed porcelain body. If stresses are high enough, to relieve them cracks will open up in the glass (Figure 5b).⁵⁶ Although the particle may be weaker than the surrounding glass, the forces present put the particle in compression, thus cracks in the glass will not travel through the filler grains, but instead, travel through the glass around and between particles, connecting cracks radiating from other grains, creating a fracture path which can become a large flaw within the material (Figure 5c).

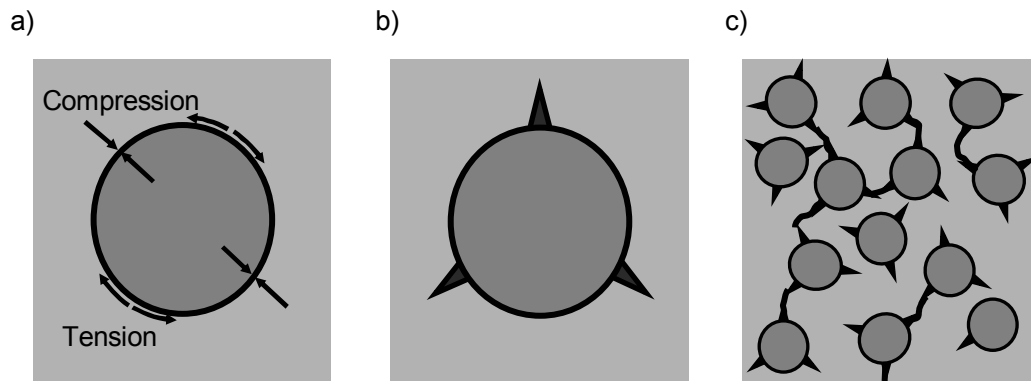


Figure 5. Schematic of glass-particle system showing a) residual stress distribution, b) crack orientation, and c) spontaneous crack behavior in a microstructure in which $CTE_{particle} < CTE_{glass}$.

These flaws can easily propagate through the material and cause failure under a relatively low external load, or in some cases (if residual stress is sufficiently high) spontaneously. Materials with this configuration typically do not have high strength; therefore it is typically unfavorable to use fillers that have lower CTE values than the glass phase.

If the CTE of the particle is instead higher than that of the glass phase, a number of possibilities can result. Highly contracting, high modulus inclusions will tend to detach from the matrix and produce a defect comparable to a void. Inclusions that are more compliant, or exhibit smaller contractions, remain attached to the matrix. The expected failure mode depends on the elastic modulus and fracture toughness of the inclusion, as well as the matrix.⁵⁷ In the case of a porcelain glass phase containing quartz grains, thermal stresses place the particle in radial tension and tangential compression (Figure 6a). Upon cooling, if sufficient stress is present, cracks form, but in the grain, not the glass, as it typically is the weaker phase (true for most porcelain fillers) and also the glass experiences compression. Because of this compression, cracks within grains will not readily move into the glass phase, but tend to travel across the grain and deflect around the interior of the grain itself in response to the compression zone at the interface (Figure 6b). In addition, the interfacial bond between the glass and the filler grain is sufficiently strong that grain failure is favored over debonding of the filler particle at the glass-particle interface (Figure 6c).

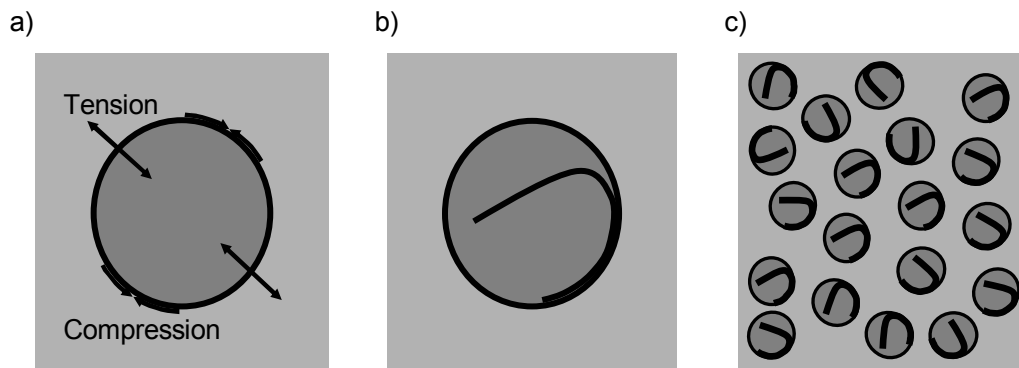


Figure 6. Schematic of glass-particle system showing a) residual stress distribution, b) crack orientation, and c) spontaneous crack behavior in a microstructure in which $CTE_{particle} > CTE_{glass}$.

The orientation of stresses placing the glass in compression is favorable, since a surface flaw in the porcelain will not as easily propagate through the glass phase when it is in compression, increasing the overall fracture toughness of the material. Materials with this configuration are also more likely to have high mechanical strength.⁵⁸

When a sufficiently high external load is applied to these materials, a surface flaw in tension will propagate through the material, inevitably causing catastrophic failure. However, the amount of applied stress the microstructure can withstand before failing (fracture toughness) is related to the relative thermal expansions between the phases, inasmuch as it depends on the distribution of stresses within the material, and the stresses are a function of the CTE mismatch. For a situation as in Figure 5, where the CTE of the particle is less than that of the glass, many interconnected cracks exist in the microstructure prior to application of external load (Figure 5c). Therefore a surface crack will move toward the grains, where the glass phase is in tangential tension, and travel between particles along a path of least resistance, connecting the pre-existing cracks, ultimately leading to failure (Figure 7a). Relatively speaking, this material would have the lowest fracture toughness, for it requires the least amount of energy to create a complete fracture path through the material.

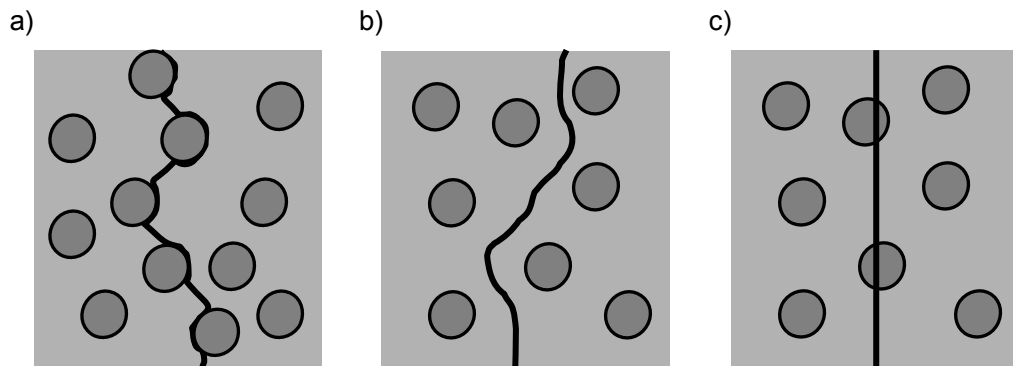


Figure 7. Schematic of glass-particle system showing the path of a surface crack when a) $CTE_{particle} < CTE_{glass}$ b) $CTE_{particle} > CTE_{glass}$ and c) $CTE_{particle} = CTE_{glass}$.

In the case where $CTE_{particle} > CTE_{glass}$, such as in Figure 6, an incoming surface crack would be deflected around the zones of relative glass compression that exist in the matrix near the particles, resulting in a meandering crack path (Figure 7b) that requires more energy to propagate than if it were to move straight through when the CTEs of the phases are the same (Figure 7c). Therefore, depending on the amount of residual stresses of this type present, a material's fracture toughness measures appreciably higher when it contains a high-thermal-expansion included phase.

1.4.3 Filler Particles in Whitewares and Porcelains

Quartz is commonly used as a filler because of its abundance and low price; hence its popularity with the whiteware manufacturing industry, where cost-to-benefit ratio is a critical factor. One of the purported main purposes of quartz use is the prevention of exaggerated deformation during firing. As it melts, glass viscosity increases, which helps to prevent pyroplastic deformation.⁵⁹ In the scientific community, however, the use of quartz as acceptable filler material for high-strength porcelain bodies is met with considerable opposition. Some investigators have concluded that quartz is entirely detrimental to a porcelain body, while others have reported some beneficial effects along with their overall negative appraisal. To date, quartz is still the most commonly used filler material; therefore, much empirical analysis has been performed to determine the proper use of quartz to produce optimum strength. A main factor of fundamental consideration is that of the body thermal expansion. For typical glazed porcelain bodies, adequate glaze-body fit occurs when the thermal expansion coefficient of the body is higher than that of the glaze. Therefore, additions to raise the thermal expansion of the body are desirable. Table III shows the approximate thermal expansion of a number of materials related to the porcelain system.

Table III. Approximate Thermal Expansion of Some Body Ingredients (from Dinsdale).⁴⁶

Material	Thermal Expansion (%) to 500°C	Thermal Expansion ($\times 10^{-6} K^{-1}$)
Earthenware body	0.35	8.3
Earthenware body without flint	0.25	5.8
Fused Silica	0.025	0.55
Mullite	0.23	5.3
Alumina	0.36	8.4
Quartz: parallel to c-axis	0.60	9.0
perpendicular to c-axis	1.02	13.0

A normal glaze would have an equivalent thermal expansion value on the order of $8.0 \times 10^{-6} K^{-1}$. In order to obtain a body expansion of $8.0 \times 10^{-6} K^{-1}$ or higher, it can be seen that quartz is by far the most effective filler material that can be added.⁴⁶ This initially seems to be an endorsement for quartz, but Dinsdale goes on to state that the addition of silica to whiteware bodies increases

the risk of dunting (failure of a ceramic brought about as a result of thermal stresses during cooling). It also adversely affects glaze appearance and reduces the mechanical strength. Therefore, it is recommended an effort be made to eliminate its use. Lundin^{58,60} reported that quartz grains, having a higher thermal expansion coefficient, strive to contract more than the glass upon cooling. As a result, tensile stresses arise within the quartz grain, having their largest value closest to the phase boundary and rapidly decreasing with distance from the grain. A common theory propagated throughout literature is that due to this thermal expansion mismatch circumferential cracks form in-situ around grains within the glass phase.^{47,55,61-66} It is well known that when cooling through 573°C (known as the quartz inversion temperature) a displacive transformation takes place (β - to α -quartz), accompanied by approximately a 2% volumetric shrinkage of the grain, its precise magnitude depending on the crystallographic orientation.⁶⁷ In a porcelain matrix the quartz grains are strongly bonded to the surrounding glass matrix. This causes a strain of quartz with radial tensile stress in the grain and tangential compressive stress within the glass matrix. With changing temperature, this, according to Liebermann, leads to intensified inner stress and the expansion of already-existing microcracks that result from the transformation of the quartz.⁶⁸ Warshaw and Seider²³ observed extensive cracking with the addition of large quartz grains. Steere observed peripheral fracturing around most quartz grains.¹⁵ Through fractographic analysis, he observed that in most cases peripherally cracked quartz grains were fracture origins and thus flaw sites for fracture initiation. Banda et al. observed considerably lower K_{Ic} values for porcelains containing large quartz grains, attributing it to extensive circumferential cracking that occurs around quartz grains that is commonly observed in polished microstructures.⁴¹ In some extreme cases coarse quartz grains were said to be partially or fully detached from the matrix on cooling below the quartz transition temperature. In other cases, quartz grains immediately adjacent to pores are said to produce these critical flaws. The prestress caused by quartz of a certain size, which is insufficient to induce matrix fracture, may strengthen the glassy phase, resulting in an increase in strength. However, if a quartz grain is combined with a pore, an additional shear stress at the contact part of the quartz, pore, and matrix is produced. This shear stress makes the pore transform into a sharp crack on the

boundary and it becomes more deleterious than the effect of an independent pore.^{65,69} Warshaw and Seider²³ reported that quartz is always deleterious to strength but in varying degrees according to particle size. They suggested that if quartz were to be used, 25- μm grains would produce an optimum strength due to the transition type of fracture, from interconnected matrix fracture at large particle size (50–150 μm) to a small amount of peripheral fracture around 25- μm grains. The decrease in strength as grain size decreased below 25 μm was thought to be caused by the dissolution of the quartz during firing.

Not all investigators conclude that quartz is to be avoided in porcelain bodies. In fact, some studies have highlighted the beneficial effects of quartz. Emphasis was placed on the issue of using the proper particle concentration and size distribution to achieve maximum strength. Sugiyama et al. created porcelain bodies with increased quartz content (50–60%) and found that the fired strength was comparable to that of conventional porcelains (80 MPa / 11600 psi).⁷⁰ Andreeva and Ordan'yan⁷¹ proposed that a quartz particle size less than that of feldspar is useful because it improves substantially the strength and produces no adverse effects on other properties of the porcelain mixture. Rado⁶¹ observed that adding quartz to a high-quartz body increased strength, but additions to a low-quartz body will cause a decrease in strength. The strengthening effect was attributed to more quartz crystals present in the glass matrix, reducing average separation distance and increasing glass-phase compression. Mattayasovsky-Zsolnay⁴⁷ suggested that 15–30- μm quartz grains improve the strength of the quartz porcelain because of favorable prestresses induced in the glass matrix. Many studies have also concluded that the amount of quartz that dissolves into the glass phase is related to particle size, in that smaller particles have higher surface area and are more readily dissolved, reducing the amount and size of residual quartz grains left to weaken the porcelain.⁷²⁻⁷⁶ Throughout studies of commercial porcelains, cracking has been found in all sizes of quartz particles down to 1 μm .¹⁵ However, Storch et al.⁴⁵ reported that cracking all the way down to room temperature is only possible for particles exceeding a certain critical size. As long as the particles are smaller, spontaneous microcracking will not occur. If the elastic energy requisite to crack formation is such that it can be achieved by an external load, cracking can be induced by external force. There was no

spontaneous microcracking found below 20 μm . This concept was further substantiated by Pinto,⁴ who observed no spontaneous cracking below 87 μm in quartz porcelains, and proposed that cracking was confined within filler particles due to the compressive forces at the interface and also the relative weakness of quartz grains compared to the surrounding glass. Any cracking observed around quartz grains was attributed to artifacts caused by stress corrosion of the glass during SEM specimen preparation (e.g., polishing in the presence of water).

Alumina (Al_2O_3) is a common filler substitution for quartz in porcelain bodies; hence it is one of the most prominent types of investigations involving porcelain filler substitution found in literature. Incrementally using 20–50% alumina in bodies containing the same clay/flux ratio, Knickerbocker⁷⁷ reported a porcelain strength increase from 131 MPa (19000 psi) to 297 MPa (43000 psi) when the alumina was vibratory milled to remove agglomerates. For unprocessed alumina bodies (those in which the alumina was not processed to remove agglomerates) flexural strength decreased with increasing alumina content, ostensibly due to the increase in flaws caused by agglomerates. The work of Austin⁷⁸ in 1947 concluded that the use of alumina to increase strength is most effective by incorporating 30–40% alumina, replacing a corresponding amount of silica, because it decreases the abrupt changes in the thermal expansion curve due to the β - to α - quartz inversion upon cooling. It also increases the overall body thermal expansion as well as broadens the firing range. Furthermore, Austin claims that the glass phase in corundum-bearing bodies should yield a glass phase with higher viscosity and result in less deformation.⁷⁸ However, based on recent research it is now known that the opposite is true; pyroplastic deformation is known to occur more readily in porcelains that contain low silica content, replaced with alumina, because the glass phase viscosity in the absence of silica is low.^{4,79} Blodgett⁸⁰ created dry-pressed alumina porcelain bodies at similar firing temperatures to conventional electrical porcelains (1315°C) and measured unglazed flexure strengths of 140–240 MPa (20000–35000 psi) versus 28–83 MPa (4060–12030 psi) for a typical feldspathic porcelain. Harada et al.⁵⁰ concluded that through the addition of alumina, flexure strengths of feldspathic porcelain could be raised from 80 MPa to 120 MPa (11600 psi to 17400 psi), attributing the increase to the decrease in the amount of quartz present in the fired microstructure, lessening the

influence of the quartz inversion. Khandelwal and Cook reported that when the porcelain is rich in alumina, it is stronger than if it is rich in silica, because it can resist more stresses without producing a crack system. They replaced quartz with alumina and a marked strength improvement was observed.⁸¹ Vazquez et al.⁸² stated that compositions containing alumina are commonly found to be free of internal cracks and, therefore, are stronger than those with comparable quartz compositions. The addition of alumina produced a 44% increase in elastic modulus using a firing temperature of 1350°C. The use of alumina favors the decrease of quartz, therefore an increase in strength is proposed. Similarly, Kreimer and Chistayakova⁸³ reported that the bending strength of porcelain is increased with a rise in the proportion of one of the alumina crystalline phases, on account of the reduction in the proportion of the second crystalline phase and the glass phase; i.e., a reduction in the amount of residual quartz and glass phase. None of these investigations gave a definitive reason why alumina would increase strength except to indicate that quartz should be avoided.

Fused silica is another material used in place of quartz in a porcelain composition, as it has a very low coefficient of thermal expansion and is proposed to dissolve more readily in feldspar than quartz. A study by Westman⁸⁴ revealed that using fused silica could eliminate the weakening effects of quartz. It supplies the glass phase with sufficient SiO₂ and results in a more linear thermal expansion behavior; the quartz inversion being absent as fused silica is a more volume- stable material.⁸⁴ Maity et al.⁸⁵ reported that the replacement of quartz with 30% (by weight) sillimanite sand (a beach sand waste product similar in composition to mullite) resulted in not only a strength increase but also an increase in thermal shock resistance. Low porosity with sufficient crystalline phase resulted in high flexural strength.⁸⁶ Avgustinik and Sintsova⁸⁷ substituted quartz with a crystallizing soda-lime silicate glass, resulting in a mechanical strength increase due to the reduction in tensile stresses that arise in the glass phase as a result of the CTE mismatch that leads to the formation of microcracks in the glass. Overall, the alternate porcelain did not differ from ordinary porcelain in external appearance or fracture characteristics, yet had a sintering temperature (~1150°C), reduced by up to 250°C. Dana et al.⁸⁸ studied fly ash (a combustion product containing quartz and mullite phases) substitutions for quartz in porcelain.

Results indicated increased strength and a lower maturation temperature, yet the glass phase had a lower viscosity, and appreciable amounts of impurities such as TiO_2 and Fe_2O_3 were introduced through the use of fly ash. Increased mullitization was also observed in the fly-ash porcelain. Dev and Cook substituted zircon for quartz in porcelain and found the flexure strength increased to as high as 130 MPa (18800 psi), thus comparable to that of alumina porcelain.⁸⁹ Frith, Heckrodt, and Schuller⁹⁰ created a zircon-based feldspar porcelain and found significant improvement in mechanical properties, mainly attributed to zircon's lower thermal expansion coefficient which was found to minimize internal stresses. Prasad et al.⁹¹ replaced both quartz and feldspar with sericitic pyrophyllite (an alumino-silicate material), which resulted in reduction of vitrification temperatures, reduction in thermal expansion coefficient and favorable increase in strength and elastic modulus attributed to the sharp drop in the quartz content and the rise of the mullite content in the microstructure. He also reported that pyrophyllite bodies were less prone to dunting and warping. Adding talc ($\text{Mg}_3\text{Si}_4\text{O}_{10}(\text{OH})_2$) to an aluminous electrical porcelain in quantities up to 2 wt% was shown by Tkalcec et al.⁹² to increase the strength due to reduction in observed porosity and increased mullite formation; in larger quantities it produces the opposite effect.

1.5 Overview of Porcelain (Subject of Study)

This investigation focuses on evaluating strength-controlling variables. The main subject material of this study is porcelain. Studying porcelain bodies provides an opportunity to investigate relationships between these variables, which aid in characterizing porcelain bodies as a material. In addition, these relationships may be independent of the composition and apply to other ceramic materials and systems as well. Porcelain was selected because it is a robust material, readily available, and contains a relatively simple microstructure that has been thoroughly characterized. Furthermore, recent data indicate that some traditional views of this material may be outdated, and a closer look at the material in general is warranted. In literature the strength-defining factors for porcelain bodies have been debated for over 50 years. Therefore, porcelain is

a prime candidate for study, as it can reveal not only insight about ceramics in general, but also specifically address issues that have been controversial for nearly half a century.

A porcelain body typically is made up of three components- clay, flux, and filler. For this reason they are referred to as triaxial whitewares. Typical compositions contain kaolin clay, ball clay, feldspar and quartz. Common porcelain raw materials are listed in Table IV.

Table IV. Primary Raw Materials Used in the Manufacture of Porcelains.⁶⁷

Raw Material	Composition	Use
Kaolin	$\text{Al}_2\text{O}_3 \cdot 2\text{SiO}_2 \cdot 2\text{H}_2\text{O}$	Clay
Ball Clay	$\text{Al}_2\text{O}_3 \cdot 2\text{SiO}_2 \cdot 2\text{H}_2\text{O}$	Clay
Soda Feldspar	$\text{Na}_2\text{O} \cdot \text{Al}_2\text{O}_3 \cdot 6\text{SiO}_2$	Flux
Potash Feldspar	$\text{K}_2\text{O} \cdot \text{Al}_2\text{O}_3 \cdot 6\text{SiO}_2$	Flux
Nepheline Syenite	$\text{K}_2\text{O} \cdot 3\text{Na}_2\text{O} \cdot 4\text{Al}_2\text{O}_3 \cdot 9\text{SiO}_2$	Flux
Alumina	Al_2O_3	Filler
Quartz	SiO_2	Filler

Clays are fine-grained materials that provide plasticity and green strength to porcelain during the forming stages and contribute to the color of the fired ware. They begin to dehydroxylate at 550–600°C. Traditional feldspathic fluxes provide SiO_2 and Al_2O_3 to the composition as well as alkali, which act to dramatically reduce the firing temperature of the material. Quartz has a melting temperature of 1723°C, but in the presence of eutectic K_2O and Al_2O_3 , melting occurs at temperatures as low as 990°C. Fillers are generally the coarsest fraction and are proposed to be used to provide network support for the body. Quartz is commonly used to provide additional SiO_2 and also increase glass-phase viscosity. Alumina is sometimes used in place of quartz, as discussed earlier, to improve the mechanical properties of the body. The significantly greater cost of alumina compared to quartz is a major drawback to its use. Collectively, fluxes and fillers are referred to as “nonplastics,” because they possess no intrinsic plasticity.^{67,93}

The microstructure of standard porcelain bodies consists of α -quartz and mullite in a glassy matrix, whereas aluminous porcelain contains corundum as well.⁹⁴ Mullite is usually formed into two different types; they are what are referred to as primary and secondary mullite. Primary

mullite is characterized as a scaly acicular crystal (<0.5 μm long) that appears to form within clay relicts, at lower temperatures ($\sim 1075^\circ\text{C}$). As alkali diffuses out of the feldspar relicts at higher temperatures ($>1200^\circ\text{C}$), secondary mullite in the form of sharp, needle-like crystals ($>1 \mu\text{m}$ long) nucleates and grows within the feldspar relicts.⁶⁷ Recent studies have challenged this view due to the proposal of a glass-formation boundary that describes circumstances under which mullite formation is possible.⁹⁵ Secondary mullite is an orthorhombic structure with preferential growth along the c-axis, resulting in the needle-like appearance of the crystals.⁹⁶ Quartz grains dissolve to some extent, providing additional silica to the glass melt. Alumina fillers have also been attributed to the formation of mullite, as there is nominal dissolution of the alumina grains into the glass phase during firing. Residual filler grains such as quartz and alumina have been the subjects of controversy.^{67,93,94,97}

1.6 Prevailing Porcelain Theory

As is evident from previous discussions, historically there has been ambiguity as to the true mechanisms that definitively control porcelain strength. Many authors have linked this property to composition, green processing, drying, and/or firing schedule, to name a few. In the literature there have emerged three prominent arguments that each claim to explain the dominant factor that determine the strength of a porcelain body. They are 1) the mullite theory, 2) the dispersion theory, and 3) the prestress theory. Each theory is supported by a plethora of experimental evidence and data. However, each respective theory also tends to refute the evidence of the other two, leaving the reader with a sense of uncertainty as to the overall picture. Some of these theories had remained virtually unchanged and unchallenged since the 1960s until recent work using modern experimental techniques and equipment has resulted in evidence that clearly supports and refutes pre-existing data.⁴ It is the intent of this overall investigation to thoroughly explain its findings in such a way to leave a clear impression as to the true mechanisms that control strength.

1.6.1 Mullite Theory

The prominent theme in the mullite theory is that mullite controls the strength of a porcelain body. This theory is supported by many investigations.^{19,34,47,61,67,81-83,91,98-107} While primary mullite forms within clay relicts, secondary mullite, an acicular needle-like phase, is often observed in feldspar relicts. The theory states that finely interlocking mullite needles result in a more resilient microstructure. The glass matrix supported by mullite needles is less prone to crack propagation. Therefore, the finer and more interlocked the needles are, the higher the resulting strength should be. High temperatures cause mullite needles to coarsen, and larger mullite crystals do not interlock as well; therefore, the resulting porcelain may have a lower strength.^{47,101} Increasing overall mullite concentration has been linked to improved mechanical strength, due to the increased prevalence of the aforementioned phenomena. In fact, Maslennikova et al.¹⁰⁸ suggest adding calcined kaolin to porcelain compositions to boost mullite concentration and therefore strength.

In a study of mullite-glass systems, Studt and Fulrath reported increased modulus of rupture with increased crystalline mullite phase due to the strong interfacial bond between mullite and glass.³⁴ Sane and Cook, while using X-ray diffraction to study the effect of grinding on porcelain bodies, noted that the fired strength, when correlated with the X-ray data was found to depend on the total mullite and glass present.¹⁰⁴ Vázquez et al. showed that increasing alumina content favors an increase in mullite; therefore, the maximum increase in strength is attained by increasing the mullite concentration and reducing the amount of residual quartz.⁸² Kraner¹⁰⁵ found that mullite solution may contribute to the weakening of overfired porcelain. Kalnin et al. observed that Young's modulus increased linearly with the total amount of mullite, implying that the strength must also increase in proportion to mullite content. However, he noted that high temperatures (>1500°C) required to produce a high mullite content also increase porosity, which more than offsets the increase in strength due to mullite.¹⁹ Although not commenting directly on the effect of mullite content versus strength, Schuller⁷⁵ reported that melts high in silica promote mullite re-dissolution, which Kreimer and Chistyakova also observed, indicating that a maximum increase in bending strength can be attained by increasing the content of mullite due to the reduction of the

amount of residual quartz and glass phase.⁸³ In a later study, they added that when a porcelain contains <10% residual quartz, an increase in mullite content occurs, leading to an increase in strength. However, when there are residual concentrations >11%, an increase in mullite produces a decrease in strength.¹⁰⁶ Flaitz¹⁰⁷ recorded a linear relation between mullite concentration and strength in 40–50% alumina bodies, but could find no relation between mullite content and Young's modulus. Maity et al.⁸⁶ found that increased strength directly correlates with the mullite content of porcelains studied; however, a decrease in mullite content when the body was fired between 1300°C and 1350°C did not correspond to a reduction in strength. Therefore, it was decided that mullite content was not the only factor responsible for high strength. In their experiment, they also deemed the presence of crystalline cordierite to play a major role. Sane¹⁰⁴ reported that intimate mixing and fine grinding of bodies reduced the free quartz content and increased the total mullite concentration, on which the fired strength was found to depend.

Opponents to this theory claim to have observed no strength trend associated with mullite content. Khandelwal and Cook studied the effect of alumina additions on porcelain strength, and concluded that mullite content did not show any effect on strength.⁸¹ Likewise, Ke⁶⁹ found no correlations between the total content of primary and secondary mullite and porcelain strength. Maity et al. more recently a strong supporter of the mullite theory, reported in an earlier work that changes in firing temperature resulted in differences in mullite content that did not correlate to strength.⁸⁶ Ece and Nakagawa⁴³ measured the bend strength of porcelain bodies as a function of mullite content and observed no relationship between mullite content and strength, stating that the strength is instead dependent on the homogenous glassy matrix. A recent article, published in 2004 by Stathis et al., noted, from their study on sanitary-ware porcelain, that the beneficial influence of mullite content on bending strength was not evident since no relationship could be identified.¹⁰⁹ Carty recently developed a model for porcelain bodies, due to data which indicate the glass-phase composition is identical in all triaxial porcelains at any given temperature and to lie on the glass formation boundary within the flux-alumina-silica system.⁹⁵ From 1150°C to 1400°C, mullite levels within the samples do not change with increasing time or temperature,

indicating that the alumina-to-flux ratio ($R_2O + RO$) within the glass phase does not change with increasing temperature. A constant mullite level in a porcelain sample is only possible if there is a constant alumina level in the glass phase. As mullite is the only crystallizing species in the body that contains alumina, then the alumina level within the glass phase is fixed once mullite is crystallized. This is a critical observation to understanding glass-phase compositions in porcelains.⁹⁵ As a result of an investigation by Pinto, it was also concluded that, although some studies observed increased strength due to increased mullite content, attributing mullite to the strength increase was an indirect conclusion, as most studies also indicated a decrease in glass phase and residual quartz concentration along with increase in mullite.⁴ To illustrate this inconsistency, Figure 8 shows four-point flexure strength of a silica porcelain body as a function of quartz particle size. Overlaid on this figure are also the concentrations of residual quartz and mullite existing within each composition (determined via quantitative XRD technique),⁴ also as a function of filler particle size. What is shown is that as filler particle size increases, the strength changes, increasing slightly in the small-particle regime, and then decreasing rapidly above 25 μm . The concentrations of mullite and quartz within the bodies are constant, independent of the filler particle size and mechanical strength. The fact that mullite and quartz concentrations remain constant, yet the mechanical strength changes clearly indicates that mullite content is not a strength-controlling factor within these bodies. This phenomenon is corroborated by the work of Hermansson and Carlsson, who found the glassy phase in thirty whitewares to be nearly of identical composition.¹¹⁰ Furthermore, since the levels of quartz and mullite remain the same throughout the different bodies, it can be said that the remaining fraction, the glass phase, also has constant concentration and composition. Therefore, this is further evidence that mullite concentration does not control strength. It also indirectly indicates the glass-phase composition is not a critical strength-controlling factor either.

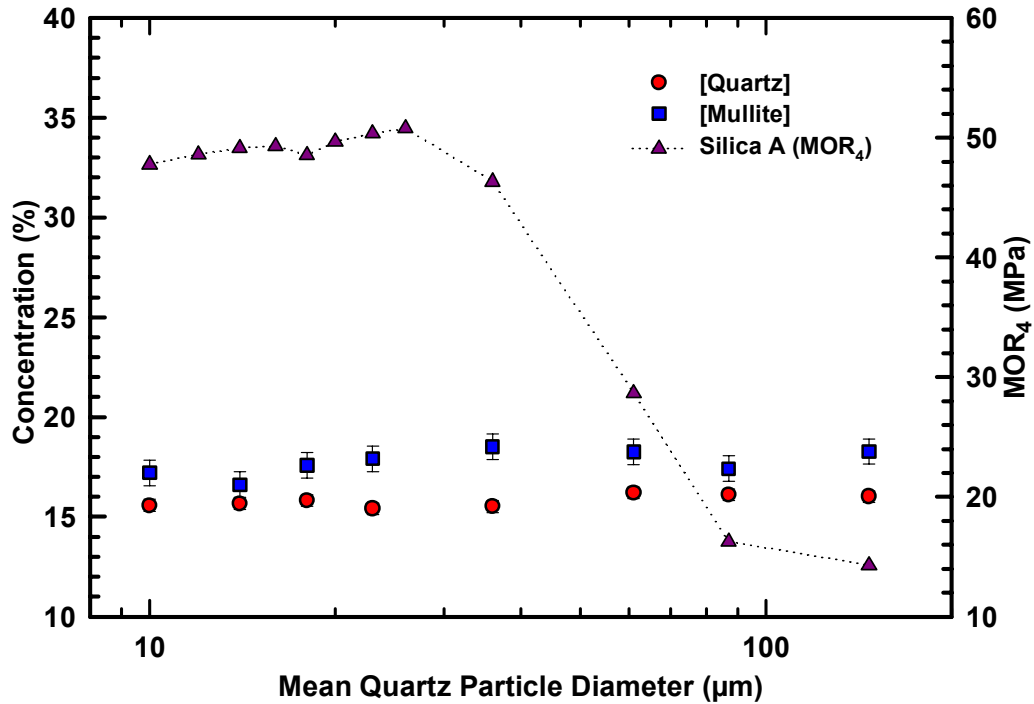


Figure 8. Plot of phase concentration and four-point flexure strength of a silica porcelain composition as a function of filler particle size.

1.6.2 Dispersion Theory

Hasselmann and Fulrath were the main proponents of the dispersion-strengthening theory.²⁴ This theory states that hard crystalline dispersions within a glass matrix will limit the size of Griffith flaws and strengthen the composite material, assuming the particles are stronger than the surrounding glass and that cracking initiates within the matrix. At low concentrations of the dispersed phase, average flaw size is reduced independent of the particle size. At high volume fractions, however, the average flaw size is governed by the average distance between particles dispersed in the matrix. More precisely, the strengthening effect depends on the mean free path between particles. If the average distance between the particles is greater than the flaw size, the strength of the glass is a function of volume fraction of particles. If instead the flaws are larger than the average particle separation distance, then glass strength is a function of volume fraction of particles and particle size. It has been hypothesized that the strength increase in porcelains is a dispersion-strengthening effect, because the particles act as dispersed solids in a glass matrix. Nivas and Fulrath further corroborated these findings by demonstrating that this effect extended

to small Griffith-type flaw sizes.³⁹ Davidge states that high values of strength may be obtained when a high concentration of small particles is present.³ Maity and Sarkar, while investigating a porcelain system involving sillimanite and alumina/cordierite substitutions for quartz and feldspar, respectively, determined that at higher firing temperatures (1500°C), although mullite dissolved in the glass, increased strength was attributed to a dispersion-strengthened glassy matrix.⁹⁹ Rounded particles of sillimanite and alumina acted as dispersion agents and helped inhibit crack propagation, increasing strength and fracture toughness values.

There are both theoretical and experimental data opposing the dispersion-strengthening theory as the explanation for porcelain strength behavior. Borom¹² challenged the dispersion theory and found that re-interpreting the results of Miyata and Jinno⁴⁰ and Frey and Mackenzie¹³ revealed that particles introduced into a brittle matrix do not limit flaw size in relation to interparticle spacing, but may produce surface flaws in proportion to particle diameter. He also reasoned that, although dispersion-strengthening may increase the overall modulus, the expected strength enhancement might not be achieved because of the particle-induced flaws. Previous work by Pinto indicates that the dispersion-strengthening theory is not applicable to a porcelain body.^{4,111} It is typical of the mindset that a glass is weak when compared to a crystal of similar composition, due to its amorphous, short-range-ordered structure. According to the dispersion-strengthening criteria, stronger filler grains are added to the weaker glass to provide structural support and increase the strength of the overall material. Recent data suggest, however, that the porcelain glass phase is not the weaker component within the microstructure. Shown in Figure 9 are residual strain measurements taken from two nearly-identical porcelain bodies, which have different fillers (e.g., alumina and quartz).⁴ Residual strain is shown to increase with filler particle size, resulting in a relative strain maximum for each respective filler. As shown, a different strain maximum was achieved for each of the bodies, resulting in a difference in strain ($\Delta\varepsilon$). This observation indicates that the glass phase is not the strength-limiting factor within the porcelain. If the glass were weaker, only one maximum value for strain would occur ($\Delta\varepsilon = 0$), which is clearly not the case. These data suggest that the filler grains are weaker than the glass phase, having their own strain limits exceeded, and failing first due to the thermally-induced stresses in the

microstructure. Quartz and alumina have been shown to be able to withstand stresses (without fracturing) of 2 GPa and 5 GPa, respectively.⁴ Although glass is typically considered a weak material, showing experimental strengths on the order of several MPa, this is often due to surface defects and stress corrosion caused by water vapor.¹⁰ In a pristine environment such as is proposed to be at the glass-grain interface, environmental effects are not a factor, and so the strength of the glass approaches its theoretical strength.

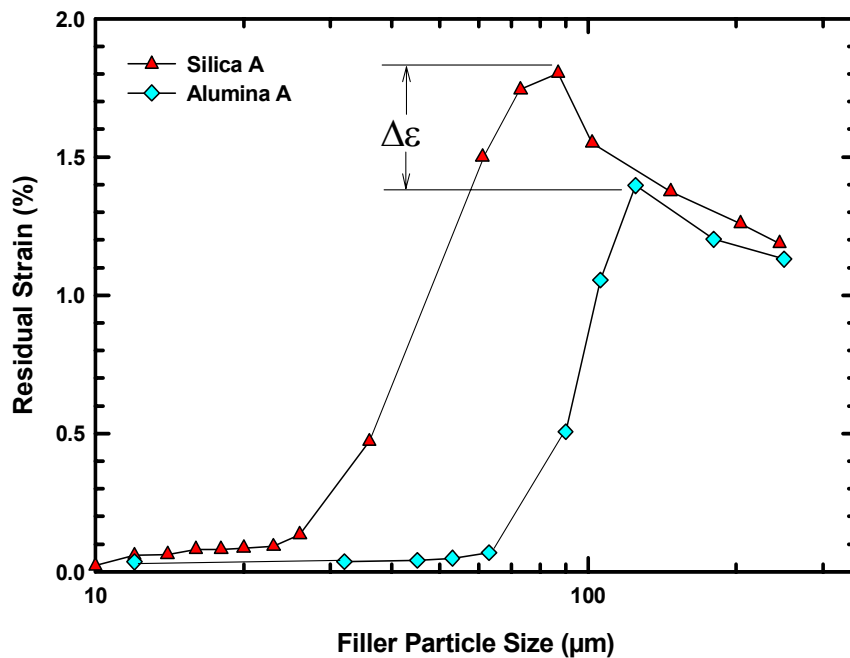


Figure 9. Plot of residual strain versus filler particle size of two porcelain bodies showing a difference in maximum residual strain.

Mattyasovszky-Zsolnay⁴⁷ reasoned that, in some microscopic areas, tensile strength may be as high as 2.9 GPa. Griffith⁶ extrapolated from his experiments the theoretical strength of glass in excess of 10 GPa, while the tensile strength of pristine glass fibers has been experimentally measured as high as 7 GPa.¹¹² Michalske and Bunker¹⁰ state that, under high-vacuum conditions, flaw-free glass can withstand tensile loads of up to 13 GPa. A theoretical model by Naray-Szabo and Ladik, incorporating the approximation of Si-O bond strengths, came up with a calculated tensile value for silica fibers of 24 GPa.⁹ With this evidence in mind, it is entirely plausible that in this environment that the glass phase is, in fact, stronger than the filler grains.

Another criterion outlined by the dispersion-strengthening theory states that cracking must initiate in the matrix. With the likelihood that the glass phase is the stronger species, and the orientation of residual stresses; the included particle in radial tension and tangential compression (outlined in Section 1.4.2), it is determined that fracture due to these stresses must initiate within the filler grain, since it is weaker and the glass around the particle is tangentially compressed.⁴ Having established these criteria applicable to a porcelain body, it is unlikely that the dispersion-strengthening theory is valid for porcelains. In addition, Stathis et al. reported that no relationship between residual quartz content and bending strength was observed while investigating the effect of particle concentration on mechanical strength of porcelain.¹⁰⁹

1.6.3 Prestress Theory

In addition to glass-phase compression provided by the CTE mismatch, additional compressive stresses placed on the glass matrix phase by included grains (quartz, alumina) are commonly referred to as “prestress.” These stresses are said to be a function of the specific surface area of the grains that act to hinder crack propagation within the glass phase of porcelain.^{47,61,113} In the case of quartz porcelain, the inversion from β - to α -quartz at 573°C on cooling is said to cause high stresses between the quartz grain and the surrounding glass matrix. Due to the distribution of these stresses, the glass surrounding the quartz is placed in compression. This occurs because the quartz has a higher thermal expansion coefficient than the surrounding glass, plus the phase transformation amplifies the effect. In order for a crack to propagate within these localized ‘zones’ of glass containing additional compression, more energy is expended, thereby slowing its growth. The amount of localized stress is related to the size of the filler particle. Only the use of a certain regime of particle sizes results in a beneficial pre-stressing effect. If particles are too large, then stresses act to create spontaneous flaws, weakening the overall microstructure. If particles are too small, additional compressive stresses are negligible. Therefore, only the prestress caused by quartz grains of a certain size range, which do not induce matrix fracture, strengthen the glassy phase, resulting in an increase in body strength.^{69,76}

2. Experimental Overview

2.1 Compositions

Porcelain bodies used in this investigation were those experimentally designed specifically for this investigation and also plastic bodies obtained from different industrial locations. For ease of identification, base body compositions have been labeled with the alphabetic identifiers 'A', 'B', and 'C', to distinguish between the sources.

2.1.1 Porcelain A

The batch composition of porcelain A is shown in Table V. Throughout the course of this investigation, the different filler materials used in porcelain A were quartz, alumina, spinel, and mullite. Table VI lists all raw materials used in the production of all the various derivatives of the porcelain A composition. All other raw materials remained constant. This composition was developed via an experimental design that optimized densification in an industrial kiln, while at the same time containing sufficient filler material such that the effect of variations in this filler could easily be observed.¹¹¹ It was wet processed, filter pressed and vacuum extruded in small 50-kg batches (40-L suspensions). Some of the batches requiring less material, on the order of 5 kg (mullite A, spinel A), were dewatered using a baroid filtration system.

Table V. Porcelain A Base Batch Composition.

Raw Material	Amount (Wt %)
Kaolin	29.2
Ball Clay	7.3
Nepheline Syenite	34.0
Filler	29.5

2.1.2 Porcelain B

Porcelain B represents two industrial-grade electrical insulator porcelain body compositions, one containing silica as the filler, the other containing alumina (e.g., silica B, alumina B). Aside from the different filler materials, both of these compositions contain the same raw materials. The chemical compositions of both silica B and alumina B are shown in Table VII.

Table VI. Raw Materials Used to Make Various Porcelain A Compositions.

Clays / Flux	Source	Location
Tile Kaolin 6	Dry Branch Kaolin	Dry Branch, GA
Huntingdon Ball Clay	United Clay	Brentwood, TN
A 400 Nepheline Syenite	Unimin	Havelock, Ontario (Canada)
A 200 Nepheline Syenite	Unimin	Havelock, Ontario (Canada)
A 270 Nepheline Syenite	Unimin	Havelock, Ontario (Canada)
Fillers	Source	Location
Quartz (SiO ₂)	U.S. Silica	Berkeley Springs, WV
Flint (SiO ₂)	Oglebay Norton	Cleveland, OH
Mullite	CE Minerals	Andersonville, GA
Mg-Aluminate Spinel	Alcoa	Point Comfort, TX
Tabular Alumina	Almatis	Leetsdale, PA
Calcined Alumina	Almatis	Leetsdale, PA

Both compositions were processed in an industrial setting (Victor Insulators, Inc., Victor, NY). The materials were wet processed in large 5000-kg batches (>2000 L suspension), filter pressed, and pug milled under high vacuum.

Table VII. Porcelain B Chemical Compositions.

	SiO ₂ (%)	Al ₂ O ₃ (%)	Na ₂ O (%)	K ₂ O (%)	MgO (%)	CaO (%)	TiO ₂ (%)	Fe ₂ O ₃ (%)	Tr. (%)
Alumina B	43.84	49.92	0.86	3.3	0.19	0.32	0.74	0.66	0.17
Silica B	71.56	21.52	0.96	3.91	0.16	0.35	0.77	0.65	0.12

2.1.3 Porcelain C

Porcelain C represents another electrical porcelain composition (Lapp Insulators, Inc. LeRoy, NY). Its chemical composition is listed in Table VIII and is referred to as 'Silica C.' The Silica C body was also similarly wet processed, filter pressed and vacuum pug milled in large 5000-kg batches (>2000-L suspensions).

Table VIII. Silica Porcelain C Chemical Composition.

SiO ₂ (%)	Al ₂ O ₃ (%)	Na ₂ O (%)	K ₂ O (%)	MgO (%)	CaO (%)	TiO ₂ (%)	Fe ₂ O ₃ (%)	Trace (%)
64.84	28.15	1.11	4.15	0.15	0.36	0.66	0.57	0.01

2.1.4 Stoneware Porcelain

For one series of experiments, a stoneware porcelain composition was used. Its chemical analysis is shown in Table IX. It has the chemical composition similar to that of industrial silica porcelain. However, the composition itself is one typically used by a ceramic artist (potter). This material was wet processed, filter pressed, and pug milled, but a vacuum was not used. This stoneware composition also contained large, irregularly-shaped particles or 'stones' which frequently are large quartz grains or 'grog' (ground up fired stoneware) that serves to alleviate the problem of heat expansion which can cause large thick pieces of pottery or sculpture to fracture during firing.

Table IX. Stoneware Porcelain Chemical Composition.

SiO ₂ (%)	Al ₂ O ₃ (%)	Na ₂ O (%)	K ₂ O (%)	MgO (%)	CaO (%)	TiO ₂ (%)	Fe ₂ O ₃ (%)	Trace (%)
59.03	25.31	0.31	1.62	0.42	0.52	1.63	1.08	0.45

2.2 Fillers / Particle Size

In this investigation, different filler materials of different particle size were systematically analyzed so as to gain an appreciation of their contributions (or lack thereof) to the strength of a porcelain body.

2.2.1 Quartz (SiO₂)

Quartz is a commonly used filler material in many porcelain compositions. There are several common names used for quartz that often refer to its particle size, including sand (>100 μm), flint (< 45 μm), and silica (60–5 μm). However, these names are sometimes used interchangeably, so a mean particle size typically is included. Table X shows the chemical analysis for the quartz material that was used in this investigation.

Table X. Chemical Analysis of Quartz Filler Material.

SiO ₂ (%)	Al ₂ O ₃ (%)	Na ₂ O (%)	K ₂ O (%)	MgO (%)	CaO (%)	TiO ₂ (%)	Fe ₂ O ₃ (%)	Trace (%)
99.02	0.31	0.01	0.02	0.01	0.02	0.01	0.04	0.16

2.2.2 Alumina (Al₂O₃)

In a fired porcelain body, undissolved alumina is often referred to as corundum, the mineral name for α -Al₂O₃. Table XI shows the chemical analysis of the alumina raw material used in this investigation.

Table XI. Chemical Analysis of Alumina Filler Material.

SiO ₂ (%)	Al ₂ O ₃ (%)	Na ₂ O (%)	MgO (%)	CaO (%)	Ba (ppm)
0.11	99.20	0.05	0.03	0.07	5.0

2.2.3 Mullite (3Al₂O₃·2SiO₂)

Mullite is a crystalline alumino-silicate product that, as discussed previously (Section 1.5), naturally occurs within a fired porcelain microstructure. It forms needle-like crystallites within the glass matrix phase. It can also be made independently of a porcelain body by firing the proper ratios of Al₂O₃ and SiO₂ raw materials. Table XII shows the chemical composition of the mullite filler material used in this investigation.

Table XII. Chemical Analysis of Mullite Filler Material.

SiO ₂ (%)	Al ₂ O ₃ (%)	Na ₂ O (%)	K ₂ O (%)	MgO (%)	CaO (%)	TiO ₂ (%)	Fe ₂ O ₃ (%)	Trace (%)
26.15	65.95	0.02	0.07	< .01	0.06	3.46	1.14	<0.01

2.2.4 Mg-Al Spinel (MgAl₂O₄)

Spinel is a crystalline material not commonly used as filler in porcelain bodies. Instead it is typically used as a refractory material. A majority of magnesia-rich spinels are made into bricks for use in transition zones of cement kilns.^{114,115} Spinel can have a range of compositions, with a variable Mg-to-Al ratio. For this investigation an alumina-rich composition was selected (AR-70, Alcoa, Inc., Point Comfort, TX). Table XIII shows the chemical composition of the spinel material used.

Table XIII. Chemical Analysis of Spinel Filler Material.

SiO ₂ (%)	Al ₂ O ₃ (%)	Na ₂ O (%)	K ₂ O (%)	MgO (%)	CaO (%)	TiO ₂ (%)	Fe ₂ O ₃ (%)	Trace (%)
< .02	86.47	0.1	< .02	9.25	0.1	< .01	0.11	<.01

2.2.5 Filler Particle Size

Table XIV lists the different filler particle sizes used in this investigation. Particles were obtained by sieving broad particle distributions and size-segregating discrete narrow size distributions with standard screen sieves. Details of this process are thoroughly outlined in Reference 4.

Table XIV. Mean Initial Filler Particle Sizes Used in All Aspects of this Investigation.

Size (µm)	Quartz	Alumina	Mullite	Spinel
12	x	-	-	-
15	x	x	-	-
17	x	-	-	-
20	x	-	-	-
22	x	-	-	-
25	x	-	-	-
28	x	-	-	-
32	x	-	-	-
45	x	x	x	x
53	-	x	x	x
63	-	x	x	x
75	x	x	x	x
90	-	x	-	-
106	x	x	x	x
125	-	x	x	x
149	-	-	x	x
180	x	x	-	-
225	x	-	-	-
250	x	x	-	-
300	-	x	-	-

2.3 Nomenclature

In some instances, multiple compositions were sometimes created or obtained from the same source. To distinguish between these compositions and allow ease of identification, the filler type accompanies the source identifier within the name (e.g., Mullite A, Alumina B, Silica C). Secondary differences between bodies, such as filler particle size and size distribution are specifically noted where appropriate. Throughout this thesis, body compositions will be identified using this nomenclature.

When referring to mechanical properties, there are several terms that are used interchangeably throughout the literature that describe the same parameters. For purposes of this document, the symbol (σ_f), will be referred to as MOR, failure stress, or flexure strength depending on the context. It refers to the same basic property; however, in the event a subscript other than 'f' appears, the precise meaning will accompany its use. Likewise the term (E) will be termed 'elastic modulus' or sometimes 'Young's modulus.' Fracture surface energy (γ) is also sometimes called surface energy or surface tension, depending on the context of the discussion. A comprehensive list of variables is presented in Appendix A.

3. General Procedures

3.1 Sample Forming

Most samples created for this investigation were originally raw-material suspensions that were dewatered in some manner. Several techniques were employed to produce plastic bodies suitable for forming and firing. Techniques used to dewater suspensions were slip casting, filter pressing, and baroid filtering. Furthermore (with the exception of those samples made directly via slip-casting), a majority of specimens were created by auger vacuum extrusion of the plastic bodies. While porcelain A compositions were processed at Alfred University according to the following procedures, B and C compositions were filter pressed and pug-milled off-site at industrial facilities. The resulting plastic bodies contained approximately 16% moisture. The stoneware body was also obtained in the plastic form; therefore the exact dewatering process is unknown. All of these compositions were vacuum extruded at Alfred University using the same instrument and the same process.

3.1.1 Slip Casting

Solid samples of several compositions were made by slip casting 2-mm thick, 50-mm diameter discs of the material. A suspension was created by adding corresponding amounts of each powder to 350 ml of de-ionized water. Each suspension was then mixed thoroughly using a high-speed blender (Model 664, Hamilton Beach, Inc., Racine, WI) on high speed for ten minutes. The solids-to-water ratio was such that the specific gravity of each suspension was approximately 1.45 g/cm³. Each suspension was thickened for slip casting by adding 0.5 ml of CaCl₂. The slip was then poured into disc-shaped gypsum molds supported by a plastic ring to provide controlled overfill. A schematic of these molds is shown in Figure 10. Each sample was allowed to cast for 30 minutes. The overfill ring was removed, the excess scraped off, and the sample, a small disk, remained in the mold cavity to dry for about one hour, as it released from the mold. The sample was then removed and dried at room temperature overnight (~24 hours). After drying, one surface of the disk was sanded flat using fine-grade silicon carbide paper. The samples were then fired accordingly.

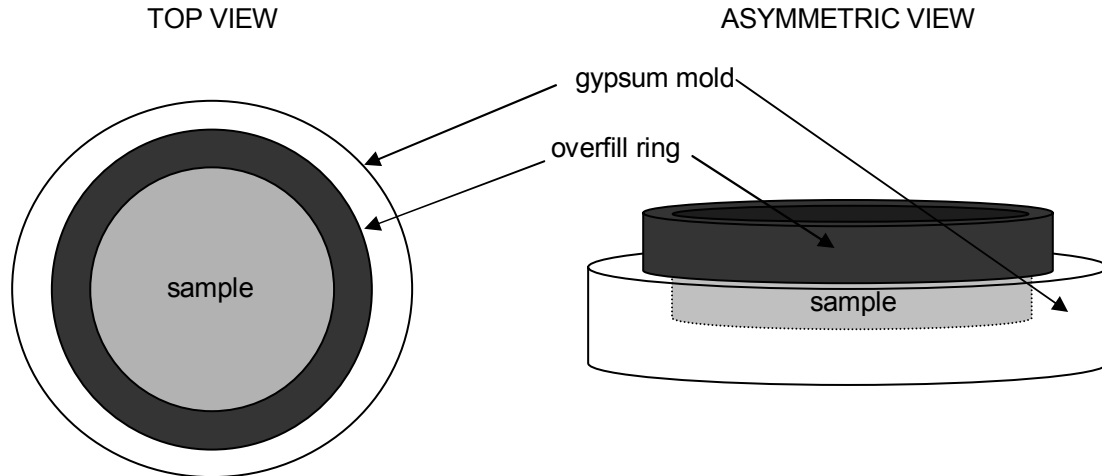


Figure 10. Schematics of gypsum casting mold containing sample.

After firing, the surface to be examined was essentially flat. No additional sanding or polishing could be carried out without ruining the specimen's suitability for testing. Slip-cast discs were used primarily for X-ray diffraction (XRD) studies; therefore, grinding or polishing the fired specimen would introduce machining damage, and could relieve some of the internal stresses present immediately below the surface where the XRD examines the sample.

3.1.2 Filter Pressing

Filter pressing was used when large quantities of samples (100+) were required for testing. For each sample a 40-liter suspension of raw materials was made, with a specific gravity of approximately 1.50 g/cm^3 . The slurry was adjusted to a viscosity of $\sim 15,000 \text{ Pa}\cdot\text{s}$ ($1.5 \times 10^7 \text{ cps}$) by additions of Darvan 7 (sodium polymethacrylate), then pumped into a laboratory-scale filter press with a mechanical diaphragm pump which, using a pressure of 120 psi, filter pressed the material into several large 'cakes.' These filter-cakes were then removed and aged for at least 24 hours before extrusion.

3.1.3 Baroid Filtration

When limited amounts of raw materials were available, or smaller quantities of samples were needed (20–30 rod specimens) a baroid filter cell was used. For each sample a 2-kg dry batch of solid raw materials was made. First, separate suspensions of the non-plastic materials (fillers, flux) were made, suspending the non-plastics in water, then adding 15% (by weight) clay. These suspensions (about 20 wt% solids) were then placed in a container with milling media and vibratory milled for 30 minutes. The goal of this process was not to mill the particles to smaller size, but rather to break up any agglomerates and coat primary non-plastic particles with clay to prevent re-agglomeration. Data indicate that 30 minutes is sufficient to break up agglomerates, yet insufficient time to create a measurable shift in the particle size distribution. Section 9.1 discusses the possible benefits of this technique.

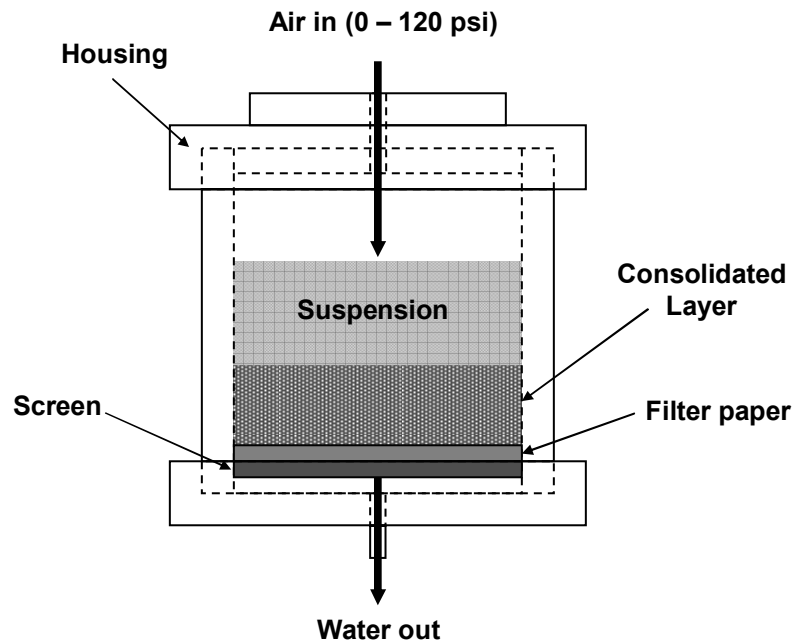


Figure 11. Schematic of a baroid filtration cell.

After this step, the remaining solid batch ingredients were added, and the resulting suspension was adjusted to a viscosity of $\sim 15,000$ Pa·s (1.5×10^7 cps) by drop-wise additions of Darvan 7. The suspension was then poured into a series of baroid cells (Figure 11), evenly distributing the suspension among 12 cells to equalize casting time. A baroid cell is made up of an aluminum

housing surrounding a sample chamber into which a liquid suspension is poured. A piece of filtration paper and a metal retaining screen resides at the bottom of the cell, allowing water to pass through, but not solids. The entire cell is pressurized with air at the top, forcing water out the bottom of the cell, creating a consolidated layer of plastic body material. Each cell was pressurized step-wise to 120 psi and held until sufficient water had been removed (12–15% body moisture remaining). The cell was then depressurized and the plastic body material was removed from the cell. The twelve portions were combined into one mass, manually kneaded together and then thoroughly mixed using a wad mill to ensure an even moisture distribution throughout the bulk material. Once completed, the body was then extruded.

3.1.4 Extrusion

Extrusion of all porcelain plastic bodies was done using a screw-auger vacuum extruder (Rawdon, Ltd., Moira Burton-on-Trent, England). The plastic body was first manually fed to one auger, which pushed the material into the vacuum chamber through a shredding device, mixing it further and also increasing the surface area exposed to the vacuum. The vacuum chamber was capable of holding a steady vacuum pressure of 25–27 inches Hg (12–13 psi). The material then, by way of a second screw auger, was forced out through an extrusion die. Long, continuous lengths (~2 m) of extrudate were drawn out onto a flat board. This was sectioned into several smaller samples (of appropriate length), any excess re-used. To maximize sample uniformity, approximately 150 mm from each end of the extrudate was removed before dividing the remainder into samples. In this way only material extruded at a constant rate was used to create specimens; it is typical for extrusion to be slower at the beginning and end of a cycle, introducing undesired striations and waviness to the appearance of the extrudate. Extruding cylindrical rods and bars of varying dimensions was possible by interchanging the extrusion dies. Samples were allowed to completely dry at room temperatures before firing.

3.2 Property Analysis

3.2.1 Bulk Density / Apparent Porosity

Bulk density measurements were taken using an ASTM standard test method (C1191-94).¹¹⁶ Specimens representative of each body composition were initially placed into a 100°C drying oven for two hours prior to testing, ensuring that all moisture was completely removed. The samples were then weighed on an analytical balance (Model AP210-0, Ohaus Co., Florham Park, NJ) to obtain the dry weight (D). They were then placed into boiling water for two hours, allowed to cool and remain submerged for 12 hours before re-weighing to obtain the suspended weight (S). To accomplish this, each sample was suspended on a loop of copper wire positioned beneath the balance immersed in water. Samples were removed and blotted with a damp cloth to remove any drops of water clinging to the surface. They were then weighed to obtain the saturated weight (W). Having these three measurements allowed the bulk density to be calculated using the following formulae:

$$V = W - S \quad (37)$$

$$\rho = D / V \quad (38)$$

Where V is the exterior volume of the sample, in cm³, and ρ is the bulk density of the sample, in g/cm³. Apparent porosity (P) is calculated in a similar way using the formula:

$$P(\%) = \frac{(W - D)}{(W - S)} * 100 \quad (39)$$

3.2.2 Flexure Strength (Failure Stress)

Three- and four-point flexure testing were carried out on porcelain samples using an Instron instrument (Model 8562, Instron Corp., Canton, MA) and a modified ASTM standard testing method (C1161-94).¹¹⁷ Each of the rods to be tested was marked for identification, and also marked on the surface that would be in tension during the test. Three-point flexure specimens were marked at the exact center of the sample, the precise location where the loading point

contacted the sample. The four-point flexure apparatus consisted of a similar support span with two loading points instead of one. Each sample was marked at the location where these loading points made contact with the sample, denoting the region between the loading points where failure of the sample should occur. Each sample was tested to fracture, the maximum load at failure (P) being recorded. Any sample that did not fail at the center during a three-point flexure test or within the inner span during a four-point flexure test was discarded.

These values were input into the standard formulae for the strength of a rod in three- and four-point flexure:

$$\text{MOR}_3 = \frac{8PL}{\pi d^3} \quad (40)$$

$$\text{MOR}_4 = \frac{8P(L-a)}{\pi d^3} \quad (41)$$

where:

P = load at failure

L = outer (support) span

a = inner (loading) span (a = L/2 for ASTM C1161)¹¹⁶

d = diameter of sample rod

3.2.3 Elastic Modulus / Poisson's Ratio

Using a pulse-echo technique as a modified version of the standard testing method for measuring ultrasonic velocity in materials (ASTM E-494),¹¹⁸ the elastic modulus (E) and Poisson's Ratio (ν) of porcelain specimens were experimentally measured. It is understood that an ASTM standard technique using resonance exists for whitewares, namely ASTM-C848-88.¹¹⁹ However, this technique strictly stipulates:

“This test method is not satisfactory for specimens that have cracks or voids that represent inhomogeneities in the material; neither is it satisfactory when these materials cannot be prepared in a suitable geometry.”¹¹⁹

It is the nature of porcelain bodies to contain microcracks and voids; therefore, it was decided this technique was unsuitable for evaluating these porcelain bodies. Also the geometry requirements would have necessitated indirect examination of similar specimens, not the actual mechanically tested specimens the pulse-echo method does allow. Although a porcelain body has crystalline components that have anisotropic properties, on the bulk scale, porcelain displays isotropic behavior. Therefore, it was deemed suitable for testing in accordance with the pulse-echo technique, with the understanding that a dispersed phase within a glassy matrix can cause some disruption to the pulse signal. Measures such as surface polishing were taken to minimize this error.

Samples were prepared by cutting 3-mm cross-sections off of fired rods using a low-speed diamond saw (Isomet model 11-1280, Buehler, Ltd., Lake Bluff, IL), creating two plane-parallel surfaces to permit clean pulse-echo measurement of sound transit times. A broadband longitudinal wave transducer and a normal-incidence shear-wave transducer were used.

The longitudinal transducer was affixed to the sample surface using honey as a coupling agent. Figure 12 shows a schematic of this experimental setup.

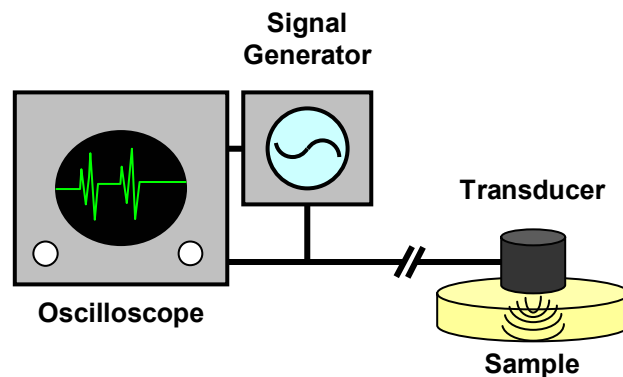


Figure 12. Schematic of pulse-echo apparatus used for elastic modulus measurement.

A pulse was sent through the material, and an oscilloscope displayed the waveform characteristic to the pulse sent through the sample. The distance between peaks in this waveform, on a time

scale, was the speed at which the sound traveled through the material, in microseconds. In order to eliminate error that could be introduced due to the nature of the material, the total distance between multiple waveforms was taken for each measurement and then divided by the number of waveforms. Several measurements also were taken for each sample. The shear wave (transverse) transducer was then affixed to the sample, and another series of speed measurements were taken. Velocities were then calculated by:

$$\text{Velocity} = \frac{\text{Thickness}}{1/2 \text{ Round-trip transit time}} \quad (42)$$

These values were inserted into the equation for Poisson's ratio (ν) as follows:

$$\nu = \frac{1 - 2(V_T/V_L)^2}{2 - 2(V_T/V_L)^2} \quad (43)$$

where V_T and V_L are transverse and longitudinal velocities, respectively. These values for Poisson's ratio, along with the sample bulk density (ρ) (Table XIV) were used to calculate the elastic modulus (E) of the material. The equation is:

$$E = V_L^2 \rho \frac{(1 + \nu)(1 - 2\nu)}{1 - \nu} \quad (44)$$

3.3 General Results

3.3.1 Bulk Density/ Apparent Porosity

Table XV lists the bulk density and apparent porosity values for all porcelain compositions studied. These values are for bodies containing typical industrial filler particle sizes (<44 μm) fired at 1260°C with a three-hour soak. Alumina porcelains show the highest bulk density, mainly due to the high density of alumina (3.9 g/cm³). Spinel and mullite porcelains have the next highest bulk densities, followed by the silica porcelains and then the stoneware composition. This has a bulk density roughly equal to that of silica porcelain, which is expected since the two body

compositions are similar. Average porosity values were all relatively low, indicating the samples were fired to a highly dense state.

3.3.2 Mechanical Properties

Table XVI lists the failure stress (MOR) and elastic modulus (E) for all porcelain bodies used in this investigation. All values are for porcelain compositions containing typical industrial filler particle sizes (<44 μm) fired at 1260°C with a three-hour soak.

Table XV. Bulk Density of Porcelain Compositions Used in this Investigation.

Composition	Avg. Bulk Density (g/cm³)	Std. Dev. (g/cm³)	Avg. Porosity (%)
Silica A	2.35	0.008	0.22
Alumina A	2.59	0.030	0.14
Mullite A	2.59	0.030	0.29
Spinel A	2.50	0.040	0.59
Silica B	2.41	0.002	0.25
Alumina B	2.72	0.004	0.15
Silica C	2.49	0.003	0.23
Stoneware	2.42	0.010	0.64

Table XVI. Four-Point MOR and Elastic Modulus Values for All Compositions Tested, Including a Ratio of the Two Properties.

Composition	Avg. MOR (σ) (MPa)	Avg. Elastic Modulus (E) (GPa)	Ratio E/σ (Pa/Pa)
Silica A	50.8	48	945
Alumina A	107.7	110	1020
Spinel A	100.4	101	1010
Mullite A	94.4	95	1010
Silica B	78.2	71	908
Alumina B	134.4	127	945
Silica C	74.4	80	1080
Stoneware	59.9	68	1140

MOR values were calculated using four-point flexure and Equation 41. Also listed is the ratio of elastic modulus to failure stress, to give some indication as to the relative magnitudes of the values. A ratio of 1000 corresponds to a factor of 1000 between E and σ .

4. Determining Critical Flaw Size via the Griffith Equation

4.1 Overview

The Griffith equation (Equation 18) describes the relationships between two fundamental material properties and strength (σ_f): elastic modulus (E), and fracture surface energy (γ). By determining that the Griffith flaw criterion applies to ceramic materials (in this case porcelains, which experience perfect brittle failure), one can exploit this relationship to calculate the remaining variable that is not so easily measured, flaw size (c). The flaw that propagates causing failure under the least amount of stress (applied and/or residual) is the critical flaw. The size of that flaw is regarded as the critical flaw size. Any flaw smaller than the critical size will not propagate at that stress level. However, if stress were to increase, previously non-critical flaws would be activated and the effective critical flaw size would decrease. The Griffith equation is such that the strength variable (σ_f) is also the failure stress. The equation itself refers to the stress level at which failure occurs and the variable (c) is therefore the critical flaw size, not just the average flaw size. With this in mind if the failure stress (σ_f), elastic modulus (E), and fracture surface energy (γ) were all known, an algebraic re-arrangement of the Griffith equation could be used to calculate the critical flaw size (c) within a particular ceramic material:

$$c = \frac{2E\gamma}{\pi\sigma_f^2} \quad (45)$$

In doing such a calculation, it is more realistic to account for several additional factors. While it can be confidently assumed that porcelain is a brittle material, the Poisson's ratio of the material (ν) should not be ignored. In addition, Griffith's model assumed an ideal elliptical crack within an infinite matrix. More realistic models include what is called the stress intensity shape factor (Y), which has a variable value, depending on the shape and location of the flaw. For internal flaws in a semi-infinite matrix, (flaw is small relative to the size of the material) Y is assumed to be unity. This adjusted version of the Griffith equation has more universal applicability and is of the form:

$$c = \frac{2E\gamma}{Y^2\pi\sigma_f^2(1-\nu^2)} \quad (46)$$

Determining σ_f , E , and ν are relatively straightforward, and values were measured for each porcelain composition studied using aforementioned procedures. Techniques for measuring fracture surface energy do exist; however, they often tend to be problematic. In this investigation a new, improved technique for measuring fracture surface energy was devised.

4.2 Fracture Surface Energy Measurement

4.2.1 Qualification of a New Technique

There are several techniques that are typically used to determine the fracture surface energy of a ceramic material. Most analytical techniques do not directly measure the actual surface energy; rather they measure the fracture toughness (K_{Ic}). Then, knowing the elastic modulus, the relationship between fracture toughness and surface energy is used to calculate fracture surface energy:

$$\gamma = \frac{K_{Ic}^2}{2E} \quad (47)$$

The most common method is through the use of a notched-beam, or the single-edge notched beam (SENB) technique. In this setup, a flaw of known dimension (several mm) is machined into the surface at the center of a rod or bar sample using a diamond or wire saw blade. The sample is then tested in three-point flexure. The extrinsic flaw propagates through the material, and a value for failure stress is then calculated through the use of a derivative of the Griffith equation (Equation 48). Figure 13 shows a schematic of this experimental setup. This technique is considered useful, because it allows the easy application of a known macroscopic flaw to the surface of a material, which acts as the critical flaw during flexure testing. However, for porcelain the technique is non-ideal. Griffith flaw criterion states the ideal flaw is assumed to be very sharp. A saw blade of any kind has significant thickness to it, and produces a flaw with a tip that has a radius, resulting in a stress concentration gradient, rather than a sharp tip as the Griffith criterion

suggests. Microcracks emanating from the machined flaw tip typically cannot be measured accurately in an opaque material such as porcelain. As a result, the true stress concentration at the tip and overall effective flaw length may vary. Therefore, to use the Griffith equation in a situation where the flaws are clearly not ideal Griffith flaws is imprecise.

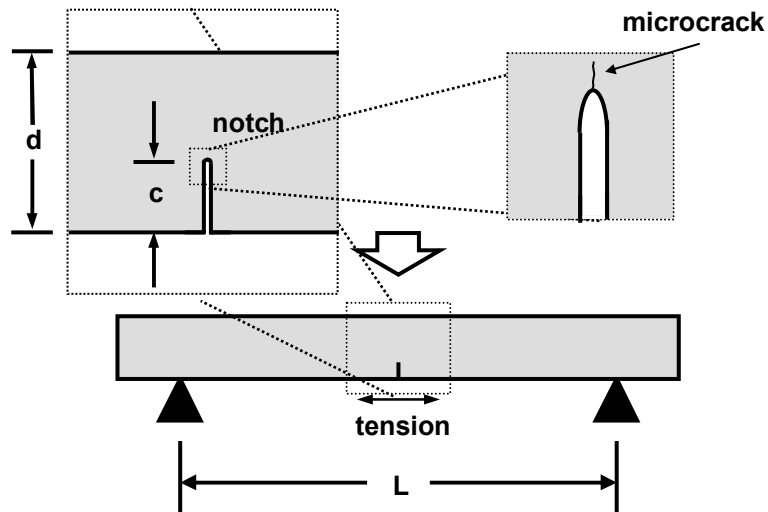


Figure 13. Schematic of SENB apparatus and setup with magnification of notch showing radius of flaw tip and microcrack.

In attempts to minimize this error, specific techniques stipulate the flaw is to be triangular in shape (called a Chevron notch) in order to create a stress concentration at a more precise location.¹²⁰

Another frequently used technique measures fracture toughness using micro-indentation. A pyramidal diamond indenter creates an impression in the material surface, resulting in an indented zone of plastic deformation with surface cracks radiating out from the corners. Figure 14 shows a schematic of a characteristic indentation marking on the surface of a material. The dimensions of this indentation (d) are related to the fracture toughness, as are the lengths of the radial cracks (c). This technique is also viewed as non-ideal for determining the fracture surface energy of a material due to the error associated with measuring fracture toughness using this technique in general.

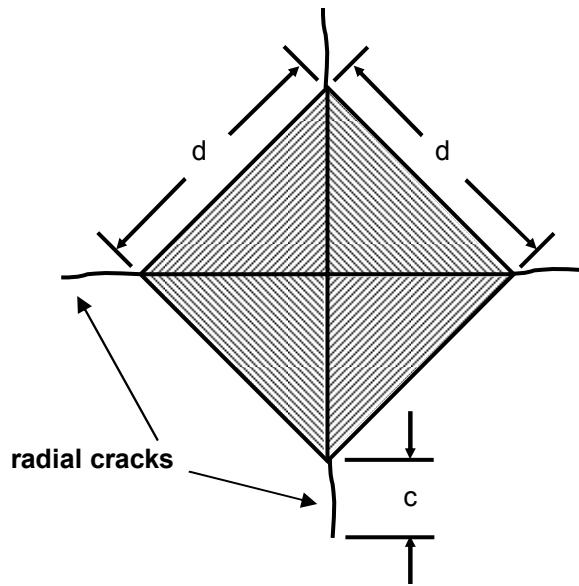


Figure 14. Schematic of a micro-indented marking on a sample surface, including radial cracks.

Measurement of radial crack length is often done using SEM or reflected light microscopy and staining of the specimen. This does not always reveal the true length of the radial cracks, which may extend beneath the surface of an opaque material, such as porcelain. In this way this technique is not only non-ideal for fracture surface energy measurement but also as a fracture toughness measurement technique it can often prove to be inadequate.

A third commonly used technique employs a combination of the two aforementioned methods. In this technique a pre-crack is introduced to the specimen surface via indentation in place of a machined-in notch. The pre-crack forms under the indentation, and then the specimen is broken in three or four-point flexure. The length of the pre-crack is not precisely controlled, but it can be accurately measured on the fracture surface after testing. This is a standard procedure used to measure fracture toughness of fine-grained ceramics, but tends to be problematic in a particularly soft or porous ceramics because a pre-crack will not necessarily form under the indentation. A porcelain material is mostly glassy, but does contain a significant amount of porosity; therefore, it may not be the most suitable candidate material for this particular test method. Furthermore,

problems associated with indentation and the manual application of a pre-crack to a porcelain body, as mentioned earlier, can also apply.

4.2.2 *Crazing*

The new technique devised for measuring fracture surface energy exploits crazing of a glaze on a ceramic body (substrate). This technique introduces sharp flaws to the material without machining or indenting the surface, making for an easy and accurate measurement technique that is less prone to extrinsic error. The flaw size can be easily controlled by changing glaze thickness. If the CTE of the glaze is higher than that of the glass phase, then upon cooling, the glass seeks to contract more than the body, resulting in stresses that build up within the glaze below T_g (glass transformation temperature).

If the stresses are sufficiently high, then the glaze will crack to relieve some of the strain, the spacing between the crazing being inversely proportional to ΔCTE . The subsequent crack pattern that results on a glazed surface where this phenomenon has taken place is called crazing. Figure 15 shows a photograph of a crazed glaze surface. In most cases (except for artistic purposes) it is regarded as an undesirable effect, since it weakens the underlying material by placing numerous macro-sized flaws at the surface of the body. In extreme cases where the CTE of the body is much higher than that of the glaze, the body fails in tension, resulting in a phenomenon called shivering. This mechanism is not as controllable as crazing and often is accompanied by pieces of the material detaching from the surface, or scaling, and is therefore unfit for use in this technique.

Crazing is not an entirely spontaneous phenomenon but rather an iterative process that takes place during cooling as a function of stress, strain, and temperature. As the glaze-body system cools, stress builds up due to the CTE mismatch, straining the strong interfacial bond between the body and glaze. Eventually the strain exceeds a critical level and the glaze fails, creating cracks that relieve the localized strains. As the sample cools down further, stresses build up

again, resulting in time-delayed additional glaze cracking. In this case, these secondary cracks tend to branch off perpendicularly to the pre-existing cracks, often connecting them.

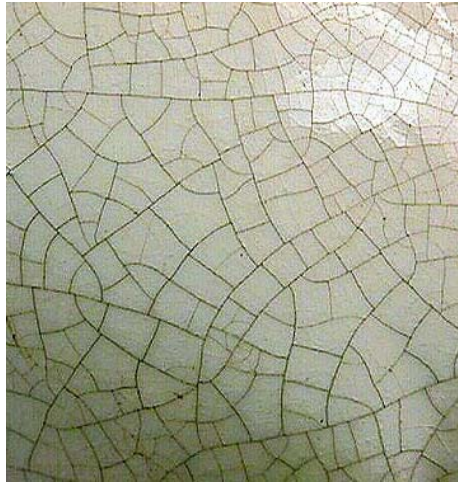


Figure 15. Photograph of pottery surface containing crazing.

As the sample continues to cool to room temperature, numerous crazing events occur, each characterized by a buildup of residual stresses between the glaze and the body and a subsequent relaxation due to glaze cracking, resulting in an intricate network of interconnected cracks in the familiar crazing pattern. Assuming a uniform glaze thickness, the degree (or fineness) of the crazing is dictated by the relative CTE mismatch between glaze and body. The higher the CTE mismatch is, the finer the resulting crazing array. As the inherent strength of the body itself is not altered, the observed reduction of flexure strength in the presence of these large flaws demonstrates they are critical flaws. Crazing cracks are ideally straight and very sharp, traveling through the glaze perpendicular to the surface. Furthermore, crazing flaws typically arrest at the glaze-body interface of a fully dense ceramic body, producing a very sharp flaw tip.

This will occur because compressive stresses at the interface prevent the crazing cracks from entering the body during the crazing phase. Microscopic evidence also supports these claims, as shown in Figure 16.

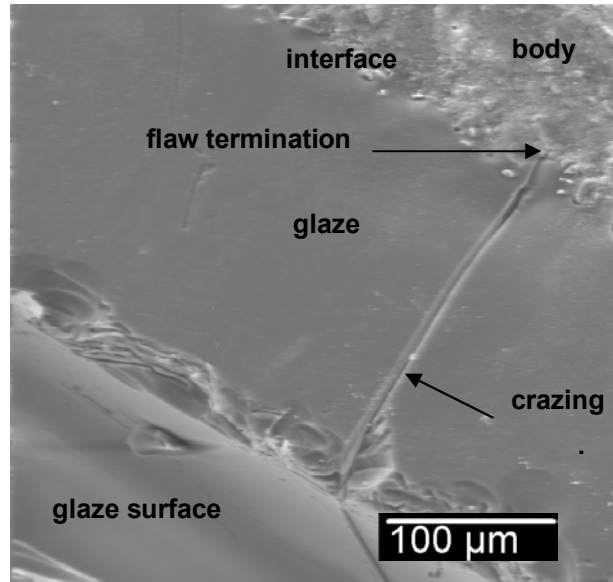


Figure 16. SEM secondary electron image showing the glaze/body interface with a crack caused by crazing.

By measuring the thickness of the glaze layer at the site of fracture the critical flaw size is known. The glaze thickness is the critical flaw size.

4.2.3 Use of Griffith Equation

Considering the fact that the Griffith flaw criterion was developed for a specific model (semi-elliptical flaw in a infinite matrix), and the one proposed by this new technique (sharp surface flaw) are different, the question arises as to whether the Griffith equation is appropriate. In the case of a SENB or Chevron notch experiment, clearly the Griffith equation should not be used. The reason has to do with the relative sizes of the notches (flaws) compared to the overall beam dimensions. Davidge and Tappin¹²¹ explain this by stating that for a notched flexure specimen, the expression for surface energy is presented in the form:

$$\gamma = \frac{9(1-\nu^2)P_F^2 l^2 f(c/d)}{8Eb^2(d-c)^3} \quad (48)$$

where P_F is the load at failure, c is the flaw length, l and b and d are geometric specimen dimensions (in this case length, breadth, and depth, respectively). Also, $f(c/d)$ is a dimensionless parameter. When (c/d) is greater than 0.1, corrections must be applied to this equation, and

various mathematical treatments are available. A typical SENB or Chevron notch test results in a very large flaw machined into the beam; therefore, one should use Equation (48) instead of the Griffith equation because the flaw is typically larger than 10% of the total beam depth. At small c/d values, however:

$$f(c/d) = \pi c(d - c)^3 / d^4 \quad (49)$$

Equation (48) reduces to:

$$\gamma = - \left(\frac{dU}{dA} \right) = \frac{(1 - \nu^2) \pi \sigma_f^2 c}{2E} \quad (50)$$

Plane-strain conditions are assumed (no displacements in the z-direction; displacements in the x- and y-directions are functions of x and y only, but not z). Equation (50) is essentially the original Griffith equation. For the specimens used in these experiments, the ratio of the flaw size to the rod diameter is very small, on the order of 0.008 (100- μ m flaw, i.e., the glaze thickness, on a 13-mm diameter rod). In this case, it is therefore acceptable to use Equation (46), which is essentially algebraically rearranged as Equation (50).

4.3 Procedure

4.3.1 Sample Preparation

Three porcelain bodies (Alumina B, Silica B, Silica C) were used in this experiment. Details about these compositions are listed in Section 2.1. These bodies were made into 170-mm long cylindrical rods having a fired diameter of 13 mm. Bisque firing of the rods was carried out prior to glazing in an attempt to establish a well-defined glaze/body interface. A fully dense body has a surface less permeable to the glaze suspension during the dipping process, resulting in only a coating of glaze on the sample surface. Dip glazing green samples in a one-fire operation resulted in a diffuse glaze-body interface as a result of capillary suction forcing glaze components into open surface pores, causing difficulties in identifying the interface when trying to determine glaze thickness. All compositions were bisque fired at 1290°C with a 3-hour dwell. Bulk density

and porosity measurements were taken after firing to ensure the samples were fully dense prior to glazing.

4.3.2 Dip Glazing

Glaze raw materials were made into a 60-wt% suspension using deionized water. Table XVII shows the glaze batch composition as well as the Unity Molecular Formula (UMF) of the glaze, which indicates the relative ratios of alkali and alkali earth oxides to SiO₂ and Al₂O₃ within the glaze composition.¹²² Using this technique allows for precise control over the CTE of the glaze as it is the molar ratios that determine the final CTE value. Once suspended, grinding media were added (to aid mixing, not particle size reduction) and the suspension was mixed in a plastic container on a ball mill for 24 hours.

The bisque fired porcelain rods that were then prepared for glazing. Paraffin was melted and each sample was partially dipped into the molten wax, coating one end of the rod. This was done to prevent glaze from covering the area of the rod that would be in contact with a sample holder during firing.

Table XVII. Glaze Composition and Raw Materials.

Material	UMF	Raw Material	Wt %
KNaO	0.30	G200 Feldspar	47.0
CaO	0.70	Calcium Carbonate	35.8
Al ₂ O ₃	0.20	EPK Clay	5.8
SiO ₂	1.20	Pearl Ash	5.3
		Soda Ash	4.1
		Flint (SiO ₂)	2.1

The glaze suspension was poured into a 250-mL graduated cylinder, and each of the rods was vertically dipped into it twice, waiting 40 seconds between the first and second dip. An area at the top, equal in length to the waxed region at the bottom (~3 cm), was left unglazed to create a centered glazed region along the rod. To reduce any settling effects within the graduated cylinder, the suspension was re-mixed after every 10 samples. Samples were also continually rotated after each dip for several seconds, to reduce preferential migration of the glaze

suspension to one side and promote an even coating. Once glazed, the rods were placed vertically (wax side down) into support holes drilled into a high-temperature refractory brick. The glaze was allowed to dry for approximately 12 hours before firing the samples at 1160°C in a box furnace (SiC elements) with a 1-hour soak time.

4.3.3 Failure Testing

Once samples were fired, the finished surface was a glossy glaze coating characterized by extensive crazing. Figure 17 shows a photograph of a typical glazed sample rod with crazing (cracks have been stained with ink for viewing purposes). The two unglazed ends of the sample allowed for easier handling of unfired samples and also for ease of vertical firing. Since the rods were broken in three-point flexure, the maximum bending moment, and hence failure, occurs at the center of the sample, eliminating the necessity for a completely glazed rod.

4.3.4 Mechanical Properties

Three-point flexure testing was carried out on the samples to determine the modulus of rupture (MOR) or failure stress (σ), using the standard procedure outlined in Section 3.2.2.

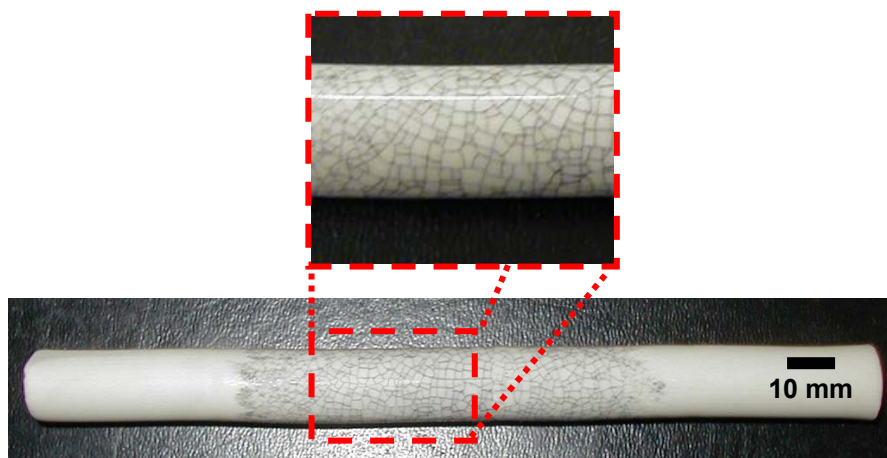


Figure 17. Photograph of glazed porcelain rod with crazing, with magnification of glaze surface. Ink was applied to a portion of the surface to allow ease of viewing.

The support span for the test was set to 90 mm, making sure that it resided within the glazed region of the sample. The Instron was programmed to set the loading rate at 0.1 mm/min. Each sample was tested to fracture, the maximum load at failure (P) was recorded. Ten samples from each composition were tested in this way. Figure 18 illustrates how the specimens were loading using the Instron device using a Mode I orientation, the maximum bending moment exactly at the center. This maximizes the probability that a crazing crack perpendicular to the length of the rod would preferentially cause the failure. Figure 18 also shows a schematic of a typical in-situ crazing crack that would be subject to tensile stresses and then propagate, causing failure of the underlying body. As a control, the MOR of unglazed specimens was measured for each of the three compositions studied. In addition, the elastic modulus of each of the bodies was also measured using the pulse-echo technique (Section 3.2.3). The elastic moduli of the glazed porcelain samples is predicted to be identical to that of the unglazed samples (Table XVI), due to the fact that the glaze crazing is very extensive, hence there should be a negligible effect of the glaze on the elastic modulus of the underlying material, measured parallel to the length of the rod sample. Flaw size was measured by observing the glaze thickness on the fracture surface of a specimen using SEM micrographs and digital calipers.

4.3.5 Microscopic Analysis

After samples had been broken, fracture surfaces were examined using a scanning electron microscope (SEM) to determine the glaze thickness at the site of failure, which is equal to the critical flaw size. Using a low-speed diamond saw (Isomet model 11-1280, Buehler, Ltd., Lake Bluff, IL), a 20-mm thick section incorporating one side of the fracture surface was cut off of each sample. To help clarify any features, the fracture surface was then chemically etched for ten seconds using a 20% aqueous solution of HF at 0°C. The samples were mounted then sputter-coated with 60:40 Au-Pd to make the surface conductive. Every sample tested was then examined to precisely determine the thickness of the glaze at the site of fracture in each case. Images at two different magnifications were taken for each sample and using digital calipers, six

measurements were taken of the glaze thickness from each image. The average and standard deviation of these measurements were recorded.

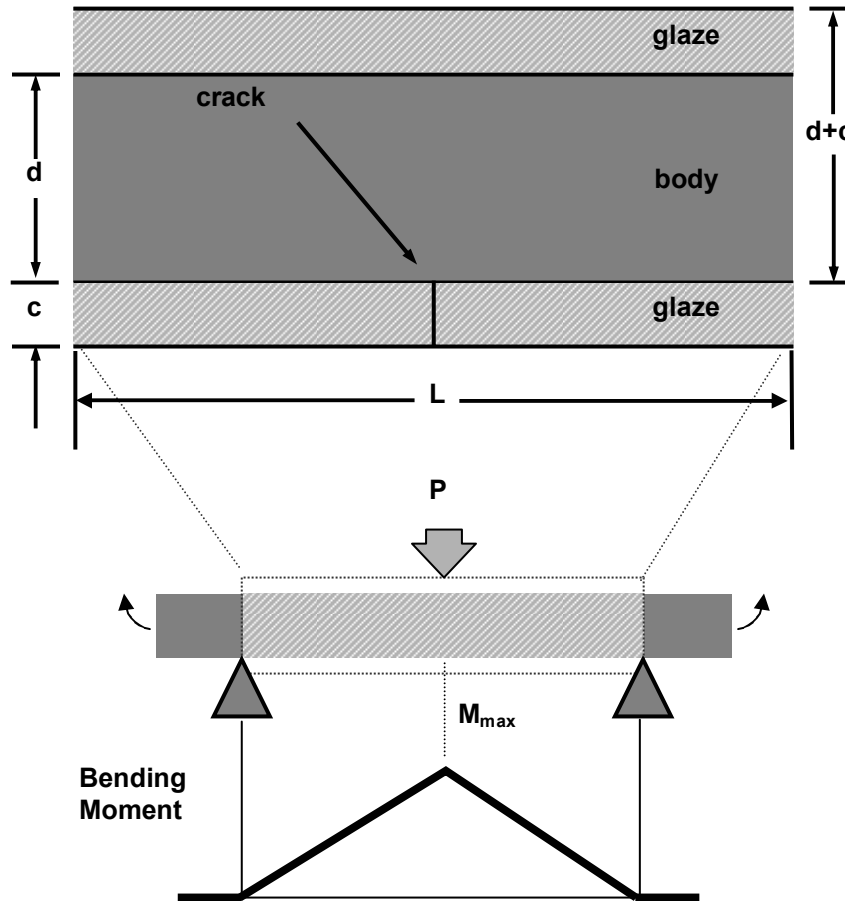


Figure 18. Schematic of three-point flexure setup for fracture surface energy testing, along with a cut-way view of a typical sample, denoting the flaw length (c) and rod length (L) and diameter (d).

4.4 Experimental Results

4.4.1 Observed Flaw Size

Each fracture surface was examined using an SEM, and at each magnification an electronic image was taken of the glaze layer cross-section for use in measuring glaze thickness and, in turn, critical flaw size. Figures 19 and 20 show the distinct glaze-body interface formed as a result of pre-firing the bodies prior to glazing.

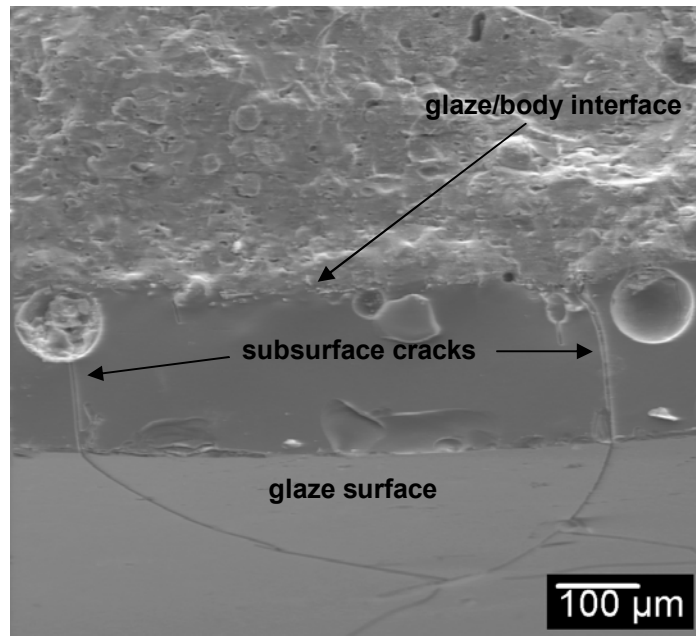


Figure 19. SEM secondary electron image showing the glaze/body interface with cracks caused by crazing. The crazed glaze surface is also visible.

Cracks within the glaze layer, caused by crazing, were also visible in each specimen, spanning the entire glaze thickness perpendicular to the surface, arresting at the glaze/body interface. This phenomenon was observed in all samples, proving that the surface flaws generated are equal to the thickness of the glaze. This fact allowed a precise measurement of critical flaw size (c). In some cases, a crack would intersect a bubble in the glaze, as in Figure 19, but it typically continued through it to the interface, as shown in Figure 20. The significance of these figures is they show an abundance of equally sized flaws inhabiting the glaze layer. Values of glaze thickness varied from sample to sample, typically on the order of 250–350 μm , but the average measured flaw size per sample indicated a uniform glaze coating. Average values of flaw size for each sample are listed in Appendix D.

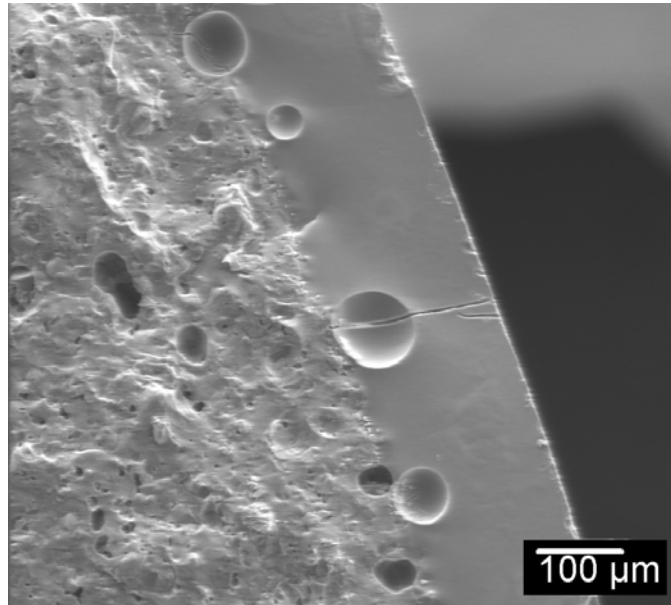


Figure 20. SEM micrograph showing the glaze/body interface with crack running through a bubble.

4.4.2 Measured Fracture Surface Energy

Once the flaw size had been measured for each individual sample, by combining this information with the known failure stress and elastic moduli of the glazed samples a characteristic relationship were established between the known parameters and fracture surface energy. Based on the results of Table XVI and Table XVIII, and rearrangement of Equation (46), the following formula was generated:

$$\frac{Y^2(1-\nu^2)\pi\sigma_f^2}{2E} = \frac{1}{c}\gamma \quad (51)$$

Equation (51) has the form of an equation for a straight line, the slope of which is the fracture surface energy. To be more concise, the left-hand side of Equation (51) was condensed into a new variable called the *reduced strength*, or σ_R :

$$\sigma_R = \frac{Y^2(1-\nu^2)\pi\sigma_f^2}{2E} \quad (52)$$

While not a true measure of strength, the units for reduced strength are still Pa, the same units used to report other forms of stress and strength. Figure 21 illustrates plots for all three compositions. As shown, the fracture energy for both Silica B and C compositions is approximately the same (4.5 and 4.7 J/m², respectively). The Alumina B body fracture energy is 8.4 J/m², a significantly higher value.

Table XVIII. MOR Values for Glazed and Unglazed Porcelain Samples.

Composition	MOR (MPa)	Std. Dev. (MPa)
Silica B (unglazed)	78.2	3.7
Silica B (glazed)	27.5	1.6
Alumina B (unglazed)	134.4	3.9
Alumina B (glazed)	34.1	2.3
Silica C (unglazed)	74.4	3.9
Silica C (glazed)	30.3	3.7

This is to be expected because the elastic modulus and strength (MOR) of alumina porcelain is significantly higher than that of silica porcelain. Without literature values for fracture surface energies of porcelains for comparison, it is difficult to know for certain whether these results are reasonable. To help qualify these results a rough approximation of fracture surface energy can be made using Equation (47), using a literature value of K_{Ic} for silica porcelain as $1.0 \text{ MPa}\cdot\text{m}^{1/2}$.¹²⁵ The resulting fracture surface energy is $\sim 4.0 \text{ J/m}^2$, which corresponds well to the experimentally measured values. Also, the analysis of a series of data generated by Benson¹²³ helps establish a frame of reference for these measured fracture surface energies. Her investigation used the same industrial porcelain compositions Silica B and Alumina B to measure the thermal expansion mismatch between the body and a series of glaze compositions. When the thermal expansion mismatch is plotted versus the mechanical strength, as shown in Figure 22, two linear relationships arise. The significance of these plots lies in their intercepts. The Silica B and Alumina B compositions cross the y-axis at 70.13 MPa and 118.15 MPa, respectively. The ratio of these numbers (1.7) is very close to that of the ratio of calculated surface energy values for both Alumina B and Silica B compositions (1.8). Since the strength of the material and its fracture

surface energy are linearly related in the same way as strength and elastic modulus, the fact that these ratios are similar gives additional merit to measured values of surface energy and their relative magnitudes.

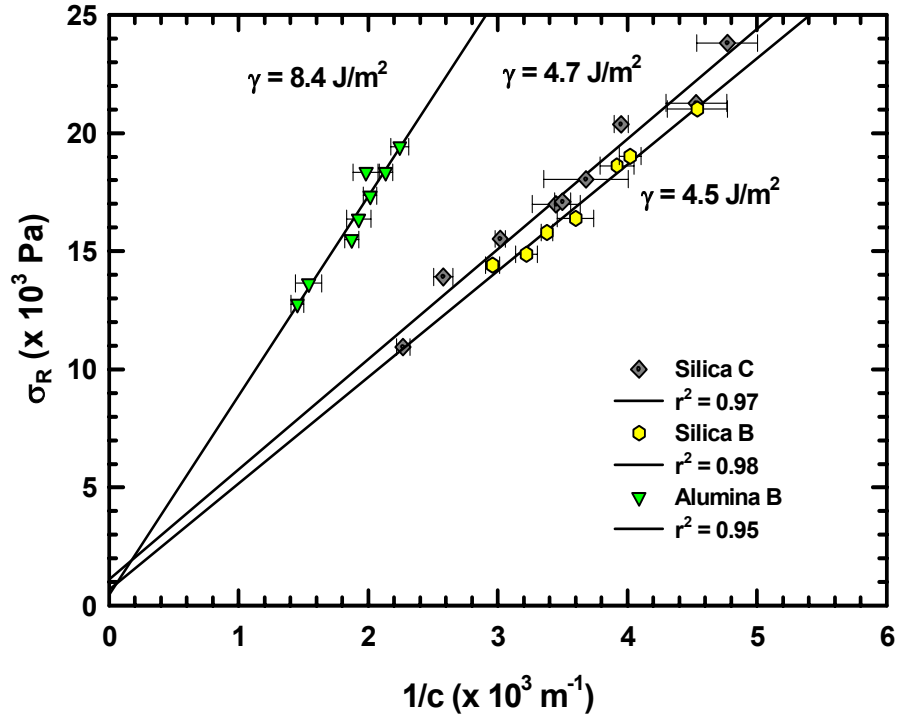


Figure 21. Plots of σ_R versus $1/c$ for all samples. The slopes of the linear regression lines are equal to surface energy (γ).

4.5 Derived Property Relationships

4.5.1 Fracture Surface Energy vs. Elastic Modulus

There is a linear correlation between experimentally generated elastic modulus and fracture surface energy data. Analysis indicates that surface energy scales with elastic modulus for these compositions. A plot of this relationship is shown in Figure 23, having a correlation coefficient of 0.994, indicating an excellent linear fit. Elastic modulus and surface energy of materials in general do not display this relationship. It is hypothesized that for materials that have similar types of bonding (and bond strengths), this linear relationship will exist, due in part to the fact that the elastic modulus of a material is related to the stiffness of bonds and fracture surface energy is related to the energy required to break those same bonds (per unit area).

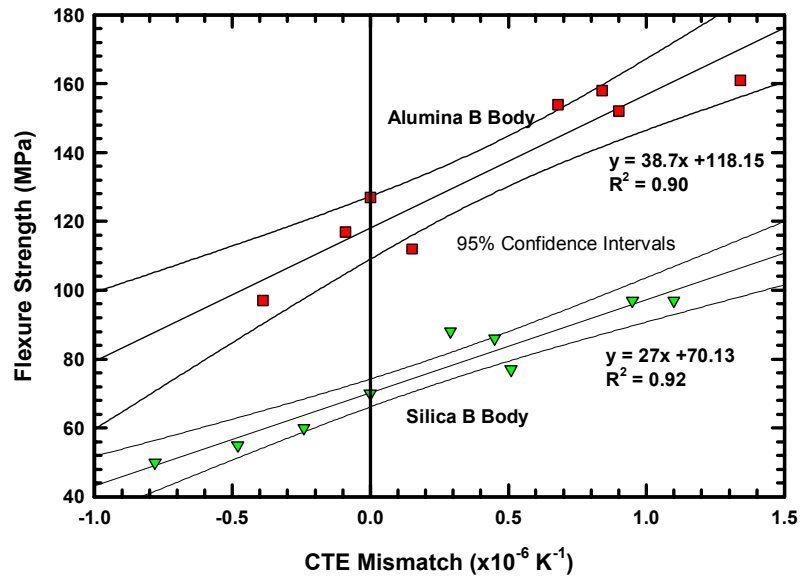


Figure 22. Flexure Strength versus CTE mismatch of a series of glazes on Silica B and Alumina B body compositions (data from Benson).¹²³

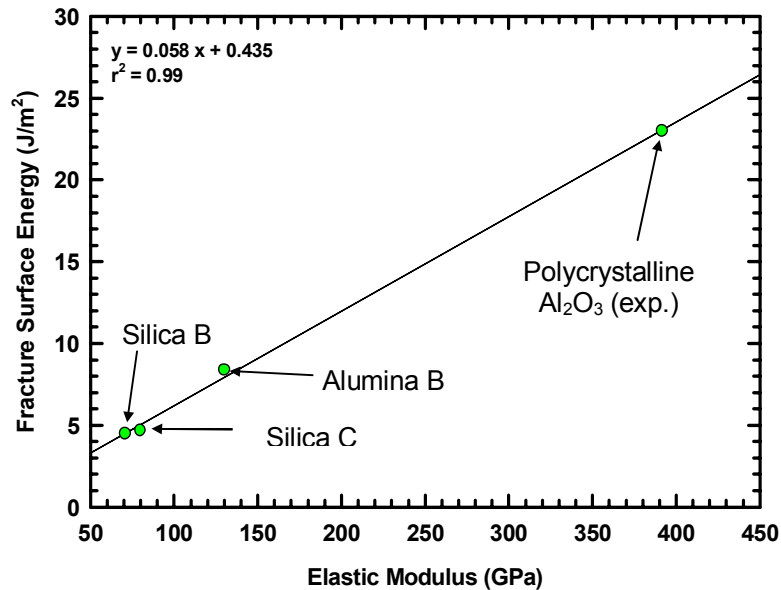


Figure 23. Plot of experimental results; fracture surface energy versus elastic modulus.

Provided energy dissipating mechanisms are the same (since porcelains experience total elastic failure they are), surface energy should also scale with bond density for like bonds, since higher bond density would require more energy to break the bonds in a specified area, as well higher

bond density would increase the overall stiffness of the bonding matrix (and, in turn, elastic modulus).

Materials that have other fundamental bonding types may not fall on this line. Table XIX was generated from the literature, which includes the elastic moduli and fracture surface energy values for several materials that possess a majority of the same bond types; that being Al–O and Si–O, which both display ~50% ionic character and have similar energies of 452 kJ/mol and 511 kJ/mol, respectively. Ca–O (402 kJ/mol), K–O (278 kJ/mol), and Na–O (256 kJ/mol) bonds are also present to some degree in a majority of the materials listed. These minority bond types are not those broken during the formation or propagation of a crack through porcelain. It is primarily the Si–O and Al–O bonds that contribute to the overall integrity of the glass structure. The concentration of these minority bonds does, however, affect the elastic modulus and fracture surface energy because due to the bonding nature of Ca, K, and Na, the presence of these atoms within the glass structure create non-bridging oxygens (NBO),¹²⁴ reducing glass network connectivity and hence the overall Si–O and Al–O bond density.

Table XIX. Surface Energies and Elastic Moduli of Various Materials (Experimental and Literature Values).

Material	γ (J/m²)	E (GPa)
Silica B	4.5	71
Alumina B	8.4	127
Silica C	4.7	79.4
Al₂O₃ (exp.)¹²⁵	23	391.6
Fused Silica	3.7	73
Concrete	0.7	30
SLS Glass	3.5	69
Al₂O₃ (99.5%)	17.5	314
Al₂O₃ (99%)	24.1	405
Al₂O₃ (96%)	20.1	379
Al₂O₃ (94%)	24.2	417

When plotted, all the data (literature values included) can be characterized by a straight line, as shown in Figure 24. It is a slightly different line than shown in Figure 23; however, the slope is almost identical, and all the points are either on or within a 99% confidence interval, with a

correlation coefficient of 0.99, indicating an excellent fit to the data set. Also shown on this figure are the relationships for selected other ceramic materials which have distinctly different bonding; MgO (strong ionic; can display limited plastic behavior), SiC (strong covalent), AlN (strong ionic). The bond energies for these bonds are 363 kJ/mol, 451.5 kJ/mol and 297 kJ/mol, respectively. For a material with different bond types a relationship between surface energy and elastic modulus still exists; however, the data points do not fall on the same line. In fact, it is likely that a separate linear relationship exists for each of these three materials, but is only apparent when comparing materials with like bonding.

The equation of the line in Figure 24 is:

$$y = 0.0683x - 0.1691 \quad (53)$$

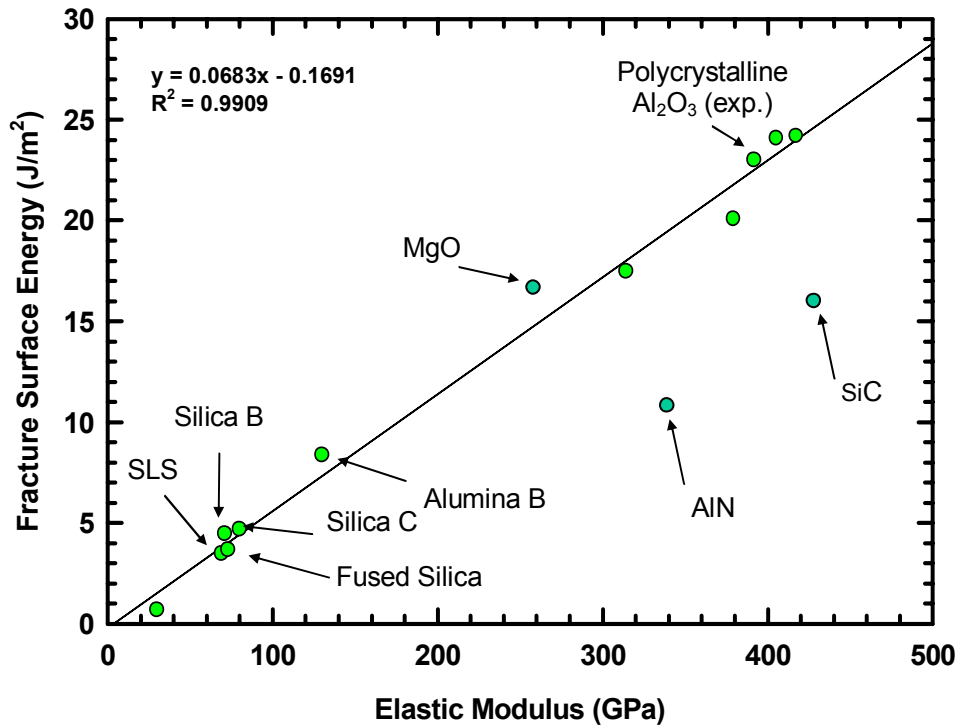


Figure 24. Plot of elastic modulus versus fracture surface energy for various ceramics and glasses (listed in Table XIX).

The equation of this line is particularly useful in that the properties of a ceramic material possessing bonding character similar to that of the included materials should fall on this line (in

this case porcelain bodies are of interest) and also display the same relationship between elastic modulus and fracture surface energy. Therefore, Figure 24 could function as a type of calibration curve, allowing the determination of elastic modulus or fracture surface energy when only one of these variables is known. Since fracture surface energy measurements are not as easily made, this relationship could be used to approximate the fracture surface energy of a material simply by measuring the elastic modulus, which is a more standard experimental practice.

4.5.2 Flexure Strength vs. Elastic Modulus

Figure 25 shows a plot of MOR versus elastic modulus for every porcelain composition studied. This plot is representative of the overall trend among all porcelain bodies, independent of firing temperature and filler particle size, although these parameters are noted on the figure.

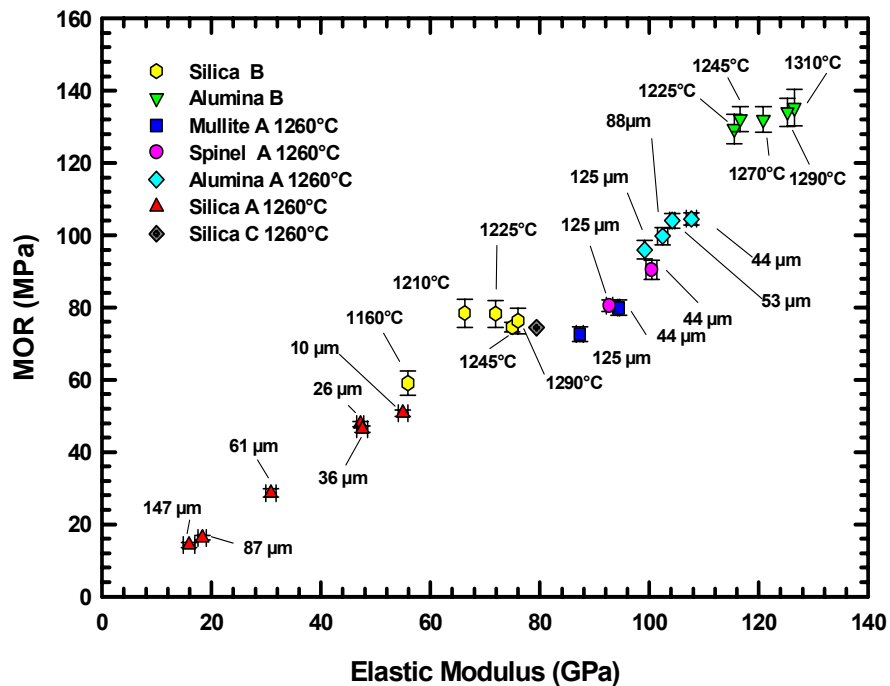


Figure 25. Plot of MOR versus elastic modulus of all porcelain compositions studied in this investigation.

What is interesting is that there appears to be a linear relationship between the two parameters, although it was not expected. By examining the Griffith equation on an empirical level it would

appear there should be a square-root relationship between strength and elastic modulus, rather than a linear one:

$$\sigma = \sqrt{\frac{2E\gamma}{\pi C}} = A\sqrt{E} \quad (54)$$

where A represents a constant comprising all the other variables and constants in the equation. Another way to represent this is using the following equation:

$$\sigma^2 = \frac{2E\gamma}{\pi C} = b_1 E \quad (55)$$

where b_1 represents a different constant term. It has already been recognized that there is a relationship between elastic modulus and fracture surface energy; therefore, γ is a function of E. By re-evaluating the constant b_1 , it is found that that:

$$b_1 = b_2 \gamma \quad (56)$$

where b_2 is different constant. Having quantitatively established that fracture surface energy is a function of elastic modulus, a modification of Equation (53) becomes:

$$\gamma = f(E) = 0.068(E) - 0.17 \quad (57)$$

Combining Equations (56) and (57) yields:

$$b_1 = b_2(0.068E - 0.17) = b_3 E - b_4 \quad (58)$$

where b_3 and b_4 are constants. Substituting this relationship into Equation (55) results in the following equations:

$$\sigma^2 = (b_3 E - b_4) E = b_3 E^2 - b_4 E \quad (59)$$

$$\sigma = \sqrt{b_5 E^2 - b_6 E} \quad (60)$$

The resulting relationship between σ and E (Equation 60) should be linear. Although the two constants b_5 and b_6 may cause a slight deviation from $y = x$, the fact that they are the same order of magnitude minimizes this effect within the (x,y) region of interest. As shown in Figure 26, a plot of this basic relationship is virtually identical to that of $y = x$. Based on this assessment, a simple linear regression was carried out on all the data points, and can be seen in Figure 27. As shown, the correlation coefficient of 0.95 indicates a good fit. Again, this uncharacteristic relationship is thought to be accurate only among materials that have compositional and bonding similarities.

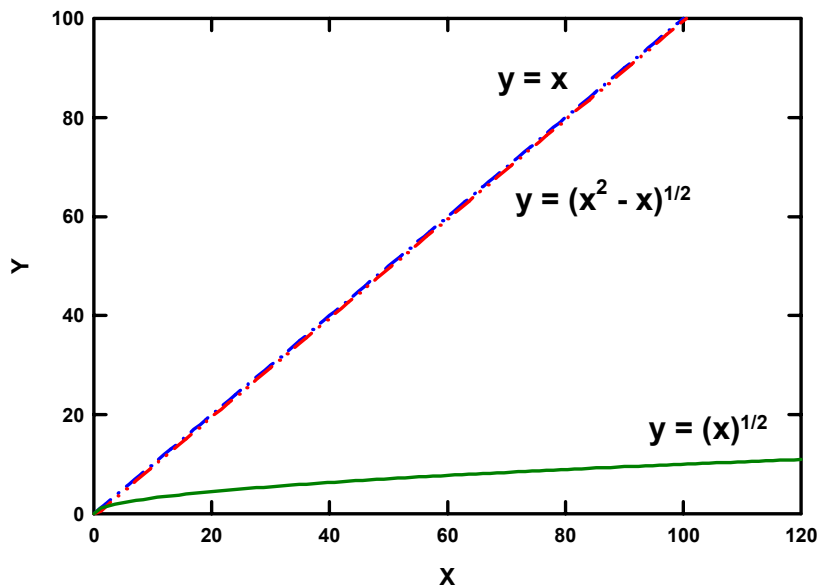


Figure 26. Plots of lines $y = x$ and $y = (x^2 - x)^{1/2}$ illustrating that both are linear in the (x, y) region of interest, along with $y = (x)^{1/2}$ for comparison.

A study by Kalnin¹⁴ of quartz-free whiteware porcelain yielded a similar linear relationship between flexural strength and Young's modulus. With this in mind, for these materials it is possible to use Figure 27 to make a reasonable approximation of elastic modulus when mechanical strength is known and vice versa. Recalling Table XVI, the ratio of E/σ for each material was approximately 1000, which is in good agreement with the equation of the regression line which multiplies E by a factor of 1000, converting MPa to GPa.

4.6 Predictions

4.6.1 Fracture Surface Energy

The relationship established between measured elastic modulus and fracture surface energy for porcelain bodies allows the prediction of fracture surface energies for each of the porcelain bodies used in this investigation. By taking the values of E from Figure 25 and solving Equation (52) for 'y', the fracture surface energies of all porcelain compositions were calculated. Figure 28 shows these calculated values of surface energy plotted versus elastic modulus along the equation of the line.

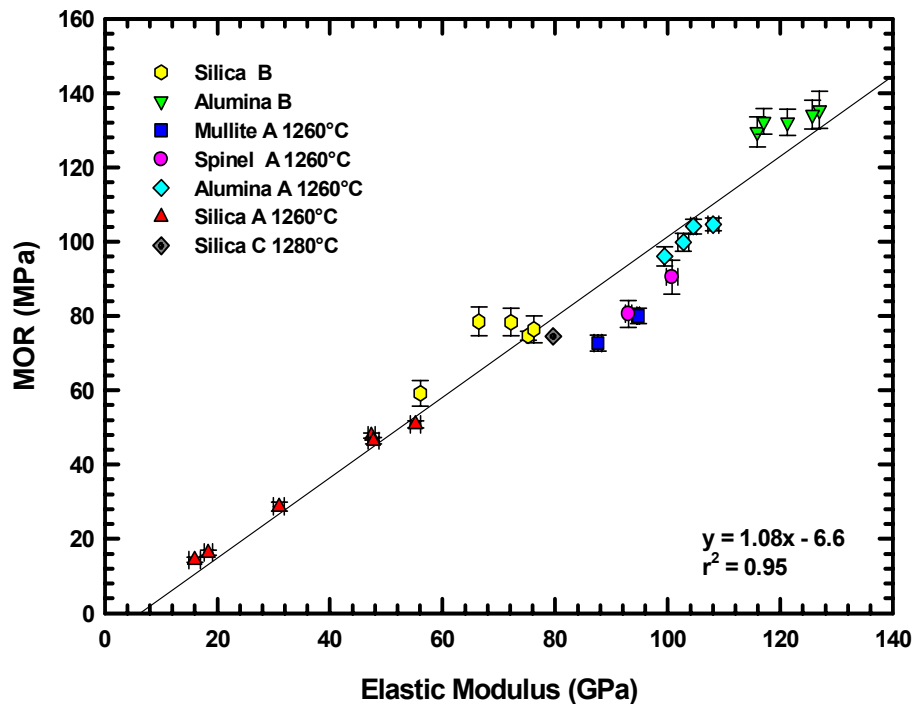


Figure 27. Plot of MOR versus elastic modulus for all porcelain bodies investigated, including a linear regression.

The fact that the data points fall along a straight line is not surprising, since in order to establish this relationship a linear correlation was assumed. What is important to note about Figure 28 is the relative values for surface energy of the various compositions. Silica A, Silica B and Stoneware compositions are on the lower end with surface energies varying from 1–4 J/m², while

Mullite A and Spinel A compositions have surface energies of about 6–7 J/m². Alumina porcelains inhabit the higher end of the plot having surface energy values between 7 and 9 J/m².

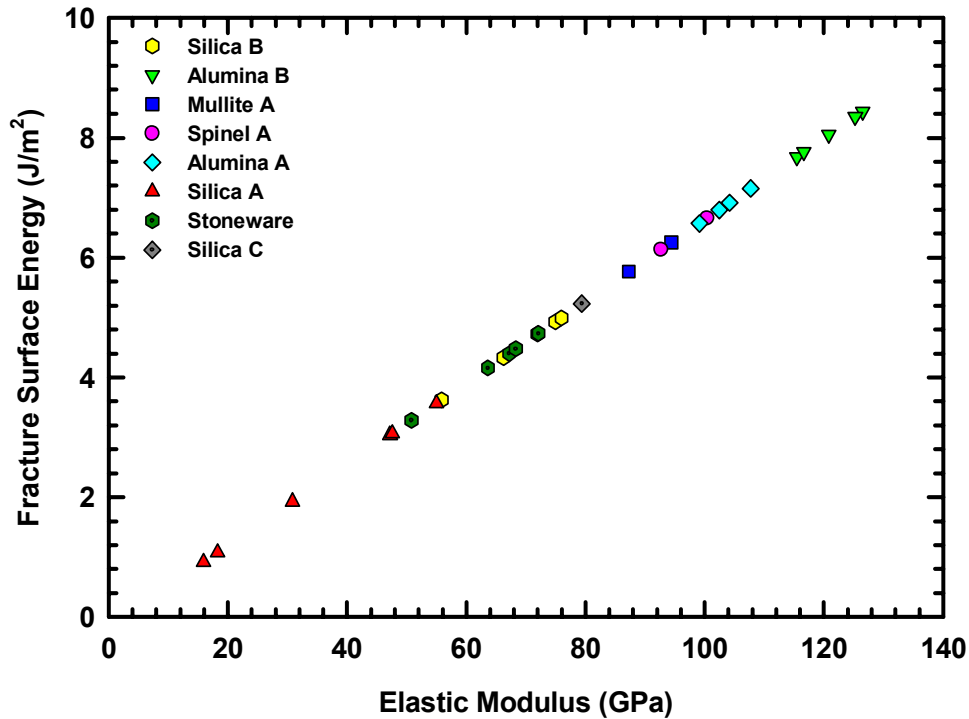


Figure 28. Plot of fracture surface energy versus elastic modulus of all porcelain compositions, assuming a linear relationship: $y = 0.0683x - 0.1691$.

4.6.2 Critical Flaw Size

One variable that is not easily measured is flaw size. As stated earlier, through the use of a newly developed technique incorporating direct glaze thickness measurement to determine critical flaw size, the fracture surface energies of materials were calculated, alongside the standard techniques for measuring failure stress and elastic modulus. Knowing the elastic modulus (E), failure stress (σ_{MOR}), and the fracture surface energy (γ) of a material allows the calculation of flaw size (c) through manipulation of Equation 18 (Griffith's equation).

$$c = \frac{2E \gamma_f}{Y^2 \pi \sigma_f^2 (1 - \nu^2)} \quad (61)$$

Since σ_{MOR} is the failure stress, then the flaw size that is calculated using Equation (60) is, in fact, the critical flaw size that caused failure of the material.

The strength of a sample containing crazed glaze was shown to be much weaker than that of a corresponding unglazed sample (Table XVIII). The lower strength is attributed to the large critical flaw that acts as a stress concentrator on the sample surface, which is on the order of 200 μm . In the unglazed sample, the critical flaw size is assumed to be smaller, since the measured strength of the body is much higher. However, the elastic modulus and fracture surface energy remain constant, regardless of whether the sample was glazed or unglazed, since it is assumed the crazed glaze doesn't contribute any appreciable stresses to the body. Therefore, by modifying Equation (60), the critical flaw size can be calculated by using the following:

$$c = \frac{2E_{ug} \gamma_g}{Y^2 \pi \sigma_{ug}^2 (1 - \nu_{ug}^2)} \quad (62)$$

where the subscripts correspond to parameters of both glazed (g) and unglazed (ug) specimens. By utilizing Equation (62), critical flaw sizes for all porcelain bodies were determined. Table XX lists the results for two selected materials. Comprehensive analysis of the critical flaw size will be discussed subsequently. A tabulation of all measured critical flaw sizes can be seen in Appendix D. What is important to note about Table XX is that critical flaw size is represented in terms of $2c$ instead of c . The reason for this is because when referring to a surface crack, such as those formed in the crazed layer on the glazed samples, the dimension is c .

Table XX. Measured and Calculated Material Properties for Silica B and Alumina B Porcelain Compositions.

Composition	σ (MPa)	E (GPa)	γ (J/m²)	$2c$ (μm)
Silica B (unglazed)	78.2	70.8	4.5	74
Alumina B (unglazed)	134.4	127	8.4	71

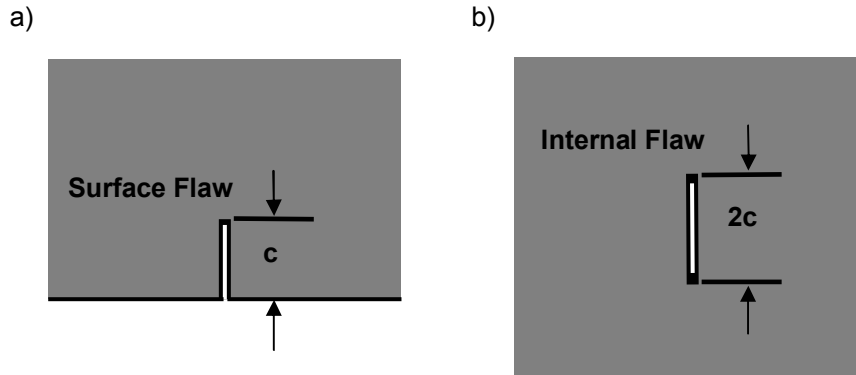


Figure 29. Schematic showing a) the dimension of surface flaw versus b) the dimension of an internal flaw.

However, when referring to critical flaws in the unglazed sample, it is assumed the critical flaw is not a surface feature (surfaces of samples are assumed macro-flaw free), but instead an internal flaw, which has the dimension $2c$, illustrated in Figure 29.

4.7 Summary

A new technique was developed for measuring fracture surface energy of a ceramic material, which is believed to be more accurate and introduce less experimental error than techniques currently in use (e.g., SENB). Using a crazed glaze surface layer to introduce controlled, idealized flaws to the surface of a specimen allowed the quantitative measurement of fracture surface energy of several porcelain bodies. With sharp flaws present at the surface, the measured flexure strength was much lower than it was in identical samples of unglazed porcelain specimens (i.e., Silica B: 78 MPa vs. 28 MPa). This is because the introduced flaws act as stress concentrators at the surface of the porcelain and, hence, are the critical flaws. The length of these flaws was directly measured using SEM, yielding the value for critical flaw size (c). Using a derivation of the Griffith equation, taking into account the Poisson's ratio and the size and geometry of the flaws in question, measured elastic modulus and flexure strength were used to calculate the fracture surface energy of glazed specimens. This was equated to unglazed specimens and the mechanical strength they possessed, since the elastic modulus and fracture surface energy is intrinsic to the porcelain, whether glazed or not. Having analyzed these results,

a unique linear relationship between elastic modulus and fracture surface energy was discovered to exist (i.e., E scales with γ). The commonality between these materials that display this behavior is that they contain similar bonding character, primarily Si–O and Al–O bonds. Using this relationship, the equation of a line was established on which many experimental and literature data lie, with a high degree of correlation. Predictions of fracture surface energy were made for similar compositions using this relationship as a calibration curve, where only the elastic modulus was known.

Using another mathematical rearrangement of the Griffith equation (Equation 61) to solve for flaw size (c) and having measured the mechanical strength and elastic modulus of the same porcelain in an unglazed state, the value of c was calculated using these variables along with the previously measured value for fracture surface energy, which is a constant. This is a straightforward method of determining the critical flaw size in a material, because the critical flaw size can be estimated in-situ, providing a legitimate alternative to performing optical or SEM fractography. The overall advantage of this technique is that through the use of the fracture mechanics, the critical flaw size that caused failure of a specimen can be predicted when other, more easily measurable mechanical properties are known.

5. Evaluation of Fired Microstructure and Strength

5.1 Overview

The fundamental impetus for firing a ceramic material is to decrease porosity and thus to increase its density and strength. In the case of a porcelain body, an ideal microstructure is characterized by a relatively homogenous glass phase, containing evenly dispersed residual filler grains and little to no porosity. If a body is allowed to soak at the maturation temperature for a sufficient amount of time (for a well-mixed porcelain >3 hours)^{4,95} the resulting microstructure will be ideal and strength is maximized. If it is fired above or below this temperature, the resulting properties are such that strength decreases due to a non-ideal microstructure. Literature suggests a strong correlation between fired density and strength, proposed to be due to presence of larger voids and flaws that can more easily propagate through a material under an applied load. This investigation looks at the effect of fired microstructure on mechanical properties, particularly its effect on mechanical strength.

5.2 Preliminary Investigation (Gradient Furnace)

5.2.1 *Experimental Procedure*

Three porcelain body compositions were used in this study; two industrial-grade electrical insulator porcelain bodies (Silica B, Alumina B) and a stoneware porcelain composition. The chemical compositions are shown in Tables VII and VIII, respectively. Silica B and Alumina B were obtained in the plastic form, vacuum pug-milled into large pieces to company specifications. The stoneware porcelain was in plastic form, also pug-milled. Whether a vacuum was applied during the process for the stoneware body is unknown, but unlikely as it is typically unnecessary for artists. Each of these compositions was extruded (in the presence of a vacuum) into 170-mm cylindrical rods with a 13-mm diameter. One rod representing each composition was sectioned into eight 20-mm segments. The initial height of each of the segments was verified using calipers to aid in determining firing shrinkage. These segments were placed inside a gradient tube furnace, programmed with a 1350°C set point and a dwell time of 3 hrs. The gradient tube furnace was set up with samples placed at 1-inch intervals along the length of the tube.

Temperatures were measured in-situ using a thermocouple at each sample location, measured during the dwell of the firing cycle.

5.2.2 Over- / Under-firing

Figure 30 shows three microstructures of the same porcelain composition (Silica B) that was fired at different temperatures, illustrating the characteristics of under-fired (Figure 30a), properly fired (Figure 30b), and over-fired (Figure 30c) porcelain microstructures. Characteristic details of these microstructures are discussed in Section 5.4.2.

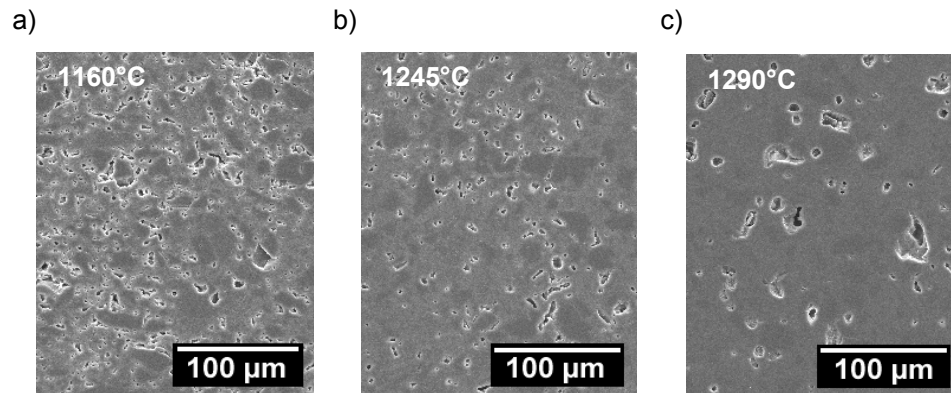


Figure 30. Characteristic secondary electron SEM images of a) under-fired porcelain ($\rho = 2.310 \text{ g/cm}^3$; porosity = 1.44%), b) ideally fired porcelain ($\rho = 2.408 \text{ g/cm}^3$; porosity = 0.11% and c) over-fired porcelain ($\rho = 2.318 \text{ g/cm}^3$; porosity = 0.18%).

Before and after firing, the height of each of the segments was again measured, to determine linear firing shrinkage. Appendix B contains the raw data from this experiment.

Figure 31 shows the linear firing shrinkage associated with firing temperature and Silica B, Alumina B and Stoneware porcelain compositions fired within the gradient furnace. As shown, firing shrinkage is minimal at low temperature, as evident by large voids and pores within the microstructure. Shrinkage increases rapidly between 1000°C and 1200°C for all bodies. Silica B appears to reach a maximum at approximately 1240°C, while Stoneware and Alumina B shrink

further at higher temperature, both attaining maximum shrinkage at about 1260°C. Above these peak temperatures, shrinkage begins to decrease due to bloating.

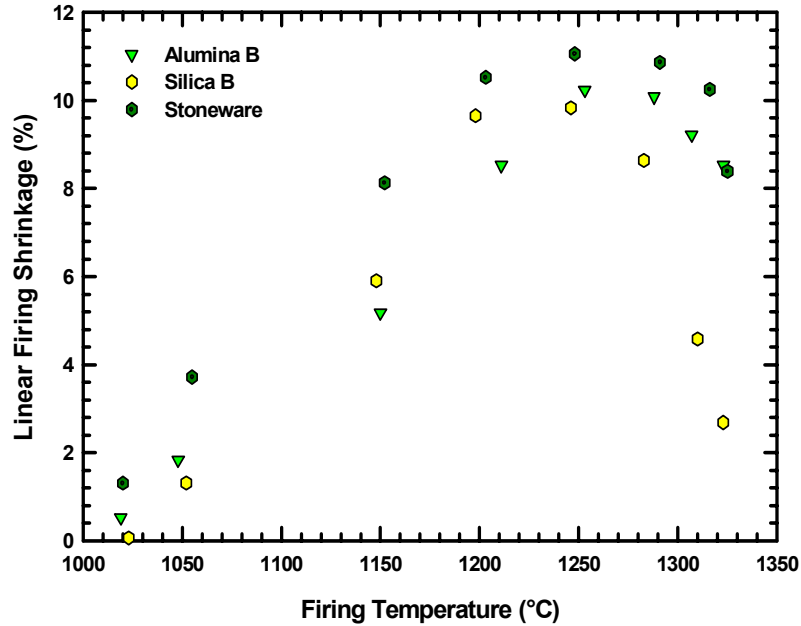


Figure 31. Linear firing shrinkage versus soak temperature for porcelain compositions within a gradient furnace.

The increased temperature caused a volumetric increase of the specimen due to expansion of the pores in the body. This expansion occurs due to the pressure in the bubble exceeding the viscosity of the glass phase. Silica B experienced the largest decrease in shrinkage at high temperature. Bulk density of the samples fired in the gradient furnace is shown in Figure 32. At temperatures below 1150°C bulk density is low, corresponding to a poorly-densified, under-fired microstructure containing voids distributed in a poorly-densified glass matrix. Much like linear shrinkage, density increased rapidly from 1000°C to 1200°C for all samples, maximizing at about 1250°C for Silica B and Stoneware compositions and at ~1260°C for Alumina B. A decrease in bulk density corresponded to over-firing the porcelain as pores tended to become spherical and expand, increasing the volume of the sample, the percent porosity, and decreasing the overall bulk density.

5.2.3 Firing Range

Each of the compositions investigated was characterized by displaying a narrow region where the change in a given property over a broad temperature range was minimal. For example, look at linear firing shrinkage versus temperature for the Silica B composition, as shown in Figure 31. Between 1150°C and 1200°C there is approximately a 2% change in the shrinkage. Between 1200°C and 1250°C, however, there is little to no change. This zone of constant shrinkage is referred to as the firing 'range.' In subsequent plots of bulk density versus temperature, a similar plateau region is also observed. This is a common phenomenon in porcelain bodies and is in part what makes them such versatile materials, insensitive to slight temperature variations that almost always occur during firing. To test the limits of this firing range and also to observe the effects of over- and under-firing on properties, five firing temperatures for each porcelain body were selected for study. These temperatures were chosen by fitting data points from plots (linear firing shrinkage and bulk density versus temperature) with a mathematical equation (parabola) and finding the maxima.

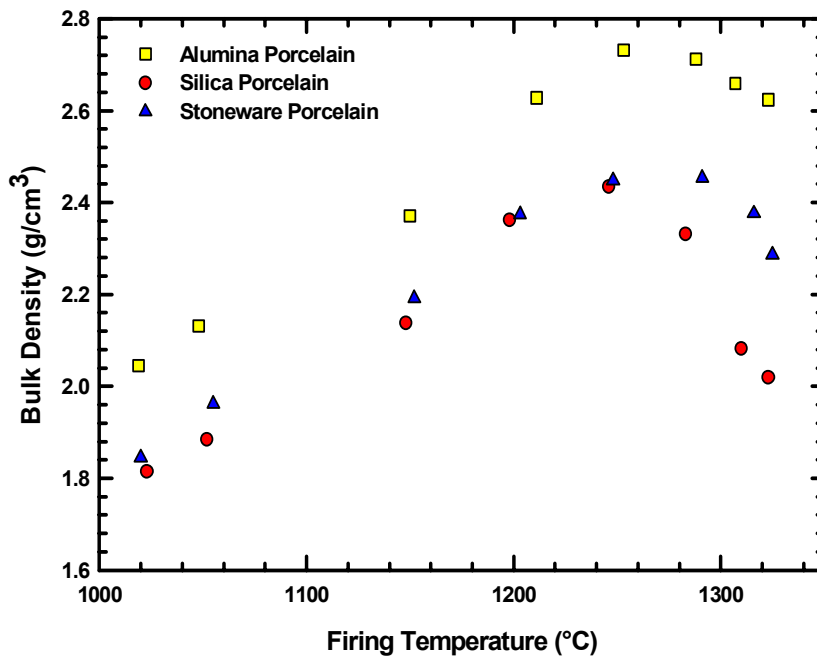


Figure 32. Bulk density versus soak temperature for porcelain compositions fired in a gradient furnace.

An example of this technique is shown in Figure 33. The temperature corresponding to the maximum was regarded as being at the center of the firing range. It is the optimum condition (temperature) for firing since it yielded both the maximum bulk density and linear shrinkage. Two other temperatures, considered to be within the firing range of the porcelain (one above and one below this maximum) were also chosen. Two endpoint temperatures were selected to serve as extremes, which were believed to represent under- and over-fired bodies.

5.3 Main Investigation

5.3.1 Experimental Procedures

One hundred rods of each body composition were fired in a box furnace (molybdenum disilicide elements), twenty to each of the five selected temperatures using a 3-hour dwell. Table XXI shows the firing temperatures chosen. Pyrometric check keys were used to verify the peak temperature during each firing (TempChek, Orton, Inc., Westerville, OH). After firing, samples from each of the temperatures were measured for bulk density, according to the ASTM standard procedure.¹¹⁶

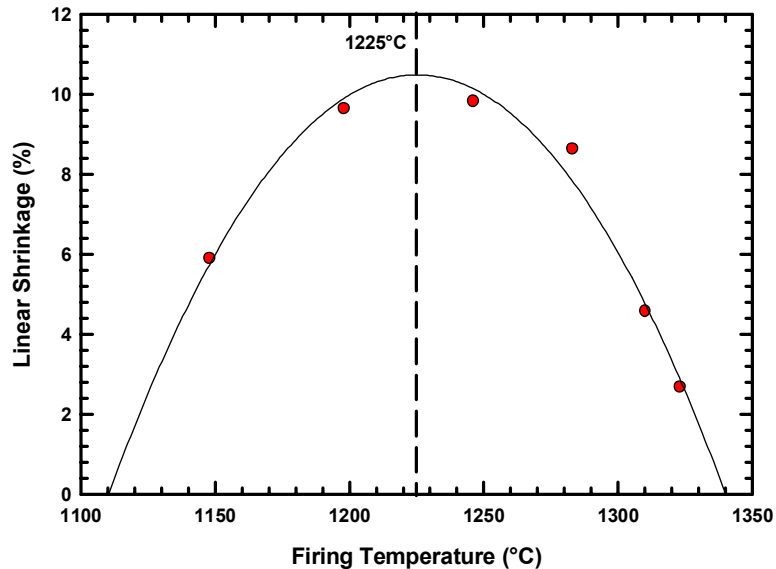


Figure 33. Plot of shrinkage versus firing temperature of Silica B composition with parabolic fit to data.

Table XXI. Firing Temperatures Selected for Study.

Firing Temp (°C)	Silica B	Alumina B	Stoneware
1160	x		x
1210	x		
1225	x	x	x
1245	x	x	x
1270		x	x
1290	x	x	
1310		x	x

□ Under-fired. ■ Within firing 'range'. ■ Over-fired.

Four-point flexure testing was carried out on the samples to determine the failure stress (MOR). The loading span for each of the rods was 63.5 mm, and the support span for the test was set at 127 mm. The loading rate for the test was 0.5 mm/min. Each sample was tested to fracture according to the standard procedure (Section 3.2.2), and the MOR was calculated. The elastic modulus of each body fired at each temperature was experimentally measured using the aforementioned pulse-echo technique, described in Section 3.2.3.

5.4 Experimental Results

5.4.1 Bulk Density vs. Temperature

Figure 34 shows bulk density measurements from the main investigation overlaid with previous results from the preliminary study (Figure 32) for comparison. Results show good agreement between preliminary samples (rod segments) fired in the gradient furnace and full-sized samples fired in a box furnace (molybdenum disilicide elements) for the main investigation.

5.4.2 Microstructures

Figures 35–49 are secondary-electron SEM micrographs of porcelain bodies fired at different soak temperatures. The first image in each series represents what was expected to be an under-fired microstructure (Figures 35, 40, 45). Characteristic features of this include large amounts of irregular voids around primary filler grains. Also, the general appearance of glass phase is that of inhomogeneity, since some of the raw materials have not fully melted and consolidated. Overall,

the under-fired microstructure has not fully densified, therefore it is expected that bulk density and linear shrinkage values are both low. Samples fired within their respective firing 'ranges' are shown in Figures 36-38 (Silica B), 40-43 (Alumina B), and 46-48 (Stoneware).

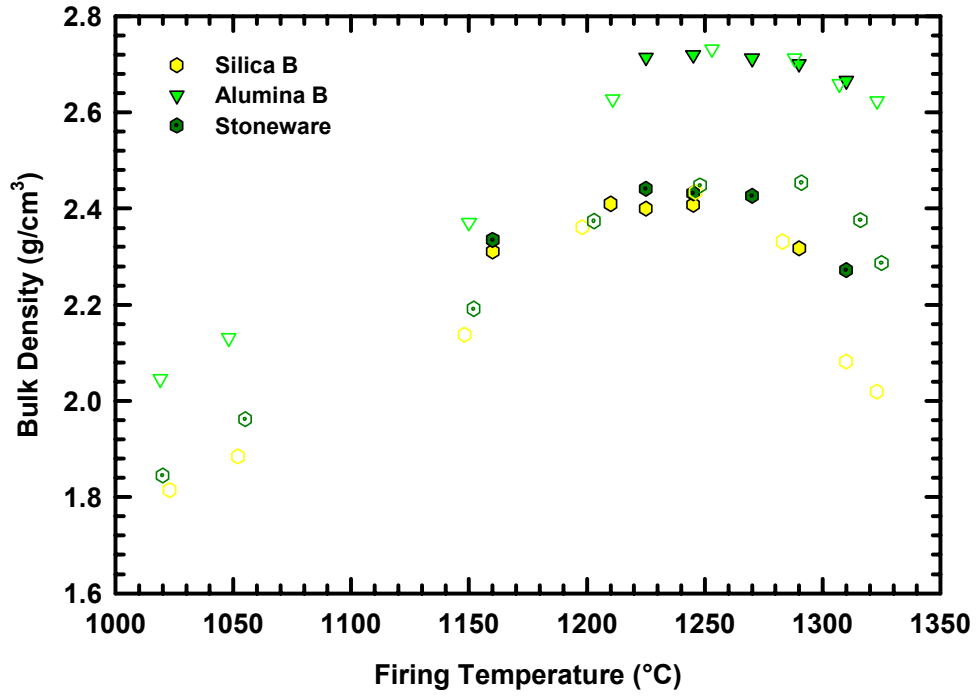


Figure 34. Bulk density versus firing temperature for porcelain compositions including preliminary (hollow) and main investigation (solid) results.

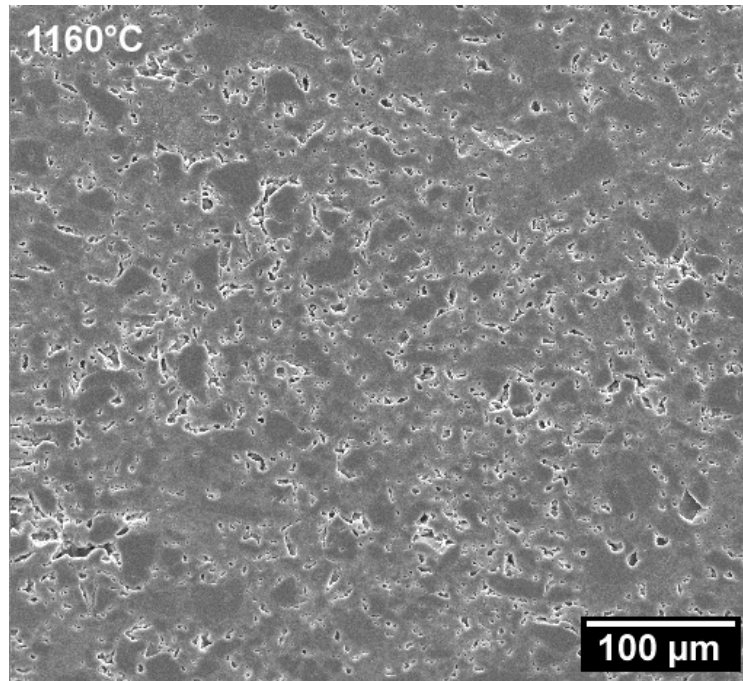


Figure 35. SEM secondary electron image of Silica B porcelain fired at 1160°C (3-hour dwell).

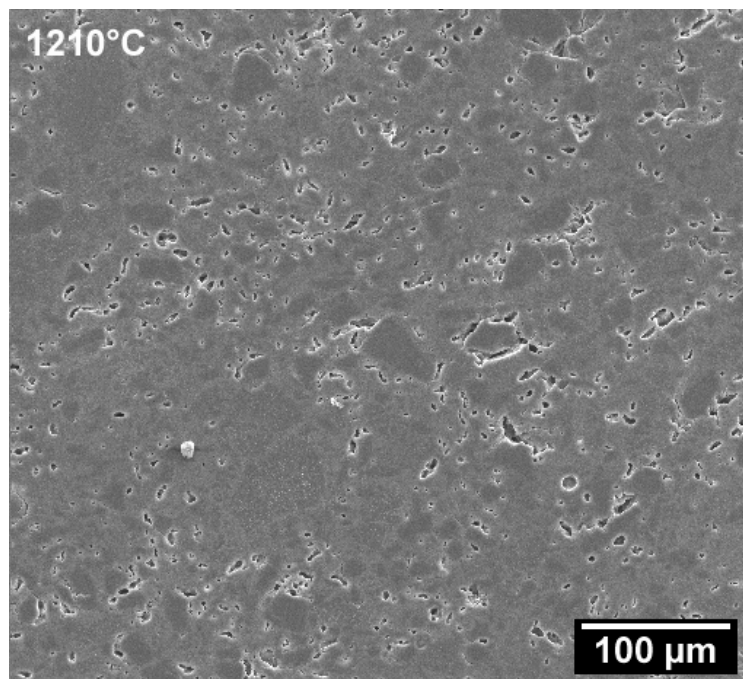


Figure 36. SEM secondary electron image of Silica B porcelain fired at 1210°C (3-hour dwell).

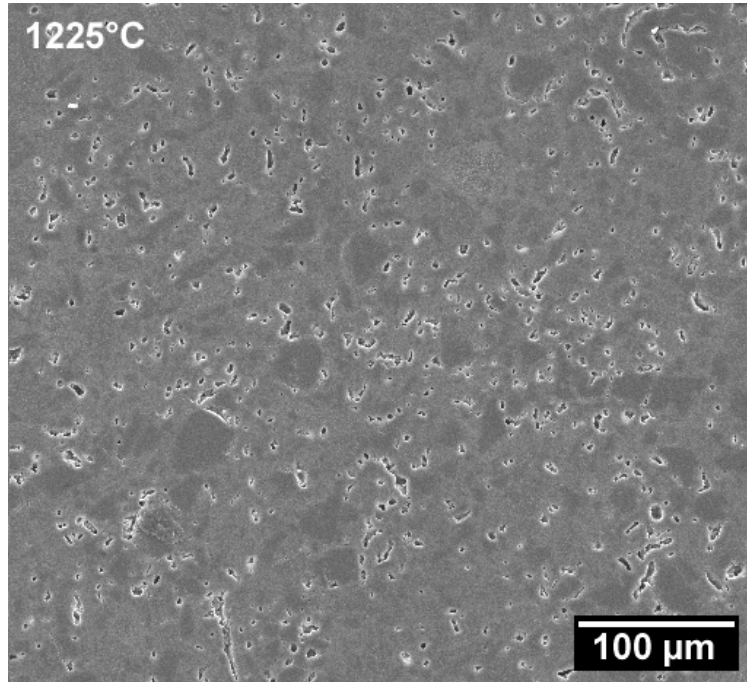


Figure 37. SEM secondary electron image of Silica B porcelain fired at 1225°C (3-hour dwell).

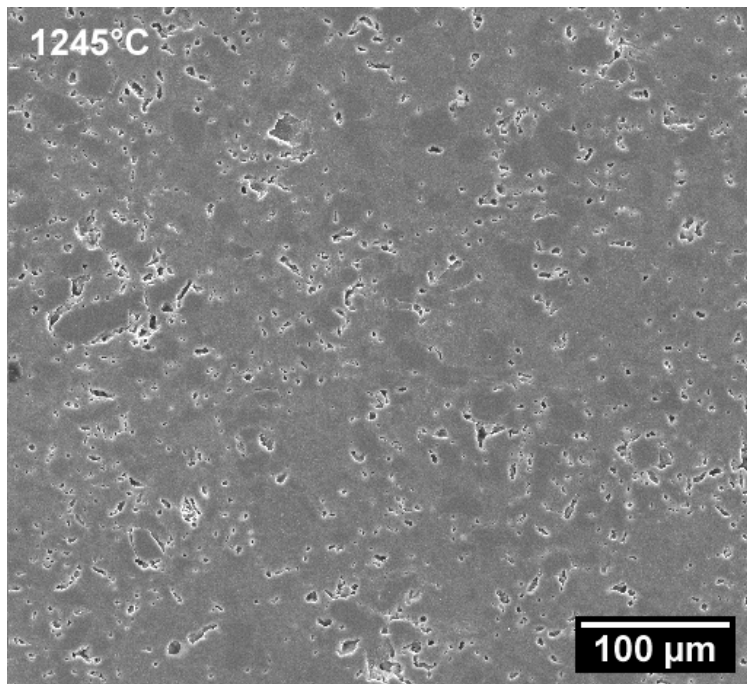


Figure 38. SEM secondary electron image of Silica B porcelain fired at 1245°C (3-hour dwell).

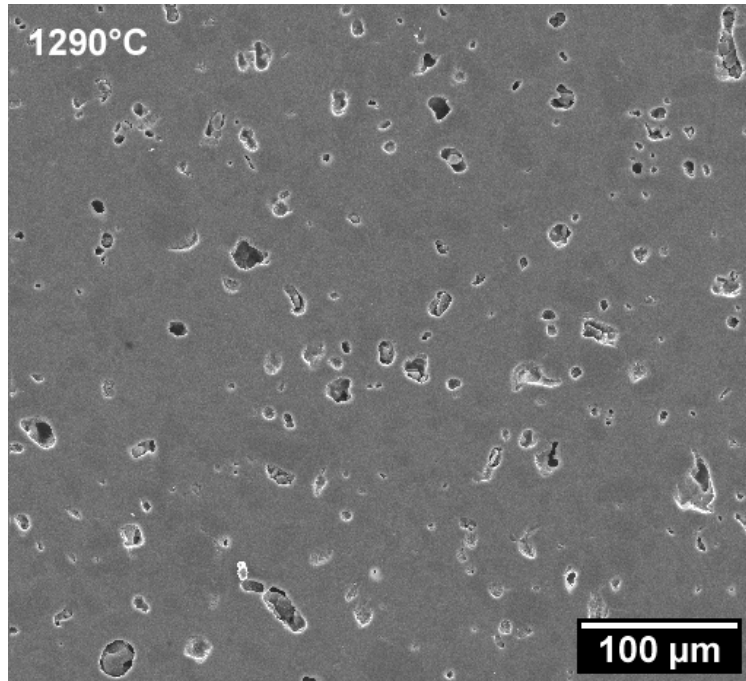


Figure 39. SEM secondary electron image of Silica B porcelain fired at 1290°C (3-hour dwell).

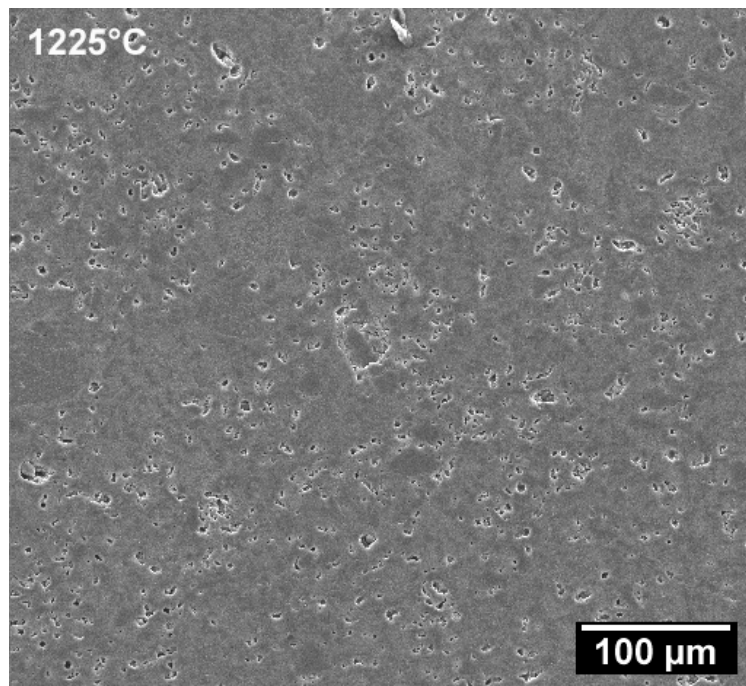


Figure 40. SEM secondary electron image of Alumina B porcelain fired at 1225°C (3-hour dwell).

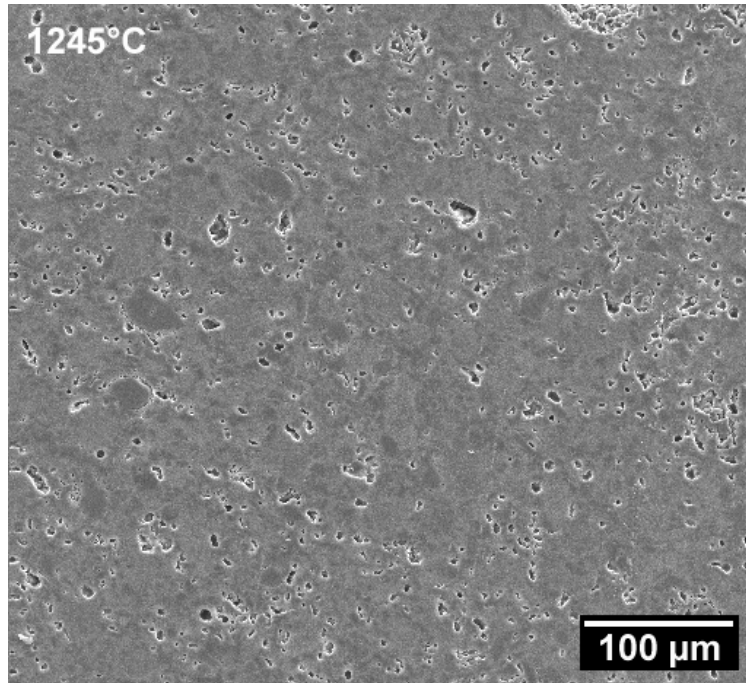


Figure 41. SEM secondary electron image of Alumina B porcelain fired at 1245°C (3-hour dwell).

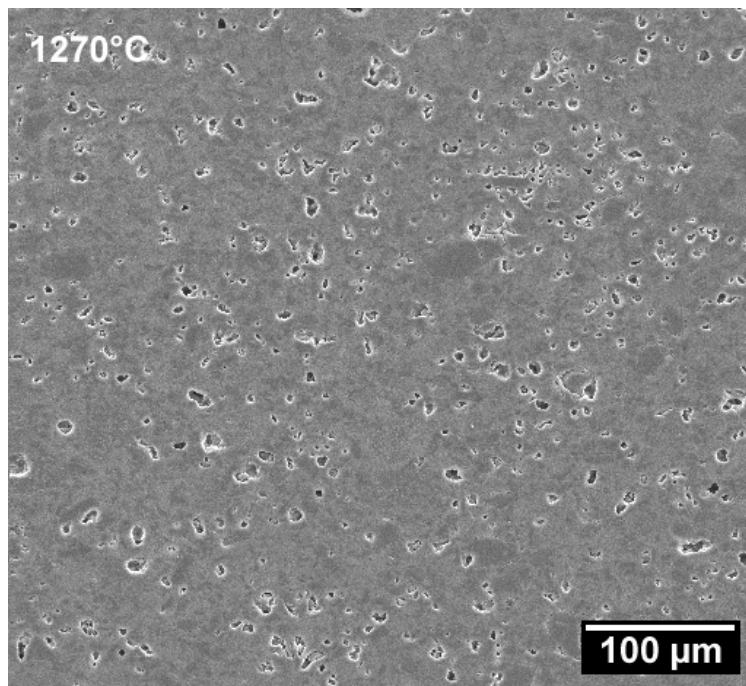


Figure 42. SEM secondary electron image of Alumina B porcelain fired at 1270°C (3-hour dwell).

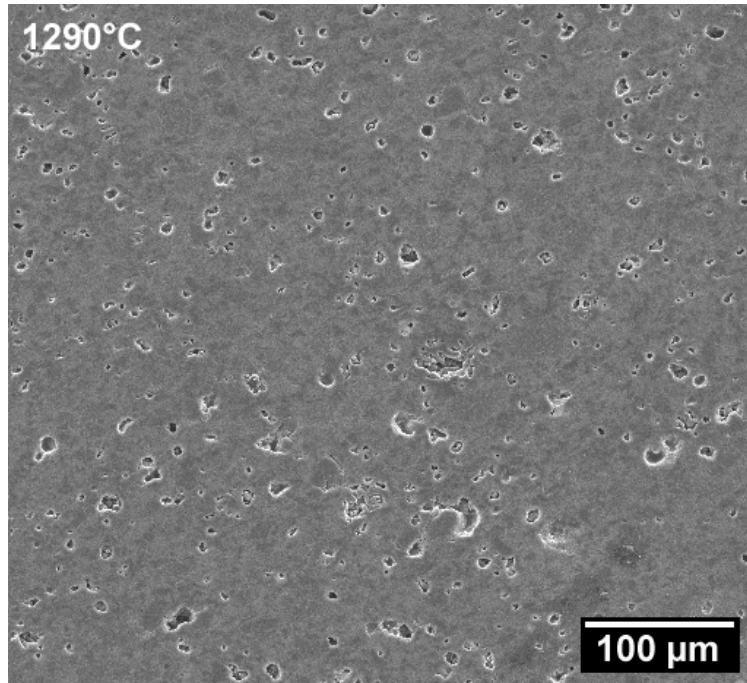


Figure 43. SEM secondary electron image of Alumina B porcelain fired at 1290°C (3-hour dwell).

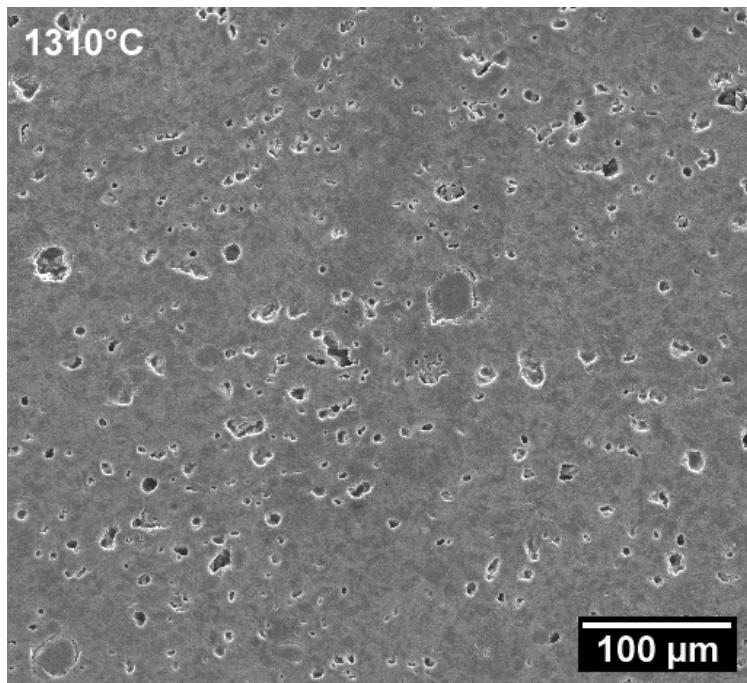


Figure 44. SEM secondary electron image of Alumina B porcelain fired at 1310°C (3-hour dwell).

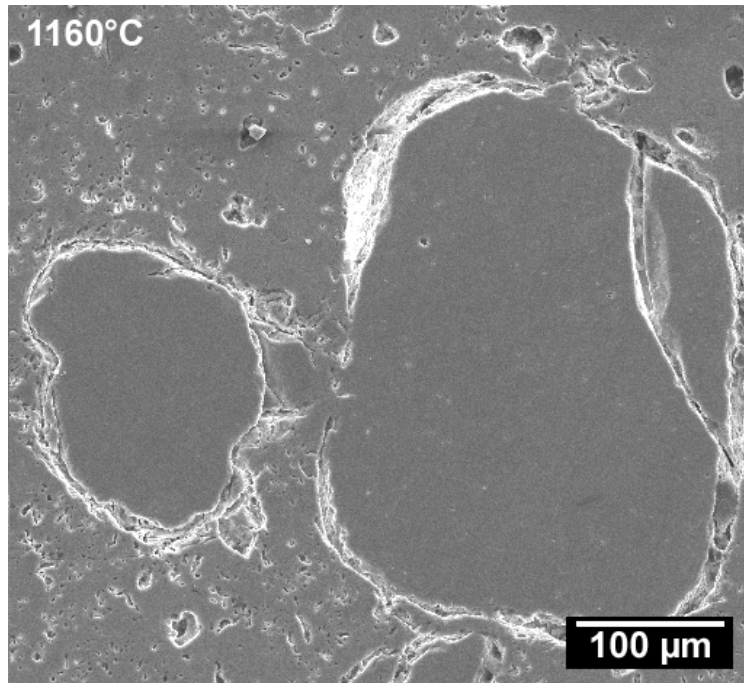


Figure 45. SEM secondary electron image of Stoneware porcelain fired at 1160°C (3-hour dwell).

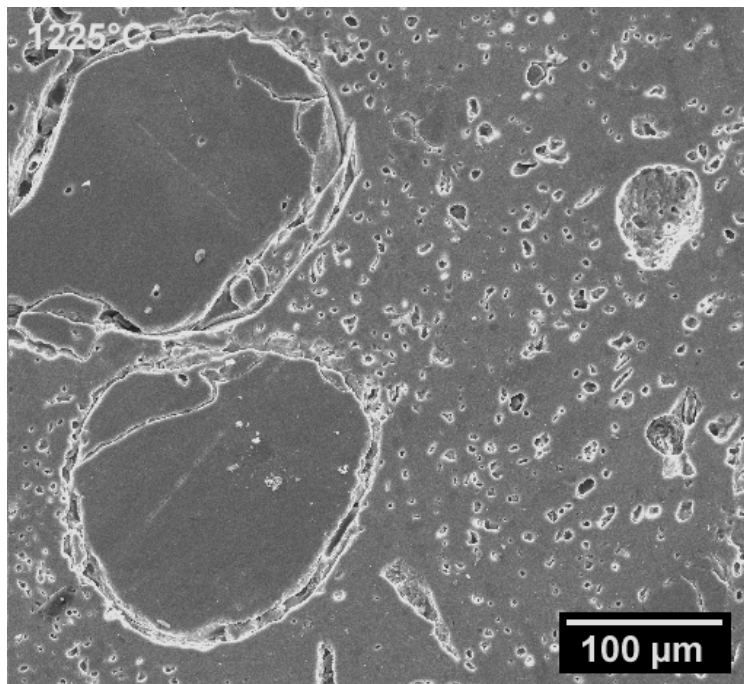


Figure 46. SEM secondary electron image of Stoneware porcelain fired at 1225°C (3-hour dwell).

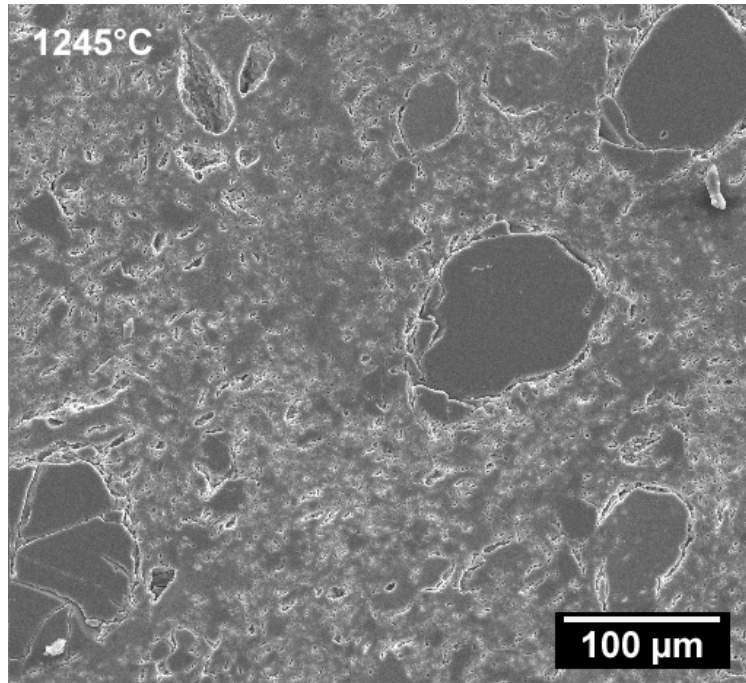


Figure 47. SEM secondary electron image of Stoneware porcelain fired at 1245°C (3-hour dwell).

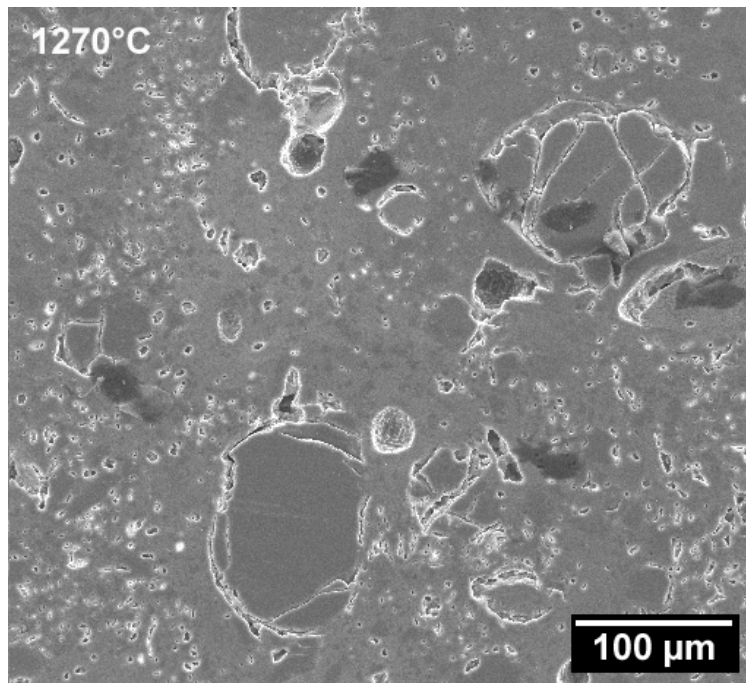


Figure 48. SEM secondary electron image of Stoneware porcelain fired at 1270°C (3-hour dwell).

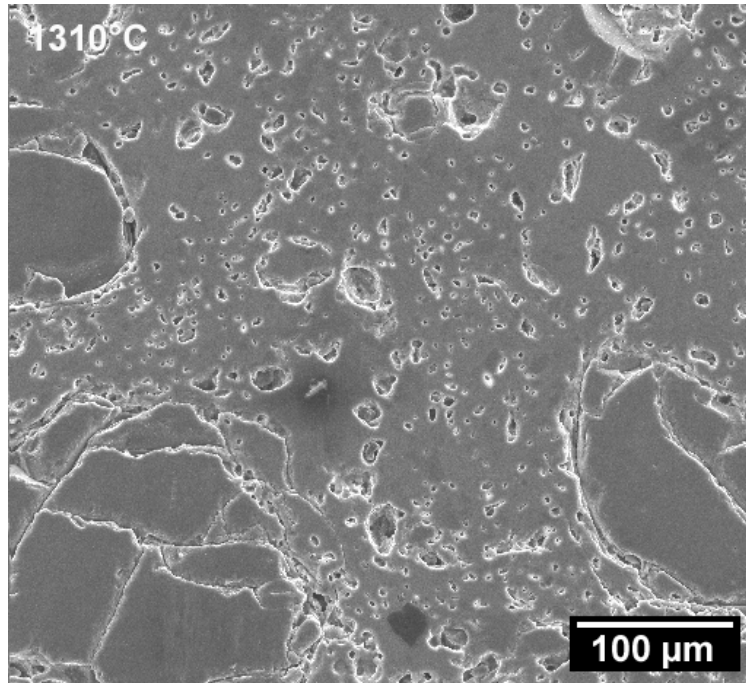


Figure 49. SEM secondary electron image of Stoneware porcelain fired at 1310°C (3-hour dwell).

With increasing firing temperature, pores decrease in size and number while the body sinters and densifies. Also, homogeneity of the glass phase appears to increase as well, adopting a more uniform tone, in contrast to the blotchy, irregular appearance of the under-fired glass phase. The last figure in each series (Figures 39, 44, 49) corresponds to what was expected to be over-fired bodies. Whereas porosity decreased with increasing temperature within the firing range, over-firing the body results in the appearance of larger, more spherical pores that contribute to a decrease in bulk density and linear firing shrinkage.

All images were taken at the same magnification, so it is evident that the filler grain size varies between compositions. Quartz grains in Silica B average about 20–25 μm; alumina grains are approximately 5–10 μm in Alumina B. The Stoneware composition contained very large (>100 μm) filler grains, presumably of quartz or grog (previously fired porcelain fragments used as filler material), since they displayed characteristic internal cracking behavior and artifact damage (caused by polishing) around the grains allowed for increased visibility of the grain shape.

5.4.3 Mechanical Properties

Figure 50 shows the relationship between firing temperature and four-point MOR for Silica B, Alumina B, and Stoneware compositions. For Silica B and Stoneware (which have similar compositions) strength is lowest for samples fired at 1160°C (under-fired). This correlates well to the material having lower density, as it has not fully sintered, leaving large voids and regions of unconsolidated material within the microstructure (Figure 35). Strength increases and becomes a maximum as temperatures increase to within the ideal firing range. This corresponds to bodies having the highest bulk density (Figure 34).

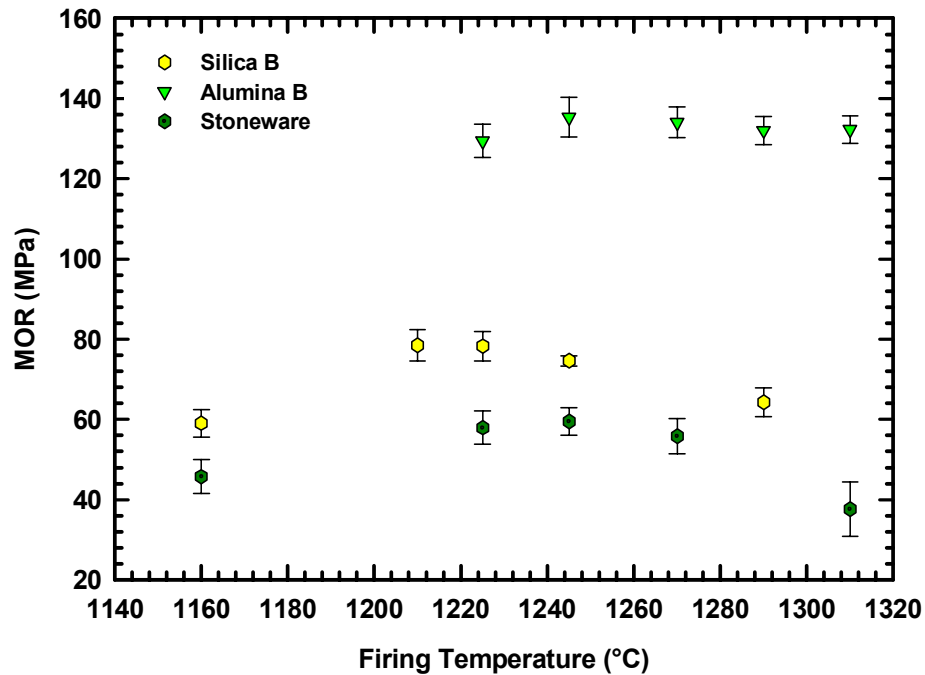


Figure 50. MOR versus firing temperature for Porcelain B compositions and Stoneware.

Temperatures that yield maximum strength for Silica B and Stoneware are 1220°C and 1250°C, respectively. Above these temperatures, the bodies begin to show signs of being over-fired. Pores start to grow larger, and bloating on the surface of the specimens becomes evident. As a result, strength decreases. For Alumina B porcelain, there is only a slight increase in MOR in samples fired at 1245°C, but overall, strength stays about the same throughout the range of firing temperatures studied.

In order to observe more precisely to what extent MOR changes with temperature, strengths were normalized and then plotted versus firing temperature (Figure 51). As shown, when going from an under-fired to a optimally-fired condition, strength of Silica B and Stoneware compositions increased by almost 25%, whereas Alumina B shows a change of approximately 5%. Likewise, when bodies were over-fired, Silica B showed a 20% decrease in strength, and Stoneware showed a 40% decrease when fired at 1310°C. This temperature resulted in a highly over-fired porcelain body, and the properties reflect this. From this plot it appears that the porcelains containing silica (Stoneware body also contains silica as a major constituent) were more temperature-sensitive than their alumina counterpart, which shows only a slight variation in strength over the entire temperature range studied.

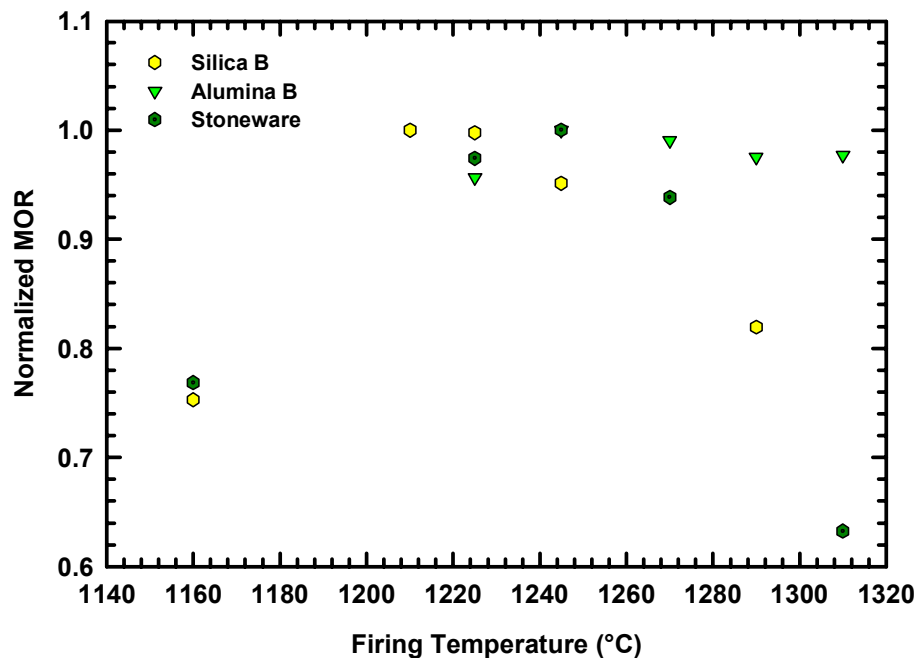


Figure 51. Normalized strength versus firing temperature for Porcelain B and Stoneware body compositions.

Figure 52 shows the effect of firing temperature on elastic modulus. Much like the other material properties measured, elastic modulus is low at low temperature, then increases, maximizing within the firing range. For Alumina B and Stoneware compositions, over-firing the body results in a slight decrease in elastic modulus, whereas for Silica B elastic modulus is at a maximum. It is

postulated that were the Silica A body fired at 1310°C, there would be an evident drop in elastic modulus, since it is only above 1270°C that the Stoneware body shows signs of decreasing elastic modulus, and Silica A and Stoneware compositions are chemically similar.

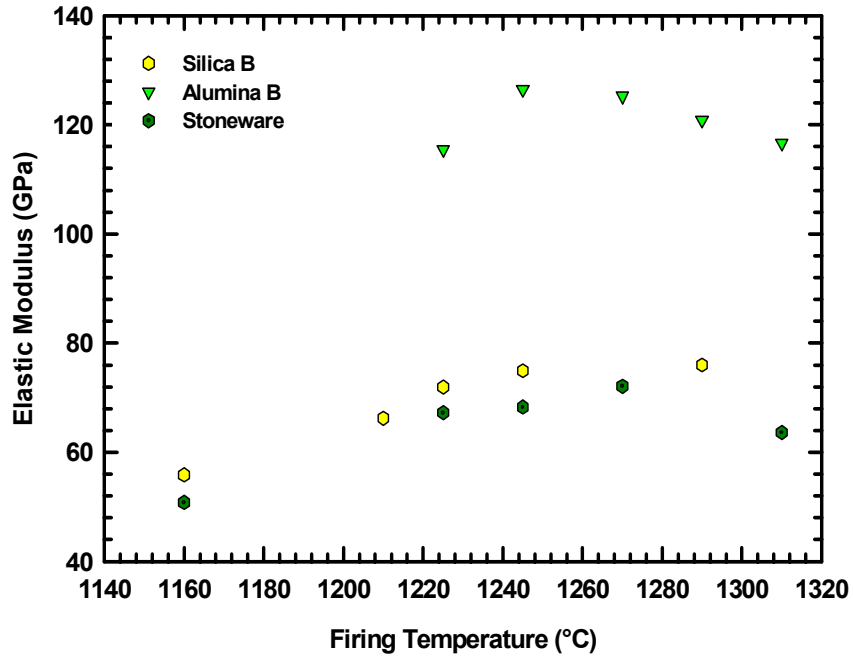


Figure 52. Effect of firing temperature variations on elastic modulus for porcelain B and Stoneware body compositions.

5.5 Property Analysis

5.5.1 Fracture Surface Energy vs. Temperature

Figure 53 shows the relationship between firing temperature and fracture surface energy. Since surface energy was linearly correlated to elastic modulus, the trends are virtually identical to that seen in Figure 52. At lower temperatures (corresponding to an under-fired system) fracture surface energy is lower. This is attributed to the poor densification of the microstructure, the excess of void space causing the elastic modulus to be low. As the system becomes more and more optimally fired (increasing temperature to the firing range) the surface energy increases for all compositions. Over-firing the bodies has a negative effect on surface energy, which decreases relative to the degree to which the body is over-fired. Elastic modulus decreases,

resulting in a lower-strength body requiring less energy to fracture the material. Bulk density decreases as well.

5.5.2 Critical Flaw Size vs. Temperature

The method for calculating critical flaw size outlined earlier in Section 4.6.2 allows the relationship between it and firing temperature to be analyzed by using measured and calculated values of σ_f , E , and γ for the porcelain B and Stoneware compositions. Figure 54 shows the results.

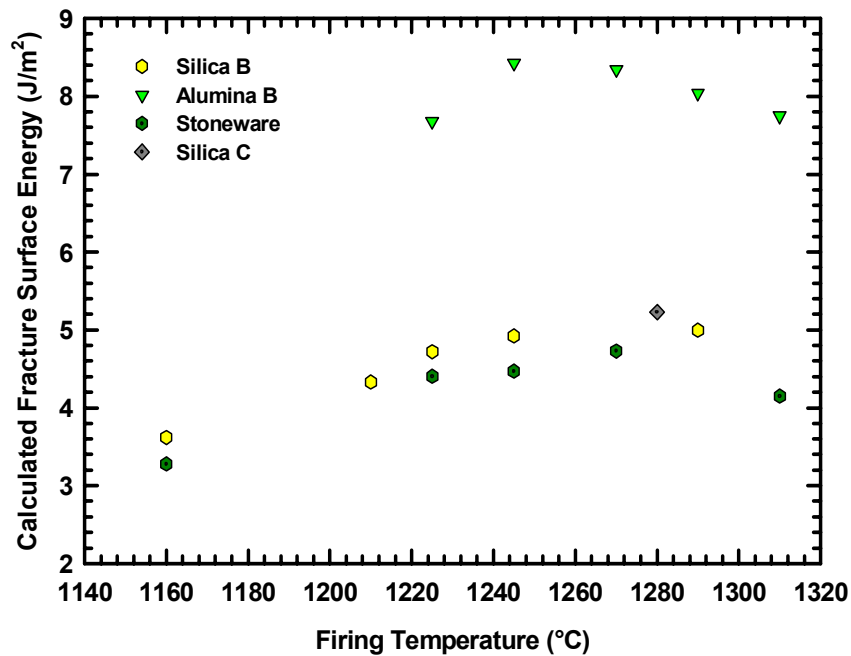


Figure 53. Fracture surface energy versus firing temperature for Porcelain B and Stoneware body compositions.

As shown in the figure there appears to be no effect of firing temperature on critical flaw size with increasing firing temperature. Silica B and Alumina B show flaw sizes on the order of 60–70 μm with little to no appreciable change in magnitude as temperature increases. The Stoneware composition also shows no change in critical flaw size with increasing temperature up to 1250°C, with a flaw size of approximately 100 μm . Above this temperature, however, there is an abrupt increase with firing temperature, such that for the samples fired at 1310°C, the critical flaw size is predicted to be 240 μm . It is speculated that the Stoneware porcelain body, which displays a

strength maximum when fired at approximately 1250°C is severely over-fired at both 1270°C and 1310°C. Also, the extremely large filler grains (presumably quartz) present in the microstructure may influence critical flaw size at high temperatures, because it has been shown that cracks due to thermal stresses spontaneously occur within filler grains upon cooling for filler particles above a critical size. Quartz, for example, displays this phenomenon in grains of 87 μm or larger.⁴

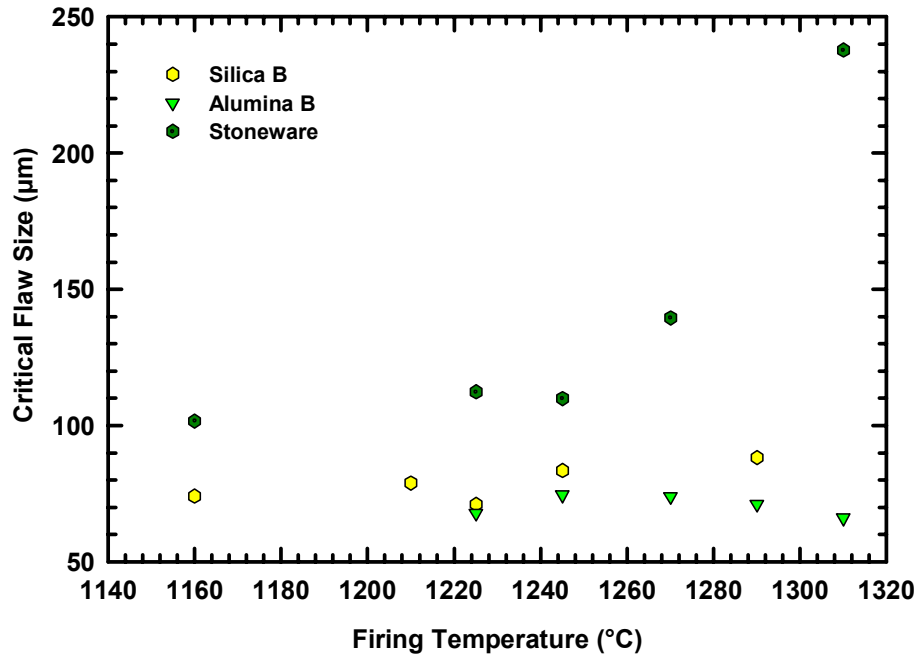


Figure 54. Critical flaw size versus firing temperature for Porcelain B and Stoneware body compositions.

There appears to be no direct effect of firing temperature on critical flaw size, and that in general critical flaw size remains constant with firing temperature for these porcelain bodies. Firing temperature is one of the more commonly investigated factors in experiments involving ceramics, because temperature is a parameter critical to microstructural development. It is also one of the more uncontrollable variables (slight temperature variations always occur depending on specimen location). The fact that critical flaw size appears to be independent of firing temperature, leads to the conclusion that something intrinsic to the porcelain microstructure, that is not temperature dependent, is controlling the critical flaw size. Even when under and over-firing the specimens, the deviation in the critical flaw size calculated was minimal, while other factors, such as bulk

density and porosity were clearly affected. Figures 35–49 give a good representation of the scale of porosity within the samples, and it can be noted that there is no evidence of individual pores approaching the calculated critical flaw size. The largest pores in most bodies are an order of magnitude smaller than would be required to qualify as critical flaws. This indicates that pores cannot be the critical flaws within these bodies. Furthermore, for the critical flaw size to remain constant in a microstructure that clearly changes with firing temperature, it can be concluded that the critical flaws must be temperature independent. It is instead proposed that a critical flaw is caused by a cluster of filler particles that contains void spaces between them on the order of the calculated critical flaw size. Further discussion on this hypothesis follows in Section 7.

5.5.3 Bulk Density Effects

Figure 55 shows a plot of critical flaw size versus normalized bulk density of the Porcelain B and Stoneware compositions. A poor correlation is observed between the two parameters, as evident by irregular scattering of the data. The lack of a relationship indicates that the critical flaw size is independent of the density of these bodies.

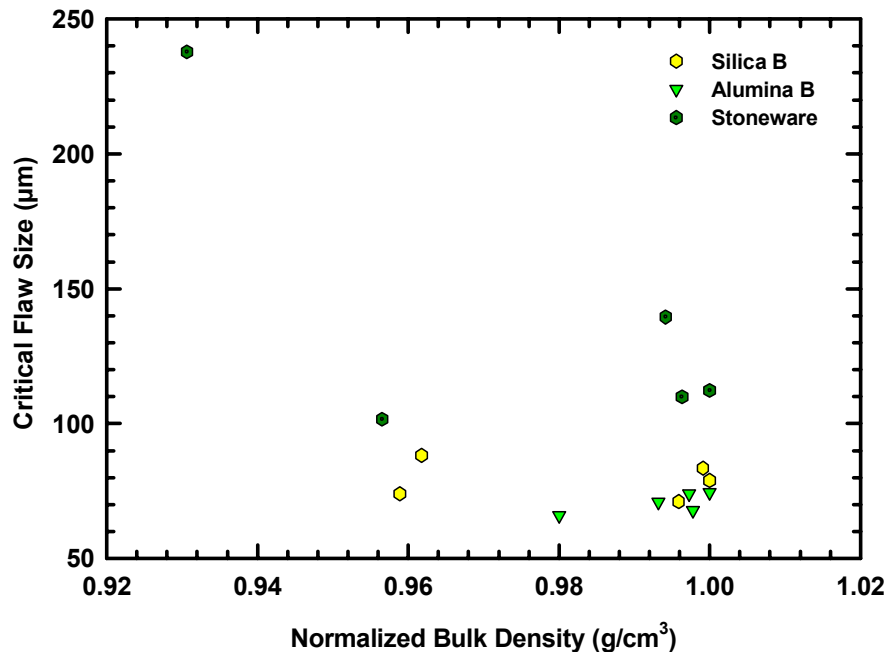


Figure 55. Critical flaw size versus normalized bulk density for Porcelain B and Stoneware body compositions.

The density of the alumina porcelain changes very little over the temperature range tested, indicating that the microstructure was well vitrified at all temperatures. Figures 40–44 show that the microstructure changes only subtly over the temperature range while the silica bodies show dramatic changes in the glass phase with temperature. Based on experimental data the original assessment of the 1225°C alumina body being truly under-fired may be incorrect. If the Alumina B porcelain were fired to a lower temperature, where the glass phase was less vitrified, it is believed a similar transition would be observed.

5.6 Summary

Firing temperature of a ceramic plays an important role in the development of its microstructure. There is an optimum firing temperature for every ceramic material that yields optimum values of density, linear shrinkage, strength, and elastic modulus. For porcelain bodies there is a range of temperatures that make up a plateau region where there is little change in properties, such as linear firing shrinkage and bulk density. This region also corresponds (to a slightly lesser extent) to regions of maximum strength and elastic modulus. Using elastic modulus data and previously developed techniques, values for fracture surface energy and critical flaw size were calculated for these compositions. When comparing parameters, it was observed that strength, elastic modulus and fracture surface energy correlated to firing temperature, showing an increase with increasing temperature, a plateau, then a decline. However, critical flaw size did not. Critical flaw size remained essentially constant over the entire range of temperatures, showing no correlation to bulk density; the plot revealed random scattering of data points.

Overall this investigation indicates that critical flaw size appears to be unaffected by changes in microstructure caused by altering firing temperature. Critical flaw size stays constant throughout the temperature range, and shows no correlation to bulk density. This is contrary to the concept that larger critical flaws result from a less-dense (over- or under-fired) ceramics. These data instead indicate that critical flaws of the same size exist in each material, regardless of firing treatment, and are the result of another influence. This experiment also rules out primary pores as the critical flaws. Microstructural evaluation at the various temperatures does not reveal any

porosity on the order of 70–80 μm (corresponding to the critical flaw size). While it is recognized that unconsolidated raw materials within an under-fired body can form large flaws, the fact that critical flaw size did not change as the body densified reveals that the same critical flaws are present in all samples, and that they are larger than any flaw in the form of a naturally occurring pore, because no transition from one critical flaw size to another with temperature was observed.

6. Evaluation of Filler Particle Contributions to Strength

6.1 Overview

Many ceramic materials are polycrystalline and contain little to no glass phase. Other materials such as porcelains have in excess of 50% glass phase, interspersed with crystallites of mullite, quartz, and occasionally cristobalite. Also within this microstructure are residual filler grains, the remnants of precursor materials not fully dissolved (in this case quartz). Commonly used filler materials are quartz (SiO_2) and alumina (Al_2O_3). While the effect of these filler particles is the subject of controversy throughout the literature, the use of these filler materials is essential in creating a strong porcelain body. While the name 'filler' may imply these materials simply fill space with minimal impact on the body itself, improper use of materials as fillers can negatively affect many properties, including mechanical strength. Conversely, using fillers with favorable characteristics has been shown to improve strength. Two key parameters involved with this phenomenon are filler type and filler particle size, which are the subject of this next series of experiments. Results of this study attempt to reveal any relationships between filler particles and mechanical properties using a controlled and systematic approach.

6.2 Porcelain Fillers

6.2.1 Filler Particles / Size Effects

Porcelains that contain quartz as the filler have been extensively studied. In short, residual stresses that result from the use of these filler material (CTE greater than the glass phase) are radial tension and tangential compression. Along with quartz and alumina fillers, two other candidate filler materials that were investigated were spinel (Mg_2AlO_4) and mullite ($3\text{Al}_2\text{O}_3 \cdot 2\text{SiO}_2$). Table XXII lists filler materials used in this investigation, along with their respective elastic moduli and linear thermal expansion coefficients.

Table XXII. Grain Composition and CTE for All Filler Materials Investigated.

Filler Grain	Chemical Composition	Avg. CTE ($\times 10^{-6} K^{-1}$)	E (GPa)	Ref.
Quartz	SiO ₂	9 [001] dir. – 12 [100] dir.	94	110
Alumina	Al ₂ O ₃	7.2 - 8.8	390	125
Spinel	MgAl ₂ O ₄	7.6	248-270	126
Mullite	3Al ₂ O ₃ ·2SiO ₂	5.1	150	127
Glass Phase	Ref. (4)	6.5	-	4

Mg-Al spinel is a close-packed arrangement of oxygen anions with cations situated on the tetrahedral and octahedral sites. It has a density of 3.56 g/cm³ and a molar volume of 39.52 cm³/mol.¹¹⁵ It was selected because its CTE ($7.6 \times 10^{-6} K^{-1}$) is very similar to that of alumina ($7.2-8.8 \times 10^{-6} K^{-1}$) but it is a weaker crystal. Previous studies indicate the mechanical strength of porcelains containing spinel is intermediate between that of similar bodies containing alumina (Al₂O₃) and quartz.⁹⁹ In addition, the microstructure is such that spinel particles will react minimally with the surrounding matrix. The reactions that occur during firing are insufficient to melt it to any great extent, as it has a cohesive melting point of 2135°C. In the presence of alkali, this temperature will be decreased, but not enough to promote significant melting. The CTE of the glass phase of the Porcelain A composition was previously measured as $\sim 6.5 \times 10^{-6} K^{-1}$ and should vary only slightly with different filler materials, since for a given firing temperature and alkali level the final glass phase dissolves only a fixed amount of Al₂O₃ and SiO₂,^{4,95} and spinel particles do not significantly dissolve.

Mullite was selected as another candidate materials due to the opportunity to investigate the controversy surrounding its presence in the porcelain microstructure (Section 1.6.1). It has a reported density of 3.15 g/cm³.¹²⁶ Mullite naturally crystallizes within a porcelain microstructure, so the impact of its presence in filler form on the glass phase is minimal. While mullite as a material is not considered suitable for high-strength applications at low temperatures,¹²⁷ it is believed by some that mullite concentration and/or needle size are strengthening mechanisms in porcelains. While some previous studies already indicate this is not the case, experimenting with mullite is useful in demonstrating the converse effect, since mullite has a lower CTE than the

glass ($5.1 \times 10^{-6} \text{ K}^{-1}$). The crack mechanism proposed for porcelain microstructures containing quartz filler should no longer be active. Due to the distribution of stresses caused by this situation, residual forces create tangential tension resulting in the potential initiation of flaws at the glass phase/ particle interface, but within the glass phase.

6.2.2 Residual Stresses and Strains (CTE mismatch)

The degree to which cracking occurs is different for each filler material because the amount of residual stress generated is a function of the relative CTE mismatch, elastic moduli of the glass and particle, and failure stress between the filler particle and the glass phase. Filler grain size also affects the amount of residual strain generated within the microstructure. Previous studies (assuming $\text{CTE}_{\text{grain}} > \text{CTE}_{\text{glass}}$ and $\sigma_{\text{glass}} > \sigma_{\text{grain}}$) indicate that for every filler type there is a critical particle size below which spontaneous cooling cracking does not occur.⁴ Within the glass phase a large filler grain will develop a larger strain field around it than a small grain. However, if the grain is sufficiently large, the system cannot support the large strains generated and cracking will occur upon cooling, relaxing the microstructure to a degree. This spontaneous cracking is believed to be undesirable, because it weakens the system. One way to observe stresses in the material (since stress is an immeasurable property) is to look at the residual strain present in the crystallographic planes of filler particles. In this way the relationship between residual strain and filler size can be investigated to see the effect of filler particle size on strength for a variety of filler materials.⁴

6.3 Experimental Procedure

In this experiment porcelain bodies were made using the Porcelain A batch composition (Table V) with direct substitution on a dry-weight basis of four different filler materials (Table VI). Discrete, narrow size fractions of quartz, alumina, spinel and mullite crystals were collected for use in this experiment. Coarse particles were ground using a ball mill, and the larger size fractions were segregated from this material using a series of sieves. In some cases, smaller particles were obtained by taking as-received -325-mesh ($<44 \mu\text{m}$) powder and sieving it without the use of a

ball mill. A series of different particle sizes were used for each material (shown in Table XIV), ranging from 300 to 12 μm . Details of this procedure are precisely outlined in Reference 4.

To measure residual strain within the filler grains, discs were created using the four porcelain A compositions and the slip-casting technique outlined in Section 3.1.1, using several size fractions of the appropriate filler material in each case. Mechanical properties (i.e., MOR, E) were tested using rod samples made from each of the four compositions, made with different filler particle size fractions as well. Silica A and Alumina A compositions were dewatered by filter pressing (Section 3.1.2), while Mullite A and Spinel A compositions were dewatered using a Baroid filtration technique (Section 3.1.3). Both methods yielded plastic bodies, which were then extruded into 150-mm long sample rods (cylindrical cross-section) having a diameter of 13 mm. All samples were fired to 1260°C with a 3-hour dwell.

6.3.1 X-Ray Residual Filler Strain Measurement

X-ray diffraction techniques can be used to measure the residual strain within filler grains along specific crystallographic orientations.^{4,53,58,128} This was accomplished by taking the location of the (112) peak for quartz in each of the Silica A samples, and comparing it to the equilibrium location for that same peak in unstressed quartz powder. The same procedure was carried out on Alumina A, Mullite A, and Spinel A samples, only instead using their precursor powders and (116), (121) and (400) peaks, respectively. Figure 56 shows a typical X-ray scan of spinel powder, with the (400) peak identified. These peaks were selected for their relatively high intensity, and the lack of other phase peaks interfering with them, allowing for easy observation of minute changes in peak location, as required by the technique. To provide in-situ calibration and ensure the accuracy of peak positions, standard reference material 640c (silicon powder) was lightly brushed onto each sample, forming a very thin layer on the surface. A scan of an X-ray peak characteristic to the filler material present was taken, ensuring the peak was not interfered with by any other phase and not subject to orientation effects. The peak selected was unique for each filler material. Three peaks of silicon were also scanned, namely 28.442°, 47.302°, and 56.122° two-theta. From each scan, the position of the filler peak was determined using the

software program Jade (Version 3.1, Materials Data, Inc.). The silicon peak locations were input into the program to automatically calibrate each diffraction pattern to adjust for minute peak shifts caused by sample position, which could be otherwise falsely attributed to residual strain.

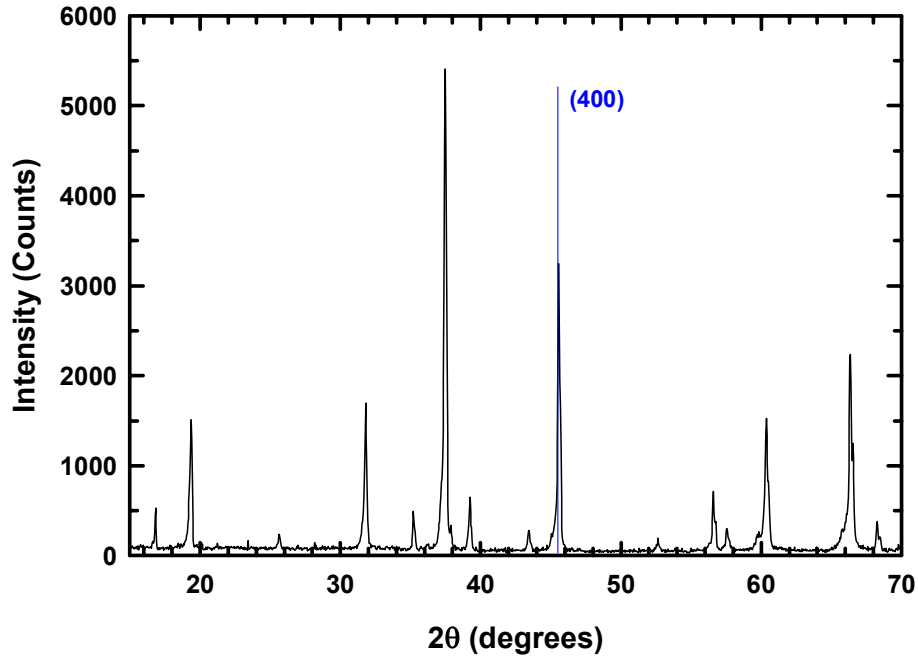


Figure 56. Equilibrium X-ray diffraction pattern of spinel powder.

The d-spacing (d) of this peak was calculated via the Bragg's law equation:

$$\lambda = 2d\sin\theta \quad (63)$$

where λ is the wavelength of the excited x-rays. In this case $\text{CuK}\alpha$ radiation was used, where $\lambda = 1.541 \text{ \AA}$. The d-spacing was compared to the d-spacing of a reference (a pure unstressed powder), which was made by scanning the same peak of a sample of unfired filler material, which was assumed to contain no stresses. The difference between these d-spacings is related to the residual strain within the filler grains through a simple equation (Equation 63):

$$\varepsilon = \frac{d - d_0}{d_0} \quad (64)$$

where d is the (hkl) d-spacing of the sample, and d_0 is the (hkl) d-spacing of the reference material. An issue that arises when this method is used in the interpretation of strain measured in this way is that of the depth of penetration of the X-rays into the sample. More specifically, is the volume of material analyzed representative of the bulk of the material? From previous calculations of interaction volume of the x-ray instrument, results showed that the sampling volume is 14.09 mm^3 , having calculated a penetration depth of 0.095 mm ($95 \text{ }\mu\text{m}$) for $\text{CuK}\alpha$ X-rays and porcelain.⁴ These results indicate that the X-ray diffractometer is sampling particles from within the bulk of the material, not just the surface layer. The number of quartz particles contained within this volume for each porcelain sample were estimated using the following equation:

$$\# \text{ of particles} = \left(\frac{\text{Interaction Volume}}{V_{\text{sphere}}} \right) \times \text{Volume Fraction Particles} \quad (65)$$

where the interaction volume is a constant (14.09 mm^3) as is the volume fraction of particles (0.13), since quartz dissolution is constant. The results are shown in Table XXIII.

Table XXIII. Number of Quartz Particles Contained Within the X-ray Diffraction Interaction Volume as a Function of Particle Size.⁴

Particle Radius (μm)	Particle Volume (mm^3)	Particles / Volume (#)
5.0	5.2×10^{-7}	2.5×10^6
6.0	9.1×10^{-7}	1.4×10^6
7.0	1.4×10^{-6}	9.1×10^5
8.0	2.1×10^{-6}	6.1×10^5
9.0	3.1×10^{-6}	4.3×10^5
10.0	4.2×10^{-6}	3.1×10^5
11.5	6.4×10^{-6}	2.0×10^5
13.0	9.2×10^{-6}	1.4×10^5
18.0	2.4×10^{-5}	5.3×10^4
30.5	1.2×10^{-4}	1.1×10^4
43.5	3.5×10^{-4}	3.8×10^3
73.5	1.7×10^{-3}	7.8×10^2

This calculation is evidence this technique is effective at measuring a strain representative of the entire sample, not just isolated grains. Also, it eliminates the possibility that the diffractometer is only looking at surface quartz particles.

6.3.2 Mechanical Testing

Fired rod samples were used to measure their strength and elastic moduli. In order to observe the effect of filler type on strength, the standard procedure for four-point flexure testing (Section 3.2.2) was utilized to measure the MOR for all of the Porcelain A compositions. For all different filler materials used, there were several different sample types, each containing a different mean particle size of filler. These were all tested to observe the effect of filler size on strength. The support span was set at 90 mm, and the loading span was 45 mm. Samples were all tested to failure using a loading rate of 0.5 mm/min. Elastic modulus of each of the sample types was also measured, using the procedure outlined in Section 3.2.3.

6.4 Experimental Results

6.4.1 Residual Filler Strain

Figure 57 shows a comprehensive plot of residual strain versus filler particle size for all four Porcelain A compositions. To clarify the 'y' axis on the plot, a positive value for % strain is indicative of a filler grain which experiences radial tension, where the crystal planes are pulled in opposite directions, or strained in the 'positive' direction. Conversely, a negative value for % strain indicates there is a 'negative' strain, where the particle experiences radial compression, which causes a compaction of crystal planes. For Silica A compositions, between samples containing 10 and 25- μm quartz grains, there is a minimal increase in residual strain. Above 25 μm , filler strain increases rapidly, peaking at 87 μm , afterward showing a rapid decrease as particle size increases further. For Silica A, 87 μm is the critical filler size above which residual strain is sufficient to cause spontaneous failure on cooling. As a result, strain values decrease. With increasing particle size beyond this critical value, more filler grains crack, resulting in a declining trend in the plot.

Alumina grains show the same characteristic behavior as quartz grains; however, the onset of significant residual strain does not occur until alumina grains are >90 μm, and the corresponding critical filler size for alumina is 180 μm. This is attributed to the fact that alumina is stronger than quartz and also has a much higher elastic modulus than quartz (90 GPa vs. 390 GPa); therefore, bonds are stiffer and will not break until the residual stress is higher.

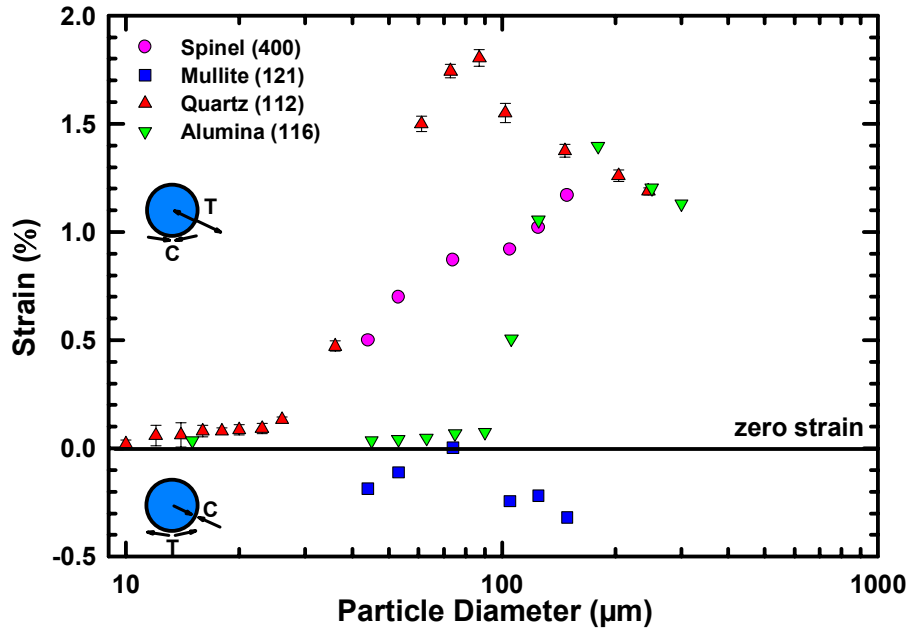


Figure 57. Plot of residual strain versus filler particle size for all Porcelain A compositions.

The maximum amount of strain in the alumina particles is less than that of the quartz particles, but stress and strain are related through the equation:

$$\sigma = E\varepsilon \tag{66}$$

The much higher elastic modulus of alumina results in a much higher stress in alumina grains at a lower strain than in quartz. This is illustrated in Figure 58. Also shown in Figure 57, spinel grains display an increase in residual strain with increasing grain size, much like quartz was observed to do.

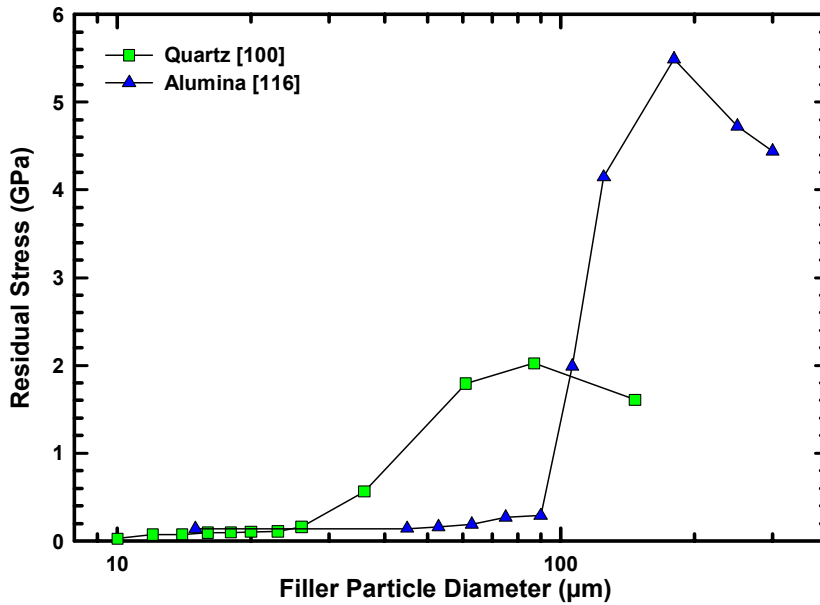


Figure 58. Residual stress versus filler particle size for alumina and silica porcelain bodies.⁴

This type of strain is similar to that found in Silica A and Alumina A bodies, in that the forces are radially tensile and tangentially compressive. This is confirmed by the fact that the d-spacing of the spinel (400) X-ray peak increases with increasing particle size, indicating that the strain increases in the positive direction. Unlike quartz, however, there appears to be no lower or upper inflection points, which would indicate the onset of substantial strain and the size that produces onset of spontaneous filler cracking and strain relaxation, respectively. This suggests that within the size range tested there is insufficient strain to cause spontaneous cracking in the spinel grains. Mullite grains show a trend with respect to particle size and strain that is unclear. This may be due to the presence of additional mullite that forms in the glass phase during firing. The XRD test cannot precisely distinguish between this mullite and the included mullite grains, and so the trend, if any, is obscured. The significance of this is that since nucleated mullite needles have never been shown to crack due to thermal stresses due to strong interfacial bonding with the glass phase,²⁴ their contribution to the total strain confounds the value of strain present between the included mullite particles and the glass, resulting in an inaccurate measure of the total effective strain. The same could be said about quartz grains, since free quartz is introduced into

the system through raw material impurities, but the CTE mismatch between quartz and the glass phase is sufficiently high and concentration is low enough that the effect of any strains caused by free quartz are inconsequential. These porcelain bodies have had quantitative measurements of up to 17% primary and secondary mullite present upon cooling, which is significant.⁴ What is clear from these results is that the strain in mullite is generated in a different manner as in spinel, alumina or quartz. Mullite has a CTE of $5.1 \times 10^{-6} \text{ K}^{-1}$, which is lower than that measured for the glass phase, causing the forces to be opposite; radially compressive and tangentially tensile. This is evident due to the fact that the resulting strain was calculated as negative, indicating a decreased d-spacing of the mullite grains (in all cases) relative to its equilibrium condition.

One possibility that was explored was the idea that there could be two distinct peaks or a (121) peak split due to the two different types of mullite (and different strain levels) present. Since the mullite particles that crystallize out of the melt are on the order of a few microns in size versus the added mullite filler grains which are at least an order of magnitude larger, it was hypothesized that the X-ray pattern may reveal this split via the visual appearance of the (121) peak. Shown in Figure 62 are the mullite peaks for samples containing two representative particle sizes (45 μm and 105 μm). As shown, the peak location is nearly identical, yet between the samples the filler particle size doubles. The reason for this is unknown, though a recent study suggests that the CTE of the glass phase may be much more similar to that of mullite; therefore, the amount of residual strain that would occur in these bodies would be minimal, and not change dramatically over a broad range of included particle sizes, as data in Figure 59 suggest. There is no peak splitting visible in these patterns, nor were there any evident in any other specimens containing mullite. Therefore, X-ray information could not be used to distinguish between the nucleated and filler fraction of mullite within the sample.

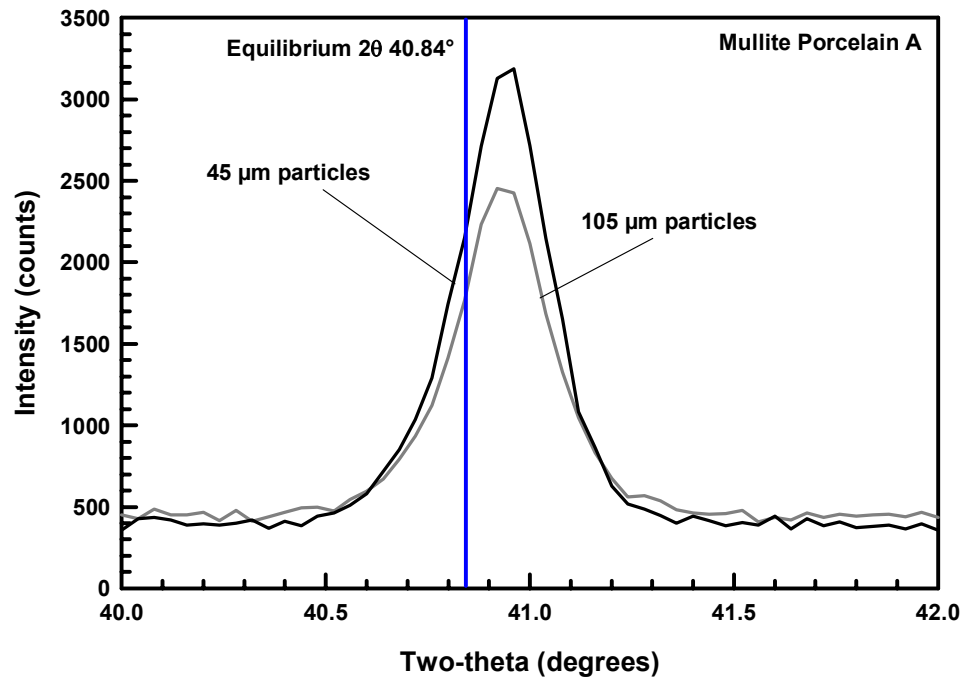


Figure 59. XRD pattern showing the (121) mullite peak in Mullite A porcelain composition for specimens containing 45- μm and 105- μm mullite particles.

6.4.2 Mechanical Properties

Figure 60 shows four-point flexure strength results for all four Porcelain A compositions (solid shapes) overlaid on the residual strain results from Figure 57 (hollow shapes). For Silica A porcelain the relationship between filler size, strength, and residual strain is clear. At low quartz sizes the strength is high and residual strain is low. There is actually a small increase in strength from 10 – 25 μm . With the onset of substantial residual quartz strain (>25 μm), strength begins to decrease rapidly and continues to decrease as quartz size increases to 150 μm . The reason for this characteristic behavior is because strain is additive. There is a set limit to how much residual strain a microstructure can sustain before cracking occurs within the filler grains and the body weakens. Although below 87 μm no spontaneous cracking of quartz occurs, there is some amount of pre-existing residual strain in the system prior to the onset of the flexure test. The test itself introduces additional strain to the system until the strain limit is exceeded and the body fails. The more residual strain that is present in the porcelain prior to testing, the less induced strain it can sustain before failing. As a result, the measured strength goes down with increasing residual

strain, because the maximum load necessary to induce the net strain required to cause fracture also decreases.

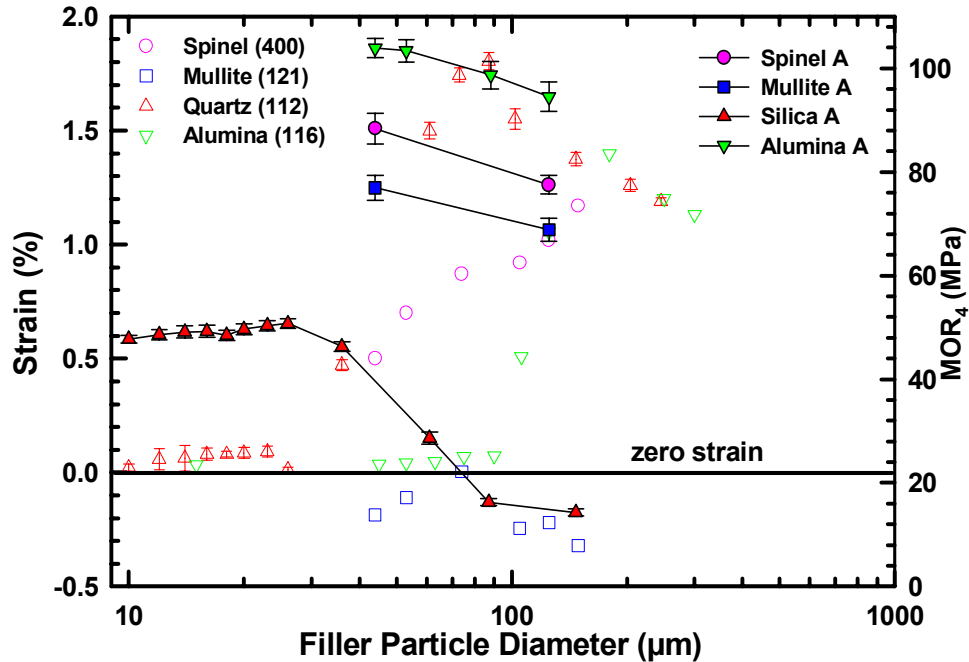


Figure 60. Comprehensive plot of MOR and residual strain versus filler particle size for all Porcelain A body compositions.

This relationship is observed to a lesser extent in the Alumina A, Mullite A, and Spinel results. The first two data points for Alumina A (44 µm and 53 µm) have virtually the same mechanical strength. The remaining two data points (88 µm and 125 µm) have lower strengths than the first two, and show an overall decrease in strength with increasing particle size. These last two points coincide with the lower inflection point on the residual-strain curve. According to the hypothesis, strength should decrease above this size. From these four data points it is proposed that for alumina particles smaller than the lower inflection point, strength shows a relative plateau (as indicated by the first two points with identical strength); but above this point, strength begins to decrease (the second two points showing a decrease in strength with increasing particle size). Were a broader range of particle sizes (vs. MOR) investigated, a more defined trend would be evident; however, for purposes of this experiment, a similar inflection point is arguably present in the Silica A strength curve as well as, to a lesser extent, in the Alumina A body. In the case of

Mullite A and Spinel A porcelains, only two different filler particle sizes were used to create samples for strength testing (44 μm and 125 μm). Since no inflection points were observed in either of the residual-strain-versus-filler-size plots, none were expected to occur on a MOR-versus-filler-size plot in that same range. The only information that can truly be obtained is that mechanical strength is lower in the samples containing larger mullite and spinel grains.

6.5 Derived Results

6.5.1 Critical Flaw Size

By utilizing the relationship established between elastic modulus and fracture surface energy (Section 4.5), critical flaw size was calculated for all Porcelain A compositions to see if there is any relationship to filler type and/or grain size. The results can be seen in Figure 61. As shown in the figure, all flaw sizes appear to be between approximately 90–120 μm , while the filler particle sizes span from 10–147 μm . This indicates that, over the entire range of filler particle sizes, critical flaw size remains very narrowly distributed, essentially constant for a given composition.

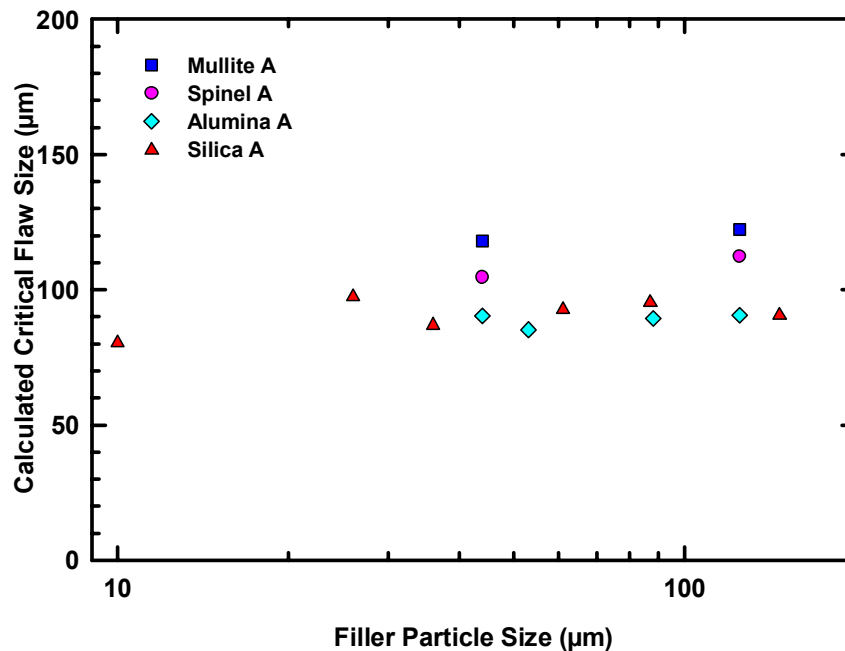


Figure 61. Plot of critical flaw size versus filler particle size for all Porcelain B body compositions.

Overall, Porcelain A compositions showed an average critical flaw size of $97 \pm 13 \mu\text{m}$, which is reasonable, but the standard deviation is rather high. When each composition is examined individually, however, the mean values of critical flaw size are slightly different for each composition, but individual standard deviations are small. Silica A showed an average flaw size of $91 \pm 6 \mu\text{m}$, Alumina A showed an average flaw size of $89 \pm 2 \mu\text{m}$, and Spinel A and Mullite A showed average flaw sizes of $108 \pm 4 \mu\text{m}$ and $120 \pm 3 \mu\text{m}$, respectively.

Some previous investigations on glass-particle systems (Section 1.2.4), resulted in the estimates of critical flaw size on the order of one to three times that of the primary inclusion size.^{12,21} While a majority of calculated critical flaw sizes for porcelain bodies seems to fit the criteria established prior by Lange²¹ and Borom,¹² closer evaluation reveals that, in fact, it does not. Previous theories are predicated on the assumption that the included particles generate hoop tensile stresses some distance into the glass phase, resulting in cracks. As outlined in Section 1.4.2, the relative CTE mismatch between porcelain glass and filler particles does not allow this to occur. The porcelain glass phase experiences compression, not tension. The glass used in Borom and Lange's experiments must have had a CTE greater than that of the particles in order to observe these phenomena. Furthermore, evaluations of alumina porcelain B with temperature (Section 5.5.2) result in the measurement of 60–70- μm critical flaw sizes when the primary particle size used is on the order of 5 μm , a factor of 12 to 14 times larger than primary particle size. Similarly, Silica A porcelain containing 10- μm quartz grains contains a measured critical flaw size of 80 μm , a factor of 8.

6.5.2 *Favorable Glass Prestresses*

Overall results of this study indicate that residual stresses develop between the glass phase and the filler grains of a porcelain body as a function of filler type and particle size. This is evident by the measurement of lattice strain versus filler particle size. Although it would appear that residual stresses are purely detrimental to the strength of the body, i.e., at the onset of substantial residual strain (stress), strength decreases rapidly. However, for Silica A compositions, it was observed

that in the size range of 10–25 μm , the strength was observed to increase from 48 to 51 MPa. Figure 62 illustrates this phenomenon. It is proposed that this beneficial effect is due to small amounts of residual stress present in the microstructure. For Porcelain A compositions, although the mean filler size is increased, the overall concentration of filler remains constant.

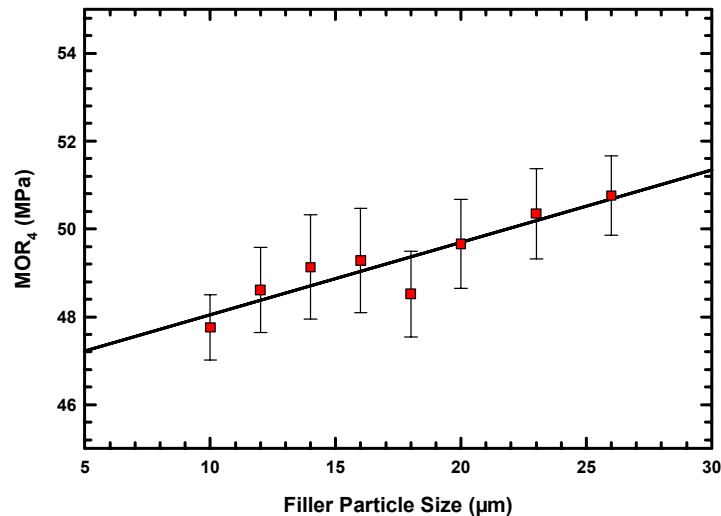


Figure 62. Plot of MOR versus filler particle size for Silica A composition showing increase in strength for bodies with grain sizes between 10 – 25 μm .

With this in mind, a sample containing 100- μm particles contains fewer particles than a sample with 10- μm particles, since the total volume of particles is the same. Thus separation distance between particles decreases with particle size (assuming particles are uniformly distributed). Surrounding each filler grain is a stress field that develops upon cooling due to the CTE mismatch. For quartz and most other fillers with a higher CTE than the glass phase, these stresses are tangentially compressive. That is, the surrounding glass phase is placed in compression. For particles in the 10–25- μm regime, particles do not spontaneously fail upon cooling; therefore, their stress fields remain intact. This compressive stress aids in strengthening the glass and the overall material. In addition, since the amount of residual stress increases with particle size, so does the ‘effective’ diameter of the corresponding stress field. In this size regime filler particles are numerous enough that the separation distance is small, and the compressive stress fields surrounding the grains are sufficiently large and close enough to one another so they

overlap, resulting in zones of increased compression that contributes to a strengthening effect. Figure 63 shows a schematic of these overlapping stress fields.

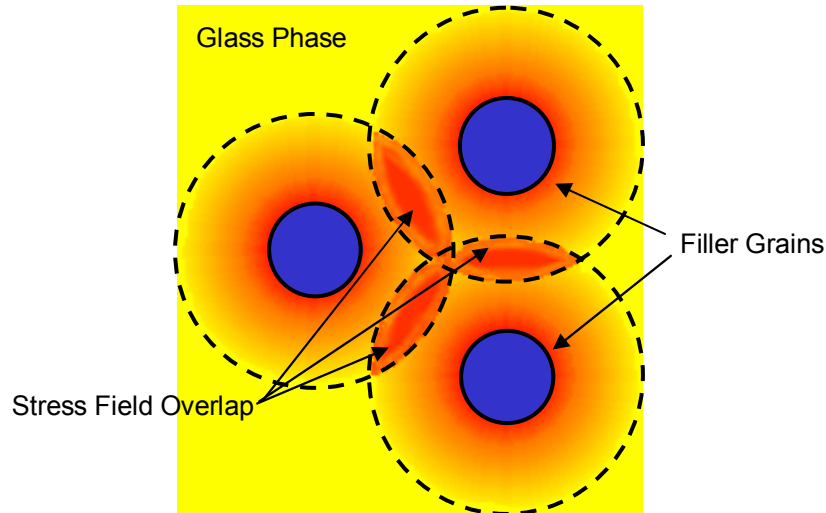


Figure 63. Schematic of in-situ filler grains with residual compressive stress field overlap in the glass phase.

In this figure, the darker areas correspond to regions of higher compression, which decays with distance away from the particle surface. However, the effect is compounded in the zones where multiple stress fields overlap. This is referred to as favorable prestressing; the addition of nominal amounts of compressive stress to the microstructure causes an increase in strength. For Silica A bodies containing 25- μm quartz, this effect is maximized, corresponding to the maximum observed strength. Below this size, the effect is present but to a lesser extent, since particles are smaller and have smaller effective stress fields surrounding them. Above this size, stress fields may overlap, causing increased compression; however, the amount of total strain in the system is such that the deleterious effects of residual strain supercede the beneficial effects of the prestressed system. The prestress may aid in strengthening the material, but the overall contribution of the significant residual strain results in a net decrease in strength. It is believed that there is a threshold particle size that will maximize this prestressing effect while minimizing the negative effect of residual strain (for Silica A it is believed to be 25 μm), resulting in higher strength.

6.6 Summary

This investigation showed that for a given filler particle type and size, the distribution and magnitude of residual strain varies. If the CTE of the grain is greater than the CTE of the surrounding glass, radially tensile and tangentially compressive stresses occur. If the CTE of the grain is less, the stresses developed are radial compression and tangential tension. It is the former situation that is ideal, since the glass is placed in compression, reducing the tendency of a flaw to form or propagate through it. The converse situation results in tensile stresses that cause cracks to more easily develop or extend through the glass phase under induced stress. Therefore, selection of filler materials with a CTE greater than that of the glass phase is recommended.

Filler particle size and type also appear to show a characteristic relationship to mechanical strength, inasmuch as it is proposed there is a threshold grain size unique to each filler material, above which strength deteriorates rapidly. As particle diameter increases, nominal amounts of residual stress arise within the microstructure upon cooling, insufficient to cause the filler grains to spontaneously fail, and instead strengthen the material by means of a favorable pre-stressing mechanism. This effect has been actively observed in quartz porcelains (critical size 25 μm), and is believed to exist in all systems containing high CTE filler particles in a lower CTE glass phase. As particle size continues to increase, the prestressing effect is negated by the more substantial detrimental strain that develops in the system. Since the strain limit of a material is fixed, increasing amounts of residual strain requires increasingly less induced strain to fail the material. Therefore, strength decreases. As particle size increases even further, residual strain exceeds the strain limit of the filler even in the presence of no applied load. As a result, the filler grains (in tension) fail spontaneously, resulting in large flaws within the microstructure. Industrial compositions typically use filler grains in the size range of 25–45 μm ; therefore, spontaneous particle failure (which occurs above 87 μm in Silica A and 180 μm in Alumina A) is not often observed.

Critical flaw size does not appear to correlate to filler particle size or type, maintaining a reasonably constant value for each Porcelain A composition over the entire size range tested. Overall, the critical flaw size was on the order of 90–120 μm , while filler particle sizes ranged from 10–150 μm . Individually, each composition maintained a critical flaw size that was essentially constant, with standard deviations on the order of $\pm 4 \mu\text{m}$ or less. This is contrary to the notion that primary filler particles are the critical flaws in porcelain bodies. In fact, critical flaw size shows no correlation to primary filler particle size at all. Therefore, it is proposed that primary filler particles, although they can influence strength under extenuating circumstances, are not the critical flaws, nor are they the strength-defining component within typical commercial porcelain bodies. Instead it is proposed that the critical flaws are the result of agglomerates of these filler particles, the effect of poor processing, creating large interstitial voids within the material that act as the critical flaws.

7. Critical Flaws and Strength

7.1 Overview

The fracture origin of any failed ceramic specimen is a critical flaw. This is because under an increasing applied stress, flaws within the body act as stress concentrators. Typically, the largest flaw in the system is the highest stress concentrator, therefore it is the one most apt to propagate and cause failure. To generalize, these critical flaws are what ultimately control the strength of any ceramic material. There are many existing theories in the literature that seek to attribute the generation of these critical flaws in porcelains to, among other things, bulk density, firing temperature and filler materials. However, this investigation has shown otherwise. Results indicate that the critical flaw size in bodies evaluated does not strictly correlate to any of these parameters, which means that it must be a function of some other factor. Based on the data collected, it is believed that critical flaws are not governed by firing temperature or primary filler grain size, but instead are a result of a more intrinsic phenomenon that has to do with the fundamental processing of the material.

7.2 Independence of Filler Size to Measurable Properties

Figure 67 shows a comprehensive plot of all compositions and their calculated critical flaw sizes, tested against filler particle size, filler type (Porcelain A), and firing temperature (Porcelain B). For each body composition the critical flaw size remains essentially constant. The numerical results are tabulated in Table XXIV. The fact that there is a relatively narrow range of critical flaw sizes common to all the different filler types demonstrates that critical flaw size is independent of filler type. Furthermore, for filler grains to be dictating strength, it would be expected that the critical filler size for compositions with the same fillers would be identical. Figure 64 shows that for Alumina A and Alumina B compositions, although the mean critical flaw sizes are very similar the scatter among each individual data set is low enough that each composition has its own distinct mean critical flaw size. Another observation made is that critical flaw size exceeds primary filler particle size, eliminating the possibility that a single cracked filler particle is the

critical flaw. Figure 65 shows a magnified view of one of the Silica B microstructures, fired at 1280°C, which had a calculated critical flaw size of 83 μm .

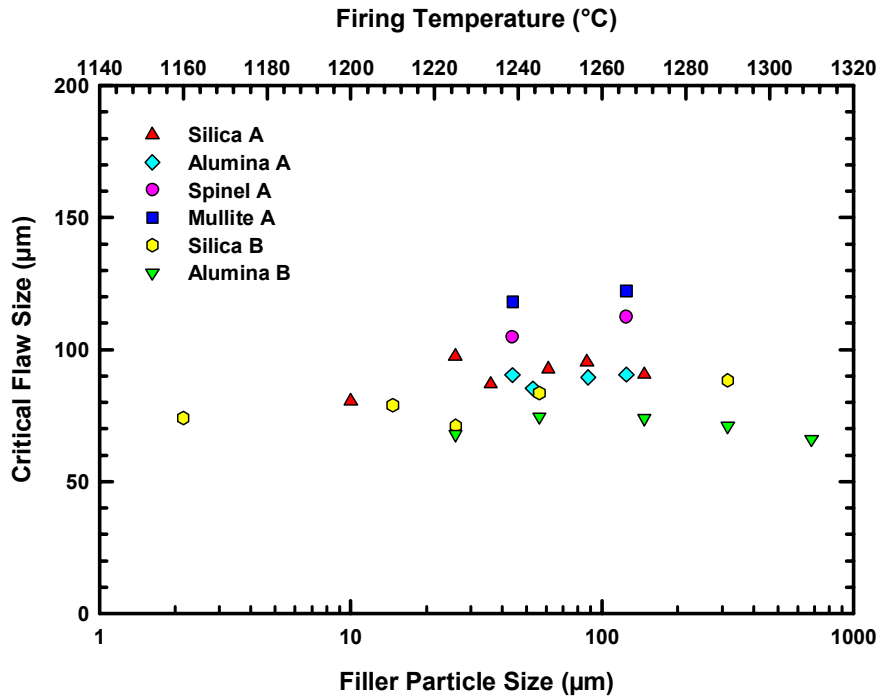


Figure 64. Comprehensive plot of critical flaw size versus filler particle size (Porcelain A) and firing temperature (Porcelain B).

Table XXIV. Critical Flaw Size for All Experimental Porcelain Compositions.

Composition	Avg. Critical Flaw Size (μm)	Std. Dev. (μm)
Silica A	90.6	6.1
Alumina A	88.9	2.5
Mullite A	120.1	2.9
Spinel A	108.5	5.4
Silica B	79.1	7.0
Alumina B	70.7	3.7

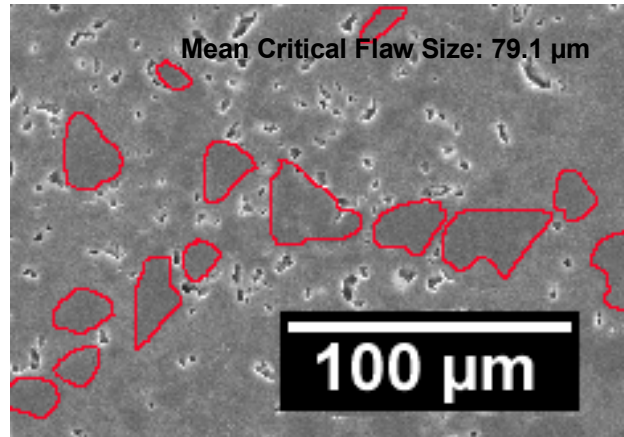


Figure 65. Secondary electron SEM image of Silica B microstructure, with residual quartz grains highlighted for ease of viewing.

As shown, residual filler grains (highlighted for ease of viewing), on average are 15–30 μm in diameter, a factor of three to five times smaller than the critical flaw size. These sizes correspond to those typically used in industrial processing of siliceous porcelains, since Silica B composition is, in fact, a product of an industrial process (Section 2.1.2). This was the case for all compositions in which the microstructure was imaged, over the entire range of firing temperatures investigated. Based on these results and observations, evidence points to some other factor in control of critical flaw size.

7.3 Constant-Flaw-Size Hypothesis

Two of the more prevalent explanations in literature as to why a porcelain body displays a distribution of strengths are: 1) There is a continuous flaw size distribution within the material, and 2) there are several different types of flaws within the material. As these experimental results indicate, there is a very narrow critical flaw size range calculated for a given porcelain body composition. The independence of flaw size and most conventional factors (density, temperature, filler size, etc.) for these bodies proves that the underlying factor that dictates the critical flaw size is not one of these variables. The flaw-size similarity of bodies processed the same way cannot be ignored. While the existence of the aforementioned strength-affecting factors under ideal conditions is not in question, it is hypothesized that it is also possible for there

to be large uniformly-sized critical flaws within the microstructure of these porcelain bodies, a function of processing efficiency, and that a distribution of mechanical strengths is not proof of the existence of a continuous flaw size distribution. Microstructural analysis reveals more than one type of flaw (e.g., porosity, microcracks) within the body. Based on calculations of critical flaw size, it is believed that within these compositions there also exists a discrete population of very large flaws, orders of magnitude larger than porosity or microcracks, which ultimately control the strength. The fact that they are so much larger than other typical intrinsic flaws found in ideally processed porcelains virtually negates the effect of porosity or any other small flaw on strength. To test this hypothesis, a series of simulated flexure tests were devised using mathematical modeling and random numbers, to duplicate the effect of having mono-sized critical flaws within a ceramic microstructure under a four-point bending load.

7.4 Flexure Test Simulation

7.4.1 Analysis of Testing Methods

In a tensile test, the entire interaction volume is in pure tension, with no bending moment. Therefore, each volume element of the specimen experiences exactly the same stress while under a constant tensile load. In a flexure test, however, there is a stress profile created by the bending moment that varies with location. During three or four-point loading, one surface of the specimen is in tension while the other is in compression. Within the interior of the sample there is a gradient of stresses, which varies with relative distance from the surface to the neutral axis. At the neutral axis tensile and compressive force components are equal and opposite, negating one another to a state of net zero stress. A tensile specimen fails at the location of the largest flaw, independent of its position within the specimen. This is because the stress profile is constant throughout the entire volume; therefore, the largest flaw acts as the critical flaw; i.e., the flaw with the highest stress concentration causes failure, though this is subject to orientation effects depending on flaw geometry. In a flexure test, this is not necessarily the case. Since a flexure test specimen always fails in tension, the compressive region above the neutral axis does not contribute to the overall flexure strength of the material. Under a constant load, stress is highest

at the tensile surface of the specimen, decreasing to zero approaching the neutral axis, making the value of stress at a given location position-sensitive. With this in mind, the fundamental criteria for failure of a specimen in bending are still the same as they are in tension. That is, when the stress level exceeds the energy required to propagate a flaw of a specific size, failure occurs. Typically larger flaws require less energy to propagate; therefore, assuming constant flaw geometry (negligible orientation effects), under a constant increasing stress the largest flaw in a system will fail first. Due to the stress gradient in a flexure specimen, however, the largest flaw present in the specimen may not always be the critical flaw.

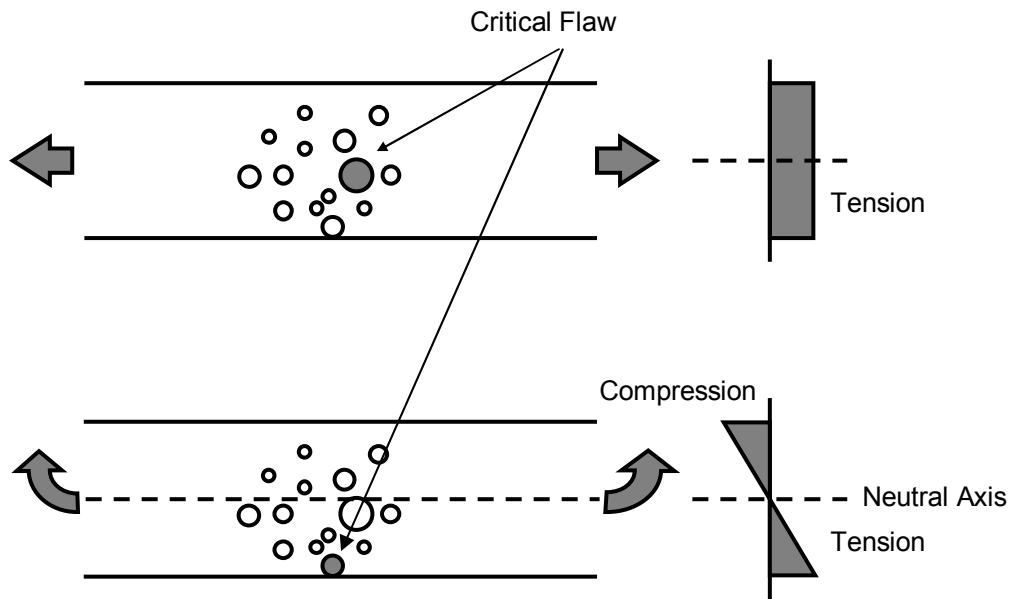


Figure 66. Schematic showing a) pure tensile forces acting on a tensile specimen versus b) bending forces acting on a flexure specimen.

If a large flaw exists near the neutral axis and a smaller flaw exists at the tensile surface of the specimen, at a given loading condition, the stress on the large flaw may be too small to propagate it, yet the stress on the smaller flaw may be sufficient to cause it to grow. Therefore, failure originates at the smaller defect, which acts as the critical flaw, even though a larger flaw is present. If a system were to have but one critical flaw size or a very narrow size distribution, the location of these flaws within the sample would be critical to the performance of specimens in a

flexure test. In terms of the porcelain bodies studied, it is proposed that, although there could be a distribution of small flaws, experimental results indicate that there is a limited population of very large flaws of similar size (much larger and more prevalent than any created by pores or errant microcracks) that act as the critical flaws, rendering the smaller, more common flaws completely ineffectual. This phenomenon would result in one large *effective* critical flaw size, thereby satisfying the aforementioned hypothesis.

In a tensile test, location of flaws is irrelevant since the entire volume is under the same stress at all times. For example, if a 100- μm critical flaw propagates at 70 MPa, when the applied load results in a tensile stress of 70 MPa a specimen will always fail at 70 MPa, provided there is at least one 100- μm flaw in the system (constant flaw geometry and orientation), independent of location. Therefore, if a series of samples were tested the mean strength would always be 70 MPa with a small standard deviation. If instead the same specimen was tested in four-point flexure, the strength becomes a function of probability. If an applied load resulted in a stress level of 70 MPa at the tensile surface of the sample and a flaw was located there, then the sample would fail at 70 MPa. However, as distance from the surface increases, stress decreases. Therefore, if the flaw is located a distance x away from the tensile surface, then the stress experienced at the flaw when the surface is at 70 MPa is not enough to cause failure. Only until the load is increased so that the stress experienced at the distance x from the surface is 70 MPa will the sample fail. This results in different loads required to fail both samples, which, through the MOR equation, results in two different strength values but only one flaw size. For a four-point flexure specimen (rectangular cross-section) under a constant applied load, the bending moment is constant within the inner span of the testing apparatus, as shown in Figure 67. As a result, at a specific load the amount of stress acting on a specific location is a function of its distance to the neutral axis in the z -direction only. Changing location in the (x,y) plane does not alter the stress state, provided it is confined within the inner span of the testing specimen.

7.4.2 Theoretical Model Parameters

A theoretical model of the interaction volume during a four-point flexure test was created using a mathematical model. A 1-cm³ cube divided equally into smaller 100-μm³ cubes results in a region containing 1.0 x 10⁶ unique domains.

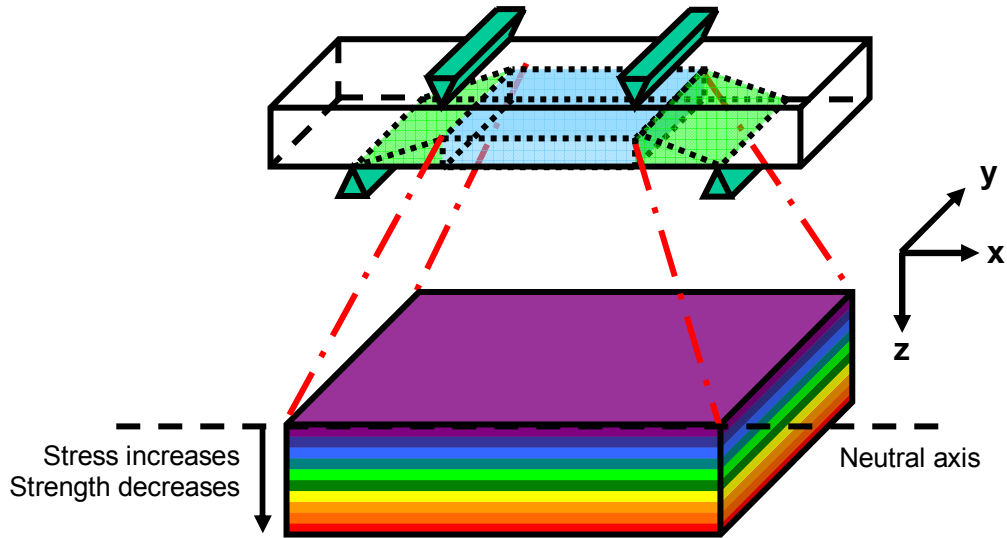


Figure 67. Schematic of four-point flexure apparatus with exploded view of stress- strength profile as a function of the inner span volume below the neutral axis.

Figure 68 shows an up-scaled example of this process using a more simplistic 10 x 10 x 10 cube divided into 1000 smaller cubes. Much smaller subdivisions were chosen for the actual model based on the result of the critical-flaw-size calculations which yielded an average flaw size of ~80 μm. This scale would allow for only one flaw to occupy one domain at a time. Using a random number generator via a computer program, several series of non-repeating random number sets were generated to simulate the randomness associated with the (x,y,z) location of critical flaws within a specific volume of a specimen to mimic the random probability of a flaw occurring in a critical location.

A typical computer program creates random numbers by generating a sequence of integers by the following recurrence:

$$x_{n+1} = P_1 x_n + P_2 \pmod{N} \quad (67)$$

where P_1 and P_2 are constants. The term x_0 is the seed number, and $n = 0, 1, 2, \dots$ etc. The notation $\text{mod } N$ means that the expression on the right of the equation is divided by N (the maximum number desired) and then is replaced with the remainder.

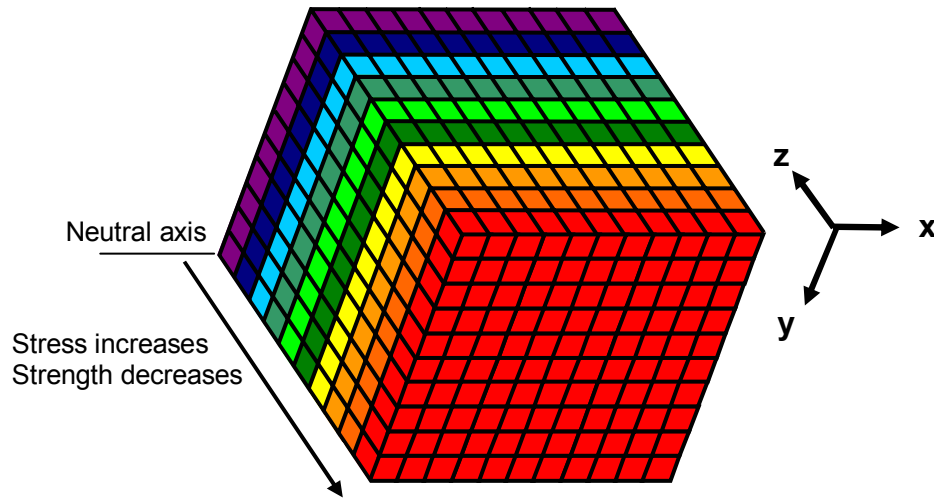


Figure 68. Schematic of 10 x 10 x 10 cube subdivided into 1000 unique domains, each 'layer' in the z direction corresponding to a different stress state.

The parameters P_1 , P_2 , and N determine the characteristics of the random number generator, and the choice of x_0 (the seed) determines the particular sequence of random numbers that is generated. If the program is run a second time with the same values of the parameters, and the same seed, it will generate a sequence identical to the previous one. In this case the numbers generated are not truly random. They are therefore sometimes referred to as pseudo-random numbers.¹²⁹ In the case of this experiment, a genuinely random series of numbers was required to truly simulate the randomness of flaws occurring in a microstructure; therefore, a more complex technique of random number generation was employed. A program designed by Haahr,¹³⁰ accessible via the Internet, generates truly random numbers. A radio is tuned into a frequency outside the commercial broadcast range. The atmospheric noise picked up by the receiver is fed into a computer where it is sampled by a program as an eight bit mono signal at a frequency of 8 KHz. The upper seven bits of each sample are discarded immediately and the remaining bits are gathered and turned into a stream of bits with a high content of entropy. Skew correction is performed on the bit stream, to ensure that there is an approximately even

distribution of 0s and 1s. Bits are read two at a time, and if there is a transition between values (the bits are 01 or 10) one of them is passed on as random. If there is no transition (the bits are 00 or 11), the bits are discarded and the next two are read. The software then converts the random binary code into base 10 digits. Constraints can be applied to the output of this random number generator, such that the upper and lower limits can be defined (all numbers generated outside this bound are discarded), and also duplicate numbers can be allowed or disallowed, as the experiment requires.

7.4.3 Experimental Procedure

For this simulation, each domain within the volume was assigned an integer value from 1 to 1×10^6 . The volume was divided into 100 equal planes, each plane one domain thick with an area of 100 x 100 domains. Each plane was assigned an ascending z value from 0 to 100, such that the plane z=0 represents the tensile surface of a rectangular bar, and z=100 represents the plane at the neutral axis of the bar. As well, each plane was assigned a specific stress value ranging from 60 MPa (z=0) to 78 MPa (z=100). This range of stress was arbitrarily chosen; it was selected because it is representative of the typical range of strengths that are measured in many porcelain flexure tests. Each domain within a plane was then numbered sequentially, granting a unique identity to each domain, in a way so that any location could be pinpointed simply by knowing a domain's assigned number (plane z=100 contains domains 1–10000, plane z=99 contains the domains 10001–20000, and so on). Each number generated represents a flaw in a specific location, the amount of these numbers correlating to the amount of total flaws within the volume.

The random number generator program was a web-page form where constraints were manually input into the system before lists of numbers were generated. For this test, the minimum was set to 1 and the maximum set to 1,000,000. Repeated numbers were eliminated from the sets, as the experimental matrix was designed such that only one flaw could occupy one domain; therefore, two of the numbers could not be duplicates. The amount of numbers per list corresponded to the number of flaws being introduced into the virtual volume. For this

experiment, lists containing 10,000, 1,000, 100, 10, and 1 numbers were generated, corresponding to volumes containing 1%, 0.1%, 0.01%, 0.001%, and 0.0001% flaws, respectively. Once these constraints were made, the program was run, and lists of random numbers were created. At each treatment level 20 lists were created in order to simulate 20 flexure test specimens for statistical purposes. Each list was then arranged numerically from highest to lowest, and the highest assigned number (corresponding to the lowest z number) in each list was recorded. The stress level corresponding to the plane with the lowest z number was then recorded as the strength of that sample. A flaw anywhere in this plane experiences the highest stress; and, assuming uniform flaw size, it would fail first; therefore, the flaw in the plane closest to the tensile surface limits the strength.

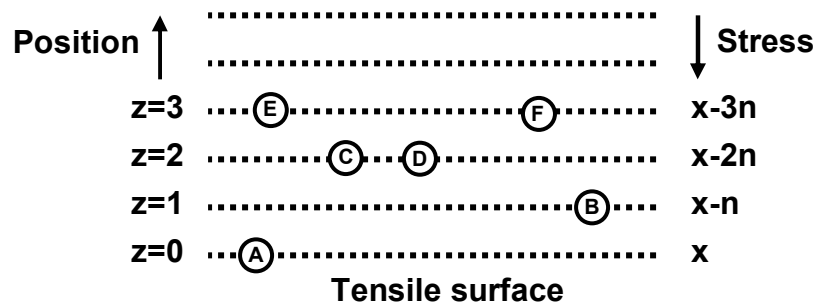


Figure 69. Schematic of side-view of four-point flexure specimen showing specific flaw placement and stress levels.

For each series of 20 samples, the average and standard deviation of simulated strength was recorded, in the same manner as an actual four-point flexure test. Figure 69 shows a simplified example of the aforementioned process. Since the tensile surface of a four-point flexure specimen is under the highest stress, it has been assigned the stress value of x units. Planes located away from the tensile surface will, at a fixed loading condition, experience less stress; therefore, a constant value (multiples of a constant, n) is subtracted from x as the distance from the tensile surface is increased. If model parameters require a flaw to experience a stress of value x before propagating, then a flaw located at position A would cause failure of the specimen at the lowest strength (60 MPa in the case of this model). If flaws occupied all locations (A – E), then the expected strength would still be 60 MPa because of the presence of the flaw at location

A, which experiences the critical stress level. The other flaws would not propagate because they are each experiencing some degree of stress less than the critical amount. If, however, there were no flaws in the plane $z=0$, then the flaw at location B would experience the highest amount of stress. Under the same loading conditions as previously, the highest stress level a flaw experiences is now x/n , a condition insufficient to cause catastrophic failure. Therefore, in order for the specimen to fail, the load must be increased such that the stress increases by n . With this increase, flaw B experiences a stress of x units, it propagates and the specimen breaks, but at a new, higher loading condition, which, through the MOR equation, results in an observed increase in measured mechanical strength.

7.5 Experimental Results

7.5.1 Flexure Test Simulation

Based on the results of the four-point flexure simulations that aim to be representative of a porcelain microstructure with random placement of known amounts of mono-sized flaws, expected strength versus number of flaws was plotted for each test series, as shown in Figure 70. What is shown is that, for a high number of flaws, the expected strength is low due to the increased probability that at least one flaw will be located at the sample surface. In fact, when the volume contained >1000 flaws, the probability of one flaw occurring at the surface was unity. Therefore, the expected strength was a minimum (60 MPa), and the standard deviation was zero. For a system containing 100 flaws, some samples contained no flaws in the zone of highest stress (tensile surface); therefore, the strength increased accordingly, resulting in a small standard deviation. With even fewer flaws, the strength increased more rapidly with increasing standard deviations as the number of flaws became fewer. This is because the probability of at least one flaw occupying a given plane within the entire volume decreases with the number of total flaws present, resulting in a higher mean strength, but a large standard deviation. As such, this substantiates the hypothesis that it is possible for a microstructure to contain one critical flaw size and still result in a distribution of mechanical strength values, because the nature of a flexure test introduces a stress gradient to the specimen; and, therefore, the locations of the critical flaws

are important and a function of probability. The strength of the sample depends on the location of the flaw nearest the tensile surface, which in turn depends on the total amount of flaws present.

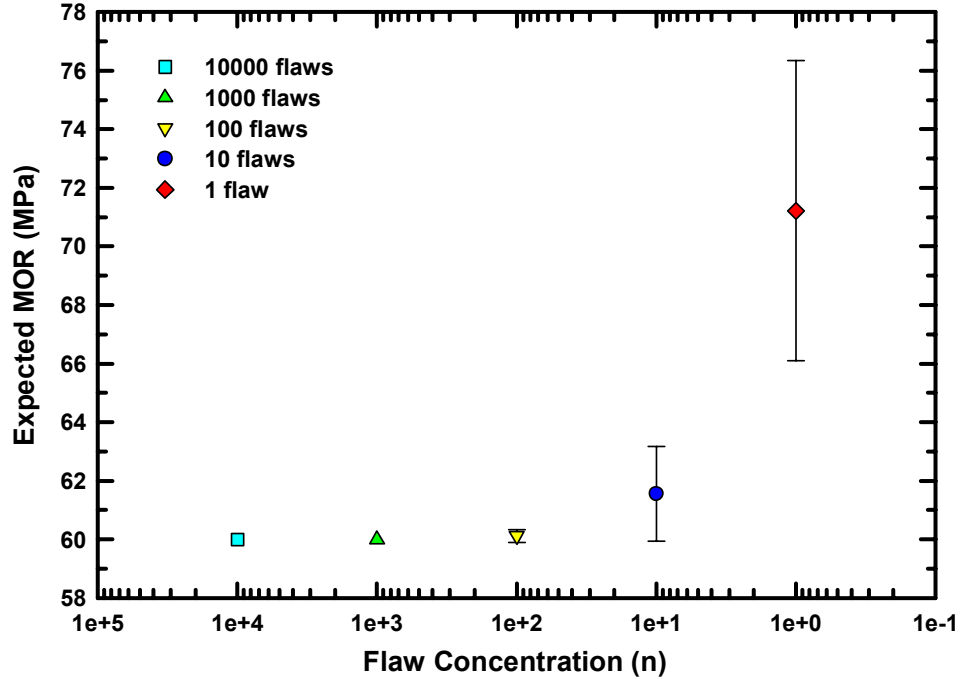


Figure 70. Plot of expected MOR versus number of flaws within a fixed volume during a simulation of a four-point flexure test.

7.5.2 Estimation of Flaw Concentration

Another observation based on the results of the simulation was the evolution of the standard deviation with the decrease in flaw concentration. The transformed value of the standard deviations (square root) was plotted versus flaw concentration, resulting in Figure 71. A logarithmic function was fitted to the data points with an equation of:

$$y = 2.223 - 0.3875 \ln(x) \quad (68)$$

It is proposed that this curve could be used to predict the flaw population within an unknown sample by inputting the square of standard deviation of strength into the equation as 'y,' and the resulting 'x' value would be the approximate number of flaws per cm³. The average four-point flexure standard deviation for rectangular specimens of Silica A porcelain body compositions was

determined to be 0.847 ± 0.18 MPa.⁴ Based on this value, using Figure 71 as a calibration curve there was estimated to be 17 ± 4 flaws per cm^3 . Based on the total interaction volume of the specimen (6.7 cm^3), there would be 114 ± 27 flaws, assuming they are all the same size (on the order of $100 \mu\text{m}$ in diameter). If this volume were divided into 50 planes $100 \mu\text{m}$ thick, in two dimensions there would only be approximately two $100\text{-}\mu\text{m}$ flaws per cm^2 .

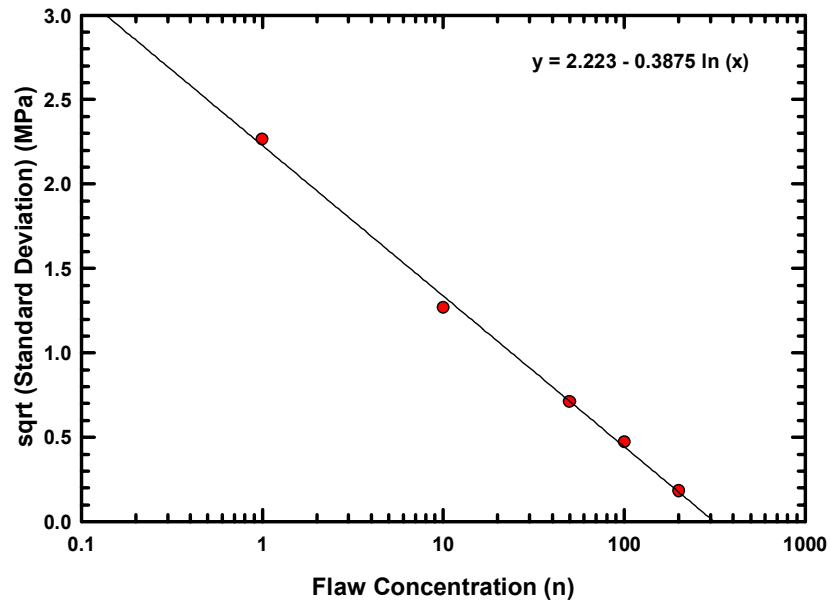


Figure 71. Plot of strength standard deviation versus flaw concentration fitted with logarithmic equation.

By examining a typical $550 \times 550\text{-}\mu\text{m}$ SEM micrograph (200x magnification) of a specimen it is unlikely to view more than one of these flaws at a time, as the viewing area is only 0.3% of the total area in which the two flaws are likely to inhabit. The random unbiased evaluation of approximately 200 micrographs would ensure the viewing of at least one of these flaws.

7.6 Origin of Critical Flaws

7.6.1 Processing Defects

Experimental results indicate that critical flaw size does not strictly correlate to any of the parameters that were investigated. It is hypothesized that, instead of an extrinsic factor like temperature or filler size determining the critical flaw size, critical flaws are the result of intrinsic

defects, a function of the mode and quality of processing. A re-evaluation of critical flaw size of all porcelain compositions is shown in Figure 72.

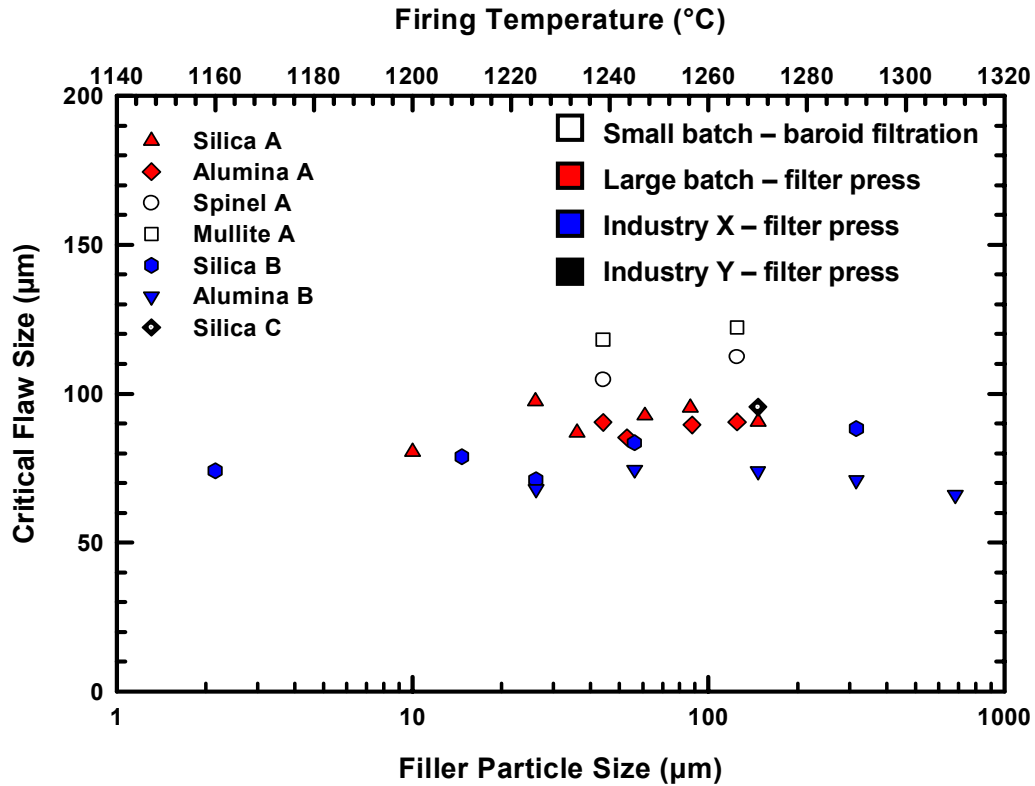


Figure 72. Graphical representation of the different processing routes taken to create Porcelain A, B, and C bodies.

What is shown in the figure is an indirect relationship between processing route and critical flaw size. Within this narrow range of critical flaw sizes, each processing route appears to correspond to a specific regime. Silica B and Alumina B, processed industrially using a filter press and a very large batch (>2000 L), appear to inhabit the smaller end of the flaw size regime, while Mullite A and Spinel A appear to contain the largest flaws, and were processed in a laboratory setting using a small batch (5 L) and a baroid filtration system. Silica A and Alumina A (white) were also processed in a laboratory but using a slightly larger batch (40 L) and a filter press. Silica C was also produced in a different industrial setting in a large batch (>2000 L) with a filter press. These results do not pinpoint the processing step which generates these critical flaws, but from these results it is evident that body compositions industrially prepared contain smaller critical flaws than

those prepared in a laboratory setting; and, as a result, fired porcelain B compositions mechanically performed better than their Porcelain A counterparts (see Figure 56). Strength and elastic moduli were also higher in both cases.

7.6.2 *Inhomogeneous Microstructure (Agglomerates)*

A particle agglomerate is defined by Reed¹³¹ as a group of particles that are bonded together that may behave as a larger pseudoparticle. Rahaman¹³² further classifies agglomerates into two categories: hard and soft. Soft agglomerates are held together by fairly weak surface forces and can be broken down into primary particles by agitation in a liquid. Hard agglomerates are instead bonded by solid bridges, and cannot be broken down by ultrasonic agitation. It is proposed that filler particles, such as quartz and alumina tend to clump together in the bulk, dry state due to relatively weak static forces forming into soft agglomerates. When added to a wet suspension, many of these particle agglomerates are dispersed by chemicals added to the suspension medium (water). However, many of these agglomerates are not broken up until the mixing process takes place, or at all. It is proposed that this processing step is the key factor that controls critical flaws (and in so doing, strength) to the extent that critical flaws are intrinsic to the batching, mixing and forming processes, not firing temperature or composition. It is hypothesized that mixing plays a decisive role in determining whether the final fired microstructure will be homogeneous or not.

By definition, the smallest agglomerate possible would consist of two adjoined particles (Figure 73a). However, it is believed that the most likely scenario involving an agglomerate of smaller particles generating a much larger flaw would involve several adjacent particles creating interconnected interstitial voids that form a defect. Given this constraint, the smallest effective agglomerate would have to consist of at least three primary particles (Figure 73b). However, in order for an interstitial defect to be larger than one of its primary particle constituents, it is necessary for many particles to be agglomerated together, the resultant flaw a function of the combined interstitial space, as shown in Figure 73c.

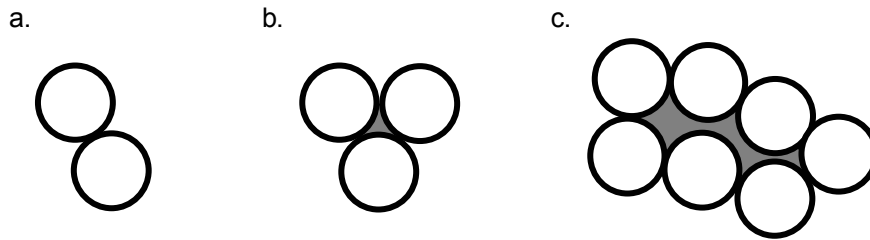


Figure 73. Schematic of particle agglomerates including a) two-particle agglomerate, b) three-particle agglomerate with interstitial defect, and c) multi-particle agglomerate resulting in large defect.

Assuming a standard porcelain body composition, its quartz grains are initially 45 μm or smaller (~ 325 mesh). In order for a cluster of 45- μm particles to form a 100- μm flaw, many grains must be within the cluster, as shown in Figure 73c. Since it was observed that a 45- μm quartz grain does not spontaneously fail due to thermal stresses within the microstructure,⁴ it is reasonable to assume that a large flaw is created due to interstitial voids created between agglomerated quartz particles, not by the coalescence of already-cracked quartz grains. Figure 74 shows this occurrence in a typical SEM micrograph. As shown in this figure, a cluster of quartz particles creates internal surface area that is inaccessible to the rest of the system during firing. Closed off to alkali fluxing agents within the glass phase that allow the quartz to dissolve at a much lower temperature, the quartz surfaces have a melting point of 1723°C¹³³ and do not react at porcelain firing temperatures (1250–1300°C), resulting in interstitial void space between the particles on the order of several times the primary particle dimension. It is proposed that it is flaws such as these that are inherent to the processing and act as the critical flaws, dictating strength. While this model assumes that it is the filler particles that make up the clusters, flux particles such as feldspars or nepheline syenite are in the size range that static agglomeration may occur in the dry raw material as well, though their propensity for melting, even in the agglomerated state, is much higher.

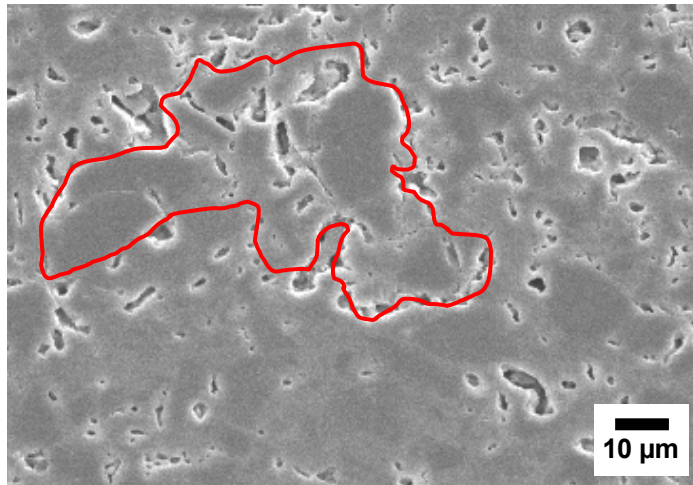


Figure 74. SEM Secondary electron image of Silica A porcelain surface showing a cluster of agglomerated particles.

In other words, feldspar agglomerates could possibly be the source of a critical flaw; however, since feldspar dissolves more readily into the glass phase at temperature than quartz, the existence of large coalesced quartz grain clusters is the more likely source. No microstructure evaluated in this study revealed a cluster of feldspar grains generating a larger flaw.

The cluster model has, thus far, assumed equally sized spheres as the agglomerate constituents. This is a highly idealized situation. In practice, depending on the industry, different grades of porcelain filler particles are sometimes used. The most common is a -325 mesh. This means that a majority of particles have been passed through a 325-mesh sieve (a screen containing 45- μm openings). This creates a distribution of particle sizes present, because all particles that pass through the screen are not exactly 45 μm . Some of them are smaller. Still other particles can be larger, because many raw material specifications allow a percentage of larger material that is retained on a 325-mesh screen or larger, though it is a minority fraction. Table XXV shows the typical sieve analysis of a -325 mesh quartz industrial product (SIL-CO-SIL 52, U.S. Silica, Berkeley Springs, WV).

Table XXV. Example of sieve analysis for industrial-grade quartz raw material.

<i>USA std. sieve size</i>		<i>% Retained</i>		<i>% Passing</i>
<i>Mesh</i>	<i>Microns</i>	<i>Individual</i>	<i>Cumulative</i>	<i>Cumulative</i>
100	150	0.0	0.0	100
140	106	0.0	0.0	100
200	75	0.3	0.3	99.7
270	53	1.7	2.0	98.0
325	45	2.5	4.5	95.5

This table can be interpreted as follows: 100 percent of the material passes through a 140-mesh (106- μm) sieve, but 0.3% of it is retained on a 200-mesh sieve. This means that 0.3% of the material is 75–106 μm in size. Another 2.0% was retained on the 270-mesh (53- μm) sieve, indicating that this percentage is between 53 and 75 μm in size. 2.5 percent more material passed all except the 325-mesh (45- μm) sieve, making this percentage of material between 45 and 53 μm in size. The remaining 95.5% of the material passes through the 325-mesh sieve; therefore, the majority of the material is smaller than 45 μm .

With this arrangement as a more realistic model, it is possible for there to be a cluster of primary particles that are of unequal size. A large flaw can still occur within the interstices of particles that are of unequal size, though it is acknowledged that spherical particles of equal size have a maximum possible packing density of only 74%, giving rise to the likelihood of more interstitial space between a cluster of monosized particles than in a cluster of unequally-sized grains. Furthermore, it is recognized that quartz grains are not ideal spheres; therefore, the most realistic model of a cluster would be the packing arrangement of a series of non-spherical particles having a distribution of sizes. It is evident from Figure 74 that the primary particles constituting the cluster are neither spherical nor do they appear to be the same size. This logically leads to the observation that this more realistic model would allow for a distribution of cluster sizes, and as such a distribution of flaw sizes. However, it is believed that this is not the case; that it is the degree or intensity of mixing that limits the maximum effective cluster size, reducing their population to that of a series of approximately equal-sized clusters within the body.

7.6.3 Degree of Mixedness

Ideally liquid suspensions are mixed with high-intensity mixers that suspend all raw materials, such that all component particles are evenly distributed throughout the material. While results indicate that primary filler particles cannot act as critical flaws, this assertion assumes that grains are evenly distributed throughout the microstructure, the result of ideal processing. In reality, this is not the case. Evidence to support this hypothesis is shown in Figure 75.

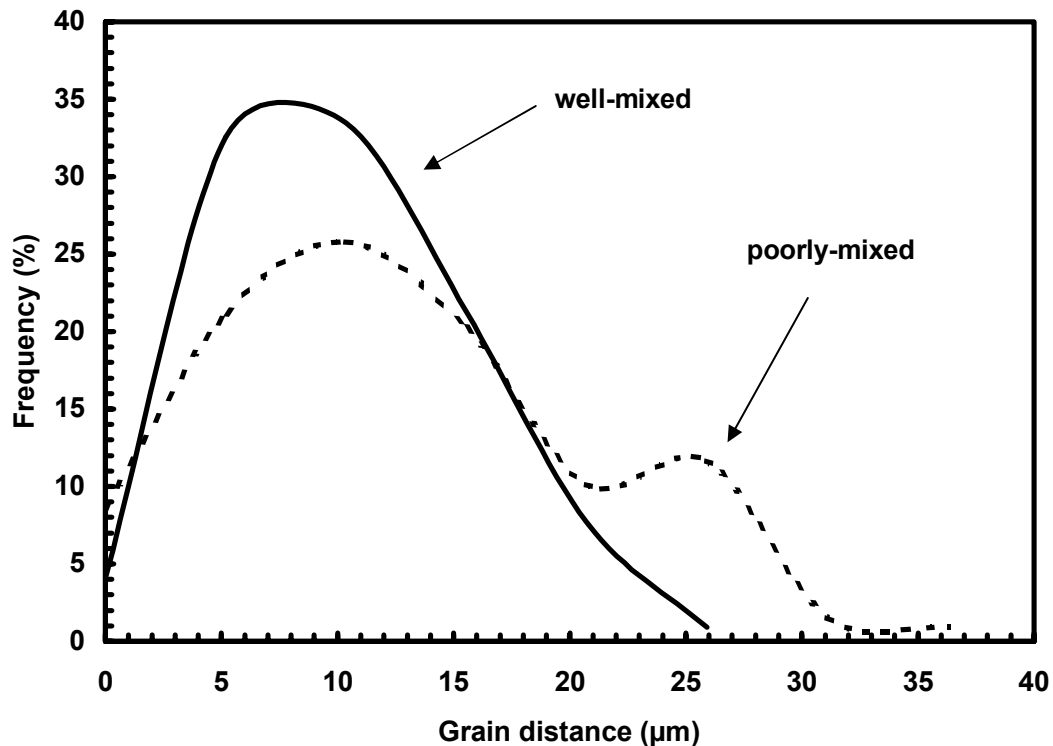


Figure 75. Plot of frequency versus grain distance for two near-identical porcelain bodies processed with different mixing routes.¹³⁴

This figure illustrates the effects of mixing on a series of two stoneware porcelain tile body compositions with the same fired composition; however, one of the bodies was industrially mixed, while the other was mixed in a laboratory setting.¹³⁴ The laboratory-mixed body is classified as a well-mixed system, while the industrially mixed body is considered to be a poorly-mixed system. In Figure 75 grain distance represents the average center-to-center nearest-neighbor distance between filler particles, measured by inspecting several SEM images representative of the

compositional microstructure. A well-mixed system will show a normal distribution, with a maximum at the mean grain distance (solid line). This occurs because in a well-mixed system particles are evenly distributed and all nearest-neighbor distances are approximately the same. This is shown in Figure 76a. For a poorly mixed system, clusters of particles are prevalent and when measuring the nearest-neighbor distance relative to a particle in a cluster, there is a bimodal distribution (dashed line). Nearest-neighbor distances reflect not only neighboring particles within the same cluster (small grain distance), but also neighboring grains within nearby clusters, which are further away. This is shown in Figure 76b. As a result, there is one maximum for a system that is well mixed, and for a poorly mixed system multiple maxima will arise (in this case two).

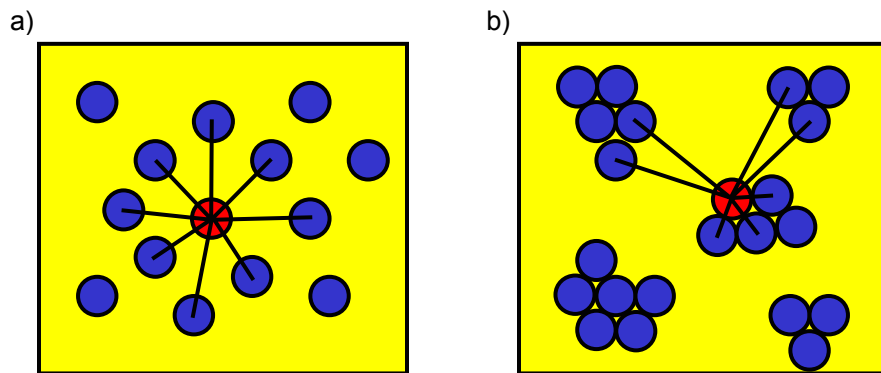


Figure 76. Schematic of glass-particle matrices illustrating nearest neighbor distances relative to a reference particle for a) a well mixed system and b) a poorly mixed system containing particle clusters.

By doing this process, it is possible to ascertain not only the existence of particle clusters, but also the relative degree to which clustering occurs, based on the intensity and number of maxima that are observed in a grain-distance-versus-frequency plot.

Typical high-intensity mixing will break up most large clusters due to the shear forces that are established within the suspension medium. However, depending on the intensity of the mixing, it is believed particle agglomerates below a certain threshold size can survive the process. It is completely plausible for substantial amounts of particle clusters to survive the wet mixing process, even in the case where a high-efficiency industrial mixer is used. As an example,

assume an industrial batch of porcelain suspension contains up to 10^6 particle clusters. If an industrial high-intensity mixer is 99.9 percent efficient at breaking up particle agglomerates, 10^3 clusters will still survive the process. Efficiencies of industrial mixers are seldom this high, and certainly a laboratory mixer is not nearly this efficient. Therefore, the presence of particle clusters in significant numbers is extremely likely. A study in which alumina porcelain was purposely left in an as-received state showed that, due to agglomerates present in the raw materials, increasing amounts of alumina added to the body composition resulted in an overall decrease in strength.⁷⁷

7.7 Elimination of Intrinsic Flaws (Reduction of 2c)

Having substantiated the hypothesis that critical flaws are intrinsic to the processing operation of a ceramic material, a series of experiments could be conducted in an attempt to reduce or eliminate the resultant flaws. The survival of raw-material agglomerates through the batching and forming processes is likely the manner in which these intrinsic flaws are introduced to the fired microstructure. It is proposed that in an alternate processing route, an additional step be added to the processing operation that may possibly reduce or eliminate these particle agglomerates as well as prevent new ones from forming. It is unlikely that an agglomerate of clay causes critical flaws; clays are very fine-grained and have a high degree of plasticity. Therefore, the focus is on the non-plastics, the fluxes and fillers. These raw materials are known to form agglomerates in the dry state, where static forces cause attraction between particles, making them stick together. When slurried with water and mixed with a high-intensity blunger, some of the agglomerates are broken up, but many of them survive. A typical industrial process combines all raw materials before mixing at high intensity, and in this manner a majority of the mixing energy is used up on the higher surface area clay fraction, resulting in ineffective mixing of the non-plastics, allowing particle agglomerates to survive. Non-plastic materials could be mixed in such a way that more energy goes into the destruction of particle clusters, and measures could be taken to ensure that primary particles remain well suspended and do not re-agglomerate. It is proposed that an additional mixing step, where non-plastics are wet mixed in the presence of milling media and low concentrations of clay, will more effectively eliminate particle agglomerates and prevent new ones

from forming. Preliminary evaluations done by McCann¹³⁵ established a relationship between degree of mixedness and pyroplastic deformation, as shown in Table XXVI. Details of each mixing process are outlined in Reference 135. Results of strength tests performed on each type of specimen did not follow the same trend as pyroplastic deformation, but it was concluded that the degree of mixing was the definitive factor in pyroplastic deformation behavior. It is believed that to some extent the same principles should hold true for the strength. What is important to note about these data is that the 'Component Milled' series was processed in a very similar manner to that proposed in this thesis. That is, non-plastics were pre-milled with clay in smaller separate batches to disperse the raw materials prior to being added to the main batch. The main batch was then mixed at low speed (900 Hz) before dewatering.

Table XXVI. Pyroplastic Deformation and Four-Point Flexure Strength Versus Mixing Mode Where Assumed Degree of Mixedness Decreases from Top to Bottom (from McCann).¹³⁵

Mixing Mode	Avg. Deformation (mm)	Avg. MOR₄ (MPa)
Shar Mixer (2500 Hz)	14.39	56
Shar Mixer (900 Hz)	16.84	47
Vibratory Mill	17.69	52
Component-Milled	18.10	64
Mix Muller	25.15	55
Eirich Mixer	34.46	52

As a result, the strength increase relative to the standard technique of dry batching all ingredients at once (no pre-milling) and high-intensity mixing (2500 Hz) was about 12% (56 MPa to 64 MPa). It is believed that, were the 'Component-Milled' batch mixed at high-intensity frequencies, the increase in strength would be even greater due to improved dispersion of agglomerates.

If the phenomenon which causes these larger critical flaws is indeed a cluster of agglomerated primary filler particles, it is proposed that in the presence of a small population of very large flaws the strength of these porcelain bodies may not be a continuous function, but possibly a step-wise function of flaw size. If mixing efficiency was sufficient to completely eliminate an entire

population of large flaws in the system, there would be a resulting discontinuous increase in strength. While it is highly unlikely for a large agglomerate to be completely disassembled into primary particles, it could be broken into smaller agglomerates. Since particle clusters can only decrease in size by discrete amounts (incrementally on the order of the primary particle size), smaller discontinuities in strength could result from the dissipation of large agglomerates into smaller ones. Figure 77 illustrates a greatly simplified example. Assuming optimal packing in two dimensions, a particle cluster of four particles loses exactly 25% of its volume and the major axis decreases by 26.7% when it becomes a cluster of three particles.

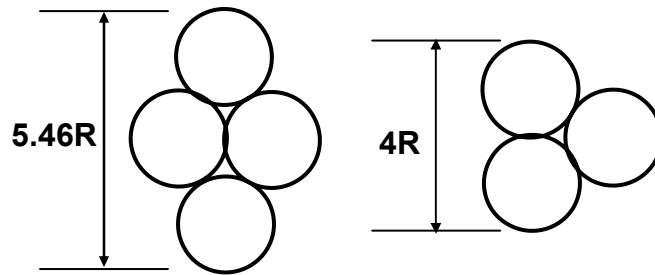


Figure 77. Schematic showing simplified four- and three- particle clusters and their dimensions (R = particle radius).

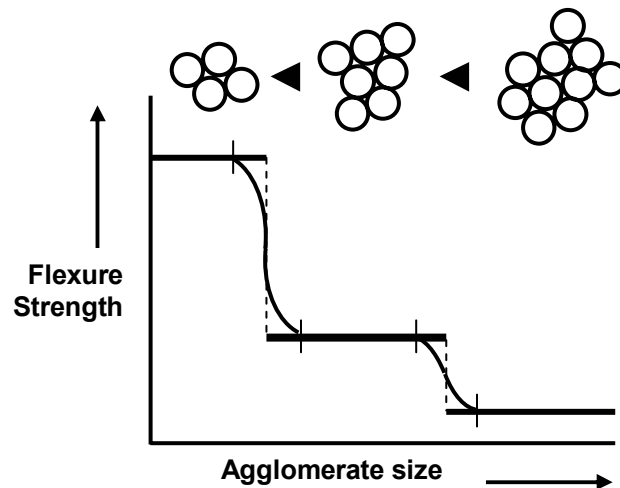


Figure 78. Schematic showing possible discontinuous strength regimes with changes in agglomerate size.

It is understood that particle clusters exist in three dimensions; therefore, multiple variations of cluster arrangements are possible. However, the purpose of this illustration is to show that, when a particle cluster is partially broken up by increased mixing efficiency, it is done by a discrete amount. Therefore, it is possible to establish discrete regimes of strength associated with the agglomerate size, rather than a continuous function. Figure 78 shows a schematic of the possible discontinuous strength regimes associated with the deconstruction of particle agglomerates. This is an idealized case, but the overall concept may explain why in industry it has been often observed that a nominal increase in mixing efficiency results in little to no increase in mechanical strength. If the additional mixing energy is insufficient to bridge one of these discontinuities, mechanical strength will stay about the same. If, however, enough energy is put into the system to decrease overall agglomerate size, the strength will markedly increase. Potential evidence of this effect may be found in flexure strength data (Figure 79) generated by Pinto,⁴ Hamano et al.,⁴⁹ and also Warshaw and Seider.²³

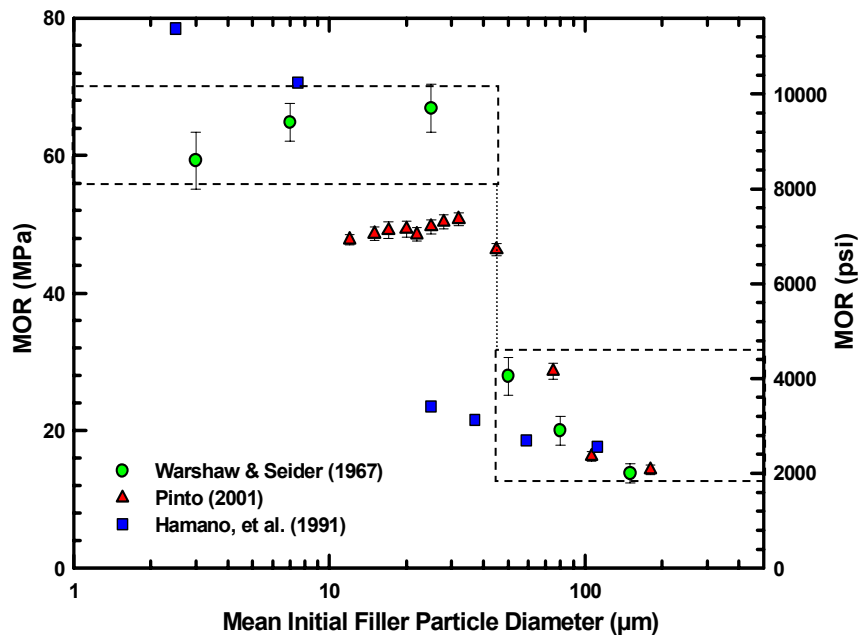


Figure 79. Flexure-strength-versus-filler-particle-size plot showing possible discontinuous strength behavior with particle size (degree of mixedness).^{4,23,49}

The abrupt decrease in strength with increasing particle size, formerly attributed to the onset of rapidly increasing residual thermal stresses within the body,⁴ could conceivably be the result of a discontinuity caused by the change in degree of mixedness with increasing particle size. What may be observed is an undetermined number of strength plateaus representative of the relative degree of microstructural homogeneity. In the case of these bodies, filler particle size varied, but the mixing route did not. However, as particle size increases, the ability for particles to stay uniformly dispersed within the suspension medium decreases. Settling may occur, and suspension homogeneity may decrease with increasing filler particle size. As a result, bodies containing large filler grains may have gravity-segregated clusters of larger particles and bodies containing small filler grains have smaller, dispersed clusters which are suspended in the medium where they can be made smaller by mixing shear forces. For typical body compositions, increasing mixing efficiency above a certain threshold may eliminate an entire flaw population completely, giving rise to a discontinuous rise in strength.

7.8 Summary

Critical flaws have been determined to dictate strength within a porcelain body. It has also been hypothesized that since there is no correlation of critical flaw size to filler particle size, type or firing temperature, that critical flaws are generated via naturally occurring particle clusters that develop among dry raw materials. When these materials are slurried together and mixed, many of these agglomerates survive the process and end up in the fired porcelain body. Therefore, it can be said that critical flaws (and critical flaw sizes) are intrinsic to the porcelain, introduced through the processing step. Results indicate that critical flaw sizes measured for industrially processed porcelain compositions were lower than those of comparable porcelain compositions processed on a smaller scale in a laboratory. It is assumed that the industrial mixing process is of higher efficiency; therefore, fewer and smaller particle clusters (critical flaws) exist within these compositions, resulting in smaller and fewer critical flaws in the fired body. As a result, the strength of these materials measures higher.

The hypothesis of having one flaw size within a microstructure was tested using a simulation of a four-point flexure test, assuming random assignment of uniform flaws to domains within a specific volume. Results of this simulation showed that a range of strengths could occur in a system without a distribution of flaw sizes due to the stress gradient present and the probability of a flaw being present at the proper location under the proper stress conditions to induce failure. A threshold concentration of 100 flaws per cm^3 was established, above which the body reduces to a single strength value. Further analysis of increasing standard deviation with decreasing flaw concentration (assuming uniform flaw size, geometry and orientation) resulted in a calibration curve that may be used to estimate flaw population in actual experimental bodies. Preliminary evaluation of Silica A porcelain resulted in a measure of 17 ± 4 flaws per cm^3 . It is speculated that complete elimination of this particular flaw population would result in a discontinuous increase in mechanical strength, because the next largest flaw size would be orders of magnitude smaller (e.g., smaller clusters, porosity, microcracks). A re-evaluation of pre-existing data may reveal this discontinuity.

8. Conclusions

This investigation presents a thorough and critical evaluation of major strength-controlling variables for a ceramic material, namely porcelain. Systematic changes made to porcelain composition, ranging from slight (alteration of filler particle size) to major (complete filler substitution) were physically and experimentally evaluated. The effects of firing temperature (over-firing/ under-firing) on mechanical properties were also evaluated. The Griffith flaw criterion served as the basis for examining the relationships between historically debated strength-dictating parameters to try and gain an understanding as to what materials and/or processes (intrinsic or extrinsic) determine the strength of the porcelain, and to what extent, if at all, they are dominant. Based on initial findings, an additional hypothesis was tested regarding the nature of flaws within these materials. It is now believed that there may be a single dominant flaw population in these porcelains, introduced as agglomerates of precursor filler particles that result in large interstitial voids when the body is fired. These critical flaws can only be eliminated through more efficient processing techniques, which involve more thoroughly dispersing particle agglomerates.

A new technique was developed for measuring fracture surface energy using a crazed glaze layer to introduce precise flaws to the surface of a porcelain body. By measuring the glaze thickness using SEM techniques, a precise measure of the flaw length was obtained, since SEM micrographs consistently show that crazing flaws extend straight through the glaze layer and arrest at the body interface. These glaze cracks act as critical flaws, as indicated by the dramatic decrease in measured mechanical strength of bodies in the presence of crazed glazes, versus identical unglazed counterparts. Therefore, the critical flaw size is equivalent to the glaze flaw length. Along with measured values for elastic modulus, Poisson's ratio, the value of flaw size was input into a derivative of the Griffith equation, modified for geometry (Equation 61), along with the failure stress of an unglazed specimen, resulting in a value for fracture surface energy of the base unglazed porcelain. Fracture surface energies for Silica B and Alumina B compositions were 4.5 J/m^2 and 8.4 J/m^2 , respectively. Silica C porcelain had a fracture surface energy value of 4.7 J/m^2 , similar to that of Silica B, which was expected due to their similar compositions.

Surface energy estimates using existing K_{Ic} values ($\sim 1.0 \text{ MPa}\cdot\text{m}^{1/2}$) resulted in a γ value of 4 J/m^2 for silica porcelain. This showed good agreement with experimental results, lending credibility to the accuracy of the new technique. A linear relationship between elastic modulus and fracture surface energy was observed for the porcelain bodies tested, as well as for other materials which possess similar bonding character (mixed ionic/covalent Si-O, Al-O bonds), including polycrystalline alumina. The relationship resulted in an equation ($y = 0.0683x - 0.1691$) that was used to predict the fracture surface energy of a series of untested porcelain bodies, knowing only their elastic moduli. Using this surface energy calculation with measured values for elastic modulus, Poisson's ratio, and failure stress, the calculation of critical flaw size for each porcelain material was made via a revised Griffith equation (Equation 60). The significance of this method is that, due to the recognition of the specific mathematical relationship between elastic modulus and fracture surface energy of porcelain bodies (γ scales with E), measurement techniques for elastic modulus and failure stress which are both relatively commonplace can be used to determine not only the fracture surface energy, a property that is sometimes dubiously quantified, but also the critical flaw size within the porcelain, which is often very difficult to measure without the use of fractography. For an opaque material with a complex microstructure such as porcelain, inspection techniques are particularly difficult to use. It is believed that this relationship is not unique to porcelains. It is quite conceivable that relationships exist between other materials that, between them, share similar bonding character. It would be only a matter of experimentally evaluating a different series of like materials in order to establish its unique relationship, and similar results could be derived. Therefore, through the use of a few routine experimental techniques and the well-established Griffith model, information about a material that previously required several more experiments to acquire can be more readily ascertained. It is believed that results calculated relating the fundamental nature of materials to their properties can often be more accurate than those measured using a standard technique because, as it has been shown, current testing techniques often contain many uncontrollable sources of experimental error.

In order to maximize both physical and mechanical properties, one of the critical parameters is firing temperature. Porcelain bodies possess a relatively wide temperature regime in which

properties are optimal, known as the firing range. Outside of this range, there was shown to be a dramatic decrease in overall performance, due to either under-firing or over-firing. Experimentally evaluating porcelain bodies in a gradient furnace by simultaneously firing many samples over a wide range of temperatures (1019–1325°C) resulted in the designation of the firing range for several porcelain compositions. This was based on the observation of a plateau region of maximum bulk density and linear firing shrinkage. Silica B porcelain showed an effective firing range of 1250–1280°C, alumina B porcelain 1260–1290°C, and stoneware porcelain showed the most versatility, with an effective firing range of 1250–1300°C. Based on these results (and a parabolic fit to the data), a series of trials were carried out in which the three compositions were fired to three different peak temperatures within the designated firing range, as well as one above and one below the ideal temperature region, ideally to obtain over- and under-fired bodies. Results showed that, for the three porcelain bodies, ideally firing the samples (within their firing range) resulted in the highest strength. Under-firing all bodies resulted in poor strength and low elastic modulus due to the presence of voids and unconsolidated raw materials, an effect of incomplete microstructural sintering, confirmed via SEM analysis. Over-firing the bodies had a similar negative effect on the strength of the Silica B and stoneware compositions; the microstructures were characterized by enlarged pores, indicative of gas evolution and bloating. Alumina B porcelain displayed only a slight declination in strength when fired at its maximum temperature (1310°C), indicating that the temperature regime selected for testing may have been inadequate to produce an over-fired microstructure. Elastic modulus results were more characteristic, showing a declination for both alumina and stoneware compositions. Silica porcelain B displayed an increase in E at its maximum firing temperature (1290°C), relative to lower temperatures. It is speculated that the silica and alumina porcelain were not fired at high enough temperatures to obtain truly over-fired microstructures; their behavior and microstructure were indicative of only nominal over-firing. The stoneware composition behaved precisely as predicted; it was fired well under (1160°C) and over (1310°C) its normal operating temperature (~1250°C).

Using the experimentally measured elastic modulus, Poisson's ratio, and mechanical strength, the previously developed characterization model was applied to these three porcelain compositions in order to obtain values for critical flaw size, observing changes with firing temperature. Results, however, indicated that measured critical flaw size was essentially unaffected by changes in firing temperature. Silica B maintained an average flaw size of 79.1 μm , for alumina B it was 70.7 μm . Stoneware porcelain showed a fairly constant average critical flaw size of 107.9 μm at lower temperatures, but flaw size increased dramatically at higher temperatures ($>1270\text{ }^{\circ}\text{C}$). A possible reason for this discrepancy involves the presence of large cracked grog particles located within the microstructure, as shown in SEM micrographs, which confound the calculation. Overall data suggest that, regardless of firing treatment, critical flaws of a constant size exist in the porcelain. Furthermore, critical flaw size showed no strong correlation to bulk density. This is contrary to the popular theory that a less-dense microstructure results in larger critical flaws. Although these parameters do affect the size of pores and microstructural defects within to an extent, in the presence of larger intrinsic flaws, their contribution to affecting critical flaw size is negligible. Data suggest the critical flaws within these porcelains transcend firing temperature and density; therefore, they must be introduced to the microstructure in a way not yet considered.

Very commonly, filler particles are cited as the critical flaws within porcelain bodies. To test this theory, several different species and sizes of filler particles were substituted into very similar porcelain body compositions. This series of experiments was meant to document the effect of different filler particle composition and particle size on measured mechanical properties of porcelain. Fillers were selected based on their relative strengths as well as thermal expansion coefficients relative to that of the glass phase. Quartz and alumina, commonly used fillers, were tested alongside Mullite and Mg-Al Spinel, two materials not commonly used as filler materials. Combined with quartz and alumina, these four filler species provide a fairly broad range of grain strengths and CTEs to carry out a systematic analysis with respect to mechanical properties. Using X-ray diffraction techniques, the residual strain generated within the filler grains as a result of the CTE mismatch was quantified for quartz (112), alumina (116), mullite (121), and spinel

(400) over a series of different bodies containing a range of filler particle sizes. The CTE of quartz, alumina and spinel being higher than that of the glass phase resulted in tensile strain between planes of atoms. Mullite, having a CTE lower than that of the glass, was subject to compressive strain, registering a net 'negative' strain. Overall results indicated a positive increase in residual strain with particle size for quartz, alumina and spinel bodies. For quartz and alumina bodies, critical particle size levels were reached (87 μm and 180 μm , respectively), above which residual strain was observed to decrease as particle size increased further. In this regime, filler particles spontaneously fail during cooling, causing a relaxation in strain. No inflection point was observed for spinel, but it is likely that one does exist for larger particle sizes outside the scope of the sizes tested. A defined trend for mullite porcelain with respect to particle size was not observed, thought perhaps to be confounded by the additional mullite that exists within the matrix phase that would contribute to the X-ray diffraction pattern. No observation of X-ray peak splitting was made; therefore, separation of nucleated mullite from included mullite strain was not mathematically possible. Based on the fact that different critical strain maxima were achieved in Silica A and Alumina A porcelain compositions, it is proposed that the glass phase is the stronger species. If it were weaker than the filler particles, the strain maxima for both compositions would be the same fixed value. Therefore, it can be said that the filler particles (quartz: 2 GPa, alumina: 5 GPa) are both weaker than the surrounding glass phase. When exposed to atmosphere, the glass becomes quite weak due to stress corrosion of the surface bonds. In a pristine environment, not unlike the interior of a porcelain specimen, glass has shown to have increased tensile strength, on the order of 7 GPa or higher. Overall, mechanical strength was shown to decrease with increasing filler particle size. Furthermore, the flexure strength of Alumina A body > Spinel A body > Mullite A body > Silica A body, in line with the relative strength of each filler material. An interesting effect observed over a regime of very small particle sizes for Silica A porcelain is that the flexure strength actually increased from 48 to 50 MPa as particle size increased from 5 to 25 μm . This is contrary to the typical observation of strength decrease with increasing filler particle size that is observed for bodies containing 25- μm or larger quartz particles. This is proposed to be due to favorable prestressing of the glass phase by filler

particles, which generates overlapping zones of increased glass phase compression. Prestressing caused by quartz grains within this size regime has a net positive effect, hindering the ease of flaw propagation through the glass, resulting in a higher observed strength. In this way, filler grains below a certain size actually may be beneficial to the strength of porcelain. Stresses generated by larger grains can provide even higher zones of compression; however, the beneficial effect is often negated due to size effects such as spontaneous or premature grain fracture due to the high amount of stored stress within the microstructure.

Data indicate no strong correlation between critical flaw size and filler particle size or species, maintaining a relatively constant value for each composition over the entire size range tested; typically two to three times the primary filler size. Overall, critical flaw sizes ranged from 90–120 μm , while filler sizes ranged from 10–150 μm . Individually, each composition maintained a critical flaw size that was essentially constant, with standard deviations of $\pm 4 \mu\text{m}$ or less. This is contrary to the notion that in the literature primary filler particles are often identified as critical flaws in porcelain bodies. In fact, data from this investigation show no correlation between critical flaw size and primary filler particle size. It is proposed that, although under extenuating circumstances, the presence of a very large included grain may adversely affect the mechanical strength of porcelain by acting as a critical flaw, primary filler particles of sizes typically used in industry ($<45 \mu\text{m}$) cannot act alone as critical flaws. It is hypothesized that an agglomerate of these particles, however, could.

The mechanical strength of these porcelain materials is to some extent dependent on a number of parameters; elastic modulus, density, firing temperature, filler particles, composition, etc. Critical flaws have been determined to be the underlying factor that governs the overall strength of the material. Variations of these aforementioned constraints will absolutely affect the grain size or pore size of a material. However, results of this study indicate that this does not affect critical flaws contained within these bodies. Data indicate no strong correlation of critical flaw size to firing temperature, bulk density, filler particle size or type. In most cases critical flaw sizes were several times larger than that of primary filler particles or pores existing within the microstructure,

which in literature are consistently defined as the critical flaws. Based on these findings, this cannot be true. In these bodies, whatever effect firing temperature and filler size have on the body is completely superceded by the presence of larger critical flaws. What was observed was that for a given composition critical flaw size is virtually identical, regardless of treatment. The question remains as to the precise identity of these flaws as well as the mechanism that controls their size.

Results of this investigation have led to the proposal that critical flaws and the size of those critical flaws are intrinsic to the porcelain, introduced to the system as a result of inefficient processing. The body compositions studied resulted in different average critical flaw sizes, but standard deviations were very small considering the broad range of systematic changes made to the overall composition and microstructure. Among those samples prepared using the same process or in the same location, critical flaw size was virtually identical. The reason for this is believed to be associated with mixing efficiency and the presence of agglomerated non-plastic particles within the material. A particle cluster that survives the mixing process into the fired body can result in a large flaw or void several times the size of a primary particle, which corresponds to the estimates of critical flaw size on the order of several particle diameters. Laboratory-prepared samples consistently contained larger flaw sizes than those prepared in an industrial setting, which makes sense in terms of the relative mixing efficiency that can be achieved on a small scale, relative to a large-scale industrial process. Porcelain B bodies were fundamentally different (one containing alumina and one containing silica filler), yet their critical flaw sizes were remarkably similar. The fact that both bodies were processed identically at the same location supports the notion that it is the processing step that is the critical factor in determining the critical flaw size. By increasing the mixing efficiency of a process, it is believed that fewer particle agglomerates will survive into the finished microstructure, and as a result the mechanical strength will increase.

To test the hypothesis that particle clusters could be the critical flaws within the microstructure, and that previous experimental results (mechanical testing, calculation of critical flaw size) could

be indicative of this phenomenon, a series of four-point flexure test simulations were developed, using flaw probability and random number theory. This model relies on the fact that the bending moment within a flexure specimen creates a stress gradient that diminishes toward the specimen neutral axis. Results indicate that in a microstructure containing only one flaw size, if there are sufficiently few flaws per unit volume, a distribution of strengths is generated and average strength increases. This is because in a system containing randomly located flaws under constant flexure load, the probability of a flaw occupying a region where the stress is sufficient to cause it to propagate is less than 1.00. Too many flaws (>100 per cm^3) will result in one strength value (weakest), since the probability of a critical flaw occupying the zone where it will extend approaches unity. Based on a cursory evaluation of the relationship between strength standard deviation and flaw population, a typical quartz porcelain body (Silica A) was estimated to have only 17.0 ± 4 large flaws per cm^3 , a number suitable for a system that satisfies the original hypothesis. Based on these overall results, it was deemed possible that there could be one population of flaws within these porcelain bodies, brought about by filler particle agglomerates inefficiently eliminated during the processing step. Verification of fracture origins as particle agglomerates on broken specimens would be extremely difficult to accomplish; however, filler particle agglomerates on the order of critical flaw size were positively identified in several SEM micrographs.

9. Suggestions for Future Work

9.1 Technique to Reduce Flaw Size

As mentioned previously, it is suggested that a major cause of defects found in porcelain bodies that lead to poor strength is inefficient processing. Agglomerates of raw materials that exist in the dry state survive the mixing process and end up in the finished body. Since these flaws are on the order of several times the magnitude of a primary particle, these defects act as critical flaws and govern the measured strength of the material. In an effort to reduce the number of these critical defects, a processing technique is proposed that should more efficiently break up agglomerates, as well as prevent in-situ agglomeration during the forming process. This step, henceforth referred to as pre-milling, consists of separately slurring the non-plastic raw materials (i.e., fillers and fluxes) in water, adding a low concentration (10–15% by weight) of clay to the suspension. The suspension is then vibratory milled in the presence of media, with enough intensity to break up agglomerates, but not reduce the effective particle size of the materials. Clay, being a high-surface-area material should be unaffected by the milling action and should coat the primary non-plastic particles, creating a physical barrier to re-agglomeration. A schematic of this phenomenon is shown in Figure 80. Furthermore, using clay is ideal, since it is a pre-existing component that will not change the overall batch composition.

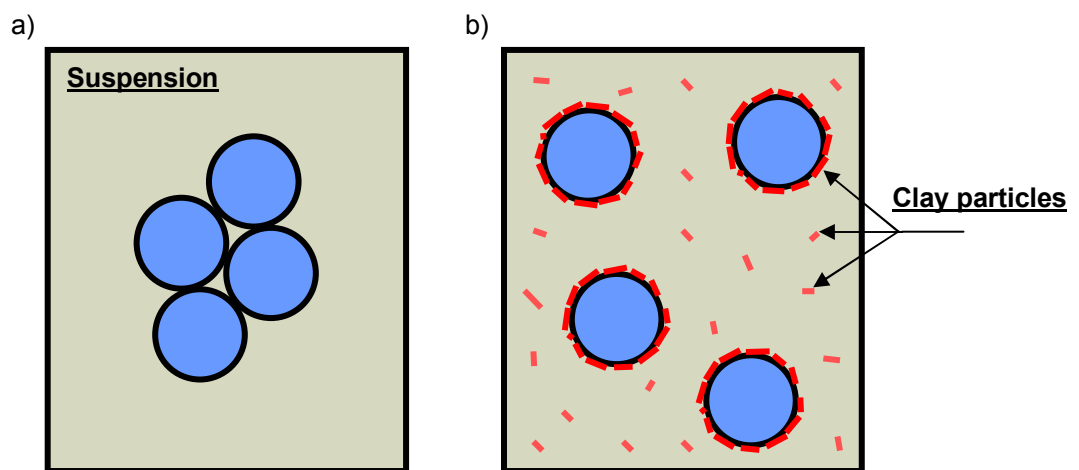


Figure 80. Schematic of particle-suspension systems showing a) agglomerate of non-plastic particles in suspension, and b) application of new technique in which clay particles coat primary grains preventing re-agglomeration.

The optimum milling times and suspension concentrations to maximize this effect are as yet unknown. This technique was used to prepare some of the samples used in the investigation (Section 3.1.3); however, the resultant mechanical strength was not explicitly correlated to mixing in any way. McCann¹³⁵ employed a variation of this procedure and observed a 14% increase in strength versus a body processed using a standard batching procedure and a low-speed mixer (900 Hz). Also, in an undocumented experiment where each raw material was separately wet-milled in the presence of 15% clay for 60 minutes then combined with the rest of the raw materials (also in the wet state) there was a dramatic 50% increase in mechanical strength.¹³⁶ The underlying reason for this is likely that, in the absence of large critical flaw-forming agglomerates, the effective flaw size within the body is reduced dramatically, in some cases to the size of porosity. In effect, smaller flaws become the new critical flaws, and because they are much smaller, they require a lot more energy to propagate; therefore, mechanical strength increases. Since clays are high-surface-area materials, the amount of energy expended mixing them is large, and they do not contribute to the generation of defects in this way. Mixing the raw materials separately from the major clay fraction applies the energy of mixing more directly to the breakup of agglomerates, which improves efficiency. It is proposed that as mixing efficiency increases, the strength of the material will increase, approaching a maximum value (Figure 81).

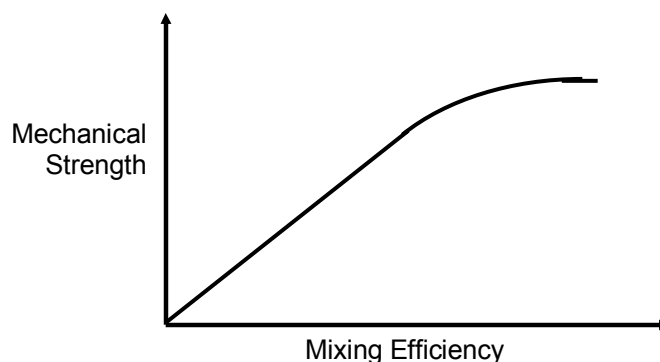


Figure 81. Predicted relationship between mechanical strength and mixing efficiency (efficiency of eliminating particle agglomerates).

This maximum value corresponds to situations in which there are no particle agglomerates left in the porcelain. Smaller defects, such as pores, will control strength in this regime. In order to increase strength further, it is these flaws that must be minimized.

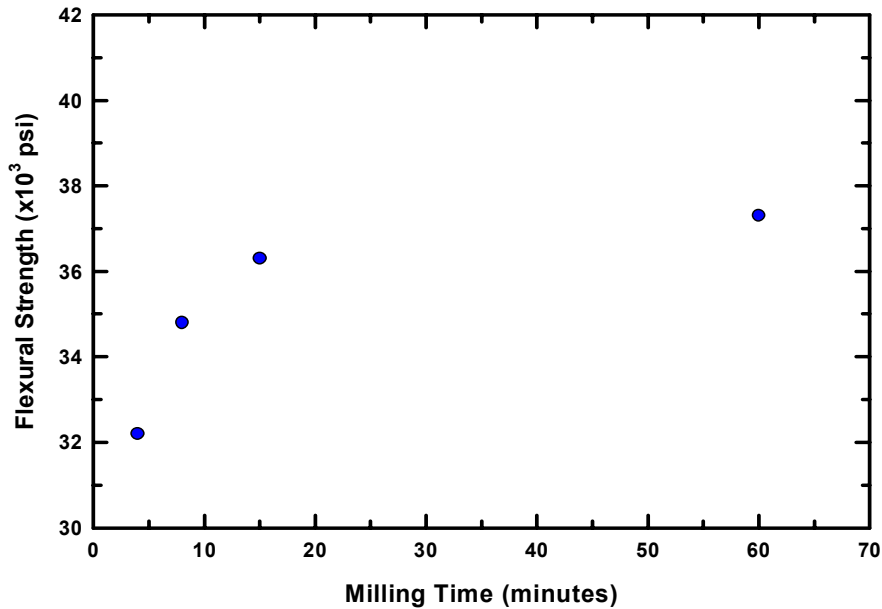


Figure 82. Plot of flexural strength versus raw material milling time for a porcelain body composition (redrawn from Knickerbocker).⁷⁷

A study by Knickerbocker et al. demonstrated a similar effect, showing the effect of milling time on flexural strength.⁷⁷ Figure 82 shows a plot of these results. Not only does the milling action decrease particle size, but it also increases the homogeneity of the mixture, breaking up agglomerates of raw materials in the process. Koenig⁷³ also concludes that ware cast from ball-milled slip is more vitreous and possesses a more glassy and homogenous microstructure. If the milling media concentration were lowered, the particle-size-reduction effect of the milling would be reduced while still maintaining the increased mixing effect. It is in this way that the addition of a relatively simple step to the processing of a ceramic body can lead to a dramatic reduction in inhomogeneities that become large flaws, thereby resulting in an overall increase in mechanical strength, regardless of composition.

9.2 Effect of Number of Surface Flaws on Strength

The technique of using a crazed glaze on the surface of a ceramic rod to measure fracture surface energy developed in this investigation results in acceptable values for fracture surface energy, but is not necessarily without error. A typical setup for measuring fracture surface energy is a flaw-free surface with one large machined-in flaw. Due to the proportionally large size of this introduced notch, the effects of any smaller flaws or microcracks co-existing on the specimen surface are often regarded as negligible. In this technique, however, many spontaneously-forming flaws of similar size occur in the glaze as a result of thermal stresses. Because of the large number of the cracks along the surface of a crazed specimen, the question arises as to whether the amount of cracks on the surface of the body affects the mechanical properties of the material, specifically the fracture surface energy. It has been assumed that the severity of the crazing is not a factor, because all crazing cracks are the same length (glaze thickness). Therefore, if any one of the crazing cracks within the loaded zone of the specimen acts as the critical flaw, the calculation of the fracture surface energy still is valid, since any one flaw is identical to the next. In addition, it is proposed that, regardless of the degree of crazing, the stress state of the glazed specimens containing crazing are nearly identical, since additional crazing of the glaze will continue to occur until the thermal stresses have been relieved to a point of equilibrium. The amount of stress remaining should be insignificant enough that it will not affect the overall surface energy of the underlying body, thereby allowing the accurate translation of this value to that of an unglazed specimen in order to calculate critical flaw size.

A study by Daniels and Moore, which entailed measuring the fracture stress of a brittle material containing varying amounts of artificial surface flaws, showed that, as the density of artificial surface flaws was increased, the fracture stress also increased.¹³⁷ This trend is contrary to that indicated by statistical fracture theories, and would suggest that the effect of the fineness of the crazing on the surface of the specimens (the number of crazing flaws) may have a significant effect on the strength of the specimen. Daniels and Moore concluded that multiple notches in a surface distribute the total amount of stress among the total number of notches, lessening the

stress concentration at any one given notch, resulting in a higher strength observed for a sample containing multiple notches compared to a sample containing only one notch.¹³⁷

Although it is assumed that there is no stress at the flaw tip caused by thermal expansion mismatch between glaze and body, a relatively simple series of experiments could test this assertion. A series of glaze compositions could be used, based on the premise that a higher CTE mismatch would result in a finer crazing array on the sample surface. The body CTE would remain the same; therefore, in order to alter the CTE mismatch, glazes with varying thermal expansion coefficients would be applied to the same body composition. As a result, specimens would be created having an identical underlying body with a coating of glaze which, depending on the sample, would have varying degrees of crazing (less or more cracks per unit surface area). These bodies could be tested in three- and four-point flexure to determine the effect, if any, the amount of surface flaws has on the bending strength and fracture surface energy. It is likely that the bending strength may vary slightly, but due to the fact that the flaw size would vary with the glaze thickness. Therefore, a calculation of the fracture surface energy, which takes into account the size of the critical flaw may be a more valid way to determine the effect, if any, of amount of localized flaws.

9.3 Triangulation of Fracture Origins

This investigation has made several assertions as to the identity of the critical flaws within porcelains. Mullite needles have never been documented as being the critical flaw in any porcelain system. They are too well-bonded to the glass matrix. Porosity in these bodies is much smaller than would be required to act as critical flaws. Experimental data clearly supports the hypothesis that they cannot be circumferential cracks around quartz grains, because the residual stresses in bodies containing typically-sized quartz grains (<45 μm) are insufficient to cause spontaneous cracking within the glass or at the grain-glass interface. Residual stresses are also inadequate to cause spontaneous internal cracking of quartz grains in this size range. Even if quartz grains were to crack, primary particles are far too small to act as critical flaws, based on calculated values of critical flaw size in the range of 80 μm . Therefore, the only way for a quartz

grain to contribute to the formation of critical flaws is to have multiple particles acting in unison as an agglomerate, the interstitial space between the particles in the cluster forming the flaw. As logical as this hypothesis sounds, it was formed using somewhat of a 'process-of-elimination' method, with data supporting the lack of feasibility of other flaw modes. The best way to confirm the suspected identity of a critical flaw is to perform fractography on the specimen and identify the flaw origin by visual inspection. For porcelains, this technique proves to be very problematic due to the high level of obscurity that one encounters when examining a porcelain fracture surface using microscopy making it extremely difficult to pinpoint the flaw origin.¹³⁸ Clusters of quartz particles were frequently observed forming a large critical-sized void in SEM micrographs (Figure 74). This verifies that indeed flaws of this nature are present; however, whether these clusters were flaw origins was not verified. The only way to say for certain that quartz agglomerates are the flaw origins is to visually observe this.

The precise location of a flaw origin can be determined if three sonic transducers are placed on a specimen in a specific manner during flexure testing, as shown in Figure 83. Two of the transducers are placed at each end of the specimen and one is placed on the surface in compression. A standard flexure test is carried out to completion and during the test each transducer sends ultrasonic pulses through the specimen. At the exact moment of failure each transducer detects the fracture because the pulse-echo time decreases when it encounters the discontinuity of the propagating critical flaw. This allows the calculation of the distance from the transducer to the critical flaw in terms of a locus of points in the form of a sphere of radius r . When three transducers are used, the intersection of all three spheres occurs at only two points, one of which lies outside the specimen completely, the other describing the exact location of the fracture origin. Using this information, the exact x,y coordinates of the origin could be transferred to an SEM micrograph of the fracture surface, pinpointing the fracture origin for one to visually observe. The same thing could be done using acoustic emission, where transducers separately pinpoint the location of acoustic signals emitted as fracture occurs negating the need of an ultrasonic signal.

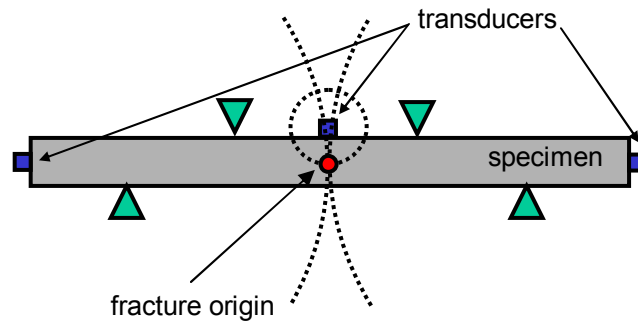


Figure 83. Schematic of experimental setup for using transducers to triangulate the exact location of a fracture origin.

This technique of triangulation was used in the development of the Global Positioning System (GPS), employing several satellites in outer space to pinpoint an object's position to within a few centimeters. Knowing this, it is reasonable to assume that, scaled down; an ultrasonic or acoustic emission method using triangulation could be used to locate in-situ the fracture origin to within a few micrometers.

REFERENCES

1. A.S. Kobayashi, *Experimental Techniques in Fracture Mechanics*; p. 149. Iowa State University Press, Ames, IA, 1973.
2. D. Broek, *Elementary Engineering Fracture Mechanics*, 4th ed.; p. 516. Martinus Nijhoff Publishers, Dordrecht, Germany, 1986.
3. R.W. Davidge, "Mechanical Properties of Ceramic Materials," *Contemp. Phys.*, **10** [2] 105-24 (1969).
4. B.M. Pinto, "Effect of Filler Particle Size on Porcelain Strength"; M.S. Thesis, New York State College of Ceramics at Alfred University, Alfred, NY, 2001.
5. R.W. Davidge and A.G. Evans, "The Strength of Ceramics," *Mater. Sci. Eng.*, **6** [2] 281-98 (1970).
6. A.A. Griffith, "The Phenomena of Rupture and Flow in Solids," pp. 33-68 in *Fracture Mechanics Retrospective*. ASTM R451, Philadelphia, PA, 1920.
7. J. Weertman, "Fracture Mechanics: A Unified View for Griffith-Irwin-Orowan Cracks," *Acta Metall.*, **26** [11] 1731 - 8 (1978).
8. C.J. Phillips, "The Strength and Weakness of Brittle Materials," *Am. Sci.*, **53** [1] 20-51 (1965).
9. I. Naray-Szabo and J. Ladik, "Strength of Silica Glass," *Nature*, **188** [4746] 226-27 (1960).
10. T.A. Michalske and B.C. Bunker, "The Fracturing of Glass," *Sci. Am.*, **257** [12] 122-9 (1987).
11. M.F. Ashby and D.R.H. Jones, International Series on Materials Science and Technology, Vol. 38, *Engineering Materials 1: An Introduction to Their Properties and Applications*; p. 278. Pergamon Press, Oxford, 1980.
12. M.P. Borom, "Dispersion-Strengthened glass Matrices - Glass-Ceramics, A Case in Point," *J. Am. Ceram. Soc.*, **60** [1-2] 17-21 (1977).
13. W.J. Frey and J.D. Mackenzie, "Mechanical Properties of Selected Glass-Crystal Composites," *J. Mater. Sci.*, **2** [1] 124-30 (1967).
14. I.L. Kalnin, "Strength and Elasticity of Whitewares: Part I, Relation Between Flexural Strength and Elasticity," *Am. Ceram. Soc. Bull.*, **46** [12] 1174-7 (1967).
15. G.W. Steere, "The Mechanical Strength of Alumina Porcelain"; M. S. Thesis, New York State College of Ceramics at Alfred University, Alfred, New York, 1977.
16. R.M. Spriggs, "Expression for Effect of Porosity on Elastic Modulus of Polycrystalline Refractory Materials, Particularly Aluminum Oxide," *J. Am. Ceram. Soc.*, **44** [12] 628-9 (1961).
17. D.P.H. Hasselman, "Relation Between Effects of Porosity on Strength and on Young's Modulus of Elasticity of Polycrystalline Materials," *J. Am. Ceram. Soc.*, **46** [11] 564-5 (1963).

18. D.P.H. Hasselman and R.M. Fulrath, "Effect of Alumina Dispersions on Young's Modulus of a Glass," *J. Am. Ceram. Soc.*, **48** [4] 218-9 (1965).
19. I.L. Kalnin, P. Cucka, S.I. Warshaw, and R. Seider, "Strength and Elasticity of Whitewares: Part II, Effect of Porosity and Mullite Content," *Am. Ceram. Soc. Bull.*, **47** [5] 498, 499, 502-4 (1968).
20. F.F. Lange, "Fracture of Brittle Matrix, Particulate Composites," pp. 1-44 in *Composite Materials*. Edited by L.J. Broutman. Academic Press, New York, 1973.
21. F.F. Lange, "Fracture Energy and Strength Behavior of a Sodium Borosilicate Glass- Al_2O_3 Composite System," *J. Am. Ceram. Soc.*, **54** [12] 614-20 (1971).
22. F.F. Lange, "The Interaction of a Crack Front with a Second-Phase Dispersion," *Philos. Mag.*, **22** [179] 983-92 (1970).
23. S.I. Warshaw and R. Seider, "Comparison of Strength of Triaxial Porcelains Containing Alumina and Silica," *J. Am. Ceram. Soc.*, **50** [7] 337-42 (1967).
24. D.P.H. Hasselman and R.M. Fulrath, "Proposed Fracture Theory of a Dispersion-Strengthened Glass Matrix," *J. Am. Ceram. Soc.*, **49** [2] 68-72 (1966).
25. D.P.H. Hasselman and R.M. Fulrath, "Micromechanical Stress Concentrations in Two-Phase Brittle Matrix Ceramic Composites," *J. Am. Ceram. Soc.*, **50** [8] 399-404 (1967).
26. F.P. Knudsen, "Dependence of Mechanical Strength of Brittle Polycrystalline Specimens on Porosity and Grain Size," *J. Am. Ceram. Soc.*, **42** [8] 376-87 (1959).
27. R.W. Rice and R.C. Pohanka, "Grain-Size Dependence of Spontaneous Cracking in Ceramics," *J. Am. Ceram. Soc.*, **62** [11-12] 559-63 (1979).
28. D.P.H. Hasselman, "Griffith Flaws and the Effect of Porosity on Tensile Strength of Brittle Ceramics," *J. Am. Ceram. Soc.*, **52** [8] 457 (1969).
29. W.C. Levengood, "Effect of Origin Flaw Characteristics on Glass Strength," *J. Appl. Phys.*, **29** [5] 820-6 (1958).
30. W.D. Kingery and R.L. Coble, "A Review of the Effect of Microstructure on the Mechanical Behavior of Polycrystalline Ceramics," *NBS Monogr. (U.S.)*, **59**, 103-13 (1963).
31. J. Selsing, "Internal Stresses in Ceramics," *J. Am. Ceram. Soc.*, **44** [8] 419 (1961).
32. W.M. Carty and B.M. Pinto, "Effect of Filler Size on Strength of Porcelain Bodies," *Ceram. Eng. Sci. Proc.*, **23** [2] 95-105 (2002).
33. R.W. Davidge and T.J. Green, "The Strength of Two-Phase Ceramic/Glass Materials," *J. Mater. Sci.*, **3** [4] 629-34 (1968).
34. P.L. Studt and R.M. Fulrath, "Mechanical Properties and Chemical Reactivity in Mullite-Glass Systems," *J. Am. Ceram. Soc.*, **45** [4] 182-8 (1962).
35. A. Dinsdale and W.T. Wilkenson, "Strength of Whiteware Bodies," *Proc. Br. Ceram. Soc.*, **6** [1] 119-36 (1966).

36. D.P.H. Hasselman, "On Porosity Dependence of Elastic Moduli of Polycrystalline Refractory Materials," *J. Am. Ceram. Soc.*, **45** [9] 452-3 (1962).
37. R.S. Piatasik and D.P.H. Hasselman, "Effect of Open and Closed Pores on Young's Modulus of Polycrystalline Ceramics," *J. Am. Ceram. Soc.*, **47** [1] 50-1 (1964).
38. V.G. Panteleev, K.S. Ramm, O.A. Vasilieva, A.V. Kiryanova, S.A. Lapshin, and J.P. Udalov, "Image Analysis in the Study of Porcelain," *Ceram. Forum. Int.*, **70** [8] 416-22 (1993).
39. Y. Nivas and R.M. Fulrath, "Limitation of Griffith Flaws in Glass-Matrix Composites," *J. Am. Ceram. Soc.*, **53** [4] 188-91 (1970).
40. N. Miyata and H. Jinno, "Theoretical Approach to the Fracture of Two-Phase Glass-Crystal Composites," *J. Mater. Sci.*, **7** [4] 973-82 (1972).
41. J.S. Banda and P.F. Messer, "The Effect of Quartz Particle Size on the Strength and Toughness of Whitewares," pp. 243-61 in *Fractography of Glasses and Ceramics II*. Edited by V.D. Frechette and J.D. Varner. The American Ceramic Society, Alfred New York, 1990.
42. C.W. Parmelee and W.R. Morgan, "Effect of Fineness of Flint on Vitrification of a Ceramic Body," *Ceram. Ind.*, **22** [3] 146-52 (1934).
43. O.I. Ece and Z. Nakagawa, "Bending Strength of Porcelains," *Ceram. Int.*, **28** [1] 131-40 (2002).
44. G. Fassbinder, "A New Ceramic Body Concept for High Strength High Voltage Insulators," *Ceram. Forum. Int.*, **79** [8] E17-E19 (2002).
45. W. Storch, H. Ruf, and H. Scholze, "Microcracking and the Strength of Quartz-Containing Clay Ceramics," *Ceram. Forum. Int.*, **61** [7] 335-42 (1984).
46. A. Dinsdale, "Crystalline Silica in Whiteware Bodies," *Trans. Br. Ceram. Soc.*, **62** [4] 321-8 (1963).
47. L. Mattyasovszky-Zsolnay, "Mechanical Strength of Porcelain," *J. Am. Ceram. Soc.*, **40** [9] 299-306 (1957).
48. E. Lee and C. Kim, "Influence of Particle Size of Quartz on the Strength of Porcelain Body," *J. Kor. Ceram. Soc.*, **21** [3] 209-15 (1983).
49. K. Hamano, Y. Wu, Z. Nakagawa, and M. Hasegawa, "Effect of Grain Size of Quartz on Mechanical Strength of Porcelain Body," *J. Ceram. Soc. Jpn.*, **99** [2] 153-7 (1991).
50. R. Harada, N. Sugiyama, and H. Ishida, "Al₂O₃-Strengthened Feldspathic Porcelain Bodies: Effects of the Amount and Particle Size of Alumina," *Ceram. Eng. Sci. Proc.*, **17** [1] 88-98 (1996).
51. P. Johnson and W.G. Robinson, "Development of Pottery Bodies - Electrical Porcelain," *Trans. Br. Ceram. Soc.*, **74** [2] 147-51 (1975).
52. M.A. Stett and R.M. Fulrath, "Mechanical Properties and Fracture Behavior of Chemically Bonded Composites," *J. Am. Ceram. Soc.*, **53** [1] 5-13 (1970).

53. R.M. Fulrath, "Internal Stresses in Model Ceramic Systems," *J. Am. Ceram. Soc.*, **42** [9] 423-9 (1959).
54. Y.M. Ito, M. Rosenblatt, L.Y. Cheng, and F.F. Lange, "Cracking in Particulate Composites Due to Thermalmechanical Stresses," *Int. J. Fract.*, **17** [5] 483 - 91 (1981).
55. G. Kirchhoff, W. Pompe, and H.A. Bahr, "Structure Dependence of Thermally Induced Microcracking in Porcelain Studied by Acoustic Emission," *J. Mater. Sci.*, **17** [10] 2809-16 (1982).
56. D.J. Green, "Stress-Induced Microcracking at Second-Phase Inclusions," *J. Am. Ceram. Soc.*, **64** [3] 138-40 (1981).
57. A.G. Evans, "Structural Reliability: A Processing-Dependent Phenomenon," *J. Am. Ceram. Soc.*, **65** [3] 127-37 (1982).
58. S.T. Lundin, "Microstructure of Porcelain," *Misc. Pub.- Natl. Bur. Stand.* **257**, 93-106 (1964).
59. S. Villegas and D.R. Dinger, "PSD Effects on Firing Properties of Porcelains I," *Am. Ceram. Soc. Bull.*, **75** [7] 71-6 (1996).
60. S.T. Lundin, *Studies on Triaxial Whiteware Bodies*. Almqvist and Wiksell, Stockholm, 1959.
61. P. Rado, "The Strange Case of Hard Porcelain," *Trans. Br. Ceram. Soc.*, **70** [4] 131-9 (1971).
62. J. Liebermann, "Avoiding Quartz in Alumina Porcelain for High-Voltage Insulators: Part I," *Am. Ceram. Soc. Bull.*, **80** [6] 37-42 (2001).
63. J. Liebermann, "Avoiding Quartz in Alumina Porcelain for High-Voltage Insulators: Part II," *Am. Ceram. Soc. Bull.*, **80** [7] 43-8 (2001).
64. I. Stubna, T. Kozik, and F. Hanic, "Young's Modulus and Mechanical Strength of Porcelain at the Firing in the Cooling Stage," *Ceram. Int.*, **18** [2] 353-4 (1992).
65. M.S. Oral, E.M.H. Sallam, and P.F. Messer, "Fracture-Initiating Flaws in Whitewares Containing Quartz," *J. Br. Ceram. Soc.*, **82** [1] 31-6 (1983).
66. Y. Ohya, Y. Takahashi, Z. Nakagawa, and K. Hamano, "Acoustic Emission From a Porcelain Body During Cooling," *J. Am. Ceram. Soc.*, **82** [2] 445-8 (1999).
67. W.M. Carty and U. Senapati, "Porcelain - Raw Materials, Processing, Phase Evolution, and Mechanical Behavior," *J. Am. Ceram. Soc.*, **81** [1] 3-20 (1998).
68. J. Liebermann, "Reliability of Materials for High-Voltage Insulators," *Am. Ceram. Soc. Bull.*, **79** [5] 55-8 (2000).
69. Z. Ke, "Fracture-Initiating Flaws in Aluminous Electrical Porcelain," *Am. Ceram. Soc. Bull.*, **69** [3] 380-90 (1990).
70. T. Sugiyama, T. Horiuchi, M. Tomizaki, and H. Takashima, "Study on High-Silica Porcelain Bodies," *Interceram*, **44** [3] 139-45 (1995).

71. N.A. Andreeva and S.S. Ordan'yan, "Technological Implications in Increasing the Strength of Porcelain," *Refract. Ind. Ceram.*, **43** [11-12] 325-8 (2002).
72. G.W. Brindley and R.M. Ougland, "Quantitative Studies of High-Temperature Reactions of Quartz-Kaolinite-Feldspar Mixture," *Trans. Br. Ceram. Soc.*, **61** [4] 599 - 614 (1962).
73. J.H. Koenig, "Particle-Size Distribution of Ingredients Versus Body Properties," *Am. Ceram. Soc. Bull.*, **19** [11] 424-30 (1940).
74. C.W. Parmelee and C.R. Amberg, "The Solubility of Quartz and Clay in Feldspar," *J. Am. Ceram. Soc.*, **12** [11] 699-710 (1929).
75. K.H. Schuller, "Reactions Between Mullite and Glassy Phase in Porcelains," *J. Br. Ceram. Soc.*, **62** [1] 103-17 (1963).
76. M.F. Tomizaki and T. Sugiyama, "Study on High-Silica Porcelain Bodies: Effects of Siliceous Stone Grain Size," *Interceram*, **44** [4] 223-5 (1995).
77. I.O. Knickerbocker, "The Research-Development-Manufacturing Cycle: A Recent Example in the Whitewares Industry," pp. 125-39 in *Technical Innovations in Whitewares: Proceedings of 1981 Alfred Whitewares Conference*. Edited by J.S. Reed, J.E. Funk, P.F. Johnson, and J.R. Varner. Alfred University Press, Alfred, New York, 1982.
78. C.R. Austin, H.Z. Schofield, and N.L. Haldy, "Alumina in Whiteware," *J. Am. Ceram. Soc.*, **29** [12] 341- 54 (1946).
79. A. Buchtel, "Pyroplastic Deformation of Whitewares"; M.S. Thesis, School of Engineering at Alfred University, Alfred, NY, 2003.
80. W.E. Blodgett, "High Strength Alumina Porcelains," *Am. Ceram. Soc. Bull.*, **40** [2] 74-7 (1961).
81. S.K. Khandelwal and R.L. Cook, "Effect of Alumina Additions on Crystalline Constituents and Fired Properties of Electrical Porcelains," *Am. Ceram. Soc. Bull.*, **49** [5] 522-6 (1970).
82. S.B. Vazquez, J.C.M. Valazquez, and J.R. Gasga, "Alumina Additions Affect Elastic Properties of Electrical Porcelains," *Am. Ceram. Soc. Bull.*, **77** [4] 81-5 (1998).
83. D.B. Kreimer and T.I. Chistyakova, "Influence of Phase Composition of Aluminous Porcelain on its Mechanical Strength," *Glass Ceram.*, **46** [11-12] 489-91 (1989).
84. A.E.R. Westman, "The Use of Fused Silica as a Raw Material in the Manufacture of Porcelain," *J. Am. Ceram. Soc.*, **11** [2] 82-9 (1928).
85. S. Maity, T.K. Mukhopadhyay, and B.K. Sarkar, "Strength of Sillimanite Sand Reinforced Porcelain Subjected to Thermal Shock," *J. Eur. Ceram. Soc.*, **17** [2] 749-52 (1997).
86. S. Maity, A. Kumar, and B. Sarkar, "Role of Nucleating Agents in the Development of High Strength Porcelain," *Ceram. Forum. Int.*, **70** [9] 483-6 (1993).
87. A.I. Avgustinik and I.T. Sintsova, "Increasing the Mechanical Strength of Porcelain by Substituting Crystallizing Glass for Quartz," *Glass Ceram.*, **24** [2] 322-6 (1967).
88. K. Dana, S. Das, and S.K. Das, "Effect of Substitution of Fly Ash for Quartz in Triaxial Kaolin-Quartz-Feldspar System," *J. Eur. Ceram. Soc.*, **24** [6] 3169-75 (2004).

89. A. Dev and R. Cook, "Zircon and Alumina Strengthen High Tension Insulators," *Ceram. Ind. (Troy, MI, U.S.)*, **7** [5-6] 24-41 (1972).
90. V. Frith, R.O. Heckrodt, and K.H. Schuller, "The Mechanical Properties of Zircon-Feldspar Porcelains," *Ceram. Forum. Int.*, **64** [10] 379-82 (1987).
91. C.S. Prasad, K.N. Maiti, and R. Venugopal, "Replacement of Quartz and Potash Feldspar with Sericitic Pyrophyllite in Whiteware Compositions," *Interceram*, **40** [2] 94-8 (1991).
92. E. Tkalcec, D. Prodanovic, W. Falz, and H.W. Hennicke, "Microstructure and Properties of Aluminous Electrical Porcelain Doped With Talc," *J. Br. Ceram. Soc.*, **83** [1] 76-80 (1984).
93. T. McVay, "Physical-Chemical Reactions in Firing Whiteware," *J. Am. Ceram. Soc.*, **19** [1] 195-7 (1936).
94. Y. Iqbal and W.E. Lee, "Fired Porcelain Microstructures Revisited," *J. Am. Ceram. Soc.*, **82** [12] 3584-90 (1999).
95. W.M. Carty, "Observations on the Glass Phase Composition in Porcelains," *Ceram. Eng. Sci. Proc.*, **23** [2] 79-94 (2002).
96. J.J. Restrepo and D.R. Dinger, "Study of the Reactions During the Firing of a Whiteware," *Ceram. Eng. Sci. Proc.*, **14** [1-2] 116-25 (1993).
97. F.H. Riddle, "Further Studies on Porcelain," *J. Am. Ceram. Soc.*, **2** [10] 812-27 (1919).
98. Y. Kobayashi, O. Ohira, T. Satoh, and E. Kato, "Compositions for Strengthening Porcelain Bodies in Alumina-Feldspar-Kaolin System," *Br. Ceram. Trans.*, **93** [2] 49-52 (1994).
99. S. Maity and B.K. Sarkar, "Development of High-Strength Whiteware Bodies," *J. Eur. Ceram. Soc.*, **16** [3] 1083-8 (1996).
100. S. Maity and B.K. Sarkar, "Phase Analysis and Role of Microstructure in the Development of High Strength Porcelains," *Ceram. Int.*, **24** [2] 259-64 (1998).
101. J.E. Schroeder, "Inexpensive High Strength Electrical Porcelain," *Am. Ceram. Soc. Bull.*, **57** [5] 526 (1978).
102. O.P. Drugoveiko, M.G. Koren, G.I. Panichev, and V.K. Petrova, "Sintering Kinetics of Electrical Porcelain," *Glass Ceram.*, **43** [1/2] 77 -9 (1986).
103. R.A. Islam, Y.C. Chan, and M.F. Islam, "Structure-Property Relationship in High Tension Ceramic Insulator Fired at High Temperature," *Mater. Sci. Eng.*, **40** [1] 132-40 (2004).
104. S.C. Sane and R.L. Cook, "Effect of Grinding and Firing Treatment on the Crystalline and Glass Content and the Physical Properties of Whiteware Bodies," *J. Am. Ceram. Soc.*, **34** [5] 145-51 (1951).
105. H.N. Kraner, "Importance of the Glass Phase in Porcelain," *J. Am. Ceram. Soc.*, **12** [6] 383-99 (1929).
106. D.B. Kreimer and T.I. Chistayakova, "Influence of Phase Composition of Aluminous Porcelain on its Mechanical Strength," *Steklo Keram.*, **22** [2] 489- 91 (1990).

107. P.L. Flaitz, "The Effect of Mullite on the Strength of High Alumina Electrical Porcelain"; M.S. Thesis, New York State College of Ceramics at Alfred University, Alfred, New York, 1977.
108. G.N. Maslennikova, V.D. Beshentsev, R.G. Orlova, and E.P. Bogdanis, "Means of Increasing The Strength of Porcelain," *Glass Ceram.*, **41** [11] 499-501 (1984).
109. G. Stathis, A. Ekonomakou, C.J. Stournaras, and C. Ftikos, "Effect of Firing Conditions, Filler Grain Size and Quartz Content on Bending Strength and Physical Properties of Sanitaryware Porcelain," *J. Eur. Ceram. Soc.*, **24** [4] 2357-66 (2004).
110. L. Hermansson and R. Carlsson, "On the Crystallization of the Glassy Phase in Whitewares," *Trans. Br. Ceram. Soc.*, **77** [1] 32-9 (1978).
111. B.M. Pinto, "Residual Strain in Quartz Particles in a Porcelain Matrix as a Function of Particle Size via X-ray Diffraction"; B.S. Thesis, New York State College of Ceramics at Alfred University, Alfred, NY, 1999.
112. Commercial Glasses, Advances in Ceramics, Vol. 18. Edited by D.C. Boyd and J.F. MacDowell, The American Ceramic Society, Columbus, OH, 1986.
113. A. Dietzel, "The Significance of Equilibrium Diagrams for the Ceramist," *Sprechsaal*, **86** [2] 253 (1953).
114. R.M. Evans, "Magnesia-Alumina-Spinel : Raw Materials, Production, and Preparation," *Am. Ceram. Soc. Bull.*, **72** [4] 59-63 (1993).
115. F.N. Cunha-Duncan and R.C. Bradt, "Synthesis of Magnesium Aluminate Spinels from Bauxites and Magnesias," *J. Am. Ceram. Soc.*, **85** [12] 2995-3003 (2002).
116. *Standard Test Method for Water Absorption, Bulk Density, Apparent Porosity, and Apparent Specific Gravity of Fired Whiteware Products*. ASTM Standard C 1191-94. Annual Book of ASTM Standards, Vol. 15.02. American Society for Testing and Materials, West Conshohocken, PA, 2000.
117. *Standard Test Method for Flexural Strength of Advanced Ceramics at Ambient Temperature*. ASTM Standard C 1161-94. Annual Book of ASTM Standards, Vol. 15.01. American Society for Testing and Materials, West Conshohocken, PA, 2000.
118. *Standard Practice for Measuring Ultrasonic Velocity in Materials*. ASTM Standard E 494-95. Annual Book of ASTM Standards, Vol 3.03. American Society for Testing and Materials, West Conshohocken, PA, 2000.
119. *Standard Test Method for Young's Modulus, Shear Modulus, and Poisson's Ratio For Ceramic Whitewares by Resonance*. ASTM Standard C 848-88. Annual Book of ASTM Standards, Vol. 15.01. American Society for Testing and Materials, West Conshohocken, PA, 2000.
120. I.C.I. Okafor and D.M. Martin, "The Effect of Temperature on the Fracture Surface Energy of a Waste Disposal Glass," *J. Am. Ceram. Soc.*, **65** [2] 87-90 (1982).
121. R.W. Davidge and G. Tappin, "The Effective Surface Energy of Brittle Materials," *J. Mater. Sci.*, **3** [1] 165-73 (1968).
122. W.M. Carty, M. Katz, and J. Gill, "The Unity Molecular Formula Approach to Glaze Development," *Ceram. Eng. Sci. Proc.*, **21** [2] 95-107 (2000).

123. J.L. Benson, "Effect of Glaze Variables on the Mechanical Strength of Whitewares"; M.S. Thesis, New York State College of Ceramics at Alfred University, Alfred, NY, 2003.
124. J.E. Shelby, *Introduction to Glass Science and Technology*; p. 73. The Royal Society of Chemistry, Cambridge, UK, 1997.
125. K.E. Sieg, "Novel Technique for Measuring Fracture Surface Energy of Ceramics"; B.S. Thesis, School of Engineering at Alfred University, Alfred, NY, 2005.
126. H. Ledbetter, S. Kim, and D. Balzar, "Elastic Properties of Mullite," *J. Am. Ceram. Soc.*, **81** [4] 1025-8 (1998).
127. I.A. Aksay, D.M. Dabbs, and M. Sarikaya, "Mullite for Structural, Electronic, and Optical Applications," *J. Am. Ceram. Soc.*, **74** [10] 2343-58 (1991).
128. L.N. Grossman, "X-Ray Strain measurement Techniques for Ceramic Bodies," *J. Am. Ceram. Soc.*, **44** [11] 567-71 (1961).
129. P. Alfeld, "Random Number Generators," (1997). University of Utah. Accessed on: July, 2005. Available at <<http://www.math.utah.edu/~alfeld/Random/Random.html>>
130. M. Haahr, "Random.org: True Random Number Service," (1998). Trinity College. Accessed on: July, 2005. Available at <www.random.org>
131. J.S. Reed, *Principles of Ceramic Processing*; p. 70. John Wiley & Sons, New York, 1995.
132. M.N. Rahaman, *Ceramic Processing and Sintering*; pp. 148-52. Marcel Dekker, New York, NY, 1995.
133. CRC Handbook of Chemistry and Physics, 77th ed. Edited by D.R. Lide. CRC Press, Inc., 1997.
134. E. Rambaldi, W.M. Carty, A. Tucci, and L. Esposito, "Glass Phase Compositions and Pyroplastic Deformation of Porcelain Stoneware Tile," 2004 (in press).
135. J.D. McCann, "Effects of Mixing on Pyroplastic Deformation"; B.S. Thesis, School of Engineering at Alfred University, Alfred, NY, 2004.
136. W.M. Carty, Alfred University, Alfred, NY, 2004, Private Communication.
137. W.H. Daniels and R.E. Moore, "Fracture Behavior of a Model Brittle Solid Containing Artificial Surface Flaws," *J. Am. Ceram. Soc.*, **48** [5] 274-5 (1965).
138. J.R. Varner, Alfred University, Alfred, NY, 2005, Private Communication.

APPENDIX A. List of Experimental Variables.

Symbol	Definition	Units
A	Area	m ²
D	Grain size	μm
E	Elastic modulus, Young's modulus	GPa
F	Force	N, kN
G	Shear modulus	GPa
G _I	Strain energy release rate	MPa·m ^{1/2}
G _{Ic}	Critical strain energy release rate	MPa·m ^{1/2}
K _I	Stress intensity factor	MPa·m ^{1/2}
K _{Ic}	Fracture toughness	MPa·m ^{1/2}
N	Bond density	bonds/m ²
P	Volume fraction porosity	no units
S ₀	Spring constant	N/m
W	Energy for crack growth	J/m
Y	Geometric shape factor	no units
b	Atomic separation distance	Å
d	Crystallographic d-spacing	Å
c	Flaw half-length	μm
r	Atomic bond distance	nm, Å
x	Separation distance	μm, nm
γ	Surface tension, Fracture surface energy	J/m ²
ε	Strain	no units
θ	Angle	degrees, radians
λ	Wavelength	nm, Å
ρ	Bulk Density	g/cm ³
ν	Poisson's ratio	no units
σ	Stress, Mechanical strength	MPa, GPa
σ _{th}	Theoretical strength	MPa, GPa
σ _c	Cohesive stress	MPa, GPa

APPENDIX B. Raw Data from Material Property Testing.

Table XXVII. Bulk Density Raw Data for Porcelain A Compositions.

Filler Size (µm)	Dry Wt. (g)	Susp. Wt. (g)	Sat. Wt. (g)	Exterior Vol. (cm ³)	Apparent Porosity (%)	Liquid Absorption (%)	Bulk Density (g/cm ³)
Silica A							
12	10.1935	6.0089	10.2113	4.202	0.424	0.175	2.426
15	10.1512	5.9432	10.1694	4.226	0.431	0.179	2.402
17	10.2056	5.9440	10.2301	4.286	0.572	0.240	2.381
20	10.2356	5.9824	10.2518	4.269	0.379	0.158	2.397
22	10.0883	5.8764	10.1051	4.229	0.397	0.167	2.386
25	9.6117	5.6028	9.6274	4.025	0.390	0.163	2.388
28	10.3375	6.0033	10.3535	4.350	0.368	0.155	2.376
32	10.4071	6.1268	10.4413	4.315	0.793	0.329	2.412
45	9.8501	5.7489	9.8687	4.120	0.451	0.189	2.391
75	9.9552	5.8143	9.9684	4.154	0.318	0.133	2.396
106	10.5562	6.1653	10.6313	4.466	1.682	0.711	2.364
180	10.3551	6.1595	10.4967	4.337	3.265	1.367	2.388
Alumina A							
125	2.7069	1.6675	2.7084	1.0409	0.1441	0.0554	2.601
88	1.7106	1.0507	1.7190	0.6683	1.2569	0.4911	2.560
53	2.4804	1.5531	2.4963	0.9432	1.6858	0.6410	2.630
44	3.1696	1.9521	3.1791	1.2270	0.7742	0.2997	2.583
Mullite A							
125	3.1628	1.9165	3.1665	1.2500	0.2960	0.1170	2.530
44	3.0107	1.8044	3.0211	1.2167	0.8548	0.3454	2.474
Spinel A							
125	4.8915	3.0308	4.9026	1.8718	0.5930	0.2269	2.613
44	3.6254	2.2303	3.6380	1.4077	0.8951	0.3475	2.575

Table XXVIII. Bulk Density Raw Data for Porcelain B Compositions and Stoneware.

Firing Temp. (°C)	Dry Wt. (g)	Susp. Wt. (g)	Sat. Wt. (g)	Exterior Vol. (cm ³)	Apparent Porosity (%)	Liquid Absorption (%)	Bulk Density (g/cm ³)
Silica B							
1160	6.7247	3.9118	6.8220	2.9102	3.3434	1.4469	2.311
1210	8.4147	4.9410	8.4328	3.4918	0.5184	0.2151	2.410
1225	6.7994	3.9658	6.7990	2.8332	-0.0141	-0.0059	2.400
1245	9.1852	5.3809	9.1959	3.8150	0.2805	0.1165	2.408
1290	5.7166	3.2609	5.7274	2.4665	0.4379	0.1889	2.318
Alumina B							
1225	5.7954	3.6661	5.8015	2.1354	0.2857	0.1053	2.714
1245	11.7211	7.4289	11.7382	4.3093	0.3968	0.1459	2.720
1270	10.0131	6.3327	10.0242	3.6915	0.3007	0.1109	2.712
1290	12.1814	7.6834	12.1927	4.5093	0.2506	0.0928	2.701
1310	8.8256	5.5258	8.8366	3.3108	0.3322	0.1246	2.666
Stoneware							
1160	7.7498	4.6319	7.9507	3.3188	6.0534	2.5923	2.335
1225	6.3420	3.7594	6.3573	2.5979	0.5889	0.2412	2.441
1245	7.1122	4.2075	7.1317	2.9242	0.6668	0.2742	2.432
1270	5.7013	3.3810	5.7302	2.3492	1.2302	0.5069	2.427
1310	5.4198	3.0820	5.4676	2.3856	2.0037	0.8820	2.272

Table XXIX. Linear Shrinkage Raw Data from Gradient Furnace Experiment.

Silica B				
Location	Green Dia. (mm)	Fired Dia. (mm)	Linear Shrinkage (%)	Temp (°C)
S1	15.26	15.25	0.07	1023
S2	15.23	15.03	1.31	1052
S3	15.24	14.34	5.91	1148
S4	15.23	13.76	9.65	1198
S5	15.25	13.75	9.84	1246
S6	15.28	13.96	8.64	1283
S7	15.27	14.57	4.58	1310
S8	15.26	14.85	2.69	1323
Alumina B				
Location	Green Dia. (mm)	Fired Dia. (mm)	Linear Shrinkage (%)	Temp (°C)
A1	15.25	15.17	0.52	1019
A2	15.26	14.98	1.83	1048
A3	15.25	14.46	5.18	1150
A4	15.24	13.94	8.53	1211
A5	15.24	13.68	10.24	1253
A6	15.27	13.73	10.09	1288
A7	15.29	13.88	9.22	1307
A8	15.25	13.95	8.52	1323
Stoneware				
Location	Green Dia. (mm)	Fired Dia. (mm)	Linear Shrinkage (%)	Temp (°C)
T1	14.53	14.34	1.31	1020
T2	14.52	13.98	3.72	1055
T3	14.51	13.33	8.13	1152
T4	14.54	13.01	10.52	1203
T5	14.56	12.95	11.06	1248
T6	14.54	12.96	10.87	1291
T7	14.53	13.04	10.25	1316
T8	14.54	13.32	8.39	1325

APPENDIX C. Raw Data from Mechanical Property Testing.

Table XXX. Four-Point Flexure Strength Raw Data for Mullite A and Spinel A Porcelain Bodies.

Mullite A- 125 μm	Mullite A- 44 μm	Spinel A- 125 μm	Spinel A- 44 μm
MOR (MPa)	MOR (MPa)	MOR (MPa)	MOR (MPa)
68.42	75.71	77.33	102.56
73.90	80.72	79.31	90.84
72.26	82.59	82.56	88.92
72.43	76.97	75.48	86.60
73.83	80.88	83.18	87.63
75.38	80.94	84.43	86.84
68.31	76.97	84.21	86.51
73.14	78.82	74.97	93.37
75.55	80.42	83.14	93.51
72.55	79.95	75.02	91.45
71.47	80.95	75.29	95.65
69.64	79.00	81.59	88.26
71.08	81.22	86.30	94.40
71.89	78.58	77.62	87.72
74.09	79.99	83.20	90.55
72.66	78.94	81.58	92.95
75.08	83.46	82.12	83.93
72.21	77.78	84.55	82.52
76.08	81.94	78.14	93.00
72.00	82.90	79.48	92.95

Table XXXI. Four-Point Flexure Strength Raw Data for Alumina A Porcelain Body.

Alumina A- 125 μm	Alumina A- 88 μm	Alumina A- 53 μm	Alumina A- 44 μm
MOR (MPa)	MOR (MPa)	MOR (MPa)	MOR (MPa)
97.05	102.21	104.14	103.34
100.89	99.71	105.02	102.20
92.39	100.08	104.72	104.27
97.41	97.10	102.02	106.07
91.22	100.08	100.20	105.48
97.66	102.23	103.00	106.33
98.85	98.22	105.63	103.35
95.43	100.76	107.16	103.27
96.81	96.26	104.62	105.22
94.41	94.70	103.03	103.34
95.71	105.30	104.92	103.50
95.86	98.50	105.76	106.28
91.29	99.40	103.25	103.63
95.87	101.22	104.76	110.21
96.03	99.65	105.19	105.57
94.56	98.21	104.13	105.23
93.71	102.54	106.06	104.22
95.49	99.81	105.47	100.91
100.04	98.27	99.90	103.44
97.98	100.44	101.03	103.63

Table XXXII. Four-Point Flexure Strength Raw Data for Silica B Porcelain Body.

Silica B 1160°C	Silica B 1210°C	Silica B 1225°C	Silica B 1245°C	Silica B 1290°C
MOR (MPa)				
58.19	78.51	78.40	74.88	61.35
58.85	78.93	82.44	76.12	69.27
60.31	69.73	76.42	76.00	63.61
64.11	81.14	71.10	75.56	58.53
60.68	76.16	77.05	72.33	69.18
55.61	76.53	79.65	74.11	61.78
55.13	76.82	74.97	74.28	68.18
54.91	81.57	81.72	72.81	63.88
64.42	81.86	77.44	75.50	63.53
58.27	82.96	83.14	74.45	63.35

Table XXXIII. Four-Point Flexure Strength Raw Data for Alumina B Porcelain Body.

Alumina B 1225°C	Alumina B 1245°C	Alumina B 1275°C	Alumina B 1290°C	Alumina B 1310°C
MOR (MPa)				
132.45	144.14	126.54	129.32	129.22
131.74	132.16	133.29	136.18	133.95
125.64	132.24	140.36	126.44	136.79
130.88	138.34	131.93	132.03	132.79
128.29	142.29	137.25	128.82	125.54
130.73	132.29	136.25	130.57	133.11
133.74	137.91	133.41	139.21	131.11
118.93	130.11	131.28	131.74	137.96
132.18	135.35	131.46	133.80	131.20
129.28	128.21	138.57	131.83	130.07

Table XXXIV. Four-Point Flexure Strength Raw Data for Stoneware Porcelain Body.

Stoneware 1160°C	Stoneware 1225°C	Stoneware 1245°C	Stoneware 1270°C	Stoneware 1310°C
MOR (MPa)				
45.66	53.42	57.60	49.26	46.34
46.95	62.51	62.41	56.92	44.29
42.99	62.06	57.51	56.83	31.75
47.91	53.78	61.19	60.43	33.19
45.58	55.59	63.11	63.04	34.45
49.02	53.79	64.01	57.25	27.82
45.93	60.48	55.66	54.24	38.48
53.07	53.83	53.26	48.90	42.55
42.46	61.26	59.36	54.76	45.81
37.30	62.50	60.48	56.27	31.36

Table XXXV. Elastic Modulus Raw Data for Porcelain A Bodies.

Filler Size (μm)	Bulk Density (kg/m^3)	Thickness (m)	V_T (m/s)	V_L (m/s)	Poisson's (μ)	Elastic Modulus (GPa)
Alumina A						
125	2583	2.27E-03	3948	6676	0.23	99.1
	2583	2.27E-03	3948	6657	0.23	98.9
	2583	2.27E-03	3948	6676	0.23	99.1
88	2560	2.76E-03	4029	6732	0.22	101.5
	2560	2.76E-03	4059	6815	0.23	103.3
	2560	2.76E-03	4029	6815	0.23	102.3
53	2630	2.57E-03	3984	6853	0.24	103.9
	2630	2.57E-03	3984	6853	0.24	103.9
	2630	2.57E-03	3984	6946	0.25	104.8
44	2601	2.57E-03	4283	6590	0.13	108.2
	2601	2.57E-03	4213	6590	0.15	106.6
	2601	2.57E-03	4283	6590	0.13	108.2
Mullite A						
125	2530	2.86E-03	3865	6085	0.16	87.8
	2530	2.86E-03	3839	6085	0.17	87.2
	2530	2.86E-03	3865	6021	0.15	86.9
44	2474	3.12E-03	3900	6783	0.25	94.3
	2474	3.12E-03	3949	6638	0.23	94.6
	2474	3.12E-03	3900	6783	0.25	94.3
Spinel A						
125	2613	2.38E-03	3839	6263	0.20	92.3
	2613	2.38E-03	3839	6347	0.21	93.3
	2613	2.38E-03	3839	6263	0.20	92.3
44	2575	2.39E-03	3950	6829	0.25	100.3
	2575	2.39E-03	3950	6732	0.24	99.5
	2575	2.39E-03	3983	6829	0.24	101.5

Table XXXVI. Elastic Modulus Raw Data for Porcelain B and Stoneware Bodies.

Temperature (°C)	Bulk Density (kg/m ³)	Thickness (m)	V _T (m/s)	V _L (m/s)	Poisson's (μ)	Elastic Modulus (GPa)
Silica B						
1160	2311	3.07E-03	3165	5203	0.21	55.9
1210	2410	2.91E-03	3549	5291	0.09	66.2
1225	2395	3.16E-03	3551	5745	0.19	71.9
1245	2408	3.15E-03	3621	5833	0.19	74.9
1290	2318	3.05E-03	3720	5980	0.18	76.0
Alumina B						
1225	2714	3.02E-03	4027	6565	0.20	105.5
1245	2720	2.81E-03	3958	6854	0.25	106.5
1270	2712	3.08E-03	4162	7000	0.23	115.3
1290	2701	2.86E-03	4086	6892	0.23	110.8
1310	2666	3.13E-03	4013	6879	0.24	106.6
Stoneware						
1160	2335	3.26E-03	3075	4794	0.15	50.8
1225	2441	3.27E-03	3593	5274	0.07	67.3
1245	2432	3.06E-03	3290	6120	0.30	68.3
1270	2427	3.31E-03	3412	6130	0.28	72.1
1310	2272	3.29E-03	3257	6327	0.32	63.6

APPENDIX D. Flaw Size Evaluation Data.

Table XXXVII. Three-Point Flexure Data and Measurements of Flaw Depth (Glaze Thickness).

Silica B		
MOR (MPa)	Mean Depth (μm)	Std. Dev. (μm)
25.52	338	18
25.91	311	12
26.73	296	22
27.22	278	7
29.03	255	8
29.33	249	12
30.82	220	4
Alumina B		
MOR (MPa)	Mean Depth (μm)	Std. Dev. (μm)
30.41	688	20
31.32	649	10
32.89	534	19
34.11	519	11
35.07	497	19
35.96	504	18
36.42	469	10
37.01	446	15
Silica C		
MOR (MPa)	Mean Depth (μm)	Std. Dev. (μm)
23.62	441	19
26.64	386	13
28.13	331	25
29.38	290	5
29.52	286	16
30.33	272	3
32.17	253	18
32.91	221	4
34.75	210	4